

University of Bath



PHD

Development of Point to Multi-Point Models for Availability and Fade Mitigation in the Millimetre Wave Frequency Range

Usman, Isa Shamsuddeen

Award date:
2005

Awarding institution:
University of Bath

[Link to publication](#)

General rights

Copyright and moral rights for the publications made accessible in the public portal are retained by the authors and/or other copyright owners and it is a condition of accessing publications that users recognise and abide by the legal requirements associated with these rights.

- Users may download and print one copy of any publication from the public portal for the purpose of private study or research.
- You may not further distribute the material or use it for any profit-making activity or commercial gain
- You may freely distribute the URL identifying the publication in the public portal ?

Take down policy

If you believe that this document breaches copyright please contact us providing details, and we will remove access to the work immediately and investigate your claim.

Download date: 13. May. 2019

Development of Point to Multi-Point Models for Availability and Fade Mitigation in the Millimetre Wave Frequency Range

A Thesis presented for the degree of Doctor of Philosophy

by

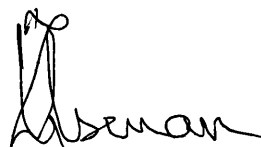
Isa Shamsuddeen Usman

Communications and Electronics Research Group
Department of of Electronic and Electrical Engineering
University of Bath

COPYRIGHT©

Attention is drawn to the fact that copyright of this thesis rests with its author. This copy of the thesis has been supplied on condition that anyone who consults it is understood to recognise that its copyright rests with its author and that no quotation from the thesis and no information derived from it may be published without the prior written consent of the author.

This thesis may be made available for consultation within the University Library and may be photocopied or lent to other libraries for the purposes of consultation



UMI Number: U487793

All rights reserved

INFORMATION TO ALL USERS

The quality of this reproduction is dependent upon the quality of the copy submitted.

In the unlikely event that the author did not send a complete manuscript and there are missing pages, these will be noted. Also, if material had to be removed, a note will indicate the deletion.



UMI U487793

Published by ProQuest LLC 2013. Copyright in the Dissertation held by the Author.
Microform Edition © ProQuest LLC.

All rights reserved. This work is protected against
unauthorized copying under Title 17, United States Code.



ProQuest LLC
789 East Eisenhower Parkway
P.O. Box 1346
Ann Arbor, MI 48106-1346

LIBRARY OF PATH
LIBRARY
70 12 JAN 2006
PKD

Fountain of Knowledge

I stand in line at the fountain
of knowledge
Waiting for my cup to be filled
And to overflow with the wisdom
Of those who paved the way
And made it possible for hard work
To elevate me to a level of
Understanding not revealed to many
It's like that path
The one less traveled

Remembrance of the past is needed
For movement into the future
How can I know where I'm going
If I don't know where I've been
And how can I attain wisdom
If I never sit at the feet of Elders
One without the other is impossible

This is a Jihad of inheritance
And in order to attain the wealth
I must stand in line at the
fountain of knowledge
And allow my cup to be filled
And to overflow with the wisdom of
Those who paved the way

I opened my mind to the
Possibilities and to the assurance
Of a new day
And I have allowed the hand of wisdom
To shade the ground on which I stand
As an open vessel I sit at the feet
Of Elders and wait to receive my
inheritance

Lakeisha Brooks

To my parents...who paved the way

Abstract

This research focuses on the study of fade mitigation in the presence of rain with particular emphasis on route diversity with selection combining for millimetre wave communications systems. This exploits the spatio-temporal properties of rainfall to enhance or maintain availability. A star network is assessed by analysing radio links over images of the radar reflectivity and differential reflectivity factors spanning two years within the UK. Two statistical measures viz. diversity gain and improvement are shown to indicate the potential benefits, especially at high attenuation, while indirectly indicating the degree of correlation. Results from analyses show that diversity advantage has a general $\sin\left(\frac{\theta}{2}\right)$ dependence.

Based on certain assumptions, a model characterisation, based on link length, availability, margin and angular separation is presented. It improves on Rec. P 1410 of the ITU-R with errors of the order of 30% and accommodating availability levels between 99-99.99%. The model is compared with cumulative distributions obtained from star-network measurements and reports within the literature, giving good agreement. Also presented is an alternative formulation to the diversity improvement, which inherently is independent of link operating frequency and allows the translation of diversity statistics from one frequency to another without need for scaling. A second model is also presented by characterising the correlation of rain attenuation on convergent links. This forms a component part of a generalised predictive model based on existing knowledge that the statistical variation of rain attenuation is log-normally distributed. Hence, the joint long term cumulative probability of fades and consequently diversity could be predicted at any frequency between 20 - 50 GHz, link length combinations less than 9 km and a variety of fade margins. Procedures are detailed in the application of both models.

The analysis results and models not only provide guidelines for route diversity design and installation, but important insights into the correlation properties of rain attenuation.

Contents

List of Figures	iv
List of Tables	vii
Notation	viii
Acknowledgements	xiv
1 Introduction	1
1.1 Millimetre Waves and the Broadband Wireless Revolution	1
1.2 The Millimetre Wave Propagation Environment	2
1.3 Proposed Systems, Standards and Research Initiatives	4
1.4 Aims and Organisation of the Thesis	5
2 Measurement and Modelling of Rainfall	9
2.1 Cloud and Rainfall Formation	9
2.2 Micro-physics of Rain	11
2.2.1 Drop Size Distributions	12
2.2.2 Drop Shape	16
2.2.3 Fall Velocities and Canting of Rain Drops	19
2.3 Rainfall Measurement Techniques	21
2.3.1 Rain Gauges	22
2.3.2 Disdrometer	23
2.3.3 Microwave Attenuation Techniques	23
2.3.4 Satellites	24
2.4 Rain Rate Distributions	25
2.4.1 Annual Statistics	25
2.4.2 Time to Space Transformations of Rain Rate Statistics	27
2.4.3 Models of Annual Rain Rate Distribution	27
2.5 Higher Order Rain Rate Statistics	29
2.5.1 Rain Rate Durations	29
2.5.2 Correlation of Rain Rates in Time and Space	31
2.5.3 Rain Cell Statistics	33
2.6 Rain Field Models	36
2.6.1 Pulse Models	37

CONTENTS

2.6.2	Markov Models	38
2.6.3	Spectral Models	39
2.7	Concluding Remarks	40
3	Radar Observations of Precipitation	42
3.1	Overview of Developments in Radar Meteorology	42
3.2	Characteristics of Meteorological Radars	45
3.2.1	Operating Frequencies	45
3.2.2	Basic Operation	45
3.2.3	Applications	49
3.2.4	Types	50
3.2.5	The Radar Equation	51
3.3	Conventional and Dual Linear Polarisation Radar Measurements	54
3.3.1	Required Accuracy in Measurements Z_H & Z_{DR}	56
3.3.2	Effect of Rain Micro-physics	58
3.4	Radar Rainfall Estimation	63
3.4.1	Reflectivity Relationships	63
3.4.2	Reflectivity and Differential Reflectivity Relationships	65
3.4.3	Identification of Non-rain Hydrometeors	67
3.5	Chilbolton Advanced Meteorological Radar	69
3.6	The CRIE Database	70
3.7	Processing and Estimation of Rain Rate	73
3.7.1	Rain Rate Estimation	74
3.7.2	Comparison of Statistics	76
3.8	Interpolation	77
3.8.1	Weighted Distance Interpolation	79
3.8.2	Radial Basis Interpolation	81
3.8.3	Data Interpolation	82
3.9	Concluding Remarks	85
4	Fade Mitigation and Route Diversity	88
4.1	The Need for Rain Mitigation	88
4.2	Scenarios Under Consideration	89
4.2.1	Point to Point	89
4.2.2	Point to Multi-point	90
4.3	Techniques	91
4.3.1	Power Control FMT	92
4.3.2	Signal Processing FMT	94
4.3.3	Diversity Selection FMT	96
4.4	FMT Implementation	97
4.4.1	Operation	97
4.4.2	Combining FMTs	98
4.5	Diversity Theory	99
4.5.1	Diversity Performance Criteria	99
4.5.2	Balanced and Un-balanced Diversity	102
4.5.3	Previous Studies	104
4.6	Diversity Simulations	105
4.7	Analysis of Results	108

CONTENTS

4.7.1	Spatial Variation	109
4.7.2	Variation with Link Length	110
4.7.3	Variation with Availability Level and Fade Depth	113
4.7.4	Effect of Frequency	115
4.7.5	Comparisons	116
4.8	Model Parameterisations	120
4.8.1	Considerations	120
4.8.2	Assumptions	122
4.8.3	Prediction Model	123
4.8.4	Symmetric Link Maximum Gain and Improvement	124
4.8.5	Link Asymmetry Reduction Factor	125
4.8.6	Angular Variation	128
4.8.7	Frequency Factor	130
4.8.8	Procedure for Calculation	130
4.8.9	Route Diversity and Model Performance	131
4.9	Concluding Remarks	135
5	Generalised Joint Statistics of Attenuation	138
5.1	Introduction	138
5.2	The Statistics of Rain and Rain Attenuation	140
5.2.1	The Statistics of Specific Attenuation	140
5.2.2	The Statistics of Rain Attenuation	141
5.3	Parameter Estimation	143
5.3.1	Parameter Estimation by Histogram Matching	143
5.3.2	Maximum likelihood Parameter Estimation	147
5.4	Auto-correlation of Log-attenuation Estimates	149
5.4.1	Theoretical Comparisons	151
5.5	Generalised Route Diversity Model	156
5.5.1	Correlation Function	156
5.5.2	Procedure for Calculation	159
5.5.3	Model Performance	160
5.5.4	Considerations	163
5.6	Concluding Remarks	164
6	Conclusions and Suggestions for Further work	166
6.1	Further Work	171
A	CRIE Data Format	174
A.1	Information Record Format	175
A.2	Raster/Scan format	176
B	Comparisons	178
B.1	Comparisons of Same Margin Diversity Model Predictions and Radar data	178
	Bibliography	182
	References and Bibliography	182

List of Figures

1.1	Configuration of a Local Multipoint Distribution System (LMDS)	6
1.2	Relationship between areas in the literature	7
2.1	The cycle of rainfall formation.	10
2.2	Variation of Ulbrich's Gamma DSD with drop diameter.	15
2.3	Variation of the normalised Gamma DSD with drop diameter.	17
2.4	Rain drop shapes.	17
2.5	Axial ratios as a function of drop size.	19
2.6	Terminal velocity of rain drops with size.	20
2.7	Features characterising the dynamics of rain rates.	30
2.8	Distribution of the rain cell ellipticity factor.	34
2.9	Rain cell profiles.	36
3.1	Basic components of a weather radar system	46
3.2	Relationships for 3 GHz radar frequency, between the radar observables, Z_H and Z_{DR} , and the drop size distribution parameters N_0 and D_0	56
3.3	Plot of Z_{DR} against D_0 for various drop shape models.	59
3.4	Differential reflectivity vs mean drop diameter using the Gamma DSD.	61
3.5	Normalised reflectivity, $10 \log \left(\frac{Z_H}{N_0} \right)$ vs mean drop diameter, D_0 when using Ulbrich's Gamma DSD.	62
3.6	Normalised reflectivity, $10 \log \left(\frac{Z_H}{N_0} \right)$ vs mean drop diameter, D_0 when using the normalised Gamma DSD.	62
3.7	Plot of horizontal reflectivity per unit rain rate as a function of differential reflectivity.	66
3.8	The Chilbolton Advanced Meteorological Radar (CAMRa) with its 25 m antenna.	69
3.9	Radar data collection scan bearing	72
3.10	Radar scan at 1.5° elevation showing reflectivity (dBZ) and differential reflectivity (dB) for range gates between 20–40 km.	74
3.11	Occurrence distribution of Z_H and Z_{DR} from the dataset.	75
3.12	Radar rainfall rate distributions for 1987/1989 showing the overall exceedance statistics (+) in conjunction with statistics obtained for the 1 st (*) and 2 nd halves (◊) of the radar PPI scans.	77
3.13	Rainfall rate statistics from the radar database and from other sources.	78
3.14	Segmented processing	83

LIST OF FIGURES

3.15	Rain rate contours derived from radar and interpolation methods	84
3.16	Comparison of the resultant rain rate statistics produced by Cressman and RBF interpolation with respect to original radar rain statistics.	86
4.1	General representation of a route-diversity link configuration.	100
4.2	Diversity gain and improvement definitions.	101
4.3	The simulation of attenuation over a rain field for a pair of convergent links.	106
4.4	Diversity gain and improvement factor at 42 GHz (V-POL) for a reference and diversity links of 3 km showing the effect of link separation.	109
4.5	Diversity gain at 42 GHz (V-POL) showing the monotonic variation of diversity with link length	110
4.6	Diversity improvement at 42 GHz (V-POL) showing the monotonic variation of diversity with link length	111
4.7	Marginal and joint attenuation distributions (at 42 GHz) for a reference 3 km link and a diversity 5 km link.	112
4.8	Marginal and joint attenuation distributions (at 42 GHz) for a reference 3 km link and a diversity 3 km link.	112
4.9	Marginal and balanced joint attenuation distributions (at 42 GHz) for a reference 3 km link and a diversity 5 km link.	113
4.10	Diversity gain (at 42 GHz) for link pairs of 3 km showing the variation with reference link availability	114
4.11	Diversity improvement (at 42 GHz) for link pairs of 3 km showing the variation with reference link fade depth	114
4.12	Diversity gain for link pairs of 3 km as a function of frequency (V-POL) at availability levels between 99–99.99%.	115
4.13	Diversity improvement for link pairs of 3 km as a function of frequency (V-POL) at fade depths exceeded at time percentages between 0.03–1%.	116
4.14	Comparison of the spatial variation sine exponent.	117
4.15	Comparisons of the normalised diversity gain (1).	118
4.16	Map of Telenor star network links	119
4.17	Marginal and joint attenuation distributions due to rain for the Norway star network.	121
4.18	Comparisons of the normalised diversity gains (2).	122
4.19	Regressions of the symmetric maximum diversity gain.	126
4.20	Regressions of the symmetric maximum diversity improvement.	127
4.21	Regressions of the diversity gain path asymmetry reduction factor.	129
4.22	Regressions of the sine exponent for various link ratios.	132
4.23	Regressions of the diversity gain frequency correction factor for availability between 99–99.99%.	133
4.24	Scattergram of model distribution errors.	134
4.25	Cumulative distribution of model prediction errors	135
5.1	Histogram distributions of log rain rate and log attenuation.	144
5.2	The different regions of the two-dimensional feature space induced by censoring	148
5.3	Correlation of log-attenuation for symmetric link lengths.	150
5.4	Correlation of log attenuation for asymmetric link lengths.	151
5.5	Correlation of log-attenuation as a function of frequency.	152
5.6	Configuration of a route diverse link pair.	153
5.7	Various functions from the literature for the correlation of rain rate.	154
5.8	Comparison of correlation estimates of for log-attenuation.	155
5.9	Regressions of the correlation of log attenuation for symmetric links.	157

LIST OF FIGURES

5.10	Regressions of the correlation of log attenuation for asymmetric links. . .	157
5.11	Ratio of link variances vs correlation offset.	158
5.12	Comparison of GBGDM vs radar (1)	161
5.13	Comparisons of GBGDM vs radar (2).	162
5.14	Model root mean square error distribution	163
5.15	Relationship between log-attenuation coefficient and joint log attenuation CDF.	164
B.1	Diversity plot for path lengths of 1.5 km and 2 km at 99.99% availability .	179
B.2	Diversity plot for path lengths of 1 km and 1 km at 99.97% availability . .	179
B.3	Diversity plot for path lengths of 2 km and 2km at 99.99% availability . .	179
B.4	Diversity plot for path lengths of 3.5 km and 5 km at 99.99% availability .	179
B.5	Diversity plot for path lengths of 2 km and 3 km at 99.9% availability . .	180
B.6	Diversity plots for path lengths of 2 km and 4 km at 99% availability. . . .	180
B.7	Diversity plot for path lengths of 3 km and 3 km at 99.99% availability . .	180
B.8	Diversity plot for path lengths of 4 km and 4 km at 99.99% availability . .	180
B.9	Diversity plot for path lengths of 6 km at 99.7% availability	180
B.10	Diversity plot for path lengths of 9 km at 99.9% availability	180
B.11	Diversity plot for path lengths of 4 km and 5 km at 99.99% availability . .	180
B.12	Diversity plot for path lengths of 5 km and 6 km at 99.99% availability . .	180
B.13	Diversity plot for path lengths of 7 km and 8 km at 99.99% availability . .	181
B.14	Diversity plot for path lengths of 5 km at 99.99% availability	181
B.15	Diversity plot for path lengths of 7 km and 7 km at 99.99% availability . .	181
B.16	Diversity plot for path lengths of 3 km and 4 km at 99.99% availability . .	181

List of Tables

2.1	Values of N_0 and Λ obtained by Joss	13
3.1	Radar operating bands with approximate wavelengths and frequencies.	45
3.2	Recent rain rate algorithm co-efficients at S-band	65
3.3	Characteristics of Z and Z_{DR} for various hydrometeor types.	67
3.4	Chilbolton radar characteristics	71
4.1	Maximum link length as a function of network availability and rain margin for networks operating at 42 GHz within the European region [CRABS 1999].	91
4.2	Nodes in the Telenor Star network.	120
4.3	Diversity gain power law parameter estimates at different availabilities for symmetric links.	124
4.4	Diversity improvement power law parameter estimates at different time percentages for symmetric links.	125
4.5	Diversity gain power law parameter values at different availabilities for asymmetric links.	128
4.6	Diversity improvement power law parameter estimates at different exceedance percentages for asymmetric links.	128
4.7	Example diversity scenarios with their resultant gains and improvements showing increases in availability levels.	132
5.1	Link estimates of the mean μ_{γ_i} ln(dB), and variance $\sigma_{\gamma_i}^2$ ln(dB) ² , of log-attenuation with increase in frequency. For each link length, the top row correspond to estimated values of the mean, while the values along the bottom are the estimated variances.	146
5.2	Parameters of the proposed log attenuation correlation model for several link configurations.	159

Notation

Roman Symbols

A_D Attenuation exceeded in the combined diversity (joint) path

A_g Gaseous attenuation

A_M Attenuation exceeded for the unprotected (single) path

$A_{ref}(t\%)$ Fade depth exceeded at time ($t\%$)

$av(\%)$ Link availability level

$\frac{b}{a}$ Ratio of major to minor rain drop axes (Axial ratio)

B Auto covariance

$B_\gamma(\tau)$ Autocovariance of specific attenuation

$B_A(\tau)$ Autocovariance of attenuation

$B_R(\tau)$ Autocovariance of rain rate

χ^2 Goodness of fit (Chi square)

$\frac{C}{I}$ Carrier to improvement ratio

C_{freq} Diversity gain frequency correction factor

C_Y Log attenuation cutoff

D Drop size

D_A Diameter of antenna

D_{cell} Rain cell diameter

D_{eq} Equivalent spherical drop diameter

D_{max} Maximum drop size

D_{min} Minimum drop size

LIST OF TABLES

D_m	Median drop size
D_o	Mean drop size
F_S	Resource request probability
$G(t)$	Diversity gain at time percent t
G_{norm}	Normalised diversity gain
$G_{symmetric}$	Maximum Symmetric (equal length) diversity gain
h	Path asymmetry diversity reduction factor
$I(A)$	Diversity improvement at fade depth A dB
$I_{symmetric}$	Maximum Symmetric (equal length) diversity improvement
K	Dielectric factor for precipitation
k	Specific attenuation coefficient
K_{DP}	Specific differential phase
L_{div}	Diversity path length
L_{max}	Maximum path length
L_{min}	Minimum path length
L_{ref}	Reference path length
M	Mean annual precipitation
M_r	Annual rainfall
$N(D)$	Drop size distribution
$N(D_{cell}, \tau)$	Rain cell diameter distribution
N_0^*	Normalised drop concentration
N_0	Drop concentration density between 0 and dD
P	Markov chain transition matrix
$P_D(A_M)$	Percentage of time in the combined diversity path with a fade depth larger than A_M
$P_M(A_M)$	Percentage of time in the unprotected path with a fade depth larger than A_M
P_{r6}	Probability of rainy 6 hour periods
P_t	Transmitter power
R	Rainfall rate
$R(t)$	Rain rate field

LIST OF TABLES

R^2	Goddness of fit (coefficient of determination)
R_C	Cressman radius of influence
R_{low}	Minimum rain rate within a rain cell
R_{max}	Maximum rain rate within a rain cell
$S(\omega)$	Spectral density function
T_s	Pulse repetition time
δV	Volume illuminated by radar
V	Rainfield advection vector
$v(D)$	Terminal velocity of rain drop
w_q	Weight of data point
X	Random variable
$X(t)$	Logarithm of rain rate field
x_g	Trigonometric coefficient for diversity gain
x_i	Trigonometric coefficient for diversity improvement
Z	Reflectivity factor
Z_{DR}	Differential reflectivity
Z_{DR}^{cal}	Differential reflectivity calibration
Z_e	Effective reflectivity factor
$Z_{H,V}$	Reflectivity for orthogonal polarisations
Z_H^{cal}	Absolute calibration of reflectivity
Greek Symbols	
α	Specific attenuation exponent
β	Thunderstorm ratio
$\rho_{A_1 A_2}(\tau)$	Attenuation correlation coefficient
$\rho_{Y_1 Y_2}(\tau)$	Log-attenuation correlation coefficient
χ	Statistical dependence index
ΔM	Difference in rain margin between radio links
η	Reflectivity per unit volume
Γ	Gamma function

LIST OF TABLES

$\Gamma(t)$	Log specific attenuation field
κ	Barnes weighting smoothing parameter
Λ	Slope of the drop size distribution
λ_n	RBF multiplier
μ	Breadth of drop size distribution
μ_X	Mean log rain rate
μ_Y	Mean of log attenuation
$\phi(x, y)$	Basis function
$\phi_{h,v}$	Phase of horizontally and vertically polarised reflectivity returns
ρ	Density
ρ_0	Density of air at standard pressure and temperature
ρ_γ	Correlation of specific attenuation
ρ_{hv}	Copolar correlation between orthogonal reflectivities
ρ_{R_1, R_2}	Correlation of point rainfall rates
ρ_R	Correlation of rain rates
ρ_w	Density of water
σ_f^2	Variance of log specific attenuation
σ_b	Backscattering cross section
$\sigma_{H,V}(D)$	Backscatter cross section for precipitation for orthogonal polarisations
σ_X^2	Variance of log rain rate
σ_Y^2	Variance of log attenuation
σ_{ZDR}	Standard deviation of differential reflectivity
σ_{ZH}	Standard deviation of reflectivity
τ	Lag between random fields
θ	Link azimuth separation angle

Abbreviations

A-TDMA	Adaptive Time Division Multiple Access
BER	Bit Error Rate
BPSK	Binary Phase Shift Keying Modulation

LIST OF TABLES

CAMRa	Chilbolton Advanced Meteorological Radar
CAPPI	Constant Altitude Plane Position Indicator
CDF	Cumulative Distribution Function
COST	European Union Collaboration on Science and Technology
CPPI	Central Plane Position Indicator
CRABS	Cellular Radio Access for Broadband Services
CRIE	Chilbolton Radar Interferometry Experiment
GBGDM	Generalised Bivariate Gaussian Route Diversity Model
dB	Decibels
DSD	Drop Size Distribution
EMBRACE	Efficient Millimetre Broadband Radio Access for Convergence and Evolution
EX-CELL	Exponential Cell model
FCT	Fade Countermeasure Techniques
FIM	Fredholm Integral Method
FMT	Fade Mitigation Techniques
FWA	Fixed Wireless Access
GHz	Giga Hertz
HY-CELL	Hybrid Cell model
IP	Internet Protocol
ITU-R	International Telecommunications Union Recommendation
LDR	Linear Depolarisation Ratio
LOS	Line of Sight
LWC	Liquid Water Content
M-P	Marshal-Palmer rain drop size distribution
Mbps	Mega bits per second
MIMO	Multiple Input Multiple Output
MP	Multiple Parameter radars
P2MP	Point to Multi-Point
P2P	Point to Point
PDF	Probability Density Function

LIST OF TABLES

PPI	Plane Position Indicator
PRF	Pulse Repetition Frequency
PSK	Phase Shift Keying Modulation
QAM	Quadrature Amplitude Modulation
QPSK	Quadrature Phase Shift Keying Modulation
RBF	Radial Basis Function Interpolation
RCRU	Radio Communications Research Unit
RHI	Range Height Indicator
RX	Receiver
SNR	Signal to Noise Ratio (dB)
TDMA	Time Division Multiple Access
TRMM	Tropical Rainfall Measuring Mission
TX	Transmitter
WLL	Wireless Local Loop

Acknowledgement

First and foremost I would like to express my gratitude to the Radio Communications Research Unit (RCRU) within the Rutherford Appleton Labs. A major part of the financial expense (both personal and official) has been funded by them, without which this PhD work would be impossible. In addition I have had the opportunity to undertake most of the research there and appreciate the help that most of the staff have extended to me at one time or the other. I consider myself fortunate to work in such a supporting and world-class environment. In particular I thank Prof Ken Craig and Dr Mike Willis for their encouraging ideas and discussions together with the opportunity to contribute to the EMBRACE and COST280 projects respectively. Also my appreciation goes to Mr John Goddard for his help especially regarding some quirks with the radar rain database. Administratively, Angela Vernon (RCRU) and Rosemary Ainsworth (University of Bath) have been very helpful. Archie Wade also deserves special mention for putting up with my variable moods and his lighthearted discussions. Other researchers who have assisted are Petter Lindholm and Terje Tjelta of Telenor for providing me with the star link network attenuation cumulative distributions.

On a personal note, I would like to thank the following for making my stay in Oxford a memorable one; Crispin and Chloe Angood, Alison Bowker, Flora Carnwath, Andrea Locascio, Udo Perdok, Alex Rhie and Jez Smith. Also my brothers and sister, Ibrahim Buba, Mustapha Abdullahi, Andrew Page and Adham Tamer have been extremely supportive over the period and for that I am deeply appreciative and grateful. Lastly but by no means least, I am especially indebted to my two supervisors Dr Kevin Paulson (formerly of RCRU) and Dr Robert Watson (University of Bath) for their inspiration, patience, encouragement and warmth.

Bath April 2005

Isa Usman

Introduction

1.1 Millimetre Waves and the Broadband Wireless Revolution

WITH the emergence of the millennium and the information age, telecommunication and broadcasting services are in a rapid phase of expansion far beyond the most optimistic expectations. Users need ever more multimedia services (e.g. digital TV, high speed internet, video conferencing, tele-education, tele-medicine, tele-working, video on demand etc.), requiring combined data rates in excess of 1 Mbit/s. The expectation is that they are available on demand, with Quality of Service (QoS) guarantees when users are mobile and within their institutions and homes.

Industry operators have a non exclusive choice of fibre, cable, and radio access networks that increasingly have to be highly integrated to deliver the high grade and capacity services to users. By using media independent transport techniques such as ATM (Asynchronous Transfer Mode) and IP (Internet Protocol), they can achieve a Broadband Integrated Services Digital Network (B-ISDN) [King 2000].

Fibre and cable have the natural capacity to carry these broadband services either within the core of the network and/or the "last mile" (i.e the connection between the operator's exchange and the customer premises). But in both cases, the cost of setting up and/or reconfiguring the network can be prohibitive. This is not likely to be so with wireless networks which offer flexibility in installation and maintenance together with lower roll out costs.

The emergence of wireless technology in general has received a boost from the wide demand for mobile wireless systems, fostered by the Global System for Mobile (GSM) standard. Cellular and personal communications services have grown

1.2. The Millimetre Wave Propagation Environment

into a global telecommunications service, with over 1 billion subscribers, far surpassing the worlds installed wired telephone base. This has made it possible to implement cost effective and reliable radio components. In conjunction, semiconductor technology has allowed for the integration of radio modules which are able to operate at frequencies of up to 100 GHz. Moreover, digital baseband technology has evolved to include a plethora of techniques in the maximisation of data rates.

Fixed wireless systems have traditionally been used as part of SDH (Synchronous Digital Hierarchy) networks. They are now extensively used in the interconnections between mobile wireless cell sites, and increasingly being used within the last mile. However, the current microwave frequency spectrum allocated by regulators around the world for such services (both terrestrial and satellite), has become congested. Proposed broadband systems require up to hundreds of MHz of bandwidth to support the high network capacities envisaged [Rouvrais 2000]. The large spectrum availability makes millimetre-wave frequencies uniquely preferable for broadband services. Therefore, future fixed wireless networks have to operate at the higher frequencies within the millimetre wave band (20-50 GHz) to provide new and existing services.

1.2 The Millimetre Wave Propagation Environment

The millimetre wave spectrum offers enormous application potential and is the new frontier for terrestrial based wireless communications. As with any emerging engineering development, the utilisation of millimetre wave frequencies also has great technical challenges. One fundamental challenge is the characterisation of radio wave propagation.

Signal reception is by direct space wave within the optical horizon, with some additional coverage due to diffraction, refraction and reflection. The surface wave tends to be rapidly attenuated, and the ionosphere does not reflect these frequencies back to earth (i.e there is no sky wave). Hence line of sight paths are required for effective communication. Due to the high propagation loss and high noise floor over a wide bandwidth, millimetre wave systems are likely to be used only for short range communications from a few metres up to a few kilometres.

The small geographical extent of any potential network allows for high frequency reuse. The reuse can be further improved by careful planning of site locations, antenna heights and antenna radiation patterns. Efficient reuse is a major

1.2. The Millimetre Wave Propagation Environment

advantage from the spectrum conservation viewpoint. By using small coverage areas with correspondingly low transmit power levels and locating antennas at lower heights, the network capacity can be increased. Also, at millimetre wave frequencies, the sizes of antennas and other radio equipment is greatly reduced. Highly directional antennas can be used to provide high power gain.

Compared to the small wavelength, leaves on vegetation will be large random scatterers, causing attenuation, depolarisation and beam broadening. Penetration losses through buildings can also pose a challenge. Furthermore, the wide-band millimetre wave channel is subject to change under different weather conditions. Atmospheric factors, such as rain, hail, gases and atmospheric turbulence will cause excess attenuation, beam bending, depolarisation, multi-path propagation and scintillation of the transmitted signal. These effects will occur with varying degrees of intensity across the spectrum. Across the channel bandwidth, such effects are not frequency selective but produce flat fading.

In particular, scattering and absorption by hydro-meteors (mainly in the form of rain) is of concern and constitutes the dominant propagation impairment in this region of the electromagnetic spectrum. These effects must be extensively studied for reliable system design and operation. System designers and operators need to establish the extent of the impairment, how often it occurs, and the means to its resolution or elimination. Across the spectrum, rain specific attenuation generally increases with rainfall rate. As rain is highly variable in space and time, the rain rate is a function of the percentage of time and depends on the climatic area. Hence, statistical models are typically used to characterise rain attenuation. Information on the cumulative distribution of rain rate and rain attenuation are available on a global basis from ITU-R recommendations.

Correspondingly, within the link power budget, a certain amount of rain fade margin will be factored in to meet the system performance requirements such as availability of service. Availability of service is defined as the long-term fraction of time that a system is in service, satisfactorily performing its intended function. Availability levels greater than 99.9% of time are nowadays common and for large portions of the millimetre wave spectrum this would require excessively high fade margins which cannot be accommodated within link power budgets due to regulatory restrictions and the need for frequency re-use. Hence imaginative Fade Mitigation Techniques (FMT) have to be employed. Several techniques are available and their use is generally conditioned on the nature of the fade and

1.3. Proposed Systems, Standards and Research Initiatives

the network.

1.3 Proposed Systems, Standards and Research Initiatives

The major markets of Europe and the USA have been at the forefront of specifying and demonstrating new systems for broadband personal communication, access and distribution, including interactivity. These aim to replace all or some parts of the network between the core network node and the subscriber terminal. Proposed systems cover a wide range of forms including multi-point distributions systems, wireless local area networks (WLAN), wireless local loop (WLL), emergent ad hoc systems and next generation mobile broadband systems [Andrisano et al. 1998].

Already, auctions of the radio spectrum have taken place for commercial exploitation around the world, but standardisation work is still going on. In particular, the USA has auctioned a large part of the millimetre wave spectrum around 28 GHz for Local Multi-point distribution services (LMDS). In Canada, 1 GHz of spectrum in the 28 GHz band is allocated for LMDS. In Europe, the proposed broadband wireless services are LMDS at 42 GHz, and Mobile Broadband Systems (MBS) at 40 GHz and 60 GHz. MBS is still in the development phase. Also, the 38 GHz band (37-39.5 GHz) has been allocated for use in personal communications network (PCN) systems to interconnect base stations. These millimetre wave links connect the base station controller and the individual cell base stations, or interconnect cell base stations.

LMDS offers users a flexible, low-cost alternative to wired local exchange and cable television services by bundling voice, video and internet services within the same channel. Typical LMDS systems have a configuration similar to mobile cellular systems as shown in Figure 1.1. Coverage areas are divided into small cells with radii of up to a few kilometres. Each cell contains a centrally located base station and multiple receivers. Point-to-point links are used to interconnect the cell with a central processing centre and/or with other cells. For point-to-multipoint links within a cell, transmitter antennas are typical sector antennas, and receiver antennas are highly directional antennas. The typical length of these links is less than 10 km. Within the UK, a fade margin of the order of 15dB is typically required to provide availabilities around 99.7% [Craig et al. 2002]. Link path diversity can be used to provide better coverage and higher availability to those users that require it. Although the system does not allow for full mobility

1.4. Aims and Organisation of the Thesis

of user terminals, it does allow for nomadic movement.

LMDS will be able to support asymmetrical transport services (typically 25 Mbit/s downstream, 1 to 2 Mbit/s upstream) [Mahonen et al. 2001]. They will be most useful in urban and suburban areas, although their use in rural areas is not foreclosed. Full coverage of all potential users by terrestrial systems will not be feasible in many areas. LMDS is therefore most suitable for competitive environments where full coverage is not an essential requirement for obtaining a significant market share.

Standardisation work of LMDS within the USA has been led by the IEEE 802.16 task group. Within Europe, the CRABS [CRABS 1998, 1999] and EMBRACE projects [Craig et al. 2002], have sought to determine the specifications for LMDS.

Also, concerted research initiatives within the European Union COST framework have sought to investigate pressing issues regarding the propagation of millimetre waves that need further understanding. In this regard, the COST 235, 255 and 280 projects (see COST235 [1996]; COST255 [1999]; COST280 [2000]) have been critical in coming up with new information and recommendations, that frame the process of system design and specification of millimetre wave systems.

1.4 Aims and Organisation of the Thesis

The main aim of this thesis is to investigate the variation of a second order statistic of rain attenuation with respect to route diverse links that occur within point-to-point and point to multi-point networks. This is the joint cumulative distribution of attenuation. It is the principal factor in evaluating the benefits due to a particular form of fade mitigation termed *Route Diversity*. Elements that contribute to its variation need to be understood and characterised.

To undertake this objective, the theory underpinning the dynamic and statistical variation of rainfall needs to be understood. In conjunction, appropriate data, theory and methods which are either directly or indirectly integral to obtaining information on rain attenuation need to be obtained. Figure 1.2 highlights the major areas and processes involved in the investigation of route diversity as a fade mitigation technique. The chapters within this thesis are organised with respect to such processes and methods.

Firstly, the theory underlying the dynamics and statistical characteristics of rainfall and rain rates are presented in Chapter 2. It ends with a summary of stochastic rain modelling techniques that allow spatio-temporal rain rates to be

1.4. Aims and Organisation of the Thesis

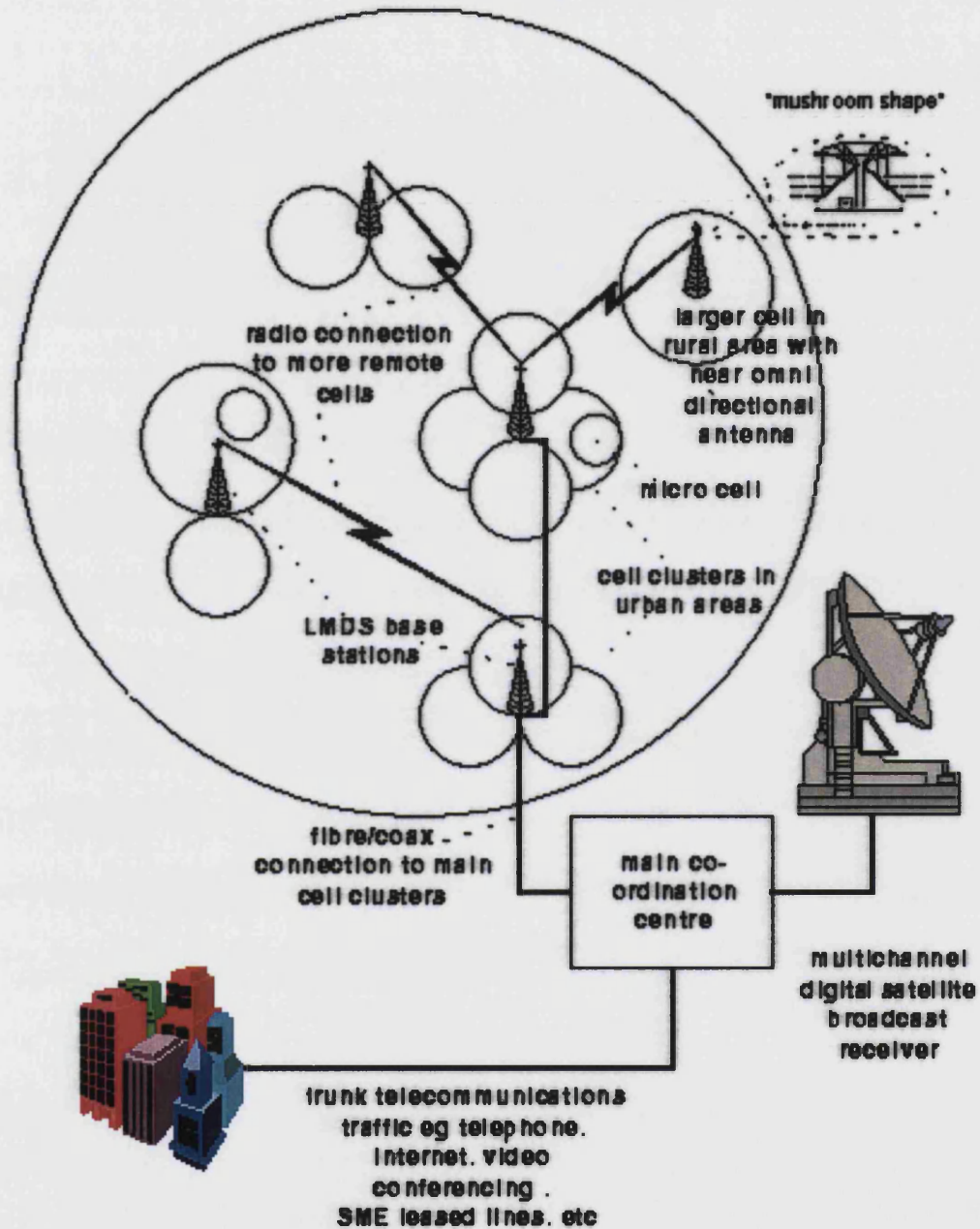


Figure 1.1: Configuration of a Local Multipoint Distribution System (LMDS)

1.4. Aims and Organisation of the Thesis

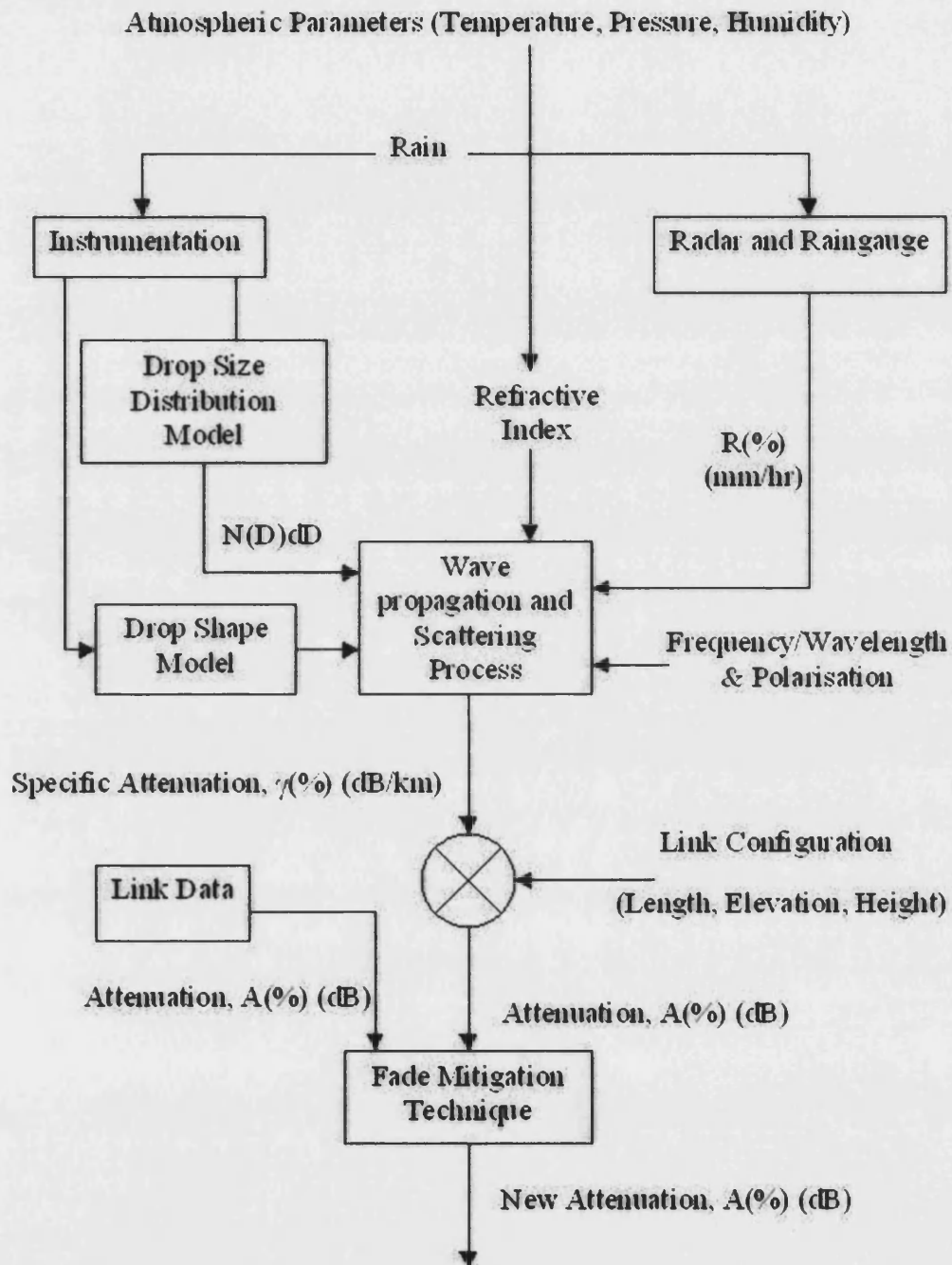


Figure 1.2: Relationship between areas in the literature

1.4. Aims and Organisation of the Thesis

generated at small scales, while still obeying the long-term statistics. Next, the use of radar as a tool for the acquisition of hydrometeor information and consequently rain rates is assessed in Chapter 3, with descriptions and analysis of precipitation data obtained over a two year period. The use of radar conveniently allows for in Chapter 4, the analysis of first order and second order rain attenuation statistics over a whole range of link configurations that would be near impossible to obtain using other more indirect techniques. In particular, statistics of route diversity variation are obtained and a prediction model is derived. In Chapter 5, an alternative but more general model formulation for the prediction of route diversity statistics is presented. Finally, Chapter 6 summarises the conclusions resulting from the investigation and suggests avenues to complement the work. Additional model comparisons together with a detailed description of the radar data format are included within the Appendix.

Measurement and Modelling of Rainfall

This chapter presents theories concerning the dynamics of rainfall formation together with the micro-physical elements (drop size distribution, drop shape and terminal velocity) that determine the rainfall rates on the ground and aloft. The spatio-temporal variation of first and second order statistics of rainfall are also presented. Existing prediction models that are used for the estimation of annual rainfall statistics are later introduced. Recent advances in the stochastic modelling of the dynamic variation of rain rates are highlighted.

2.1 Cloud and Rainfall Formation

THE lower troposphere to a height of 10 km above the earth, is the main area where the cycle of cloud formation and rainfall occurs. Cloud droplets, typically 10 μm in size and in concentrations of 10^8 m^{-3} , are formed by the process of nucleation and condensation of water vapour. Ice crystals within the cloud melt to form water drops, becoming sufficiently large to fall as rain. The two main mechanisms that lead to rainfall formation are the Bergeron process and collision/coalescence process [Lutgens and Tarbuck 2001].

The Bergeron process is the dominant rainfall mechanism in temperate regions. Supercooled cloud droplets impact on ice crystals, making larger crystals and snow flakes. As they fall below a certain height, termed the melting layer, they become water drops. The melting layer altitude is determined by the temperature profile (lapse rate), through the atmosphere. Consequently, the height of

2.1. Cloud and Rainfall Formation

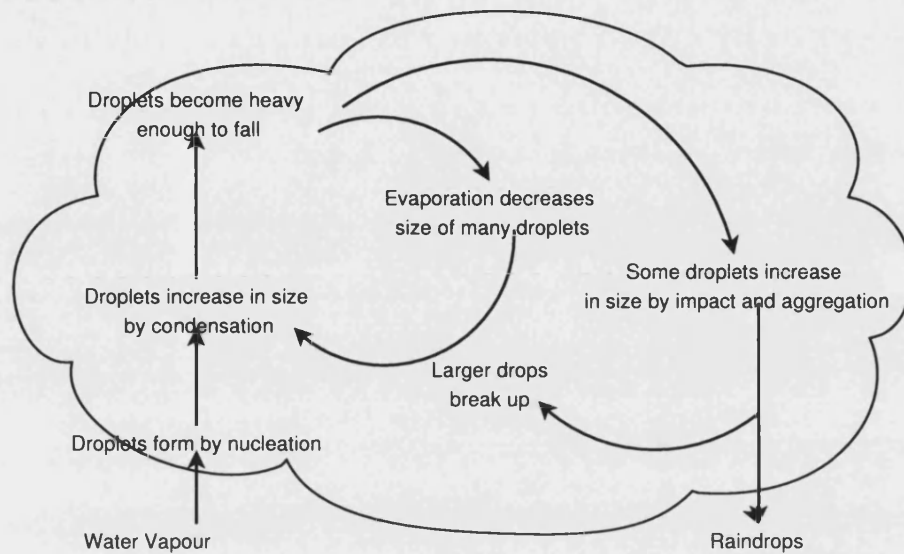


Figure 2.1: *The cycle of rainfall formation.*

the melting layer varies with season and location. In temperate regions, the height ranges from 2–4 km, with a maximum altitude during the summer months.

In tropical regions, the process of drop collision and coalescence is of more importance in rain formation. Falling small drops collide, forming larger drops until a drop becomes large enough to break up. Large drops falling near their terminal velocity will experience unstable oscillations and break up into smaller drops, restarting the cycle. These processes of impact, aggregation and disintegration produce a whole spectrum of drops in the range 0.5–10 mm in diameter. Fig 2.1 describes the general cycle of rain formation from the earth to the clouds and back again. This cycle of rain formation is driven by the way water vapour is carried aloft and leads to convective, orographic and frontal rainfall.

Convective rainfall is created when there is an abundance of moist air created by intense surface heating. These typically result in thunderstorms that produce intense rainfall. As would be expected, convective showers frequently occur within tropical areas, where large clouds of warm moist air are carried inland from the sea. But they also occur within temperate regions, especially in the summer months. In general, showers that have rain rates greater than 20 mm/h are likely to be convective. In temperate climates such as within Europe, the upper limits in convective rain rates are between 100–150 mm/hr whereas rain rates ex-

2.2. Micro-physics of Rain

ceeding 200 mm/h can be observed within tropical climates.

Orographic rain occurs when air is forced to rise due to terrain features. An example is when land areas such as mountain ranges lie in the path of extensive air masses. In such areas, the distribution of rainfall can be quite marked with the leeward side of such mountains being dry and in some cases leading to desert conditions.

The movement of moist air into a low pressure area produces frontal (or stratiform) rainfall that is widespread (can extend more than 100–1000 km) and protracted. It is generally an order of magnitude less intense than convective rainfall and in general more prevalent at mid latitudes, during the spring and summer months. Stratiform rain typically varies between 0.2–10 mm/h, with the upper limit being exceeded only very rarely. Practically all weather systems to some degree, will display a combination of both stratified and convective elements.

The amount of rain falling may vary considerably within an area. A rain shower is clearly limited horizontally, and even within widespread rain associated with fronts, there are horizontally localised areas with higher intensity rainfall. These locally intense precipitation areas are called “cells” and have well defined centres, decreasing in rainfall intensity as the distance from the cell centre increases. The order of magnitude of these rain cells can range from 2–10 km in horizontal scale and may extend up to 10 km in height, with time duration scales below 1 hour [Crane 1996].

Although the subject of investigation for more than 40 years, there remain many unanswered questions regarding the formation of clouds and rain drops (by cloud physicists and meteorologists). In particular, an accurate understanding of the distribution of drops with size has applications for better rainfall measurement, leading to the derivation of better statistics on attenuation caused by rainfall on radio links. This would help radio engineers to meet the requirements of present radio problems.

2.2 Micro-physics of Rain

An important descriptive statistic of rainfall is given by the drop size distribution (DSD). It expresses the number of drops per unit volume and per unit size interval. If all the drops fall at their terminal velocity in still air, the rainfall rate (mm/h) is

2.2. Micro-physics of Rain

related to the DSD by the following equation,

$$R = C \int_{D_{\min}}^{D_{\max}} D^3 v(D) N(D) dD, \quad (2.1)$$

where $N(D)$ is the drop size distribution, D is the drop size, $v(D)$ is the terminal velocity of drops falling in air and C is a constant whose value depends on the units of measurement of the parameters. For $N(D)$ in $\text{cm}^{-1}\text{m}^{-3}$, $v(D)$ in ms^{-1} and D in cm , $C = \frac{\pi}{6}$. Another rainfall measure often used is the total liquid water content (LWC, g m^{-3}) or accumulation given by,

$$\text{LWC} = \frac{\pi}{6} \rho_w \int_{D_{\min}}^{D_{\max}} D^3 N(D) dD, \quad (2.2)$$

where ρ_w (g cm^{-3}) is the density of water, $N(D)$ and D are expressed in the same units as equation 2.1. It is pertinent to note that in most cases where investigations of DSDs are carried out, the convention is to describe the drop spectra in terms of an equivalent spherical diameter D_{eq} . This is defined as the diameter of a sphere of the same volume as the deformed drop. This is discussed more in detail in § 2.2.2. Therefore all references to the drop size, D in this discussion refer to the equivalent drop size D_{eq} .

2.2.1 Drop Size Distributions

Research since the 1940s, has focused on providing information on the measurement and analytical description of rain drop spectra evolution. Early investigators such as Laws & Parsons [1943] used the technique of counting the drops falling in un-compacted flour to obtain drop sizes. These were quite crude and involved averaging the mass of the flour pellets to determine the drop size. Later, more sophisticated techniques using synchronised cameras and drop impact sensors like the disdrometer developed by Joss & Waldvogel [1977] were used. Lately, devices such as optical counters [Illingworth et al. 1990] and probes mounted on aircraft are increasingly being used, but in most cases the ground based disdrometer is the instrument of choice. The sensitive area of a disdrometer is often constrained by its inability to distinguish multiple, simultaneous, drop impacts. This leads to poor sampling statistics for the larger drop classes. Also a dead-time correction is often introduced to correct for the loss of sensitivity of the transducer to measure the small drops that fall within the dead-time period.

2.2. Micro-physics of Rain

Table 2.1: Values of N_0 and Λ obtained by Joss [1968].

Type of Rain	N_0	Λ
Drizzle	3×10^5	$57R^{0.21}$
Widespread	7×10^4	$41R^{0.21}$
Thunderstorm	14×10^3	$30R^{0.21}$

Marshal-Palmer Distribution

Although Laws & Parsons [1943] (L-P) had produced tables of DSD measurements which is still much used, the first analytical description of DSDs was presented by Marshall & Palmer [1948] in the form of an exponential model (M-P). Using dyed filter paper, they measured the distribution of rain drops in light and moderate rainfall, between 1 mm and 8 mm in diameter. They fitted an exponential to the measured distributions:

$$N(D)dD = N_0 \exp(-\Lambda D) dD \quad (0 \leq D \leq D_{\max}). \quad (2.3)$$

$N(D)dD$ is the number of drops per unit volume per unit interval of D , N_0 is the theoretical concentration density of drops with sizes between 0 and dD . The values of the intercept parameter N_0 ($\text{cm}^{-1}\text{m}^{-3}$) and slope Λ (cm^{-1}) are given by,

$$\begin{aligned} N_0 &= 80000 \\ \Lambda &= 41R^{0.21} \end{aligned} \quad (2.4)$$

where R is the rainfall rate in mm/h.

The M-P distribution is still frequently reported and used. Although DSD derived from small sample volumes can vary widely, it has been shown that measurements over large volumes tend to yield exponential distributions [Joss et al. 1968]. By implication, short-term and small area measurements of the DSD in time and location can differ markedly from the the empirical exponential M-P model. Joss et al. [1968], Waldvogel [1970] & Ulbrich [1978] have reported situations where the values of N_0 and Λ undergo large deviations within a rainfall event and from one rainfall event to another. Joss [1968] has presented values of N_0 and Λ that vary by rainfall type. The N_0 and Λ values for widespread rain are close to the values presented by M-P. These are listed in Table 2.1.

2.2. Micro-physics of Rain

Gamma Distribution

Atlas & Ulbrich [1984] have remarked that a three parameter distribution yields a better approximation to empirical distributions than the 2 parameter M-P DSD. Ulbrich [1983] has shown that a Gamma distribution of the form,

$$N(D)dD = N_0 D^\mu \exp(-\Lambda D) dD \quad (0 \leq D \leq D_{\max}), \quad (2.5)$$

accurately models DSD variation. Here the exponent μ , governs the shape of the distribution and was introduced to represent the DSD deviating from the exponential shape. It mostly varies in the range -1 to 10 from physical observations [Tokay and Short 1996]. The preponderance of small drops changes radically depending on the sign of μ . As $D \rightarrow 0$,

$$N(D)dD \rightarrow \begin{cases} \infty & \mu < 0 \\ N_0 & \mu = 0 \\ 0 & \mu > 0 \end{cases} . \quad (2.6)$$

Applications sensitive to this parameter. Values of $\mu < 0$ generally infer an orographic rain process (i.e the lifting of warm moist air over mountain ranges), with values of $0 \leq \mu \leq 1$ corresponding to convective rain and $\mu > 2$ representing stratiform rain. For the UK, Illingworth & Johnson [1999] show that a mean value of $\mu = 5$ seems to be appropriate for rainfall estimation. In the notation of equation 2.5, the slope parameter Λ is given by,

$$\Lambda = \frac{3.67 + \mu}{D_o}, \quad (2.7)$$

where D_o is the mean diameter. If we define D_m as the median diameter, such that drops with diameter less than D_m contribute half of the liquid water content and is given by,

$$\int_0^{D_m} D^3 N(D) dD = \int_{D_m}^{D_{\max}} D^3 N(D) dD, \quad (2.8)$$

then from equation 2.8, it is possible to show that $\Lambda = \frac{4+\mu}{D_m}$; thus D_m is close to D_o . N_0 in this case varies with DSD breadth μ and is given by,

$$N_0 = 6 \times 10^4 \exp(3.2\mu) \quad m^{-3} cm^{-1-\mu}. \quad (2.9)$$

2.2. Micro-physics of Rain

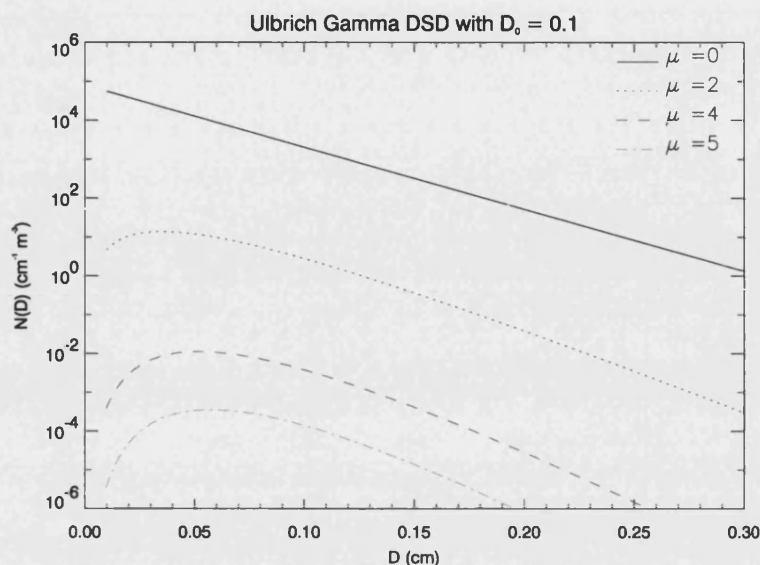


Figure 2.2: Variation of Ulbrich's Gamma DSD as a function of drop diameter with $N_0 = 80000 \text{ cm}^{-1} \text{ m}^{-3}$ and $\mu = 2, 4, 5$. The concentration of drops rapidly decreases with increasing μ .

with a range from $10^{5.5} \exp(2.8\mu)$ to $10^{4.2} \exp(3.57\mu) \text{ m}^{-3} \text{ cm}^{-1-\mu}$. Ulbrich [1983] derived equation 2.9 and its bounds by comparing 69 published radar reflectivity – rain rate relationships reported by Battan [1973]. When $\mu = 0$, equation 2.5 reduces to the M-P exponential distribution. The Gamma distribution also better accounts for the shape of the observed drop spectrum at high rainfall rates where there is a shortage of small drops.

From equation 2.9, the implication is that the parameters N_0 and μ of the Gamma distribution (equation 2.5) are not independent. Recent investigations by Testud et al. [2001] and Illingworth & Blackman [2002] show that for high values of μ , the $N_0 - \mu$ relationship presented by Ulbrich leads to values of N_0 that are not physically possible in rain. This is shown in Figure 2.2 for $N_0 = 80000 \text{ cm}^{-1} \text{ m}^{-3}$. Here, the drop concentration falls dramatically as μ increases, leading to values of rainfall rate of 2 mm/h, 0.22 mm/h and 0.009 mm/h for μ equal to 0, 2 and 5 respectively when the distribution is integrated. Also, N_0 by definition has no physical basis for non-zero values of μ , since it gives the drop concentration at a theoretical drop size of 0 mm and its units are ill-defined [Testud et al. 2001].

To overcome this difficulty, the normalised gamma distribution provides an alternative formulation, whereby all three parameters are independent of one an-

2.2. Micro-physics of Rain

other, each representing something physically meaningful and is given by,

$$N(D) = \frac{N_0^* 0.33(3.67 + \mu)^{\mu+4}}{\Gamma(\mu + 4)} \left(\frac{D}{D_0}\right)^\mu \exp\left[-(3.67 + \mu)\frac{D}{D_0}\right], \quad (2.10)$$

where D_0 and μ are the same as defined in equations 2.5 and 2.7. In this case, the drop concentration N_0^* is normalised, with respect to the total liquid water content and when $\mu = 0$, equation 2.10 reduces to the M-P expression, with $N_0^* = N_0$. N_0^* has been observed to vary over two decades centred upon the Marshall and Palmer N_0 value [Illingworth and Johnson 1999].

Therefore, physical interpretation of the normalised Gamma DSD implies that whatever the breadth of the distribution, the value N_0^* is equal to N_0 of an "equivalent" M-P DSD having the same liquid water content and D_0 . Integration of equation 2.10 over all drop sizes leads to a constant liquid water content, that is independent of μ and is obtained by multiplying equation 2.3 by the normalisation factor,

$$\frac{0.033D_0^4 \Lambda^{\mu+4}}{\Gamma(\mu + 4)} = \frac{0.033(3.67 + \mu)^{\mu+4}}{\Gamma(\mu + 4)D_0^\mu}. \quad (2.11)$$

Figure 2.3 shows the normalised Gamma distribution over the same values of μ as in Figure 2.2. In this case, the variation of drop concentration is not as marked and leads to values of rainfall between 2.01–1.99 mm/h when the distribution is integrated. Therefore, the assumption on the type of drop size distribution to use has significance on the range of error expected from estimates using integrated rainfall measurements. This is discussed in detail in chap. 3.

2.2.2 Drop Shape

Rain drops have a size dependent shape that cannot be characterised by a single length. Rain drops range in size from the very small to the fairly large in the range 0.5–10 mm in diameter, with drops greater than 8 mm being hydro-dynamically unstable and breakup as they fall. Thunderstorm or convective rain generally tends to produce a wider range of drop sizes, compared to stratiform rain but there is no exact relationship between the rainfall type produced and the size distribution of drops.

As drops increase in size, they fall faster and the surface drag due to air resistance has an increasing effect on the drop shape. Drops larger than 1 mm diameter are oblate with much larger drops having a concavity on the base. Figure 2.4 gives

2.2. Micro-physics of Rain

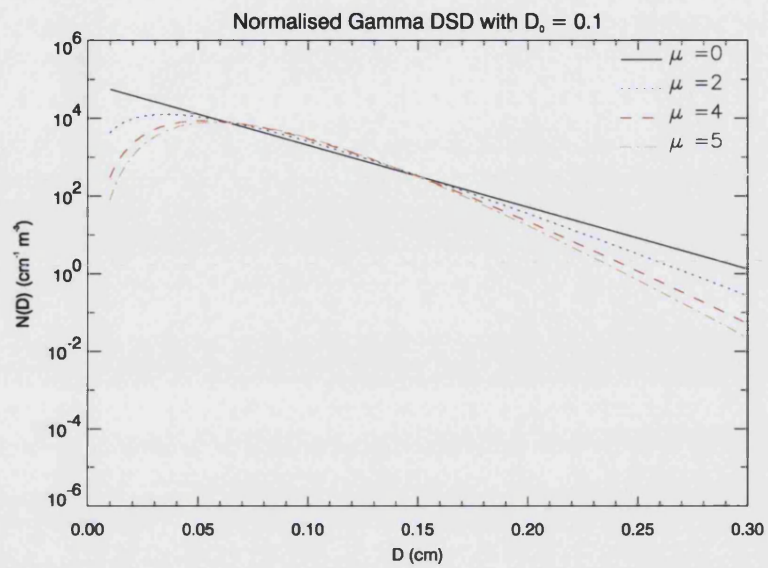


Figure 2.3: Variation of the normalised Gamma DSD as a function of drop diameter with $N_0^* = 80000 \text{ cm}^{-1} \text{ m}^{-3}$ and $\mu = 0, 2, 4$ & 5 .

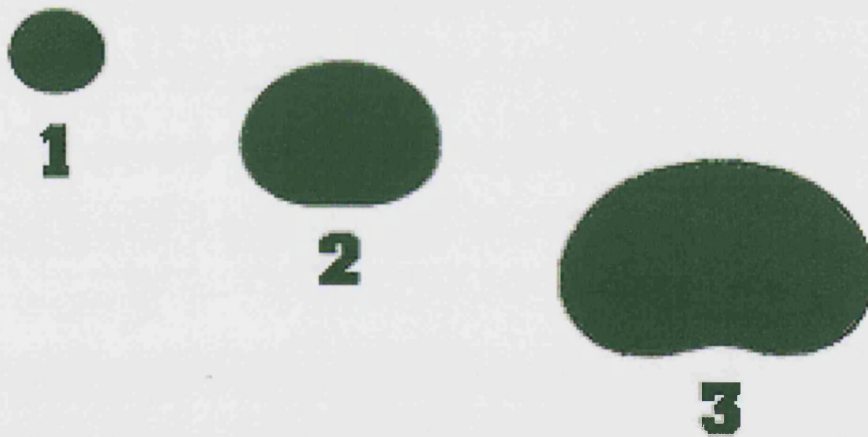


Figure 2.4: Rain drop shapes with the numbers below indicating their equi-volumetric radii in millimetres.

2.2. Micro-physics of Rain

an example of the shape of drops with varying drop size.

One of the earliest extensive measurements of drop shape were carried out by Pruppacher & Beard [1970]. Using photographs of water drops suspended in a wind tunnel, they showed that water drops falling at terminal velocity were deformed into oblate spheroids. Drops within the range of 1–4 mm were found to have a linear relationship between the axial ratios and drop size. The empirical expression is given by,

$$\frac{b}{a} = 1.03 - 0.62D, \quad (2.12)$$

where a and b are the minor and major axes of the drop respectively. This empirical relationship is only valid for drop sizes greater than 1 mm.

It can be seen that as the drops increase in size, the shape changes from a spherical shape to an oblate spheroid that is symmetrical along the fall direction. Pruppacher & Pitter [1971] later theoretically confirmed the empirical values of equation 2.12, by the numerical evaluation of the balance of forces acting on a drop falling under gravity. Another linear relation later proposed was by Morrison & Cross [1971], based on the analysis of electromagnetic wave scattering by raindrops. This is given by,

$$\frac{b}{a} = 1.0 - 0.5D. \quad (2.13)$$

More detailed calculations of internal hydrostatic pressure and external aerodynamic pressures exerted on raindrops by Beard & Chuang [1987], show that the linear model of equation 2.12 overestimates the axis ratio for large drops (>4 mm). This was motivated by increased interest to evaluate the effect of depolarisation, which causes cross-polar interference. A polynomial approximation of their empirical results is given by equation 2.14.

$$\frac{b}{a} = 1.005 + 0.0057D - 2.628D^2 + 3.682D^3 - 1.677D^4. \quad (2.14)$$

Goddard & Cherry [1984a] also made corrections to the axis ratios of Beard & Chuang for small drops. This was based on the discrepancy between observations of integrated rainfall measurements using polarisation radar compared with disdrometer measurements. They provide a polynomial expression given by,

$$\frac{b}{a} = \begin{cases} 1.075 - 0.065D - 0.036D^2 + 0.04D^3 & D \geq 0.11 \text{ cm} \\ 1.0 & D < 0.11 \text{ cm} \end{cases} \quad (2.15)$$

2.2. Micro-physics of Rain

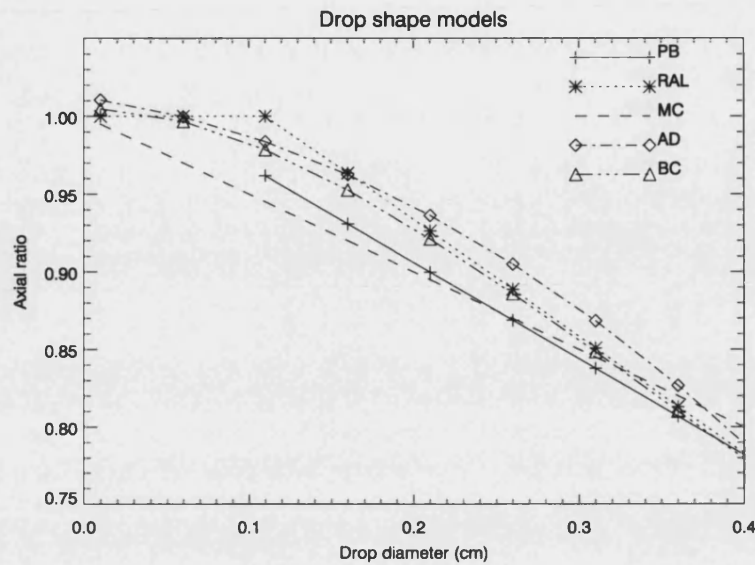


Figure 2.5: Axial ratio as a function of drop size for Pruppacher & Beard (PB), Goddard & Cherry (RAL), Morrison & Cross (MC), Andasager et al. (AD), and Beard & Chuang (BC) drop shapes.

Further wind tunnel experiments by Andasager et al. [1999] produced a polynomial model that agreed well with equation 2.15 and is given by,

$$\frac{b}{a} = 1.012 - 0.144D - 1.028D^2. \quad (2.16)$$

They also confirmed that drop oscillations considerably affect the drop mean axis ratio, and the early linear model of equations 2.12 and 2.13 were inappropriate to represent drop shapes. Figure 2.5 shows the axial ratio as a function of drop size using equations 2.12–2.16. These adjustments on axial ratio values have forced a re-evaluation of rainfall estimates obtained from integrated measurements, especially from radars.

2.2.3 Fall Velocities and Canting of Rain Drops

Terminal velocities of rain drops have been investigated by Gunn & Kinzer [1949] and Laws [1941], with the former being the best available data on drop fall velocity. Their investigations showed that the terminal velocity increases with drop size, with the rate of increase gradually decreasing for drop sizes greater than 1 mm diameter. Drops greater than 2.5 mm in diameter experienced a maximum

2.2. Micro-physics of Rain

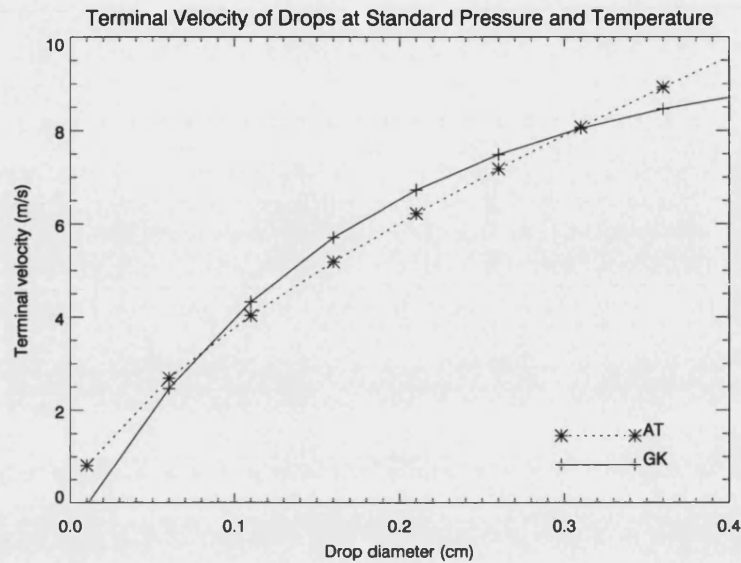


Figure 2.6: Terminal velocity of drops as a function of drop size for the expressions given by Atlas (AT), and Gunn & Kinzer (GK).

terminal velocity of approximately 9 m/s. Also, the pressure and temperature were shown to affect the terminal velocity. Their effect could be considered negligible compared to variation in drop size. At standard atmospheric pressure and temperature, the terminal velocity (m/s) is given by,

$$v(D) = 9.6 - 10.3 \exp(-6D). \quad (2.17)$$

Atlas [1984] also presented an alternative formula that is more appropriate for very small drop sizes, as equation 2.17 gives negative values of velocity for very small drops. This is given by,

$$v(D) \approx 17.7D^{0.67}. \quad (2.18)$$

Comparisons of equation 2.17 and equation 2.18 are shown in Figure 2.6. Foote & du Toit [1969] have also proposed a correction to the terminal velocity, based on the effect of atmospheric pressure that is related to the air density,

$$v(D, \rho) = v(D) \left(\frac{\rho}{\rho_0} \right)^{0.4}, \quad (2.19)$$

2.3. Rainfall Measurement Techniques

where ρ_0 is the air density at standard atmospheric pressure and temperature (1000 mbar and 20°C) respectively.

Wind shear may also distort the angle of fall (canting) of rain drops i.e the drops fall with their axis tilted from the vertical. Measurements of drop canting have been made by Hendry & McCormick [1976]. Beard & Jameson [1983] have also made theoretical analysis of drop canting. Their evaluations confirm measurements made by Hendry & McCormick, showing that the canting angle of falling drops has a narrow distribution centred around a mean value of zero, with most drops having a canting angle that is less than 10°.

2.3 Rainfall Measurement Techniques

Rainfall rate is affected by a collection of random variables parameterised by location in time and space. Factors such as atmospheric pressure, temperature, prevailing winds and topography all influence the amount of rainfall experienced within a given location. For example, the rainfall on the leeward side of mountains and hills can be significantly lower than on the windward side. Also on slightly higher ground, the rainfall can be as much as 10% higher than on flatter ground.

Principal sources of rain rate data are rain gauges, disdrometers, meteorological radars, microwave links, aircraft and space borne sensors flying on satellites. The latter are equipped mainly with passive radiometers, measuring emissions from the Earth's surface and clouds, but recent space missions include also rainfall radars. Surface-based weather radars [Bringi and Chandrasekar 2001] provide high spatial and temporal resolution rainfall measurements, but their coverage is in practice limited to Western Europe, USA and Japan. Also, significant problems (ground clutter, bright band, variability of raindrop size distribution) still persist in the interpretation of radar echoes.

Rain gauges provide the only source of direct rainfall measurement but can only provide data for a specific location. They are often used as "ground truth" when comparing rain rate estimates from other techniques. Over the seas, virtually no extensive rainfall monitoring is provided, except for satellites and radars (within coastal regions). The satellite data offer global availability, but with poor spatial and temporal resolution and large estimation uncertainties.

Each of these techniques has its own systematic and random measurement error. Also, their temporal and spatial averaging of rain rate is not similar. For

2.3. Rainfall Measurement Techniques

example, rain gauge measurements are usually integrated over a period of minutes but the collection area is small (~150 cm²). On the other hand, radar measurements are almost instantaneous in time but involve averaging over a pulse volume that can be of the order of hundreds of metres long and tens of metres high. Hence, it is often difficult to compare rainfall measurements with different instruments.

Furthermore, none of these techniques are automatic. They require constant monitoring to make sure that the equipment is adequately operational. Rain gauges can be blocked and need cleaning. Radars and microwave links need to be accurately calibrated. Data acquisition equipment in a lot of cases also needs to be reset as a result of system crashes. An overview of the measurement techniques is discussed further with the exception of radars, which will be discussed in Chapter 3.

2.3.1 Rain Gauges

Rain gauges at present represent the most common and reliable source of information about rainfall within a site. Gauges physically collect the rain falling through some horizontal area, usually using a funnel, and measure the quantity of water that accumulates over the same period. There are various gauge designs [Nystuen and Proni 1996] such as weighing, tipping bucket and drop counting rain gauges [Norbury 1971].

The weighing rain gauge operates on the principle of measuring the rain water weight collected by the instrument. Since there is a direct relationship between the weight and accumulated rain water, the resulting estimate of rain rate is the difference in the accumulated rainfall over time. These gauges do not distinguish between water and ice.

Tipping bucket rain gauges measure rain rate by allowing water to drain into a bucket that tips and drains after a certain level of water has been collected. The tipping action triggers a switch that counts the time elapsed from the last tip. The drop counting gauge quantises the water collected into drops of a fixed sized. Drops are detected by a photo transistor and the rate at which drops are produced is directly related to the rain fall rate. Unless the gauge is heated, ice accumulates in the funnel. Heated gauges tend to underestimate light rain due to increased evaporation.

A source of measurement error for all of these gauges is flow rate irregularities

2.3. Rainfall Measurement Techniques

between the collection area and the measurement enclosure. The chambers can become blocked with debris such as grass seeds, and insects or air pockets can alter the flow rate. This affects the accuracy of the measurements especially at low rain fall rates. Typical standard errors for such gauges are of the order of 10% for rain rates up to 100 mm/hr.

Gauges are difficult to site due to their sensitivity to wind. Updrafts and wind shear over the funnel may greatly reduce the collector efficiency. The gauge needs to be sited a long way from buildings and trees, sometimes at a horizontal distance of up to ten times the height of these obstructions. Sensitivity to siting and wind, difficulties with non-liquid hydrometeors and the need for human attention means that rain gauge data is expensive and often unreliable.

2.3.2 Disdrometer

The most prevalent type of disdrometer measures the drop size distribution by converting the momentum of drop impacts on sensors into electrical signals [Tokay et al. 2003]. The momentum of each drop is directly proportional to its drop size and may be used to classify the drops into categories. These categories generally range from 0.3 to 6.0 mm diameter. For very high rain rates, the disdrometer may truncate drop measurements in the smallest categories especially for drop diameters less than 1.0 mm. This is due to “dead time” and the presence of background noise. Furthermore impact disdrometers assume that all raindrops fall at their terminal fall speed. Ignoring the influence of vertical air motion on raindrop fall speed results in errors in determining the raindrop size.

The latest disdrometers also employ either microwave, optical or laser technologies for measurement. These are able to take 2D profiles of drops together with their fall velocities leading to more accurate estimates of rain rate [Tokay et al. 2001].

2.3.3 Microwave Attenuation Techniques

The principle of estimation of rain rates from microwave attenuation is based on the observation that attenuation is directly proportional to the rainfall rate at 1 cm wavelengths (30 GHz) [Gunn and East 1954]. In an early study, Medhurst [1965] made detailed comparisons of theoretical and experimental values with disappointing results. In most experimental cases observed [Atlas et al. 1984], the measured attenuations were larger than the maximum theoretical values and the

2.3. Rainfall Measurement Techniques

effect of winds has been cited for the discrepancy. Recently, Hardaker et al. [1997] have presented theoretical and experimental analysis using the attenuation difference at two frequencies (12.5 & 20 GHz) to estimate rainfall rate. They obtain good correlation between measured and simulated values. The Bolton-Mantissa experiment [Holt et al. 2000] also explores the use of the dual frequency technique for rainfall monitoring. It has to be noted that the rain rate derived from link attenuation, is an average along the link path. Path averaged rain rates are difficult to compare with point measurements from rain gauges.

2.3.4 Satellites

Passive sensors on-board satellites, are used to detect radiation emissions from the Earth's surface, atmosphere and clouds. They measure the brightness temperature within the infra-red, visible and mm-wave bands of the spectrum. Most sensors have a spatial resolution of the order of 5 km (0.05°) and an infra-red scan can be produced every 30 minutes. In most cases their effectiveness is limited to identifying rainfall structures on land and sea. However, research is now much more oriented toward finding reliable methods of quantifying precipitation [Tournaire 1998].

Space borne radars are also increasingly being used for rainfall analysis. Notable among them is the worlds first precipitation radar, flying on the TRMM (Tropical Rainfall Measuring Mission) satellite. This is a joint USA and Japan space mission [TRMM 1997] to observe tropical and subtropical rainfall, and it was launched in November 1997. Vertical profiles of rainfall are generated up to 15 km in height, with a range resolution of 250 m, the spatial resolution at the footprint being around 5 km. The main products supplied routinely are monthly amount and average rainfall over 5°x5° grid. This time and space resolution is in line with the belief that currently, rainfall estimates based on satellite imagery are reliable only when averaged over large space and time scales. For radio propagation applications, these outputs are inadequate. But it is only a matter of time before improved precipitation algorithms are produced to satisfaction at smaller spatial resolutions.

2.4 Rain Rate Distributions

2.4.1 Annual Statistics

To adequately characterise the random variations of rainfall in time, yearly statistics of cumulative distributions of rain rate are usually presented. Point rainfall statistics using gauges have been amassed at thousands of locations all over the world for more than 50 years. The majority of the data collection has been focused toward hydrological and meteorological applications, for which hourly, daily, and monthly integration times were used. Much shorter periods are of interest in radio propagation applications, i.e 10s or 1 minute [Ruthroff 1970]. In practice, this information is rarely available. International Telecommunications Union (ITU) recommendations have been based on one-minute integration times as, historically, these were the shortest practical integration times from conventional tipping bucket rain gauges.

Moreover, precise estimates of rain rate exceeded at small percentages of an average year can be challenging to obtain. Rain rates that occur for only five minutes a year (i.e. 0.001% of time) are of interest when estimating the expected availability of a link. Firstly, the rainfall rates which occur for very small percentages may be expected to change considerably from one year to another. Additionally, there is considerable local variation of the amount of rainfall that occurs for very small percentages of time. Moreover, typical rain gauges require significant maintenance effort and often fail for several days a year. This has severe effects on measured rain rates at small time percentages.

Therefore for accurate statistics down to 0.001% of time, rain rates integrated over a minute, with measurements over periods of up to 10 years or more are required. In most cases, data from rain gauges are sufficient when considering a single site, but they are impracticable for obtaining statistics over large areas. Radars provide maps of near instantaneous rain rate, averaged over relatively small voxels, for large areas. This information is useful in the study of rain field structures and allows the averaging over of local variations. However, systematic long-term measurement campaigns are required to estimate average annual statistics as year to year variation of rain rate cumulative distribution functions (CDFs) is still a factor.

2.4. Rain Rate Distributions

Variation of Rain Rate Statistics from the Long-Term Average

An analysis of seven year rain gauge data within the UK between 1970 – 1976 by Harden et al. [1977], has shown that there are large variations from year to year in the calculated annual rain rate probability distributions compared to the long term average. For some years, the ratio of times that high rain rates, e.g., those exceeded for less than 0.01% of the time, exceeded in a given year were shown to have an order of magnitude in variation.

Similarly, Crane [1996] has indicated a factor of 6 difference in yearly distributions for high rain rates. Lower rain rates were more stable in variation of their distributions. This emphasises that account must be taken of the characteristics of the intense rain affecting radio transmissions during limited observing periods if probability distributions of attenuation measured at those times are to be extrapolated to long-term estimates of link performance.

Crane [1996] has also shown from rain gauge measurements in the eastern USA, that large variability in the rain rate distributions do occur on a monthly and seasonal basis, with rain rates of 10 mm/h and 70 mm/h at 0.01% probability of exceedance for winter and summer seasons respectively. This shows that there are higher occurrences of high intensity thunderstorms for the summer months. Hence, yearly statistics are not enough for radio propagation planning and a most unfavourable "worst" month statistic also needs to be used for radio propagation planning. A general rule of thumb – for a specific rain rate threshold, the exceedance probability for the worst month is four times greater than the exceedance probability for the whole year.

Effect of Integration Time

The time interval over which the analyst or instrument averages the data affects the distribution of rain rates. Using 10 years of data from a rain gauge network in Canada, Drufuca & Zawadzki [1975] show that the effect of increasing the integration time over a few minutes was to suppress the heaviest rainfall rates and shift the distribution at low rain rates. This implied that for accurate point rainfall statistics to be obtained, rainfall rates with an integration time of 1 minute or less had to be used.

Similar results have been obtained by Harden et al. [1978b] from 20 year rainfall data in the UK. Rain rates for an integration time of 1 minute were on average 93% of what would be measured within an integration time of 10s. For longer in-

2.4. Rain Rate Distributions

tegration times of 2 and 5 minutes, the rain rates were 85% and 76% respectively of instantaneous measurements. Therefore, the longer the rain rate measurement integration time, the farther the derived statistics depart from reality.

2.4.2 Time to Space Transformations of Rain Rate Statistics

The rain rate time series measured at a point is effected both by the advection of the rain field and its evolution. In most cases advection is the dominant effect. If the rain field is assumed to be a frozen pattern of rain rate, advecting with the ambient wind, the point rain rate time series is the same as rain rate measured instantaneously along a line through the rain field.

This assumption is frequently used in the time to space transformation of rain stats, and is known as the Frozen Storm or Synthetic Storm model. The results of Drufuca & Zawadzki [1975] employ the use of the synthetic storm technique to obtain spatial statistics from temporal statistics. They assume a constant storm translation speed of 50 km/h. This estimate of storm speed was based on wind speeds at the 700 mbar level that were shown to have a strong correlation with the motion of storms [Harden et al. 1974, 1977].

A weaker assumption is that the evolution of the rain field is negligible compared to the point rain rate variation due to advection. This leads to Taylor's Hypothesis [Taylor 1938], which can be stated as the statistics of a point rain rate time series are the same as the statistics of the rain field restricted to lines parallel to the direction of advection. If $R(x, t)$ is the rain rate at point x at time t , then Taylors Hypothesis can be written as:

$$R(x_0, t) == R(x_0 + Vt, 0). \quad (2.20)$$

Where V is the advection vector and $==$ means has the same statistics. Taylor's Hypothesis has been tested many times and has been shown to be valid for periods up to 40 minutes [Zawadzki 1973]. The advection vector has been found to vary with rain type being larger for convective compared to stratiform rain [Matriccioni and Pawlina 2000].

2.4.3 Models of Annual Rain Rate Distribution

Most models fall into the category of statistical temporal models i.e. they are only able to predict yearly one minute distributions. Also, in most cases the models are only applicable for a given region or climate. Recently, there has also been a

2.4. Rain Rate Distributions

shift toward producing high resolution models that take into account the stochastic variation of rain in time and space. Some of the common statistical temporal models in the literature are highlighted but it is in no way exhaustive. An excellent review of 1 min non-stochastic rainfall prediction models is given by Tattelman and Grantham [1985].

The model proposed by Rice & Holmberg [1973] estimates the percentage of an average year that t min (where t = intervals of 1 minute to 1 day) surface rainfall rates exceed a given value. For 1 minute rain rates, the model has two main parameters for a specific location:

1. The mean annual precipitation, M
2. The ratio of annual thunderstorm rainfall to total annual rainfall (β)

These two parameters are not given and have to be obtained from meteorological data. They do though provide world contour maps of M and β but interpolation is required for a specific location as the maps are of poor resolution. The model was developed mainly using data collected in the USA but is applicable for locations around the globe. It performs poorly when estimating probabilities for high rainfall rates. Therefore, the range of applicability of the model is within the 0.1%–1% probability range. Dutton & Dougherty [Dutton and Dougherty 1979, 1984], have also extended the Rice–Holmberg model to take into account year to year variability, by providing empirical expressions on the standard deviation of the rainfall cumulative distribution. They also provide a simpler formulation to the Rice–Holmberg model.

Using 7 years of data mainly from locations in the eastern USA, Crane [1980] proposed a model that divides the world into eight regions of “homogeneous” rainfall rates based on the total rain accumulation and the number of thunderstorm days using climatological maps. It addresses the year to year variability within each region, but there are large variations in rainfall rates for individual locations within regions. The model is presented in tabular form and performs well for probabilities within 0.01%–1% of time.

Moupfouma [1985; 1993] also provides a very simple empirical model to predict the rain rate cumulative distribution. The model approximates a Gamma distribution for high rainfall rates and a log-normal distribution for low rain fall rates. The model requires as input the point rainfall rate exceeded for 0.01% of

2.5. Higher Order Rain Rate Statistics

time and has been compared with data from temperate and tropical locations with good agreement.

Salonen & Baptista [1997] present a model developed from global climate data for 1987–1996. They use six hourly data from various regions around the globe to provide statistics on yearly cumulative distributions of rain rate valid for down to 1.5° latitude and longitude spacings. The model requires as inputs:

1. Annual rainfall amount, M_r
2. Probability of rainy 6 hour periods, $P_{r6}(\%)$
3. Ratio of heavy convective rain to all rain, β
4. Location latitude and longitude

Their results give lower errors for several percentages of time compared to the previous recommendation using the ITU database of rainfall measurements and the Rice–Holmberg model. This has been adopted as the latest recommendation (Rec. ITU-R P. 837–4).

2.5 Higher Order Rain Rate Statistics

The rain fade experienced by a link is an integrated effect of all the rain within the first Fresnel zone. Hence link rain fade, by its nature, depends upon the rain rates experienced along the link path. For this reason, the spatial variation of rain rate is important in radio propagation studies. The distributed nature of radio networks means that it is important to understand the spatial variation of rain rate over scales from a few hundred metres to thousands of kilometres. Area statistics of rain rate can be derived using measurements from meteorological radar, satellites or numerical models, with radars yielding the highest spatial resolution.

Moreover, information on the return periods and durations of high rain rates are also needed for estimation of similar statistics for attenuation. Understanding their variation is important for the design of fade mitigation systems. Also, these statistics are useful as inputs for developing statistical prediction models, which can reproduce the rain variation for any given location within climatic regions.

2.5.1 Rain Rate Durations

Most studies have supplied distributions of rain rate, but only a few have also provided information on the dynamic character of precipitation. For example

2.5. Higher Order Rain Rate Statistics

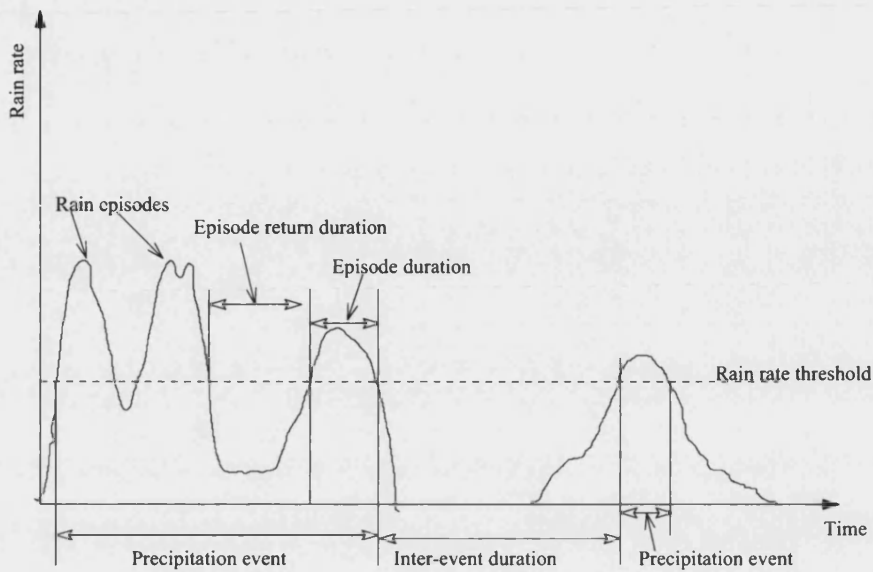


Figure 2.7: Features characterising the dynamics of rain rates.

statistics for the intervals when rain rate exceeds a defined threshold. Information on the durations and return periods of intense rain is needed for estimating the same characteristics of attenuation. Its importance will depend on the required link reliabilities and data rates appropriate to different communication systems.

Rainfall occurs in the form of events that can have intervals of hours or days. Within each event, the rain rate series has several peaks and troughs with short intervals between each other. Hence, rain duration statistics can be subdivided into 4 classes; episodes duration, episode return duration, (precipitation) events duration, and inter-event duration. Figure 2.7 shows the definition of these terms with respect to an arbitrary rain rate threshold. A rain event is delimited by the rain rate crossing a predefined threshold for the first time and ends when it falls below the threshold, and is followed by a period of no rain (event return duration). Within the event, there can be several episodes. These have short peaks with short gaps between them (episode return duration). The episode duration can be defined as the period between the time at which the rain rate crosses a given threshold, with positive slope to the time at which the rain rate falls below the threshold, with negative slope.

Observations by Vogel et al. [1993] using four year rain gauge data within Texas, USA show that the distributions of events and return periods are log-normally

2.5. Higher Order Rain Rate Statistics

distributed. In general, inter-event return durations for rain were greater than 4 hours. This value is close to observations from rain gauge data in Canada [Dru-fuca and Zawadzki 1975]. Additionally, event durations at rain rate thresholds of 10, 30 and 60 mm/h for 50% probability were 17, 8 and 4 minutes respectively. Furthermore, rain rate episode durations for the same thresholds were 2.5, 1 and 0.5 minutes.

Goldhirsh [1995] and Timothy et al. [1998] have also analysed episode dura-tions within the mid-Atlantic coast of the USA and north western India respec-tively. Their results agree well with the results of Vogel. This indicates that al-though the annual cumulative distribution of rain-rate at a threshold varies from location to location, the duration statistics at each threshold may have a very weak variation with location. For the UK, studies show that majority of episode du-rations are less than 2 minutes for all thresholds considered (30, 50, 70 and 100 mm/h) [Harden et al. 1978b] with fewer than 10% exceeding 2 minutes.

Regression fits [Goldhirsh 1995; Timothy et al. 1998] to rain episode duration, D , show a best-fit model is given by a power law of the form:

$$D = A(p)R^{-B(p)}, \quad (2.21)$$

where the values of A and B are functions of the probability level. Using rain gauge data within the UK, Gibbins & Paulson [2000] have proposed a lognor-mal model for the estimation of the number of events per year having a rain rate threshold greater than R mm/h and durations greater than D seconds.

$$n_D(D) = 1.70 \cdot 10^4 R^{-1.76} \exp\left(\frac{-(\ln D - 2)^2}{3.86 - 0.0409R}\right). \quad (2.22)$$

From this equation, the number of seconds, $n_S(D)$ composed of events of duration D can be obtained and is given by $n_S(D) = Dn_D(D)$.

2.5.2 Correlation of Rain Rates in Time and Space

The relationship between the random variation of rain rates observed at two or more locations in time or space is provided either by their joint distributions or correlation. The correlation of a random sample is in general given by:

$$\rho_{R_1 R_2} = \frac{\text{cov}(R_1, R_2)}{[\text{var}(R_1) \cdot \text{var}(R_2)]^{1/2}} \quad \rho \in [-1, 1], \quad (2.23)$$

2.5. Higher Order Rain Rate Statistics

where ρ is the correlation co-efficient, $R_{1,2}$ are the rainfall rates at two points in time/space, and $\text{cov}(\sim)$ and $\text{var}(\sim)$ are the covariance and variance respectively. Zawadzki [1973] has analysed and presented rain patterns from radar through the normalised autocorrelation functions and finds that rainfall de-correlates nearly exponentially with time or space. The de-correlation time and distance (defined in this case as the value for which ρ falls to $1/e$ of its maximum value) were 32 min and 20 km respectively.

Within the UK, Fukuchi [1988] has analysed ten year rain gauge data from the meteorological office to study the effect of integration time and seasonal variation on the spatial correlation co-efficient for several locations. Empirical analysis showed that the distance dependence is approximated by an exponential model, with the correlation decreasing with increasing separation in the observed rain rates. The correlation co-efficient at long integration times exhibited higher values. This is because the longer the rain rates are averaged, the higher the probability of observing joint events.

For the seasonal effects, correlation co-efficients during the winter months were larger than for summer months. This is explained by the dominance of stratiform and convective rains respectively. Convective rains are less dispersed and therefore there is a lower probability of observing joint occurrences.

Gremont [2002; 2003] also provides exponential expressions for the space-time correlation of rain. The formulae take into account birth/decay of rain cells, the average speed/direction of their movement and their characteristic dimension based on the assumption of Taylor's hypothesis.

An alternative and closely related measure to correlation is given by the statistical dependence index. It expresses the ratio of the joint distribution to the product of the marginal distributions. Intuitively, for two random variables that are independent, the joint distribution is equivalent to the product of the marginal distributions and the statistical dependence index takes a value of 1. It is easier to experimentally evaluate than the correlation because it does not depend on excessively low values of rain rate, which can be difficult to measure. It is expressed as,

$$\chi_{R_1, R_2} = \frac{\text{Pr}(R_1, R_2)}{\text{Pr}(R_1) \cdot \text{Pr}(R_2)} \quad \chi \geq 1, \quad (2.24)$$

where $\text{Pr}(\sim)$ is the probability. Similar observations on the trends observed by Fukuchi [Ordano 1987; Barbaliscia et al. 1992], have been made in Italy using the

2.5. Higher Order Rain Rate Statistics

statistical dependence index. For distances less than 100 km, the statistical dependence between rain rates is strong ($\chi \gg 1$) but beyond 800 km, rain rates are completely de-correlated ($\chi \simeq 1$). Similar statistics can be calculated for log rain rate.

2.5.3 Rain Cell Statistics

As noted previously, the fundamental structure within any rain event is the rain cell, which is defined to be an area of locally intense rain, higher than some rain rate threshold. Statistical information on the cell size distribution, ellipticity of cells, average and maximum rain rates within cells, together with the area covered by such cells provides us with a characteristic description of the intense parts of a rain field. Additional information on the incidence of convective and stratiform rainfall is also useful. The horizontal structure of rain for various climatic regions can be obtained using radars for small to meso-scales and recently through passive airborne sensors for large to global scales. Rain gauges are also able to supply useful structural information.

A large number of investigations on rain cell sizes, based on radar records have been done [Konrad 1978; Pawlina 1984; Goldhirsh and Musiani 1992; Crane 1990]. All of them present distributions of rain cell sizes as a function of rain intensity. Early measurements in propagation by Hogg [1973] using a radiometer at 16 and 30 GHz, managed to indirectly infer the average size of cells with rain rate, by relating the ratio of attenuations at the two frequencies, with the rainfall expected along a link. The empirical results showed a clear trend with cell size decreasing with increasing rain rate.

Crane [1990] has noted that cells are typically 2 km in size with a lifetime of 15 minutes before they dissipate. Goldhirsh [1983; 1986; 1992] has also observed that 90% of cells with a threshold greater than 20 mm/h had diameters less than 4 km with the average cell size being 2 km. Long term (10 year) rain gauge time series, with sufficient resolution (1 min), can also be used for the statistical estimation of rain cell sizes using the synthetic storm technique [Yau and Rogers 1984; Matricciani and Pawlina 2000]. The results of Matricciani and Pawlina [2000] employing this method compare well with radar derived statistics.

Due to the random distribution of rainfall on the ground, the shape of rain cells themselves have no exact characteristic shape. But for easy modelling, investigators have usually compared the perimeter of cells to ellipses, with in most cases, a

2.5. Higher Order Rain Rate Statistics

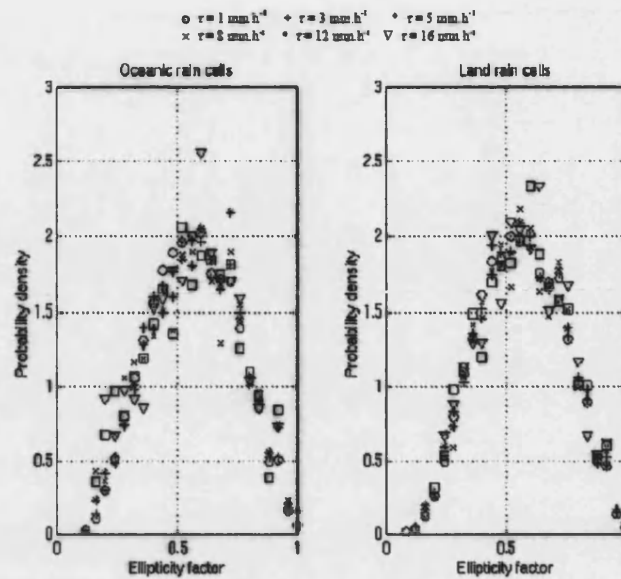


Figure 2.8: Distribution of rain cell ellipticity factor for cells observed on land and at sea for different rain thresholds, τ . From Feral et al [2000].

simplifying assumption of circular symmetry. In contrast, irregular shapes of rain patterns often show the tendency to elongate in a particular direction, possibly due to the movement of fronts or prevailing winds.

Pawlina [1995] looked at the ellipticity of cells categorised by rain type (stratiform or convective). The median values of the ellipticity were found to be in the range 0.45–0.55. It meant that on average cells were twice as long than wide. Only 15% of cells were categorised as being round. The differences in ellipticity for the types of rain was found to be small. Also, extensive investigations by Feral et al. [2000] on the statistics of rain cell geometrical features derived from meteorological radar, showed that the ellipticity of rain cells independent of their location and threshold was on average 0.5. Figure 2.8 highlights their results from radar measurements.

Rain Cell Models

For rain cell diameter distributions, Sauvageot et al. [1999] reviewed other investigations in the literature and showed that the rain cell diameter distribution for a given rain rate threshold, is accurately described by an exponential distribution given by,

$$N(D_{\text{cell}}, \tau) = N_0^{\text{cell}}(\tau) \exp(-\lambda(\tau)D_{\text{cell}}) \quad \text{A}^{-1}\text{km}^{-1}. \quad (2.25)$$

2.5. Higher Order Rain Rate Statistics

Here, D_{cell} is the diameter of an equivalent circular cell having a threshold greater than τ mm/h. $N(D_{\text{cell}}, \tau)$ denotes the number of cells with a diameter D per unit area within an observed area A . The parameters $N_0^{\text{cell}}(\tau)$ and $\lambda(\tau)$ are the intercept and slope of the distribution respectively. The slope parameter has a very weak dependence on the cell rain rate threshold and geographical location with the range of variation between 0.3–0.37. The value of N_0^{cell} though is dependent on the size of the observation area. The valid range of D_{cell} is between 0.5 km and 20 km. The distribution of equation 2.25 is useful especially in the modelling of rain fields.

Harden et al. [1974; 1977], have also used wind speeds measured at the 700 mbar level to obtain spatial rain cell profiles by the time-space transformation of the synthetic storm technique. Using 6 years of 10 second rain gauge data in the UK, they showed that rain rate intensity decreases exponentially with distance, with the spatial features being substantially retained over a few kilometres.

Additionally, Capsoni [1987] has analysed the variation of rainfall within cells and presented an exponential model (EX-CELL) with circular symmetry that describes the spatial profile of rain rate. For each rain cell, the point rainfall rate at a distance l from the centre with respect to the peak rain rate value is given by,

$$R(l) = (R_{\text{max}} + R_{\text{low}}) \exp\left(-\frac{l}{l_0}\right) - R_{\text{low}}, \quad (2.26)$$

where R_{max} and R_{low} are the maximum and minimum rain rates within the cell. l_0 defines the characteristic cell size. The population of cells is defined by the spatial density of cells with a given radii. The peak rain rate values are obtained from empirically derived expressions related to the annual rain rate cumulative distribution.

Although the exponential shape for the spatial distribution of rainfall within the cell was not new, the novelty and later popularity of the model in the prediction of various propagation scenarios was due to the computationally simple construction of the population of realistic cells, reproducing the local rain rate statistics. Using the EX-CELL model, Goldhirsh [2000] and Paraboni et al. [1998] detail methods of generating rain fields having a predefined cell population, with the centres of the cells being randomly distributed over a simulated area.

Other cell profile models of cylindrical and Gaussian shape have been presented in the literature [Mass 1987; Bryant et al. 2001]. The models are illustrated

2.6. Rain Field Models

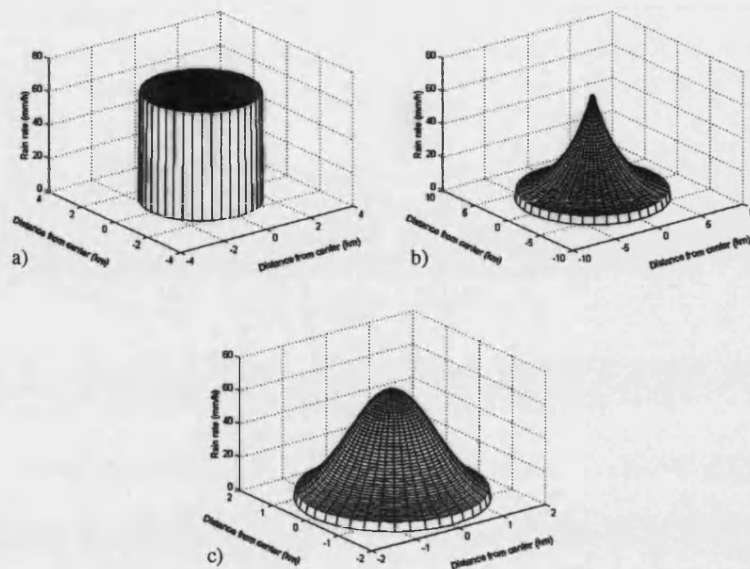


Figure 2.9: Cylindrical (a), exponential (b), and Gaussian (c) shaped rain shower models.

in Figure 2.9 with a maximum rain rate of 65 mm/h and a minimum of 5 mm/h at the edge of the cell for the exponential and Gaussian models. A hybrid cell (HY-CELL) model that combines the structures of the exponential and Gaussian cells has been recently presented [Feral et al. 2003b,a]. It models the high intensity convective rain centres as Gaussian with the surrounding widespread rain having an exponential variation. It has been shown to be a more realistic descriptor of rain cells from radar observations.

2.6 Rain Field Models

The need for models that are able to predict the rain rate cumulative statistics in conjunction with second order statistics of rain rate (rain rate duration and rain rate return times) is pushing research into stochastic models of rain rate. Millimetre wave links can have lengths from a few hundred metres up to 30 km. Furthermore, the duration of fades can span periods of 1s to several hours. Hence there is a need for prediction models that span these scales. Additionally, they are useful as inputs for the evaluation network channel models.

The tradition of mathematical modelling of spatio-temporal rainfall fields is quite long among the hydrologists but for radio propagation applications this is an emerging area of study. Most existing models of rain rate variation have been

2.6. Rain Field Models

developed for hydrological problems such as erosion modelling, watershed and river management. In these applications “fine or small scale” is often interpreted as an order of magnitude larger than the scales of interest in millimetre wave propagation applications.

2.6.1 Pulse Models

These stochastic models are based on rain fields generated from a Poisson point process. Cells are born randomly through the storm and their rain is spread in time and space according to functions which may include random parameters [Cox and Isham 1988]. From empirical evidence [Austin and Houze 1972], rain cells tend to form in the vicinity of existing cells so that they form a cluster within storms. Rodriguez et al. [1988], have used such information to produce a single site time series model, using a clustered point process for the arrival times of rain cells. The underlying process that generates the field can be a Bartlett-Lewis or Neyman-Scott scheme. In a Bartlett-Lewis scheme, the generated cells follow the storm origin compared to the symmetric scatter of cells using a Neyman-Scott scheme. Within the cells, the rain rate variation is defined to be constant.

Cowpertwait [1995] has presented extensions to the modelling in both space and time. The rain cells are represented as circular discs, each having a random radius, with the locations of the rain cell driven by a two-dimensional Poisson process. Further modifications, using information on spatial autocorrelation of storms from radar have been made by Northrop [1998] to allow for elliptical rain cells having an exponential decay. The cells, storms and fields all move with the same velocity. The resulting total rainfall intensity at a point in time or space is then the sum contributions of the cells active at that point.

Such models have been used to fit rain events [Onof et al. 2000; Wheeler et al. 2000] with encouraging results but the estimation of the model parameters is non-trivial. Typical parameters of the models incorporate the storm arrival rate, cell duration, mean and variance of cell intensity, mean cell area, cell orientation, eccentricity and cell velocity. No account of the seasonal dependence of rainfall is currently incorporated. Typical outputs that the models are able to provide are,

1. Rain intensity as a function of time and/or space with periods of rain and no-rain, usually down to hourly intervals.
2. Marginal cumulative statistics.

2.6. Rain Field Models

3. Rainfall correlation.

2.6.2 Markov Models

Markov chains involve the definition of the states of the underlying random process of rain rate. This is described by the state transition matrix given by,

$$P_{ij} = \Pr\{X(n+1) = j \mid X(n) = i\} \quad \{i, j\} \in \Omega, \quad (2.27)$$

where n denotes the time or space sample of the random process, X . The transition matrix P defines the probability of the next value $X(n+1)$ having some value based on the previous values of $X(n), X(n-1), X(n-2) \dots$. Hence the transition matrix can be expressed as,

$$P_{ij} = \frac{\int_{i-\epsilon}^{i+\epsilon} \int_{j-\epsilon}^{j+\epsilon} f(i, j) di dj}{\int_{i-\epsilon}^{i+\epsilon} f(i) di}, \quad (2.28)$$

where $\epsilon = dX/2$, $f(i, j)$ is the joint PDF and $f(i)$ is the marginal PDF. Since rain rate is approximately log-normally distributed [Lin 1973; Galante 1975], the joint and univariate PDFs are given by,

$$f(i, j) = \frac{1}{2\pi\sigma^2\sqrt{1-r^2}} \exp\left[-\frac{1}{2(1-r^2)\sigma^2}(A^2 - 2rAB + B^2)\right], \quad (2.29)$$

$$f(i) = \frac{1}{\sqrt{2\pi\sigma^2}} \exp\left[-\frac{1}{2}\left(\frac{\ln(i) - m}{\sigma}\right)^2\right], \quad (2.30)$$

with $A = \ln(i) - m$ and $B = \ln(j) - m$. The parameters m, σ and r are the mean, standard deviation and correlation respectively of log rain rate. As the estimation of the current sample depends on previous samples, then the correlation between samples is implicitly exponential.

In the general application of Markov models, an initial rain rate state is first generated. This is then passed to the state transition matrix and a decision is taken on the next value to be generated based on previous values. For a sufficiently long period of time, all the states of the matrix are reachable. Maseng & Bakken [1981] and Gremont & Tawfik [2003] have detailed techniques for the generation of time series using Markov chains. Although in the papers time series of attenuation were generated, the principle involved for the generation of rain rate time se-

2.6. Rain Field Models

ries is the same. Fiebig [2002] also proposes a Markov type model together with Gaussian random variables for the parameters. The parameter sets describe the dynamic variations of the random series using 3 segments; increasing, decreasing and constant values. These parameter sets are obtained from recorded data for the location of interest, with the resultant time series almost identical to the recorded data.

Although Markov methods are applicable to the generation of area rain rate time series, the estimation of the huge number of transition probabilities from one vector-state to the next can be intractable. Though, they can easily take into account periods of no rain.

2.6.3 Spectral Models

Paulson [2002] has proposed a spectral density model of log rain rate when raining. This is based on the assumption that log rain rate is an isotropic, homogeneous, Gaussian random field with a spectral density function following a specific power law. Theoretical analysis and observations of rain rates from radars and rain gauges show that the slope of this power law is $-\frac{5}{3}$ for one dimensional fields [Kolmogorov 1941; Crane 1990]. For such fields, the mean, variance and auto-covariance or autocorrelation completely characterise the process.

Let $X(\mathbf{t})$ be the log rain rate random field, where \mathbf{t} is a vector that denotes a combination of time and/or space units (x, y, t) . Since X is an homogeneous Gaussian random variable, its mean and variance is given by,

$$\begin{aligned} m(\mathbf{t}) &\equiv E[X(\mathbf{t})] = \mu_X, \\ \text{Var}[X(\mathbf{t})] &\equiv E[X(\mathbf{t}) - m(\mathbf{t})]^2 = \sigma_X^2, \end{aligned} \quad (2.31)$$

where $E[\cdot]$ is the expected value. The auto-covariance is given by:

$$B_X(\mathbf{t}_1, \mathbf{t}_2) = \text{Cov}[X(\mathbf{t}_1), X(\mathbf{t}_2)] = E[X(\mathbf{t}_1)X(\mathbf{t}_2)] - m(\mathbf{t}_1)m(\mathbf{t}_2), \quad (2.32)$$

and describes the relationship between the random variables at two space-time locations. Since, X is assumed to be homogeneous, the auto-covariance depends only on the lag $\boldsymbol{\tau} = \mathbf{t}_1 - \mathbf{t}_2$. The spectral density is related to the auto-covariance,

$$\begin{aligned} B(\boldsymbol{\tau}) &= \int_{-\infty}^{\infty} S(\boldsymbol{\omega}) \exp^{i\boldsymbol{\omega}\boldsymbol{\tau}} d\boldsymbol{\omega}, \\ S(\boldsymbol{\omega}) &= \frac{1}{(2\pi)^n} \int_{-\infty}^{\infty} B(\boldsymbol{\tau}) \exp^{-i\boldsymbol{\omega}\boldsymbol{\tau}} d\boldsymbol{\tau}, \end{aligned} \quad (2.33)$$

2.7. Concluding Remarks

where the integral denotes integration over n -dimensions. Then the log rain rate spectral density model of Paulson [2002] when raining is given by,

$$S_X(\omega) = K \left(1 + \frac{|\omega|^2}{\omega_0^2} \right)^{-0.5(\frac{5}{3}+n)}, \quad (2.34)$$

where ω is a vector of the n -dimensional coordinates, $\omega_0 \approx 0.01 \text{ km}^{-1}$ and K is a normalising constant to ensure that $\sigma_X^2 = \int_{-\infty}^{\infty} S(\omega) d\omega$. The autocorrelation can then be obtained using equation 2.33. Using such a model, temporal and spatial rain rate fields can be simulated at all scales of interest [Paulson 2003b; Callaghan and Vilar 2003]. Such models of log rain rate are clearly only valid in areas of non-zero rain rate.

2.7 Concluding Remarks

It is crucial to understand rainfall dynamics in approaching the study of rain attenuation on radio links. The general cycle of rainfall formation has been presented, showing how the action of drop impact and aggregation leads to a spectrum or distribution of drop sizes. The sizes of these drops vary widely from the very small to the fairly large (0.5–8 mm), having shapes ranging from spherical to oblate.

In general, the DSD spectrum can be approximated with sufficient averaging to the exponential Marshal–Palmer drop size distribution. But for instantaneous measurements of DSDs and accurate estimation of rainfall rates, a Gamma drop size distribution normalised to the total liquid water content provides the best approximation. In this formulation, all the parameters of the distribution are independent and have a physical basis.

In terms of instrumentation, rain gauges and radars are the most frequently used for the estimation of rain rates. In particular rain gauges are considered as “ground truth” instruments when comparing other measurements. The factors affecting annual cumulative statistics of point rainfall rates have also been presented, indicating that integrated measurements of 1 minute rain fall rates are adequate to give suitable cumulative yearly statistics for radio propagation use. For such yearly statistics, the rain rates exceeded between 0.001–1% of time are often used for the design of radio systems. Using the synthetic storm technique and methods such as Taylor’s Hypothesis, rain rate spatial statistics such as cor-

2.7. Concluding Remarks

relation of rain rates and rain cell size diameters can be obtained from time series data.

Recommendations on the use of yearly and monthly statistics in radio propagation applications, for locations around the world, have been provided by the ITU-R. Other prediction models in the literature for the estimation of cumulative yearly statistics have also been highlighted.

Convective and stratiform rain contain clusters of cells. Such cells for both types of rain have elliptical shapes that are twice as long as they are wide. Within such cells, rain rates tend to decrease exponentially from the centre of the cell. At high rain rates, these cells have small dimensional extent with the average cell diameter being approximately 2 km. In addition, several models on the structure of rain cells have been highlighted.

Recent investigations are now moving towards stochastic modelling. The stochastic dynamic variations of rain fields can be modelled using either pulse models, Markov chains or power spectral density models. These models are able to reproduce the first and second order statistics for a site and are useful as inputs to evaluate channel models and fade mitigation design for radio links.

Radar Observations of Precipitation

In this chapter we discuss the use of radar in the estimation of rain rate. In particular, it is shown that dual polarisation measurements allow for the estimation of rain rates to within 25% and compares favourably with rain gauge accuracies of 10%. It overcomes the problems normally associated with predicting rainfall from conventional radar data namely: uncertainties in the statistical distribution of drop sizes in rain, and reliably distinguishing between ice and rain particles. Besides the definition of dual polarisation measurements, we also summarise the limits of their accuracy. Using the Chilbolton radar operating at 3 GHz with high angular resolution, we describe the measurement campaign carried out between 1987–1989. From the resulting database, estimates of rain rates are obtained. Furthermore, an analysis of interpolation techniques, suitable for the transformation of the database, into a form appropriate for the simulation of attenuation along hypothetical route diverse links is presented.

3.1 Overview of Developments in Radar

Meteorology

RADAR meteorology's beginnings can be traced back to the 1940s [Atlas 1990]. In that time, the development of radar systems was pushed by the advent of the Second World War. Prior to that, there had been very little interest in the operational use of radar. Radar systems provided the capability to detect aircraft, ships and other projectiles from a considerable distance, providing an early warning of impending attack. But such detection was sometimes obscured by arealy extensive echoes across the radar field of view. These were later to be identified

3.1. Overview of Developments in Radar Meteorology

as meteorological phenomena such as rain, hail, sleet and snow.

Early research was therefore concerned with comparing the received signals from military and precipitation targets to facilitate the unambiguous determination of the type of target. The work of the Rydes [1941; 1944] on the scatter and attenuation by precipitation was substantial in this regard, and laid the foundation for studies in both radar meteorology and radio propagation in rain. Although to the military, the detection of precipitation echoes was unwanted, the meteorological community recognised its utility in the observation of weather patterns. Initial efforts in obtaining quantitative measurements of radar returns from precipitation produced large discrepancies between the theory and observations, with the observed measurements being less than calculations by an average of 2 dB. The work of Probert-Jones [1962] on the derivation of the radar equation for meteorological targets enabled close agreement to be obtained.

The radars up to then were of continuous wave-type, with separate antennas for transmission and reception (i.e. bi-static). The transition from continuous wave to pulsed radars in the 1960s, together with the use of higher frequencies especially at 3 GHz and above, provided improvements in range and angular resolution. Also, it made possible the use of the same antenna (mono-static) for both transmission and reception.

By the 1970s, significant advancements had been made in the use of radar for precipitation estimation, due to technological advancements in signal processing and data storage. Measurements could be digitally processed and stored, allowing for the development of data reduction, analysis and display techniques. Countries such as the United States and within Europe were also in the process of establishing extensive radar networks to provide better forecasting capabilities.

Towards the end of the 1970s, there was a realisation that no universal empirical relationship was possible to estimate rainfall rates from conventional radar reflectivity measurements, for all locations and time. As many as 200 different relations had been reported [Battan 1973], which were mainly governed by the statistical distribution of rain drop sizes at the time of measurement. Additional discrepancies between radar derived rain rates and rainfall rates from rain gauges were sometimes as large as 200%, and could only be reduced by averaging in space and time. This motivated further research into the evolution and modelling of rain drop size distributions.

The addition of switched polarisation capabilities [Seliga and Bringi 1976; Seliga

3.1. Overview of Developments in Radar Meteorology

et al. 1981] to meteorological radars considerably increased their effectiveness, but also increased their costs. Rain rates could be estimated with greater accuracy; better discrimination could be obtained for precipitation phase (i.e. ice/water); further knowledge into the internal structure of storms and their hazards could be inferred. Furthermore, the additional Doppler capabilities of radars have formed the basis into various studies of wind and rain drop speeds. Pioneering investigations by Doviak et al. [1977] showed that Doppler radar can give a picture of wind speeds within a storm, together with their motion and dissipation. Investigations by Doppler radar have also helped to establish that raindrops of different sizes, fall with different speeds (see § 2.2.3).

With the greater accuracy provided by dual polarisation radars, there have been concerted efforts over the last twenty years to produce more robust empirical estimators of rain rate. These combine the outputs of dual polarisation radars to minimise the physical uncertainty in the assumed rain drop size distribution, together with the statistical uncertainties of the measured outputs. Also, it has enabled the development of better algorithms for the identification of regions of snow, hail etc. within precipitation fields.

Although early meteorological radars used S-band, most meteorological radars now operate within C-band and above. The higher frequencies at which these radars operate have a greater potential for further increased accuracy in rainfall estimation, coupled with a reduction in cost compared to S-band radars. But their effectiveness is limited by the amount of attenuation the signal experiences through the precipitation medium.

Lately, the last decade has seen the increased development and use of mobile radar platforms. Space borne radars that can provide coverage for large regions across the earth such as TRMM (Tropical Rainfall Measurement Mission) [1997], are providing valuable products for meteorological research and forecasting of global weather. Airborne radars are also providing data for cloud studies.

Furthermore solid state transmitters, capable of producing the very high peak powers required for the detection of precipitation are emerging to challenge vacuum tube transmitters, which have been used since the genesis of meteorological radars. Modern radars now use computer displays for displaying their products. The evolution of radar meteorology has grown in leaps and bounds with the main driver being technological advancements in computing over the decades. Today, radar is an essential tool for analysing and predicting the weather and its products

3.2. Characteristics of Meteorological Radars

Table 3.1: Radar operating bands with approximate wavelengths and frequencies. Included is the antenna size for 1° resolution.

Band	Wavelength (cm)	Frequency (GHz)	Antenna diameter (m)
L	30	1	22
S	10	3	7.3
C	5	6	3.6
X	3	10	2.2
K	1	30	0.7

are indispensable in other areas of science and engineering.

3.2 Characteristics of Meteorological Radars

3.2.1 Operating Frequencies

Most current weather radar systems designed for precipitation observations operate at centimetre wavelengths, but millimetre wave radars also are common. The region of spectrum where they operate determines the band designation. This is shown in Table 3.1 with the characteristic operating frequencies.

S-band radar is the most suitable for rainfall measurements, with the ability to profile intense rain events without the return signals suffering much attenuation. They are widely used within the USA for operational purposes. Within Europe most national weather radar networks operate at C-band. Radars operating at K-band and above are usually used for cloud studies. As described in Table 3.1, operation in the higher frequency bands means smaller dish diameters for the same beam width. This has cost advantages but at the expense of higher signal attenuations.

3.2.2 Basic Operation

The simplest of weather radars operate with a single polarisation and are able to measure reflectivity. More advanced radars are able to use dual and circular polarisations with a larger number of measurement variables. This is discussed later in § 3.3. Figure 3.1 describes the basic components that are universal to modern meteorological radars.

Primarily, the radar consists of a transmitter to generate the high energy electromagnetic wave of required wavelength and a receiver to measure the received echoes. In most cases such transmitters are either magnetrons, klystrons or trav-

3.2. Characteristics of Meteorological Radars

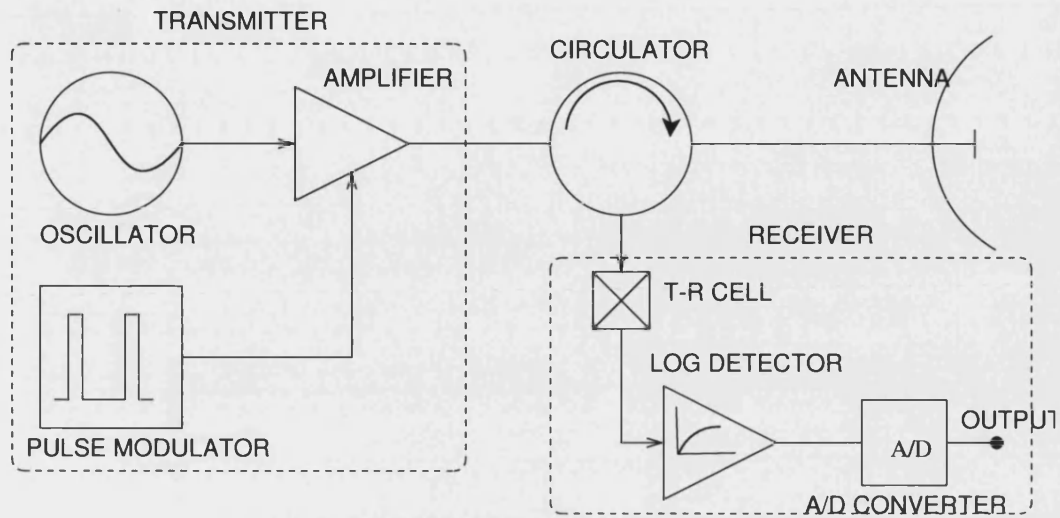


Figure 3.1: Basic components of a weather radar system

elling wave tubes that are sometimes mechanically controlled and produce peak pulse powers that are typically between 250 kW to 1 MW. Though solid-state transmitters are becoming available, their limited power range has precluded their widespread use.

An antenna of high gain and directivity is used to send and focus the microwave energy into a narrow beam out to space, and to receive the scattered energy (echoes) by the precipitation targets around. Since high spatial resolution is important for meteorological radars, the antennas are very highly directive with larger antenna sizes providing smaller resolutions. But radar performance can be degraded using very large antennas without due consideration to the rigidity of the antenna during windy conditions [Chandrasekar and Keeler 1993]. The half-power beam width of the antenna main lobe determines the angular resolution approximated by,

$$\theta \simeq 1.27 \frac{\lambda}{D_A} \text{ radians,} \quad (3.1)$$

where D_A and λ are the antenna diameter and wavelength respectively in metres. It is generally accepted that resolutions $\leq 1^\circ$ are required for the observation of precipitation. Typical antenna sizes for a 1° beam width are indicated in Table 3.1.

3.2. Characteristics of Meteorological Radars

Scanning and Echo Reception

The antenna generally rotates about its vertical axis scanning the atmosphere in azimuth. Such scans are Plan Position Indicator (PPI) scans which give information about the horizontal structure of precipitation. It is also capable of changing its elevation at fixed intervals in azimuth to acquire vertical profiles of the atmosphere (Range Height Indicator, RHI scans). Furthermore, a combination of both scan strategies is also possible. For example, Constant Altitude Plane Position Indicator (CAPPI) scans, which show horizontal precipitation profiles at a fixed altitude above the earth are also common.

Short high power pulses of short duration are transmitted before the echoes of the signal from the atmosphere arrive back at the antenna. This is then transferred to the receiver. The circulator (see Figure 3.1) enables the use of a single antenna for transmission and reception with the T/R cell providing a short circuit mechanism to prevent the higher transmit powers leaking into the sensitive receiver. Echoes of meteorological relevance typically span a wide range of power say from -100 dBm to -10 dBm, with the former value defining the required receiver sensitivity. Hence the receiver is required to have a wide dynamic range (ideally between 70–90 dB). A logarithmic amplifier enables the measurement of the signal over such a wide range, but performance can be degraded at low powers. Linear amplifiers with good performance over the whole power spectrum range are becoming available.

In modern radars, the signal processing is done by a dedicated computer with digital signal processing (DSP) units, data storage and a screen to display the processed echoes. Nowadays, such a computer is constructed from off the shelf components. The DSP unit performs analogue to digital conversion, quality assurance and applying various statistical and data correction algorithms before display and storage.

Range resolution and averaging

As the signal travels close to the speed of light, it typically takes a few microseconds to cover tens of kilometres and back to the radar. The time delay, t from the transmission of the pulse to the reception of the echo determines the range to target,

$$r = \frac{ct}{2}, \quad (3.2)$$

3.2. Characteristics of Meteorological Radars

where c is the speed of light. The minimum range resolution is determined by the pulse duration. The maximum range, R_{\max} is determined by the period between successive pulses. This is given by,

$$R_{\max} = \frac{cT_s}{2}, \quad (3.3)$$

where T_s is the pulse repetition time with the pulse repetition frequency (PRF) equivalent to the reciprocal of the pulse repetition time i.e. $\text{PRF} = \frac{1}{T_s}$.

Hence, splitting the receive time into a number of intervals enables measurements to be made over a number of range intervals or range gates. The volume over the range gate and beam width constitutes the bin size. For example, with a receiver sampling time of $1\mu\text{s}$ and a 1° beam width, the bin size is $150\text{m} \times 1^\circ$. For a maximum range of 300 km, the pulse repetition frequency would be less than or equal to 500 Hz with the pulse repetition time equal to 2 ms.

Time averaging is usually used to average pulses received within the beam width of the radar, so as to reduce statistical uncertainty. Assuming the radar scans in azimuth at a rate of 3 rpm, the scan period for 1° in azimuth would be around 56 ms, during which period returns from nearly 28 pulses would be available for averaging. Hence, the radar beam must effectively dwell this time interval or greater before an adequate sample size is achieved. A series of data points or bins thus averaged between two positions would constitute a ray with a collection of rays forming a slice.

The time averaging period is not completely dependent on the radar scan rate. Other factors such as the type of rain being observed and the application of the radar would affect the averaging time [Reid 1970; Bringi et al. 1978]. For instance a rain storm of highly turbulent and developing cells would produce a larger number of independent echoes per second compared with non-turbulent rain. As such, a radar with high spatial resolution cannot afford to dwell for a long time on one part of the storm.

Spatial averaging across the range gates is also used to improve echo estimation at the expense of a reduction in radial resolution. Typically, range gates that do not overlap contain different sets of drops and are therefore independent of each other. Providing rain is uniform over the pulse volume to be included in the spatial average, then each volume may be regarded as contributing a set of independent samples to one average. Usually averaging across 300 m radial dis-

3.2. Characteristics of Meteorological Radars

tances is sufficient. Hence, in our example above, two 150 m range gates may be averaged.

3.2.3 Applications

Besides radar's meteorological applications for weather prediction, its products are also useful in the fields of radio engineering and hydrology.

Within such fields, the advantage of radar is that it can seek out regions of rain and acquire in three dimensional space, a quasi-photograph of the precipitation field over large areas down to resolutions of a few hundred metres. In contrast, rain gauge networks that would cover an equivalent area are often widely-spaced, require constant monitoring and for 90% or greater of the year would lie un-utilised. Radar on the other hand can be configured to only acquire measurements when raining, saving resources. Additionally, the spatial inhomogeneity of rain imposes a constraint on the minimum number of rain gauges needed for adequate analysis, increasing experimental costs in the process.

For radio engineering applications in particular, it is possible to obtain a significantly larger database towards predicting rain attenuation statistics than acquired directly through a radio link path which must wait for the rain to intersect it. Two and three dimensional radar scans can be used to simulate various link geometries and thus to predict attenuation at any desired frequency of transmission. Such a property of radars is appealing as it is prohibitive to build a large number of radio links of various geometries and frequencies for obtaining long-term statistics. Crane [1989] has also commented that only radar observations are capable of amassing the required number of rain observations to produce adequate rain attenuation statistics for model analysis.

Some of the notable applications of radars [Goldhirsh 1975; Goddard and Cherry 1984a; Capsoni and Matricciani 1985; Goddard and Thurai 1997; Bandera et al. 1999; Cherry and Goddard 1985; Leitao and Watson 1984; Hall 1984; Goldhirsh 1979], for predicting propagation effects on radio links are listed:

- Attenuation due to rain as a function of elevation angle, orientation, polarisation, and frequency.
- Attenuation due to ice and melting hydrometeors.
- Diversity advantage as a function of spacing, radio path length, elevation and frequency.

3.2. Characteristics of Meteorological Radars

- Frequency scaling of attenuation distributions.
- Micro-climate effects and spatial variability statistics for radio links separated by a few kilometres.
- Depolarisation and interference on radio links.
- The statistical variation of the melting layer height which can be used to determine the portion of the path that is affected by precipitation on earth-space paths.
- Simulation of wide area wireless networks.

The results of radio link studies from radar measurements would be in the form of statistical distributions instead of time series data as it is usually not viable to operate radars around the clock for several years. Other applications of radars are:

- Testing models of ice forms and raindrops (including shapes, canting and distribution of hydrometeor sizes).
- Rainfall statistics for different rain types.
- Relationships between path integrated rainfall rate and point rates (and correlation distance of rainfall rate) .
- The determination of area rainfall rates.
- Evolution of rain cells and their characteristics.
- Assessment of water resources within catchment areas (river flow, urban drainage etc) and flash flood warning.
- "Ground truth" tests for remote sensing from space borne platforms.

3.2.4 Types

The types of meteorological radars in use can be generally grouped into two depending on the number of measurements that are possible. These are single (conventional) and multiple parameter (MP) radars. Single parameter radars are only able to measure reflectivity while MP radars are able to obtain up to 5 measurements. MP radars can be further divided into various types. These are:

3.2. Characteristics of Meteorological Radars

Multiple-wavelength radars. These measure the reflectivity at a wavelength long enough for the precipitation to cause Rayleigh scattering, and at another wavelength short enough to measure the attenuation through rain and/or non-Rayleigh scattering by large drops, to reduce the measured reflectivity.

Vertical incidence Doppler radars. These measure the Doppler spectrum to deduce the distribution of fall speeds of hydrometeors. Also vertical air motions can be profiled.

Dual linear polarisation radars. These measure the differential reflectivity, Z_{DR} for horizontally and vertically polarised transmission. Such radars enable the orientation and types of hydrometeor types to be distinguished together with their size distribution. A subset of this type of radar are circular depolarisation radars which measure the depolarisation of the backscattered signal when using circularly polarised transmissions.

A review of the above mentioned radars with the notable observations made by them is given by Rogers [1984]. Our discussion would be mainly restricted to precipitation estimation using dual polarisation radar at S-band which is relevant to this study.

3.2.5 The Radar Equation

The received power reflected from a radar point target is given by [Skolnik 2002],

$$P_r = \frac{P_t G^2 \lambda^2 \sigma_b}{(4\pi)^3 r^4}, \quad (3.4)$$

where σ_b is the backscattering cross section of the target, G is the antenna gain, λ is the wavelength, r is the range to target and P_t is the transmitter power. Equation 3.4 is known as the radar equation and applies universally for point targets as large as the moon and as small as a rain drop. It shows that the received power for a point object is inversely proportional to r^4 .

For meteorological radars, the radar pulse volume contains not one target but an ensemble of targets e.g. rain drops. Due to the ever changing distances between the illuminating radar and the individual rain drops and that between one rain drop and another, the resultant scattered field from a volume of rain undergoes amplitude and phase fluctuations in a random manner. Hence, it does not make much sense to talk in terms of values attained at particular instants of

3.2. Characteristics of Meteorological Radars

time. Statistical averages are more meaningful. Moreover, in radar applications decisions are generally made by adding (integration) several pulse returns rather than on single hits. Over a period of the order of 10 ms, the averaged returns converge to a reliable echo estimate [Marshall and Hitschfield 1953]. We can express the average received power for precipitation illuminated by an antenna as

$$\bar{P}_r = \frac{P_t G^2 \lambda^2 \theta \phi h}{512(2 \ln 2) \pi^2 r^2 \eta}, \quad (3.5)$$

where h is the pulse length and η is the reflectivity per unit volume given by

$$\eta = \frac{1}{\Delta V} \sum_{\Delta V} \sigma_{b(i)}. \quad (3.6)$$

ΔV represents the volume illuminated at any instant and is given approximately by

$$\Delta V = \pi \frac{h}{2} \left(r \frac{\theta}{2} \right) \left(r \frac{\phi}{2} \right), \quad (3.7)$$

where θ and ϕ are the horizontal and vertical antenna beam-widths respectively.

Equation 3.5 represents the form of the radar equation for meteorological targets derived by Probert-Jones [1962]. It shows that the received power from a volume of precipitation has an $1/r^2$ dependence. It assumes a conical beam shape, whose cross section is an ellipse with major and minor axes defined by their beam widths, and a Gaussian distribution is assumed over the principal axes of the main lobe.

For radars operating at S-band, the scattering produced by rain drops can be approximated by Rayleigh scattering. In this case the reflectivity per unit volume is

$$\eta = \frac{\pi^5}{\lambda^4} |K|^2 Z, \quad (3.8)$$

where $|K|^2$ is a dielectric factor for hydrometeors and is typically taken to be 0.93 for raindrops at temperatures ranging from 0°C to 20°C at S-band [Gunn and East 1954]. Other hydrometeor phases would have different values for the dielectric factor. The reflectivity factor Z is given by

$$Z \equiv \frac{1}{\Delta V} \sum_{\Delta V} D_i^6, \quad (3.9)$$

3.2. Characteristics of Meteorological Radars

and is directly proportional to the sixth power of the particle diameter. Also from equation 3.9, the reflectivity factor is a frequency independent parameter of the radar backscatter from rain when Rayleigh scattering applies.

At higher operating bands, the Rayleigh approximation is not an adequate description but because of the widespread use of Z , and for reasons of comparability, an effective reflectivity factor Z_e is used given by

$$Z_e = \frac{\lambda^4}{\pi^5 |K|^2} \eta. \quad (3.10)$$

In this case, η is given by equation 3.8 using rigorously derived backscatter cross sections. The units of the reflectivity factor are mm^6m^{-3} but conventionally, it is usually expressed in terms of dBZ, which is $10 \text{ dBZ} = 10\log(10 \text{ mm}^6\text{m}^{-3})$.

Attenuation of the radar signal

The radar equation 3.5 is not complete in that it assumes the transmission from the radar to the target and back again suffers no attenuation. Over the cm and mm wavelength bands, the attenuation effects due to atmospheric gases varies widely. The gases that cause attenuation are oxygen and water vapour. Water vapour two-way attenuation at S-band is about 0.0004 dB/km and hence has a negligible effect. But centred around the resonance band of 22 GHz, the two-way attenuation is 0.02 dB/km.

Radars operating at frequencies less than 10 GHz typically experience two-way attenuation of 0.01 dB/km as a result of oxygen attenuation [Skolnik 2002]. Although not significant for very short ranges, this has to be taken into account at longer distances. The total attenuation along a radar beam due to gases also depends on density and consequently radar elevation. Hence, for a radar operating at S-band with an elevation angle of 0.5° , the total two way attenuation over 50, 100, and 150 km is 0.8, 1.4 and 2 dB respectively. Generally this attenuation can be corrected for without complication. Doviak & Zrnich [1992], provide an empirical formula relating to the two way attenuation for ranges less than 200 km given by

$$A_g = 0.4 + 3.45 \exp(\theta/1.8) \left\{ 1 - \exp\left(\frac{r}{27.8 + 154 \exp[-\theta/2.2]}\right) \right\} \text{ dB}, \quad (3.11)$$

where the elevation angle $\theta < 10^\circ$. Millimetric radar systems ($> 35 \text{ GHz}$), such as those for observing clouds have to employ more sophisticated models [Brussard

3.3. Conventional and Dual Linear Polarisation Radar Measurements

and Watson 1994] and would experience two-way attenuations of the order of 1 dB/km.

Also received echoes are attenuated by the precipitation itself that intervenes between the radar and the rain under observation. This will depend on the underlying rainfall rate and temperature. Typically at S-band, the two way attenuation would be 0.01, 0.1 and 0.3 dB/km for rain rates of 10, 50 and 100 mm/h respectively [Cherry and Goddard 1984]. Hence measured echoes need only be corrected for attenuation when the intervening rain is exceptionally strong. At other higher operating bands, the attenuation is orders of magnitude higher and cannot be neglected even for rain rates as low as 5 mm/h.

3.3 Conventional and Dual Linear Polarisation Radar Measurements

As stated earlier conventional radars are only able to obtain one measurement from the precipitation field. This is the reflectivity factor. It is the summation of the backscattered cross sections of all the individual hydrometeors within the radar pulse volume. More precisely, for hydrometeors with size distributions $N(D)dD$, and back scatter cross sections $\sigma(D)$, the reflectivity factor is

$$Z_{H,V} = \frac{\lambda^4}{\pi^5 |K|^2} \int_{D_{\min}}^{D_{\max}} \sigma_{H,V}(D) N(D) dD, \quad (3.12)$$

where H and V represent the orthogonal linear polarisation states, and D_{\max} , D_{\min} are the maximum and minimum diameters of the drops sampled in the pulse volume respectively. For rain drops, the size distribution is suitably approximated by exponential and Gamma distributions as described in § 2.2.1. But to define the DSD, at least two parameters are required i.e. N_0 and D_0 .

Hence in the estimation of rainfall rate from reflectivity measurements, assumptions have to be made on the values of one of these parameters. Generally N_0 , which typically varies with rainfall type, is assumed to be fixed at $80000 \text{ cm}^{-1}\text{m}^{-3}$. D_0 which varies with rainfall rate, can then be obtained from reflectivity measurements. This introduces large uncertainty in radar rainfall estimation from reflectivity as the fixed value of N_0 represents an average within rain types. Therefore, to remove the need for assumptions described, it is necessary that the radar measures more than just the reflectivity.

3.3. Conventional and Dual Linear Polarisation Radar Measurements

Polarisation diversity radars that are capable of switching between orthogonal (dual) polarisation states can provide such additional information. A dual polarisation radar takes advantage of the fact that rain drops have a degree of oblateness that is directly proportional to the drop diameter. The field of drops, as a whole, will have a larger cross-section of water in the horizontal plane compared to the vertical plane. A horizontally-polarised radar pulse will, therefore, be backscattered more in this field of drops than a vertically-polarised pulse, resulting in more radar return for the horizontal pulse than the vertical pulse. Hence, $\sigma_H(D)$ is greater than $\sigma_V(D)$. This leads to the measurement of differential reflectivity defined in decibels as,

$$Z_{DR} = 10 \log \left(\frac{Z_H}{Z_V} \right). \quad (3.13)$$

First proposed by Seliga & Bringi [1976], it senses the mean shape of rain drops. For rain with an exponential distribution, Z_{DR} is given by

$$Z_{DR} = 10 \log \left(\frac{\int_0^{D_{max}} \sigma_H(D) \exp(-\Lambda D) dD}{\int_0^{D_{max}} \sigma_V(D) \exp(-\Lambda D) dD} \right), \quad (3.14)$$

and depends only on Λ , which is a function of D_0 alone. Z_{DR} values for meteorological echoes typically range between -2 to 5 dB. Values of Z_{DR} well above zero indicate the hydrometeors in the volume are horizontally oriented, with the larger values of Z_{DR} indicating more heavy rain. Values of Z_{DR} well below zero indicate the hydrometeors in the volume are vertically oriented. Values of Z_{DR} near zero indicate the hydrometeors in the volume have a nearly spherical shape, and mostly occur in light rain or drizzle.

Then knowing D_0 , N_0 may be obtained from Z_H or Z_V where,

$$N_0 = Z_{H,V} \left(\frac{\lambda^4}{\pi^5 |K|^2} \int_0^{D_{max}} \sigma_{H,V}(D) \exp(-\Lambda D) dD \right). \quad (3.15)$$

Figure 3.2 shows Z_{DR} and Z_H/N_0 as a function of D_0 for a 3 GHz radar and rain temperature of 5°C.

The actual implementation of the Z_{DR} technique is not straight forward due to the rapidly fluctuating echoes from successive radar pulses as large numbers of rain drops reshuffle their positions. Very rapid switching of the polarisations is often required (faster than the 10 ms decorrelation time of echoes) and due to the high peak powers involved, good switching stability between polarisations must

3.3. Conventional and Dual Linear Polarisation Radar Measurements

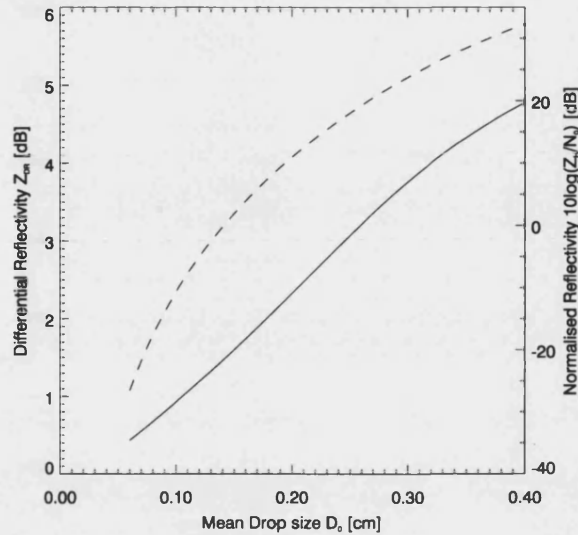


Figure 3.2: Relationships for 3 GHz radar frequency, between the radar observables, Z_H and Z_{DR} , and the drop size distribution parameters N_0 and D_0 . The solid line is for the differential reflectivity while the dashed line shows the normalised reflectivity. The plots are for a rain temperature of 5°C with Pruppacher & Beard drop shapes.

be achieved.

Other useful parameters that can be measured by dual polarisation radars are the co-polar correlation, ρ_{hv} between time series of successive estimates of Z_H and Z_V ; the linear depolarisation ratio, $\text{LDR} = 10 \log \left(\frac{Z_{DR}}{Z_H} \right)$; and if the radar is Dopplerised, the phase of the horizontally and vertically polarised returns, ϕ_h and ϕ_v . For this study only Z_H and Z_{DR} are of relevance, and we shall simply quote the relevant formulae and analyses within the literature. In-depth information on these and other measurements and their derivations can be obtained from within the following: [Bringi and Chandrasekar 2001; Doviak and Zrnich 1992].

3.3.1 Required Accuracy in Measurements Z_H & Z_{DR}

Systematic Errors

To minimise systematic errors in the measurement of reflectivity, the radar has to be well calibrated. The absolute calibration of the radar depends on several factors such as the antenna gain, gain of the amplifiers, loss in the waveguides

3.3. Conventional and Dual Linear Polarisation Radar Measurements

etc. Simplifying equation 3.5, we can express the average received power as

$$\bar{P}_r = C \frac{Z_H}{r^2}, \quad (3.16)$$

where C is the radar constant which depends on the aforementioned factors. Accurate knowledge of C is very important for estimating Z_H from the received power.

Calibration can be performed in many ways. A common method is to inject a signal of known power into the receiver from which the radar receiver can be adjusted to give the correct signal level. Another is to compare resulting rain rate estimates with rain gauges. These are only good to within 3 dB.

Alternatively, the reflectivity per unit volume of precipitation, η is compared with the back scatter cross-section of a metal sphere of known cross section. This is done using an aluminium sphere, tethered to balloons and raised to a height of about 200 m. It requires clear weather with low wind speeds to raise the sphere to the required height and is quite costly. In most cases calibration can be achieved to within 1 dB.

For dual polarisation radars, new techniques have also been presented which achieve reflectivity calibration using properties of the rain medium. Goddard et al. [1994b], describe a technique of calibrating reflectivity measurements to within 0.5 dB using observed and modelled values of the differential propagation phase shift, ϕ together with Z_{DR} in moderate to heavy rain. The technique is automatic in that there is no requirement to allocate a specific period for calibration correction during operations. A similar method is described by Gorgucci et al. [1999], but in this case using the specific differential phase, K_{DP} . However in all cases described, the radar constant is expected to change over time. Hence periodic calibration corrections have to be carried out.

For the differential reflectivity, calibration is achieved by pointing the antenna vertically. Since Z_{DR} measures the mean shape of rain drops, and raindrops are generally oriented with their symmetry axis in the vertical direction. Rain drops observed vertically will then be circular. This implies that measurements of Z_{DR} would be zero. Any deviation from this value when observations are taken vertically implies a bias. Such calibrations are normally carried out in drizzle but there are limitations to achieving a 0 dB value of Z_{DR} . This would be from any canting of the rain drops from the vertical direction (see § 2.2.3 and § 3.3.2) but in most

3.3. Conventional and Dual Linear Polarisation Radar Measurements

cases a systematic error of less than ± 0.1 dB can be achieved. As Z_{DR} represents a ratio of reflectivity values, it is “self calibrating” with minimal deviations of the calibration over time.

Random errors

As noted, there is a requirement that independent samples of the received power from radar targets have to be averaged to achieve a reliable estimate of the reflectivity. This introduces a random error which is dependent on the number of samples that are averaged. Marshall & Hitchens [1953], have noted that the width of the probability density distribution of averaged received power is inversely proportional to the number of independent samples averaged. For sample sizes greater than 10, the peak of the distribution is centred over the true average received power. This leads to an expression for the standard deviation associated with the average of reflectivity in dBZ given by

$$\sigma_{Z_H} = 10 \log \left(1 + \frac{1}{\sqrt{N}} \right). \quad (3.17)$$

Typically the measurement of Z_H is required to be better than 1 dB. From equation 3.17, this implies that 50 or more samples are necessary.

For precision measurement of Z_{DR} , the standard deviation is approximated by [Bringi et al. 1978; Cherry and Goddard 1984],

$$\sigma_{DR} = 10 \log \left(1 + \sqrt{\frac{2}{N(1-\rho)}} \right), \quad (3.18)$$

where ρ is the correlation between the horizontal and vertical polarisations of the reflectivity measurements. Over a wide range of Z_{DR} measurements, $\rho \geq 0.98$. Typically the precision of Z_{DR} is required to be better than 0.2 dB. Hence from equation 3.18, 50 or more independent samples having a correlation of 0.98 between polarisations would imply a standard deviation of less than 0.125 dB. In practice, other factors such as reflectivity gradients and mismatch in H and V patterns may limit the accuracy of Z_{DR} .

3.3.2 Effect of Rain Micro-physics on Dual Polarisation Measurements

Micro-physical effects such as variation in temperature, rain drop shape, drop canting, and DSD effect the range of dual polarisation measurements. For the re-

3.3. Conventional and Dual Linear Polarisation Radar Measurements

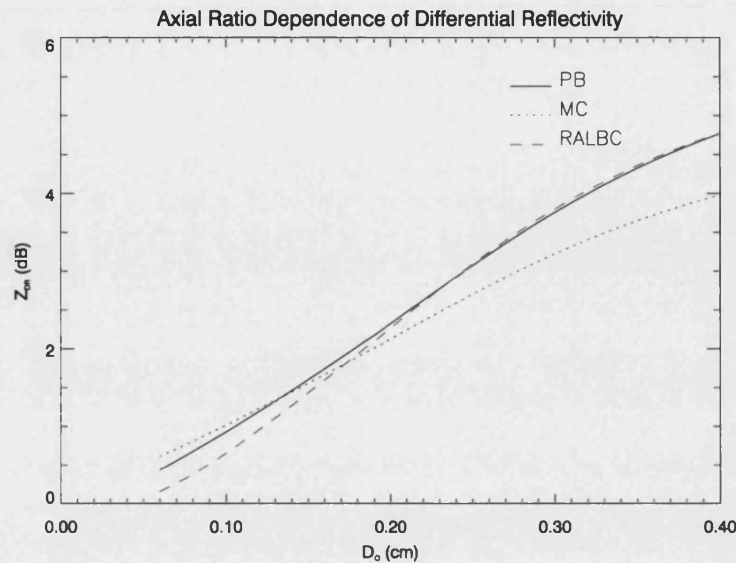


Figure 3.3: Plot of Z_{DR} against D_0 for the drop shape models of Pruppacher & Beard [PB] (solid), Morrison & Cross [MC] (dotted), and Goddard et al. [RAL] (dashed).

flectivity, such micro-physical variations have a negligible effect (except for DSD variations) on measurements but appear with varying significance for measurements of differential reflectivity.

Variation with Ambient Temperature

Cherry & Goddard [1984] have shown over temperature ranges of 5–20°C, the variation of Z_{DR} is very small. Z_{DR} shows a maximum variation of 0.03 dB at the top end of the temperature range for mean drop sizes greater than 3 mm. Since precision in Z_{DR} is required to be within 0.2 dB, such temperature variation is likely to be up to 15% of such precision. But this would only be significant at higher temperatures and high Z_{DR} values.

Variations in Drop Shape

As Z_{DR} measures the mean shape of drops, the assumption on the underlying shape of rain drops would have an effect on the rain estimate. Early radar estimates of rainfall through the use of differential reflectivity measurements assumed such drop axial ratios of Pruppacher & Beard [1970] (see § 2.2.2).

But investigations by Goddard et al. [1982], found that observed values of Z_{DR} in the range 0–1.5 dB were from 0.5 to 0.2 dB lower than the values computed

3.3. Conventional and Dual Linear Polarisation Radar Measurements

using first degree drop axial ratios from disdrometer measurements. Such deviations would cause inaccuracies in the estimation of rainfall rate. Based on their observations, they proposed a new rain drop shape model [Goddard and Cherry 1984a], that resolves the discrepancy (see equation 2.15). Figure 3.3 shows the variation of Z_{DR} for the linear drop shapes of Pruppacher & Beard, Morrison & Cross [1971] and the new drop shape proposed by Goddard et al.

Canting of Rain Drops

The relationship between Z_{DR} and D_0 shown in Figure 3.2 assumed that the axis of symmetry of the rain drops was vertical and that the radar observes rain at zero elevation. In reality rain drops tend to cant as a result of wind shear, and of course the elevation of the radar beam is unlikely to be zero. The effect of raindrop canting on Z_{DR} have been investigated by Al-Katib et al. [1979]. They show that the non zero elevation of the radar beam causes an effective canting in the plane of incidence. The effect is negligible for elevation angles $<5^\circ$, but becomes appreciable for angles $>10^\circ$, with variations up to 1 dB at the largest Z_{DR} values. Therefore measured Z_{DR} values would have to be corrected for when radar elevation angles are greater than 10° .

Wind shear can also produce canting in either the plane of incidence or perpendicular to the plane of incidence. Brussard [1976], Beard & Jameson [1983], and Stapor & Pratt [1984] show that such canting is unlikely to exceed 5° at the heights at which radar observes rain (above 100 m). They also conclude that canting angles of this magnitude will have a negligible effect due to wind shear on the interpretation of Z_{DR} measurements.

DSD Variation

It is often found in nature that rain drop size distributions not only display pronounced variations in both N_0 and D_0 , but in addition show deviations from linearity on a semilogarithmic plot of $N(D)$ vs D . The Gamma DSD proposed by Ulbrich [1983], provides a good approximation to the deviation. Recall equation 2.5 in § 2.2.1

$$N(D)dD = N_0 D^\mu \exp(-\lambda D) dD \quad (0 \leq D \leq D_{\max}). \quad (3.19)$$

The parameter μ approximates the shape of the distribution. For $\mu = 0$, the DSD reduces to the exponential of Marshall & Palmer.

3.3. Conventional and Dual Linear Polarisation Radar Measurements

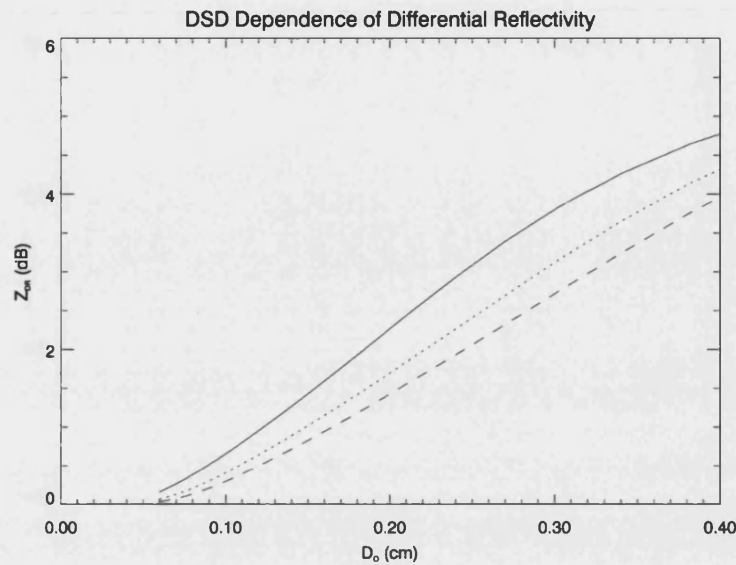


Figure 3.4: Differential reflectivity, Z_{DR} vs mean drop diameter, D_0 using the Gamma DSD with variations in μ of 0 (solid), 2 (dotted) and 4 (dashed).

Typical values of μ are within the range 0–5 but larger values have been observed [Kozu and Nakamura 1991; Tokay and Short 1996]. Ulbrich [1986] has shown that for a given value of D_0 , Z_{DR} increases as μ increases, and the variation is sufficient to produce inaccurate estimates of rain rates. For values of μ in the range 0–4, Z_{DR} values show a variation of 0.5 dB when D_0 is 0.1 cm. At higher values of D_0 (0.3 cm), the variation is about 1.5 dB (see Figure 3.4).

Furthermore, the variation of μ scales the reflectivity measurements by a factor which is a constant multiplicative offset (see Figure 3.5). To correct this effect of an increase in μ leading to a marked decrease in the concentration of the DSD (which does not happen in natural drop spectra) and consequently a decrease in the reflectivity, Ulbrich proposed a relationship to relate N_0 to μ (see equation 2.9). This was obtained from Z-R relationships reported at the time [Battan 1973].

Recent investigations by Testud et al. [2001; 2001], Illingworth & Blackman [2002] and Bringi & Chandrasekar [2001] have shown that such an $N - \mu$ relationship has no physical basis and a normalised Gamma distribution (see § 2.2.1) where all three parameters N_0 , D_0 , and μ are independent, provides a better description of the DSD. For such a distribution, the effect of varying μ on the reflectivity is negligible as the drop spectra have the same liquid water content irre-

3.3. Conventional and Dual Linear Polarisation Radar Measurements

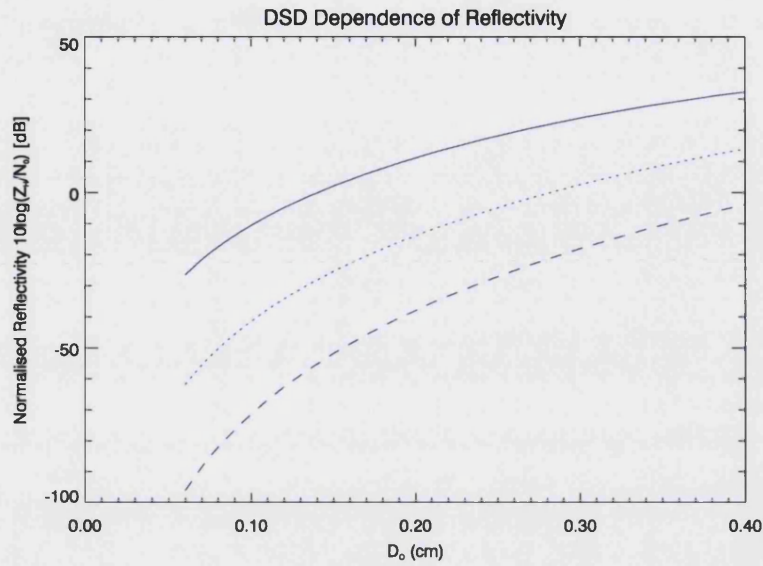


Figure 3.5: Normalised reflectivity, $10\log\left(\frac{Z}{N_0}\right)$ vs mean drop diameter, D_0 when using Ulbrich's Gamma DSD with variations in μ of 0 (solid), 2 (dotted) and 4 (dashed).

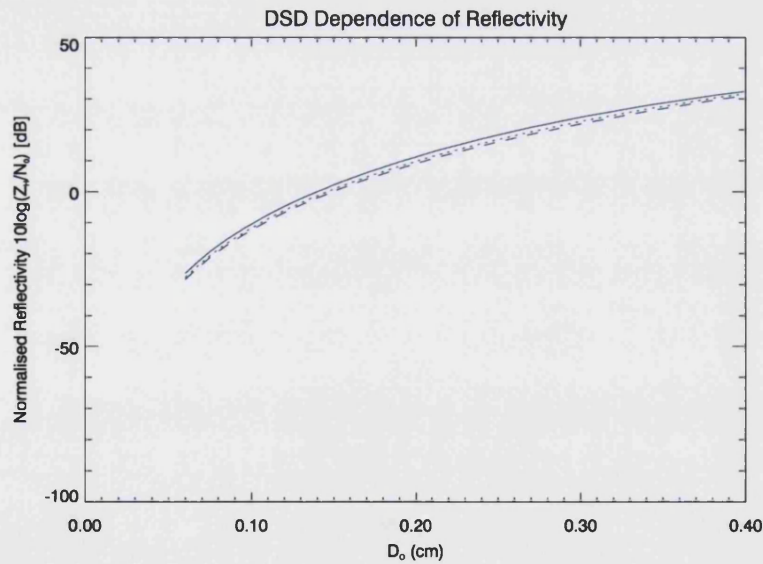


Figure 3.6: Normalised reflectivity, $10\log\left(\frac{Z}{N_0}\right)$ vs mean drop diameter, D_0 when using the normalised Gamma DSD with variations in μ of 0 (solid), 2 (dotted) and 4 (dashed).

3.4. Radar Rainfall Estimation

spective of μ . This is shown in Figure 3.6.

But even for the normalised distribution, the effect of μ on Z_{DR} does not change from that shown in Figure 3.4, with Ulbrich's Gamma DSD. But the objective in the measurement of precipitation is to estimate R not D_0 , and R is both a function of D_0 and μ . As we shall see in § 3.4.2, with the use of the normalised DSD the effect of μ is reduced in rain rate estimation.

3.4 Radar Rainfall Estimation

The most frequent requirement of a meteorological radar is to estimate rain rate. As stated earlier, weather radars are incapable of directly measuring rain rate, but in combination with one or more of the measurement variables, the rain rate can be inferred. This inference is done through the development of empirical relationships that relate rain rate to the radar measurables. For radio communications, a relationship to the attenuation (or specific attenuation) is also commonly sought. It has to be stressed that the result of such estimations have to be compared with other sources so as to verify the consistency of the estimates and also to detect any deviations in calibration of the radar measurements over time. Usually estimates from radar are compared with local measurements from a rain gauge but measurements of DSDs from a disdrometer are also used in verifications. Before we endeavour to highlight the approaches to rain rate estimation using radar, it is worth briefly listing certain issues which have to be considered in the estimation process. Some of these have already been stated. They are;

- Uncertainties associated with the radar constant
- Radar processing errors such as quantisation of measurements
- Uncertainties due to reflectivity gradients
- Sources of error intrinsic to the medium such as; variability of DSD in space and time; other precipitation particles; and lower path reflectivity assumptions.

3.4.1 Reflectivity Relationships

Rainfall is commonly estimated from radar data with a $Z - R$ relationship,

$$Z_H = aR^b \quad (3.20)$$

3.4. Radar Rainfall Estimation

which converts bulk reflectivity to a rainfall rate. Such relations are by no means unique. Several $Z - R$ relationships exist, for different rain types (convective, stratiform, winter, tropical etc). The first classic $Z_H - R$ relation, where $a = 200$, and $b = 1.6$ is derived from the Marshall & Palmer DSD. Battan [1973] has reported over 200 proposed relations covering numerous different geographic locations and events. But since then, the number of relationships has exceeded 300 [Goddard et al. 1994a].

The lack of a unique formulation is not surprising since Z depends on the sixth power of the drop diameter, whereas rain rate depends on approximately the third power of the drop diameter. Additionally, the equation relating Z_H to R varies according to the DSD of the rain in the volume of interest, which can vary widely from one event to another. Because of the drop size dependence, Z measured for a few large drops, which would cause a low rainfall rate, could equal the Z_H measured for many small drops, which would cause a high rainfall rate.

We have highlighted that the range of naturally occurring drop spectra is well approximated by a normalised Gamma DSD (see chap. 2). Following the treatment of Bringi & Chandrasekar [2001], integrating the normalised DSD leads to expressions of reflectivity and rain rate in the form:

$$\begin{aligned} Z_H &= F_Z(\mu) N_0^* D_0^7, \\ R &= F_R(\mu) N_0^* D_0^{4.67}. \end{aligned} \quad (3.21)$$

Eliminating D_0 and re-arranging gives,

$$Z_H = \frac{H(\mu) R^{1.5}}{\sqrt{N_0^*}}. \quad (3.22)$$

Hence a from equation 3.20 is a function of both μ and N_0^* , with the value of b being close to the M-P value. The variation of μ from 0 to 5 and 10 leads to a change in the value of $H(\mu)$ by a factor of 1.5 (2 dB) and 1.8 (2.5 dB). Also the observed standard deviation of N_0^* is a factor of three from the M-P value [Tokay and Short 1996; Testud et al. 2001]. The combination of both variations will lead to an estimation error for the rain rate by about 65%. If the range of values of N_0^* is a factor of ten, then this increases to a factor of two error in the rainfall rate.

Hence, this shows that the use of a simple $Z_H = aR^b$ relationship will lead to

3.4. Radar Rainfall Estimation

Table 3.2: Recent rain rate algorithm co-efficients at S-band for equation 3.23 presented within the literature

Authors	C	α	β	Comments
Bringi and Chandrasekar [2001]	6.7×10^{-3}	0.93	-0.343	Derived from polynomial drop shapes
Gorgucci et al. [1995]	12×10^{-3}	0.91	-0.403	Derived from linear drop shapes
Gorgucci et al. [1994]	10×10^{-3}	0.92	-0.369	Derived from linear drop shapes

estimation errors of up to 100%. Use of more sophisticated correction techniques, or local measurement of precipitation drop size spectra, may bring these down to 30–50% . In addition, the use of this method does not enable for the correction of very high Z_H values found in ice mixtures (snow, hail, etc.), leading to the potential for gross over estimation of rain rates when ice mixtures are present. Finally, besides the aforementioned factors, the relationship is sensitive to any bias in radar calibration.

3.4.2 Reflectivity and Differential Reflectivity Relationships

In high reflectivity regions, differential reflectivity can provide an estimate of the DSD, reducing errors from calculations using Z alone by a factor of two. Several forms of $Z_H - Z_{DR}$ relations have been proposed. An approach which has been widely adopted in the literature is given by

$$R = CZ_H^\alpha 10^{\beta Z_{DR}}, \quad (3.23)$$

where Z_H is in standard units (i.e mm^6m^{-3}) and Z_{DR} is in dB.

The co-efficients are chosen by allowing N_0 , D_0 and μ to vary over values proposed by Ulbrich [1983]. Similar relations to equation 3.23 have also been proposed by Ulbrich [1986]. The list of recently proposed values is given in Table 3.2.

Illingworth [1989; 2003] has also proposed a relationship for both linear and polynomial drop shapes in which Z scales with R for a constant Z_{DR} in the form

$$\frac{Z_H}{R} = Cf(Z_{DR}), \quad (3.24)$$

The function, $f(Z_{DR})$ is well approximated by a third order polynomial. Figure 3.7 shows Z_H/R as a function of Z_{DR} which have been obtained from Fredholm

3.4. Radar Rainfall Estimation

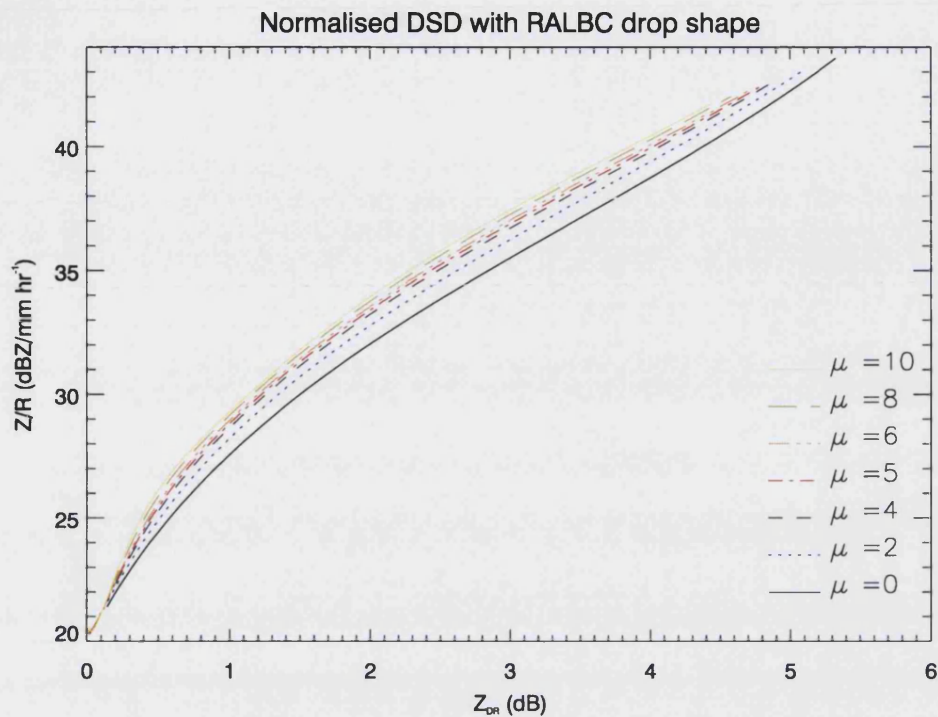


Figure 3.7: Plot of horizontal reflectivity per unit rain rate as a function of differential reflectivity.

Integral Method (FIM) [Uzunoglu et al. 1976] scattering simulations at S-band using polynomial drop shapes of Goddard et al. [1995] and the normalised Gamma DSD for values of μ between 0–10. The curves can be interpreted as the Z_H which would give R of 1 mm/h. So if for a given Z_{DR} the observed value of Z_H is x dB above the line, then the rain rate is x dB above 1 mm/hr.

It can be seen that the value of Z_H per unit R as a function of Z_{DR} has a much reduced dependence on μ with the curves being on average only 1 dB apart over the range of Z_{DR} . The use of linear shapes will lead to curves which are approximately 2 dB lower for a given μ . The variability of μ would introduce an uncertainty in the rainfall estimate by about $\pm 12\%$.

The accuracy of the rain rate estimate using such a relationship is determined by the slope of the curve. A 25% accuracy in R implies that Z_H/R should be known to 1 dB which from the slope of the curves imposes a limit of 0.2 dB for the accuracy of the Z_{DR} measurement. Generally for rain rates lower than 10 mm/hr the $Z_H - Z_{DR}$ algorithms are prone to errors of up to 50% [Gorgucci et al. 1994] and

3.4. Radar Rainfall Estimation

Table 3.3: Characteristics of Z and Z_{DR} for various hydrometeor types after Doviak and Zrnica [1992] and Straka et al. [2000].

Hydrometeor Type	Z (dBZ)	Z_{DR} (dB)
Rain	<60	>0
Snow	<35	0.5–3
Graupel/Small Hail	20–50	-0.5–2
Hail	45–80	<-2–0.5
Rain-Wet Hail	45–80	-1–6

hence would only be slightly better than estimates from the reflectivity alone. To achieve accuracies to within 25% at such low rates imposes an accuracy to within 0.1 dB in Z_{DR} which is difficult to achieve. In addition, $Z_H - Z_{DR}$ derived estimates can still suffer from errors due to hail and inadequate radar calibration. The following provides a brief discussion on the identification of non-rain hydrometeors which can help reduce the error in rain estimates.

3.4.3 Identification of Non-rain Hydrometeors

Consideration has to be made to situations when the radar beam may be scanning a region containing icy hydrometeors. Firstly, in the summer time graupel and hail in convective clouds can occur at lower levels where the temperature is above freezing. Secondly, in the winter time and at longer ranges in all seasons, the radar beam will be dwelling regions above the freezing level and can expect to encounter icy particles such as snow.

Let us consider a resolution volume with a mixture of raindrops and hailstones. We know that, among other things, the reflectivity factor is a function of the average diameter of the hydrometeors in the volume to the 6th power, and the dielectric constant of the hydrometeors. Adding hailstones to a field of raindrops increases the average hydrometeor diameter, leading to a much higher reflectivity factor. This would lead to a much higher estimate for the rain rate when using reflectivity alone.

We have shown that the addition of Z_{DR} would lead to better estimates of rain rate. However the usefulness of Z_{DR} does not stop at improved precipitation measurement. Z_{DR} also has a sensitivity to the differing dielectric properties of ice and water.

In contrast to rain drops, dry ice particles exhibit a much reduced polarisation

3.4. Radar Rainfall Estimation

difference for a similar shape. When falling, they appear nearly spherical to the radar, and because such particles are much more reflective than raindrops, the reflectivity for horizontally-polarised radar pulses should be about the same as that for vertically-polarised pulses. Thus many forms of ice such as snowflakes and hail exhibit only a small Z_{DR} signature (close to zero) until they begin to melt. As this process begins, they show the combined effect of quite asymmetrical shapes together with an increased dielectric constant. A pronounced increase in Z_{DR} is the result, and the phase of the hydrometeors can be inferred. Some graupel and hail hydrometeors with a conical shape can fall with their major axes oriented in the vertical. In this case, observed values of Z_{DR} would be negative. Table 3.3 describes the range of values of which the Z_H and Z_{DR} can take in the presence of different hydrometeors.

From this we can see that there is considerable overlap in these values especially for snow and graupel and extra measurements are needed for their identification. Hail on the other hand can be identified to some degree but not unambiguously. The reason for this is that there are no definitive relations between axis ratio and size for hail [Straka et al. 2000]. The general consensus is that reflectivities greater than 55 dB are indicative of hail. Leitao & Watson [1984] have presented an algorithm for the identification of hail from a study of convective storms in the UK given by

$$H_{DR} = Z_H - f(Z_{DR}), \quad (3.25)$$

where H_{DR} is the hail signal and,

$$\begin{aligned} f(Z_{DR}) &= 37.5 + 19Z_{DR} - 4Z_{DR}^2 \quad 0 < Z_{DR} < 2.5 \\ f(Z_{DR}) &= 60 \quad Z_{DR} \geq 2.5. \end{aligned} \quad (3.26)$$

Investigations by Aydin et al. [1986] have also presented a similar relationship that agrees well with equation 3.26 but there is a 5 dB difference in the curves for Z_{DR} values in the range 0–0.5 dB.

Also of note, Liu & Chandrasekar [2000] have presented the use of a fuzzy logic scheme to identify hydrometeor types from a combination of 5 radar measurables. Since there is overlap in the range of particle measurements, weighting functions are applied to each combination of measurements to arrive at a decision on the hydrometeor type.

3.5. Chilbolton Advanced Meteorological Radar



Figure 3.8: The Chilbolton Advanced Meteorological Radar (CAMRA) with its 25 m antenna.

3.5 The Chilbolton Advanced Meteorological Radar

Managed by the Radio Communications Research Unit (RCRU), the Chilbolton Advanced Meteorological Radar (CAMRA) has been at the forefront of meteorological and radio propagation research for over thirty years. Initially built for air surveillance in the 1960s, it was converted for meteorological use in the 1970s. Situated at Chilbolton near Winchester in Hampshire, it operates at S-band and is the worlds largest meteorological radar with a 25 m antenna (see Figure 3.8).

In the late 70s, the radar was the first in the world to provide dual polarisation measurements. During the mid 1980s, the radar was upgraded to provide cross polar measurements of reflectivity together with measurements of co-polar correlation through the use of pulse-to-pulse recording. The superb performance of this switch revealed spectacular new insights into the structure of rain and snow, and led to the subsequent implementation of polarisation systems in many countries. Table 3.4 describes the radar parameters up to the period 1992/93, which is relevant to the radar database used in this study.

The well calibrated CAMRA typically operates in a non continuous, event based mode, where measurements are not taken until the occurrence of rainfall within

3.6. The CRIE Database

the radar field of view, and/or when time has been allocated for a particular experiment. The large antenna size enables high resolution (0.25° beamwidth) with the radar. When scanning, 64 pulse pairs are averaged over a period of 210 ms in addition to taking range gate averages to achieve Z and Z_{DR} measurements to within 0.75 dB and 0.2 dB respectively. This enables estimates of rain rates to be within 25%.

Since the early 90s, the receiver system has been significantly changed with the only remnant from its genesis being the mechanically tunable magnetron. The design of a dual channel receiver with increased dynamic range has enabled simultaneous measurements of co-polar and cross-polar returns. Addition of phase and Doppler capabilities to the radar also facilitated the measurement of extra radar parameters. A detailed description of the current CAMRa sub-system hardware and signal processing scheme is given in Goddard et al. [1994a]. We now describe the database used for this study, involving the systematic collection of reflectivity and differential reflectivity data over a two year period, with a view to estimating rain rates.

3.6 The CRIE Database

The Chilbolton Radar Infererometry Experiment (CRIE) was a two year rain measurement campaign between 1987–1989, designed primarily for development and testing of rain scatter interference models as part of the COST 210 project [COST210 1991].

To make use of the data statistically, it was important that the rain sampling strategy involved in the radar measurements was not biased. Set PPI and RHI scan patterns were recorded in a ten minute cycle for 9 out of 28 days. The acquisition of each scan was on the condition of rain (defined as rain with Z greater than 25 dBZ) within the scan area, and was checked by a radar operator. This was to allow for system maintenance and other experimental programmes. The days of operation were chosen well in advance and no reference was to made to weather forecasts as to the likelihood of rain, or not.

Each day was defined to start at 1200 GMT, lasting through to 1200 GMT the next day. The first 5 days of a period began at 1200 GMT on Monday, and continued through to 1200 GMT on the following Saturday. The final four days started at 1200 GMT on the next Monday and ended at 1200 GMT on the following Friday. If more than 24 hrs were lost due to, for example, equipment failures or lack of

3.6. The CRIE Database

Table 3.4: Chilbolton radar characteristics

ANTENNA	
Type	Prime focus fed parabolic dish
Diameter	25 m
Half-power beam width	0.25°
Gain	53.5 dB
Side lobe level	-20 dB
Cross-polarisation level	-30 dB
Polarisation radiated	Horizontal and Vertical
Scan type	PPI, RHI & combined
Steering and scanning rate	Computer controlled, 1° /second
TRANSMITTER	
Type	Cavity magnetron
Frequency	3.075 GHz
Peak power	560 kW
Pulse width	0.5µs
PRF	610 Hz
Minimum and Maximum range	4.8 km and 158 km
RECEIVER	
Noise figure	3.5 dB
I.F Amplification	Logarithmic
Dynamic range	80 dB
Minimum detectable signal	-100 dBm
DATA ACQUISITION	
Digitisation range	64 dB in 256 steps of 0.25 dB
Number of range gates	256
Range gate spacing	75, 150 or 300 m
Range/Spatial averaging	4 pulse volumes (300 m)
Time averaging	64 pulses each for H and V
Averaging period	210 ms
Output resolution	0.25 dB for Z and 0.125 dB for Z _{DR}
MEASUREMENT ACCURACY	
Reflectivity, Z	±0.75 dB
Differential reflectivity, Z _{DR}	±0.2 dB

3.6. The CRIE Database

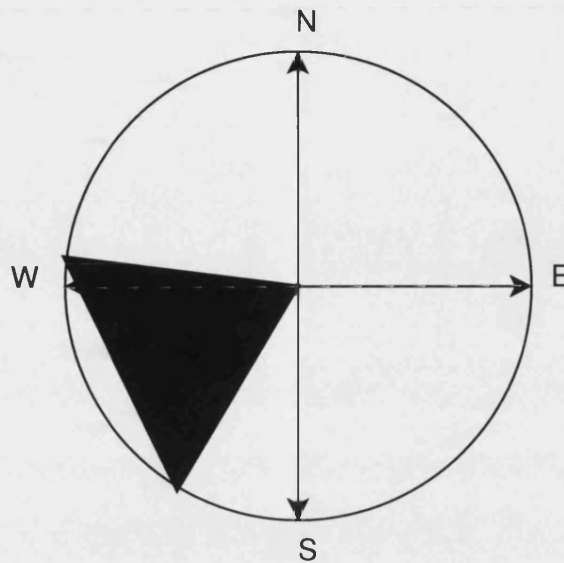


Figure 3.9: Radar data collection scan bearing

manpower, then extra time was allocated at the end of the period. In this way, all weather conditions during the campaign period should have been sampled with equal probability. If no rain was present, a record was made in the observation log to this effect, and no further action was taken. Hence, assuming the total collection period is an adequate representation of a whole year, the statistics can be presented as annual statistics.

For the PPI scans, each scan, at an elevation of 1.5° , covered an area approximately 50° in azimuth due south west of the radar. This is shown in Figure 3.9. As the scan rate of the radar is 1 degree/second it takes approximately 1 minute to complete a scan. Hence, the scan duration is well within the 20-30 minute duration for the lifetime of rain [Zawadzki 1973] and each scan represents a good snapshot of the rain field before any significant structural change has taken place.

Data were originally recorded in tapes but transferred to optical disk for storage. Even with the transfer to optical disk, the original data format was still retained. Gated records of Z_H and Z_{DR} along a ray, for multiple azimuths are stored within a raster of block size 4092 bytes. A new raster always begins in a new block with the start of each raster containing a 64 byte information record. This is used to provide information such as the time, number of rays in the raster and other housekeeping records. After this, the corresponding gate by gate measure-

3.7. Processing and Estimation of Rain Rate

ments (300 m in length), containing up to 512 gates of Z_H and Z_{DR} for each ray are recorded in 1/4 dB and 1/8 dB units respectively.

The radar data acquisition system also applies a swept gain correction to the measured reflectivity values, to correct for the $1/r^2$ dependence so that recorded data are range normalised. Radar calibration of Z_H and Z_{DR} was done at specified periods during the campaign and the values are contained within the file format. The complete data format of the raw database is given in Appendix A.

3.7 Processing and Estimation of Rain Rate

The resulting raw measurements from the CRIE campaign are contained within a total of 107 files. Each data file was accompanied with a summary file stating the number of rasters within each file and other information such as the radar operator at the time of measurement. For each raster, the computed of values Z and Z_{DR} were obtained using the following summarised procedure:

- Values of Z_H are already range normalised and recorded as single bytes in the range 0–255 in 1/4 dB units. Thus Z_H in dBZ is:

$$Z_H = \frac{Z}{4} + Z_H^{cal} + 0.01r, \quad (3.27)$$

where Z_H^{cal} is the absolute calibration of the reflectivity and is 6.5 dBZ. The third term corrects for oxygen absorption with range (in km).

- Values of Z_{DR} are recorded as two's complement single bytes in the range -128–127 in 1/8 dB units. Thus Z_{DR} in dB:

$$Z_{DR} = \frac{Z_{DR}}{8} + Z_{DR}^{cal}, \quad (3.28)$$

where Z_{DR}^{cal} is the calibration correction for the differential reflectivity and is 5 dB.

- Any values of reflectivity close to the noise level (10 dBZ) are identified and the corresponding pair of measurements are excluded.
- Negative values of Z_{DR} due to anomalous propagation and other forms of ice particles were also filtered from the dataset. Hall et al. [1984] have shown that anomalous propagation will produce noisy estimates of Z_{DR} which fluctuate between ± 3 dB from gate to gate.

3.7. Processing and Estimation of Rain Rate

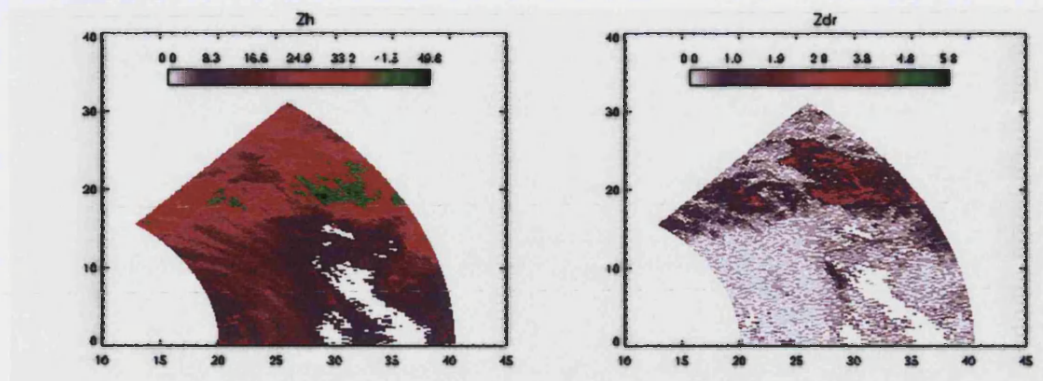


Figure 3.10: Radar scan at 1.5° elevation showing reflectivity (dBZ) and differential reflectivity (dB) for range gates between 20–40 km.

- Also negative values of Z_{DR} close to 0 dB occur due to quantisation errors in the radar measurements. Negative values within twice the quantisation interval (0.25 dB) are rounded to 0 dB.

The consistency of radar calibration values given above have also been confirmed with disdrometer records with a mean difference of 0.07 dBZ and 0.03 dB for Z_H and Z_{DR} respectively (see Goddard and Thurai [1992]).

Although data were collected between 4.8–158 km range gates, for the simulation of rain attenuation on terrestrial links, we are restricted to range gates between 20 km and 40 km. This is to avoid any volumes being within the freezing level and also to ensure that there is not a large difference in the volumes due to beam spreading. At 20 km, the azimuthal volume width is 87 m, while at 40 km the azimuthal width is 174.5 m. This restricted number of range gates represents a total of 68 range gates per ray, spaced 300 m apart radially.

For all the PPI scans in the database, the number of rays within each scan was between 208 and 210 rays, and the lower limit was thus chosen to represent the number of rays within the scan, representing the estimated rainfall rate. Therefore each PPI scan consequently is composed in total of $208 * 68$ bins. In total there were 3199 PPI scans available over the two year period for the estimation of rain rate. Figure 3.10 shows a sample scan from the radar database.

3.7.1 Rain Rate Estimation

As a first step before the estimation of rain rate, areas of hail have to be identified or else the resulting estimates would be grossly overvalued. The rain hail

3.7. Processing and Estimation of Rain Rate

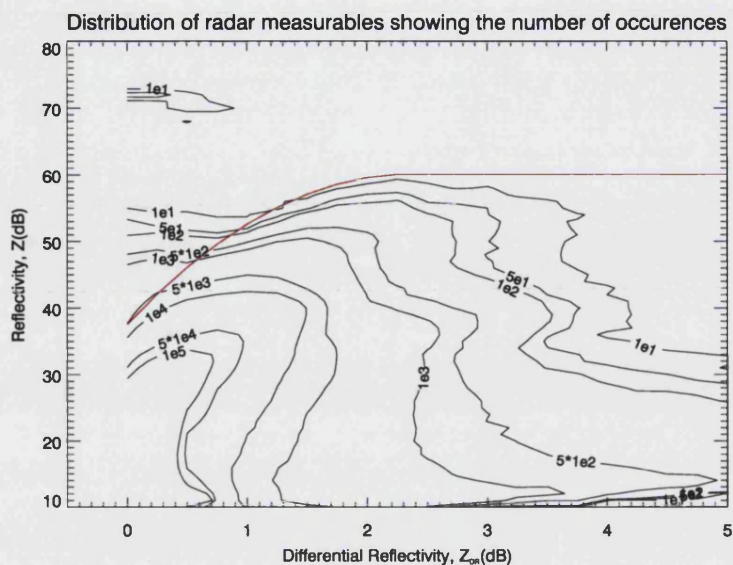


Figure 3.11: Occurrence distribution of Z_H and Z_{DR} from the dataset. Superimposed is the rain-hail envelope suggested by Leitao & Watson [1984].

algorithm of Leitao & Watson [1984] has been used for this purpose (see § 3.4.3). Figure 3.11 shows the envelope superimposed over the occurrence of Z_H and Z_{DR} over the whole data set.

The overall effect of this filtering procedure, however, was minimal. It reduced the total data set by less than 1%. Any remaining occurrences of hail and rain wet hail mixtures within the data would result in very high rain fall rates, and their probability of occurrence would be far less than that of rain fall. Hence, such estimates would be expected to show up at extremely low probability levels (i.e. less than 0.001% of time) and would not affect further analyses with the data.

In the estimation of rain rate, the following has been assumed;

- A uniform rain drop temperature of 5°C.
- A rain drop shape given by equation 2.15 in chap. 2.
- Rain drop size distribution defined by the normalised Gamma function with a breadth of 5 (see equation 2.10 in chap. 2).
- Rain drop terminal velocity defined by equation 2.17 in chap. 2.

3.7. Processing and Estimation of Rain Rate

- The rain rate estimated within the volume of the radar above the ground is the same as the ground rain rate, hence ignoring any possible contribution of pulse volume averaging, rain drop canting and wind shear.

Simulated values of Z_H/R vs Z_{DR} (see Figure 3.7) based on the above assumptions and obtained from FIM scattering calculations [Uzunoglu et al. 1976], were used in a lookup table to automatically estimate the rain rate from measured reflectivity records. We have already highlighted the effect in the variability of such micro-physical parameters on the expected radar measurements and consequently on rain rate estimates (see § 3.3.2 and 3.4.2).

3.7.2 Comparison of Statistics

Before the presentation of the estimated rain rate statistics, a discussion of the database statistical validity and internal consistency is in order. We have already indicated that restrictions on operation precludes continuous scanning with CAMRa. For the 2 year database with a 9 out of 28 day duty cycle, this corresponds to a total continuous measurement time of 8 months. The typical duration of rain events is between 20–30 min. With a scan every 10 min, this represents an average of 2.5 scans per event. Hence this gives approximately 1280 events over a 2 year period. Therefore statistical information for time percentages less than 0.1% often rely on 1 event.

Even though rain events are unevenly distributed spatially, and any given event will not be equally sampled over all range gates, the difference in statistics for each range gate, over the entire two year period should be small. Also, the effect of radar beam spreading (increase in radar volume with range) may bias the rain rate statistics. As a check, Figure 3.12 shows rain rate statistics for the first 34 and second 34 range gates, compared with the whole. It can be seen that statistics for greater than 0.01% of time exhibit little difference. The lack of enough samples for rain rate statistics less than 0.01% is apparent with the gradual divergence of the distributions.

Figure 3.13 also shows the estimated radar rain rate statistics compared with rain gauge statistics at the same site [Goddard and Thurai 1996]. Also included are statistics from ITU recommendations P. 837-1 (zones) for the UK and P. 837-2 (rain maps) for Chilbolton in particular. It can be seen that the radar distribution for rain rate exceedance percentages greater than 0.01% are consistently greater than rain gauge estimates and results in a difference of approximately 5 mm/h at

3.8. Interpolation

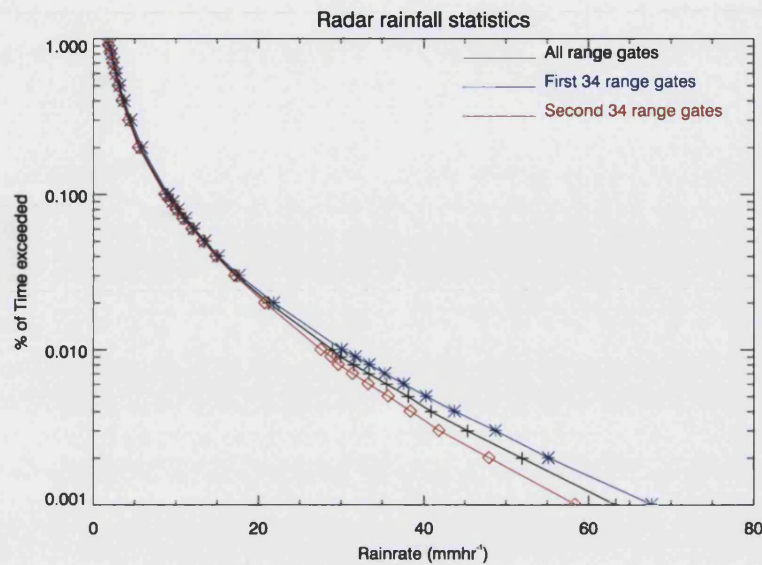


Figure 3.12: Radar rainfall rate distributions for 1987/1989 showing the overall exceedance statistics (+) in conjunction with statistics obtained for the 1st (*) and 2nd halves (◇) of the radar PPI scans.

0.01%. For statistics less than 0.01%, the distribution becomes closer to rain gauge and the other ITU distributions but such statistics are not well sampled within the database. As a whole, considering the rain rate estimates can be up to 25% in error, the radar statistics are well representative of rain statistics within the region.

3.8 Interpolation

In several situations there arises a requirement to interpolate radar data points onto a secondary set of points for further analysis. For example, rain rate estimates from radar are usually compared with a network of rain gauges and disdrometers situated within the scanning field of the radar. Also, some schemes for the assimilation of radar data into numerical models require some level of interpolation. In our case, the objective is to simulate rain attenuation on a point to multi-point grid, derived from PPI radar and having links radiating outward from the centre.

In all such cases, there are fundamental attributes of radar that pose a challenge. Firstly, the spatial distribution of data points varies continuously across a radar PPI scan. Moreover, the data point separation in the radial direction can

3.8. Interpolation

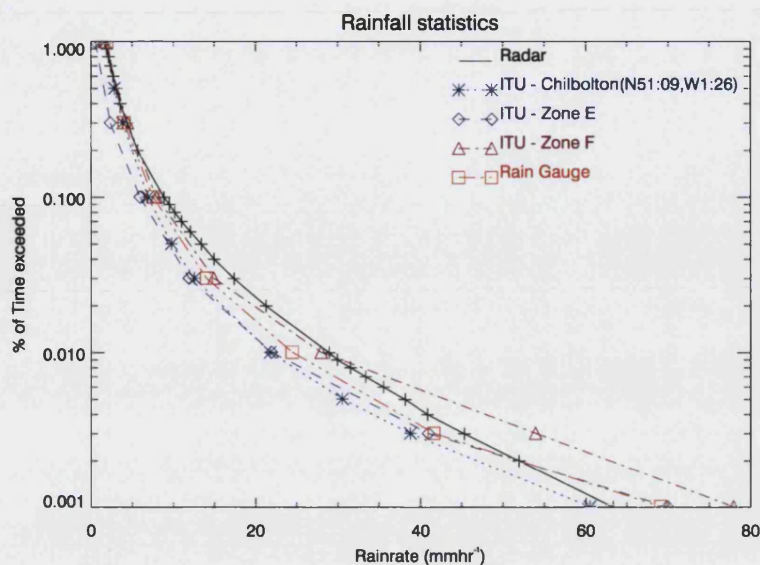


Figure 3.13: Rainfall rate statistics from the radar database and from other sources.

differ by at least an order of magnitude from the separation in the azimuthal direction. Hence, rain rate estimates may be well sampled close to the radar, but less sampled at longer ranges.

Additionally, the interpolation grid is not Cartesian (most applications of radar data interpolation are to this form) but polar, and the coordinate axes are not aligned with the radar data coordinate axes. Furthermore, we are faced with the difficulty of producing a two dimensional rain field that reproduces to the fullest extent, the spatial characteristics (e.g rain rate correlation) and intensity of the original rain field. Therefore, the interpolation problem can be generally considered as interpolating from a set of irregularly spaced data points, to another set of irregularly spaced data points.

A large number of interpolation techniques exist which aim to tackle such a problem. They can be grouped into two distinct methods. Local methods such as weighted distance and nearest neighbour interpolation, which use a certain number of points nearest to the point to be interpolated [Shepard 1968]. Global methods such as radial basis functions, which take all points within the domain to produce a surface fit [Franke 1982]. Let us highlight their properties.

3.8. Interpolation

3.8.1 Weighted Distance Interpolation

Studies within the field of radar meteorology have traditionally used weighted distance interpolation schemes to transform radar data products onto other analysis grids. In such schemes the points within the data domain are weighted according to the distance between the interpolation point and data points.

The basic process of a weighted distance interpolation scheme can be described by

$$f'_p = \frac{\sum_{q=1}^N w_q f_q}{\sum_{q=1}^N w_q} \quad (3.29)$$

where f'_p is the interpolated value at point p , f_q is the value at the data point q and w_q is the weight associated with the value of the data points. Two weighting functions have been often cited within the literature. These are due to Cressman [1959] and Barnes [1964]. The Cressman weight function can be expressed as

$$w_q = \begin{cases} \frac{R_c^2 - r'^2}{R_c^2 + r'^2}, & r' \leq R_c \\ 0, & r' > R_c, \end{cases} \quad (3.30)$$

where r' is the radial distance separating an interpolation point from a data point and R_c is the radius of influence. The Barnes weight function is Gaussian in nature and is expressed as

$$w_q = \exp\left(-\frac{r'^2}{\kappa}\right), \quad (3.31)$$

where κ is a smoothing parameter. Since this scheme is Gaussian in nature, then the "influence radius", R_c may be thought of as the radius where $w_q = e^{-1}$ and is proportional to κ . The weights given in equations 3.30 and 3.31 are isotropic but can be modified to employ different weighting in co-ordinate directions (anisotropy) to accommodate the data distribution. One important difference in the two weighting functions is that the Cressman weights do not asymptotically approach zero with increasing distance as they do in the Barnes technique, but instead abruptly become zero at $r' \geq R_c$. Both Barnes and Cressman weighting schemes essentially act as low pass filters and high frequency characteristics of the field would be smoothed out.

3.8. Interpolation

The advantage of both schemes lies in their mathematical and computational simplicity. The disadvantage is the tendency to smooth out all small variations in the field, whether caused by data errors or actual meteorological disturbances in the field. To differing degrees this would affect any corresponding interpretations and/or analysis of the interpolated field.

But even with their simplicity, their use without due consideration as to the nature of the data distribution may lead to poor performance. Several studies have investigated the performance of such schemes in general and also within the radar context, attempting to characterise the sensitivity to choices of influence radius, weight function (isotropic or anisotropic), and data spacing and distribution.

It has been suggested that an isotropic influence radius be adjusted, based on the radar data spacing to accommodate the anisotropy of radar data, together with the systematic decrease in data density with range. Askelson et al. [2000] and Trapp and Doswell [2000] have investigated such a procedure. They come to the conclusion that although such a scheme may facilitate the retention of the maximum amount of information from the data, there is a potential for the rain field to be modified along spatial variations of the weight function. Subsequent interpretations of the rain field may be biased with this artifact, with the possibility of inferring a change in the physical state of the rain field when none has taken place. Similar observations were reported when using anisotropic weighting but with the influence radius being independent of the data spacing and distribution.

The influence radius should be the optimum value that minimises spectral modification of the data field. From classical sampling theory, a wave must be sampled at least twice the wavelength to be unambiguously resolved. For fields that are sampled onto a Cartesian grid, the influence radius is determined by the sampling interval with R_c greater than twice the sampling interval. On the other hand, for data points that have varying data spacing, an objective measure of data spacing within the domain is crucial to determining the optimum influence radius. Several investigators have proposed optimum relationships for the influence radius for irregularly spaced data. Optimum values with R_c/d greater than 1.25 and 1.75, where

$$d = \left(\sqrt{\frac{\text{Area sampled}}{\text{number of data points}}} \right)^2, \quad (3.32)$$

and is the average data spacing, have been proposed by Stephens and Polan [1971]

3.8. Interpolation

and Stephens and Stitt [1970] respectively for randomly distributed data sets. Givens and Ray [1994], from an analysis of synthetic wind fields show that for data distributed on radar grids, the optimum influence radii is within the range,

$$1.85 \leq \frac{R_c}{d} \leq 2.25. \quad (3.33)$$

Trapp and Doswell [2000] take the conservative viewpoint that the influence radius should be defined with respect to the maximum data spacing. In this case some signal may be lost through smoothing in order to avoid under-smoothing the data in regions of the most coarse data point spacing.

3.8.2 Radial Basis Interpolation

Radial basis function (RBF) interpolation is just starting to find wide application compared to weighted distance schemes within fields of topography, hydrology, surveying, mapping, geology and geophysics. The method is global in scope and produces a surface defined by

$$f(x, y) = p(x, y) + \sum_{n=1}^N \lambda_n \phi(x, y), \quad (3.34)$$

where $\phi(x, y)$ is a basis function. Popular choices of basis functions are thin plate splines and multiquadrics. The λ_n are a set of coefficients or multipliers corresponding to the N data points and $p(x)$ is a polynomial of low degree.

RBF interpolation is within a class of techniques that can be termed as optimal for the following reasons. It reproduces exactly the original data points. The resulting surface has derivative continuity. The interpolation is independent of the grid size, hence the domain can be scaled, translated and rotated. It can inherently incorporate spatially dependent (anisotropic) behaviour. It automatically adjusts to the data density by placing a basis function at each data point. The resulting field can have exact Fourier processing operations applied without the need for padding or data filling. The smoothness of the resulting interpolation function can be adjusted based on the choice of basis function with thin plate splines providing the smoothest function.

For thin plate splines the basis function is given by

$$\phi(r) = r^2 \log r, \quad (3.35)$$

3.8. Interpolation

where r is the distance between points. With N data points and a polynomial of degree 3, a system of $N + 3$ simultaneous linear equations must be solved of the form

$$\begin{bmatrix} \Phi & P \\ P^T & 0 \end{bmatrix} \begin{bmatrix} \lambda \\ \alpha \end{bmatrix} = \begin{bmatrix} f \\ 0 \end{bmatrix} \quad (3.36)$$

where α are the vectors of polynomial coefficients.

Experience with RBF interpolants on small problems has been almost universally positive [Franke 1982]. However, applications to large applications with 10,000 or more data points have been limited due to the prohibitive computational and memory costs. A usually full and often ill-condition matrix has to be inverted to compute optimal multipliers. Sophisticated methods can be employed to reduce the computational burden [Beatson et al. 1999] but these can be imposing to apply.

3.8.3 Data Interpolation

Based on the Cressman and RBF interpolation methods described, we have evaluated their performance using rain events sampled from the CRIE data set. The analysis grid (a Central PPI scan, hereafter CPPI) to be interpolated to, represents a point to multi-point circular cell, where hypothetical links radiating outward with lengths up 9 km would be placed. Each PPI scan has range gates spaced 300 m apart with each ray having an azimuthal spacing of 0.25 degrees. It is possible to interpolate down to intervals of 100 m radially and azimuthal separations of 1 degree for the CPPI scan. Computationally, it would not be feasible to evaluate the interpolation weights with the resulting number of PPI points (68*208 points) and CPPI points (360*90 points) in one step. Hence a segmentation procedure was developed to evaluate the interpolation points. This is shown in Figure 3.14.

For example, within a segment, the respective data and interpolation points are identified for the PPI and CPPI grids. To avoid boundary effects (i.e where points lie on the boundary of a segment) and to ensure continuity of the field, data points from segments surrounding the main segment have also been combined in the evaluation of the interpolation points. The segmentation procedure also avoids the evaluation of interpolation points, where the corresponding data points represent an area of zero rain rate or constant rainfall rate. In this case, all interpolation points that fall within this segment are assigned the value of the data points within the segment. This considerably improves the time involved in pro-

3.8. Interpolation

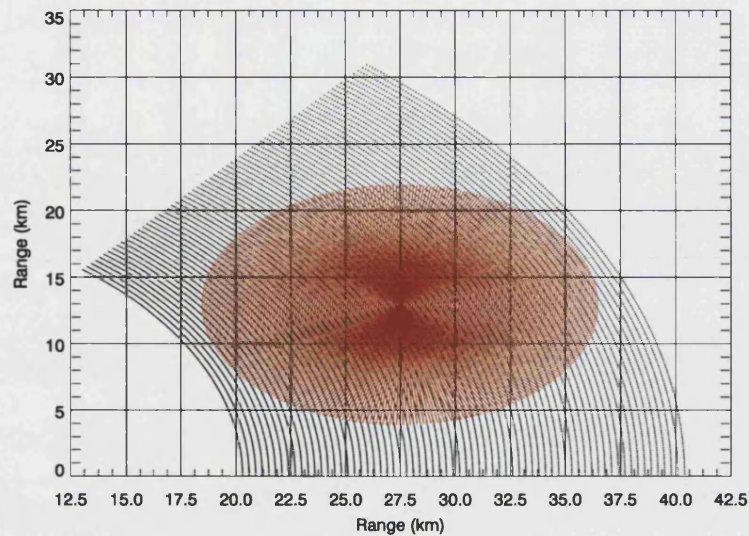


Figure 3.14: *Segmented processing. The subdivision of the domain for interpolating between the PPI and CPPI scan. The interpolation points within a given segment are computed from data points in this segment and from points in the neighbouring ones.*

cessing. In total, the number of segments constructed over the domain were 50×50 segments, with 24 neighbouring segments used to interpolate each segment. In the use of Cressman weights, we have followed the recommendation of Givens & Ray [1994] (see equation 3.33) and set the influence radius equivalent to twice the data spacing, since there is not a large variation in data spacing within the data set over the ranges that we wish to interpolate from.

Using the above segmentation procedure, Figure 3.15 shows the performance of Cressman and RBF interpolation for 2 events. It can be seen that the contours from the use of Cressman weighting are considerably smoothed, hence changing the spatial characteristics of the rain field which would determine the correlation properties. Also, some of the contours, especially the high values undergo a reduction in intensity. Such a field would be useful for diagnostic purposes but would be unsuitable for further evaluation. This is not the case with RBF interpolation where the resulting contours represent to a very good degree, the contours of the original data points.

Figure 3.16 also shows the cumulative distribution of rain rates for the complete measurement period derived from PPI and CPPI datasets, using the two in-

3.8. Interpolation

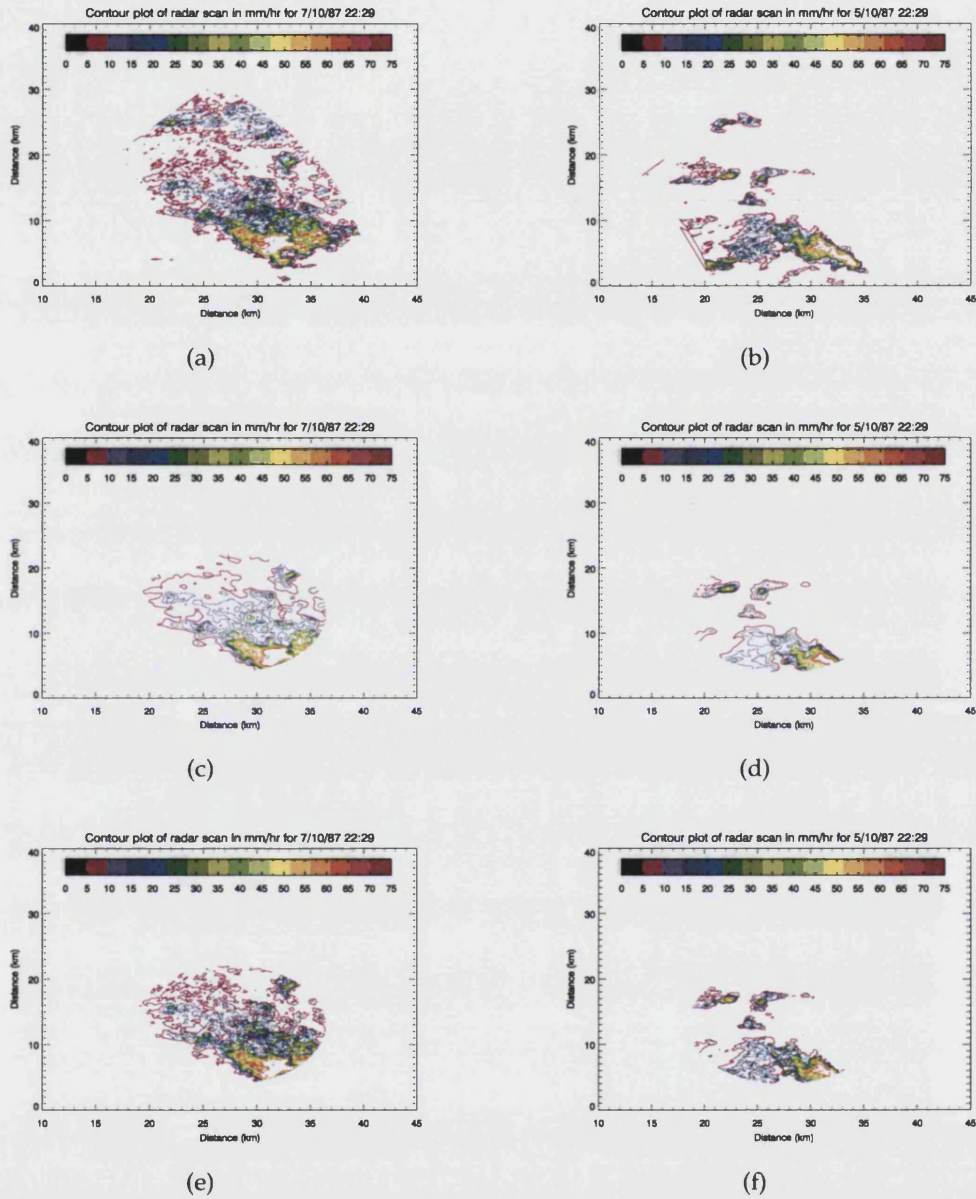


Figure 3.15: (a) & (b) Rain rate radar PPI contours for two events; (c) & (d) events interpolated using Cressman weighting onto a CPPI grid; (e) & (f) events interpolated using RBF with thin plate spline onto a CPPI grid.

3.9. Concluding Remarks

terpolation schemes. The reduction of rain rates with high values is apparent in the Cressman scheme, with the distribution departing significantly from the PPI data set. Therefore, only the CPPI data set derived from the RBF interpolation scheme has been employed for further analysis.

3.9 Concluding Remarks

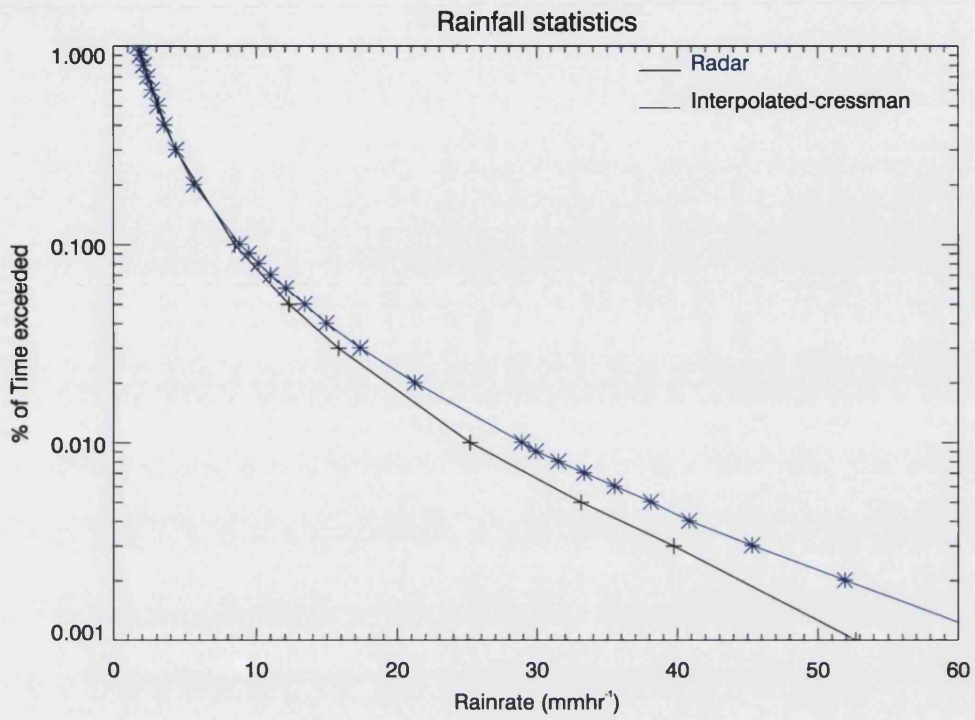
Radars provide a distinct advantage in the observation of precipitation over wide areas. In addition their products have wide application within the areas of radio propagation and communications. We have highlighted the historical genesis of radar meteorology and presented the principles of its operation in the measurement of the back scattered power from a spectrum of rain drops falling towards the ground. In particular, it has been shown that compared to conventional radar, dual polarisation radar measurements reduce the statistical uncertainties of the DSD parameters which are integral to the estimation of rain rates.

To achieve estimation errors to within 25%, dual polarisation radars have to be calibrated to within 1 dB for Z_H and 0.2 dB for Z_{DR} . The S-band CAMRa with its relative insensitivity to attenuation by rain, superior receiver performance, excellent calibration and high resolution satisfies these minimum constraints.

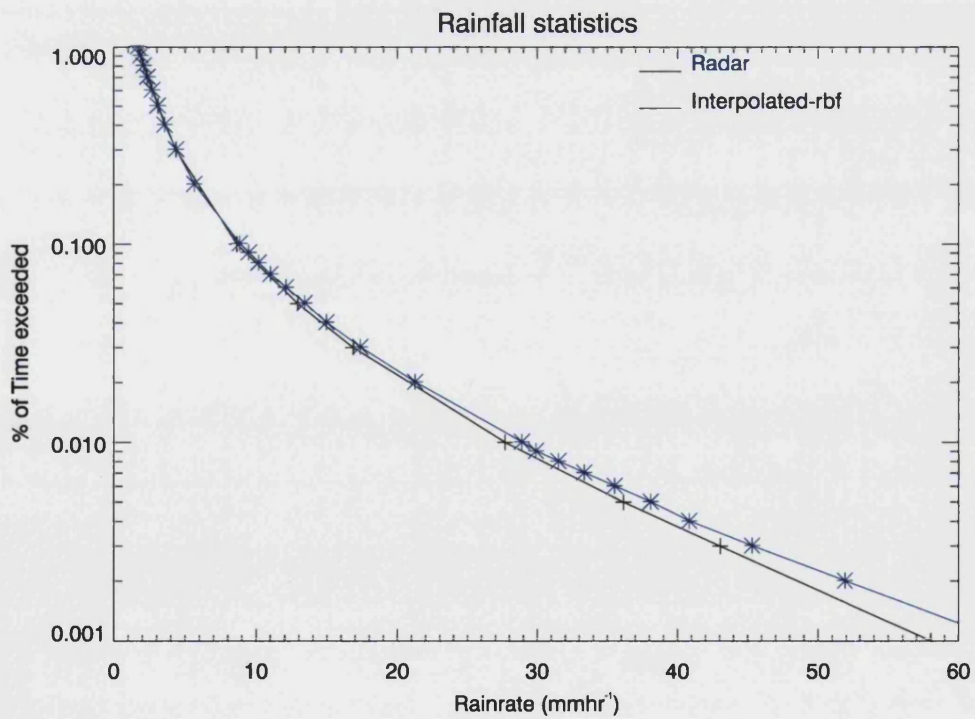
We have discussed the CRIE measurement campaign where PPI scans of precipitation were systematically collected over two years with no recourse to weather forecasts. In total, the database contained 3199 scans of roughly 1280 events. Resultant rain rates were estimated based on comparing measured and FIM derived Z_H and Z_{DR} values within a lookup table using a functional relationship in which Z_H scales with R for a constant Z_{DR} . This was after occurrences of hail were filtered from the dataset. Radar rain estimated statistics have to be compared with statistics from other sources to confirm their veracity. Statistics acquired from rain gauge, disdrometer and ITU recommendations show good agreement for the probability range that the rain database is statistically valid (i.e. for exceedance probabilities greater than 0.01% of time).

For the evaluation of attenuation statistics for point to multi-point links, the rain rates have been interpolated using a global RBF interpolation scheme onto a CPPI grid and down to intervals of 100 m. The performance of such an interpolation scheme proved superior compared to weighted distance methods in the retention of information contained within the PPI scans and adjusting to the varying data distribution of the radar. The use of segmented processing to reduce

3.9. Concluding Remarks



(a)



(b)

86

Figure 3.16: Comparison of the resultant rain rate statistics produced by (a) Cressman (+) and (b) RBF (+) interpolation with respect to original radar rain statistics (*).

3.9. Concluding Remarks

computation times can equally be applied to weighted interpolation schemes if required.

Fade Mitigation and Route Diversity

An overview of the fade mitigation techniques for use on millimetre wave systems is introduced. The chapter then presents the investigations carried out simulating route diverse links using rain rate estimates obtained from the CRIE database where rain rates are assumed to be homogeneous over a spatial scale of 100m. The elements affecting the resulting diversity statistics are discussed. A simple but accurate diversity prediction model formulation is presented, which takes into account the elements considered and comparisons are made with similar studies and link measurements. Finally, the performance of the model predictions is discussed.

4.1 The Need for Rain Mitigation

PRESSURE on the limited radio frequency spectrum available within the microwave bands for terrestrial services, is leading to the use of higher frequencies within the millimetre wave band. This has been motivated by the increasing demand for multimedia data services such as video streaming, file transfer and I.P telephony, whose use is expected to grow exponentially over the coming years. These services require large bandwidths (>500 kbps), which are not available at lower frequencies. Moreover, the expectation from the users of these services is that the service is always available on demand. This puts pressure on system operators to ensure that their communications systems meet contractual quality of service requirements.

As the operating frequency is increased, the attenuation effects due to rain become larger, making it necessary to use larger margins to provide the required

4.2. Scenarios Under Consideration

availability. Traditionally, links are specified to have an outage period caused by rain fading not exceeding some small percentage of the year. Typically this figure will be 0.01% or 0.1% of time, and the rain fade margin is built into the link budget by estimating the rain attenuation exceeded for this time. Many models exist to perform this calculation (e.g. [COST235 1996], ITU-R P. 837).

There is however a limit to how large these system margins can be due to technological (e.g. antenna size, interference limits, etc) and cost constraints. Therefore, link signal fading must be avoided or compensated for by other means in order to increase or maintain the system availability. These alternatives are known as Fade Mitigation Techniques (FMT) or Fade Countermeasure Techniques (FCT). The use of the word *mitigation* is preferred as the word *countermeasure* could infer the techniques seek to use methods that could interfere with the performance of neighbouring networks.

4.2 Scenarios Under Consideration

Two network scenarios can be identified that apply to this study. These are point to point (P2P) and point to multi-point (P2MP) networks. Each has its specific applications and constraints, which will determine the characteristic link distance, availability level and associated rain fade margins required.

4.2.1 Point to Point

Point to point networks are used as primary or secondary trunking/back-haul networks for mobile cellular, fixed wireless access (FWA) and land-line communications providers. Reliable back-haul is critical for any communication network. Communications providers have a choice of copper lines, fibre optic or radio systems to route data between parts of their networks. P2P radio links have a number of advantages over other options; they are quick and cheap to setup and maintain, and there is no reliance on another party or organisation to provide the connections.

Large businesses also use such infrastructure for dedicated services such as video conferencing, data ware-housing and enterprise intra-nets. Additionally, governments use such networks for the control and monitoring of many systems such as air traffic control, gas pipelines, power distribution networks and tactical communications.

Since P2P links act as major arteries for communication networks, high reli-

4.2. Scenarios Under Consideration

ability and efficiency is essential throughout the year. These networks require a high availability of the order of 99.99% or greater. Large fade margins would yield such high availability levels for individual links. However, the use of large transmit power levels causes interference with other neighbouring networks, either lowering their availability or increasing the network's frequency re-use distance.

Such links may have approximately constant data rates of the order of 150 Mbps. Additionally, antennas for such networks are of high gain and directivity, with the effects of multi-path being negligible within the millimetre wave band. Millimetre wave links are generally designed to be line of sight. Maximum link lengths are typically between 20–30 km for link frequencies below 20 GHz, dropping to 5–10 km at 38 GHz and 1 km at 50 GHz. The characteristic lengths for such links would be of the order of 3 km or more for base station to base station connectivity in the case of mobile cellular and FWA networks. When part of a regional or nation wide transmission network, multi-hop links are used. Typical lengths of such hops are between 10–30 km depending on the frequency of operation.

4.2.2 Point to Multi-point

Two point to multi-point scenarios are relevant within the context of this study. Firstly, P2MP networks are used in broadcast situations to provide a combination of different services such as telephony, multi-channel TV, Internet etc. to small businesses and homes. They are particularly suited for dense urban areas, but deployments within rural areas is also possible.

The network configuration can be of cellular type where users are within a cell covered by a base station. The base station antennas would be high gain, with antennas on the user premises being smaller and consequently low gain. A high amount of frequency re-use within the network is possible using sectorisation strategies (i.e. division of the cell into smaller sectors). Secondly, mesh network configurations are considered where each user acts as a base station to neighbouring users. In this situation, the antennas on both ends of the link would be of low gain. Such a scheme requires a high degree of signalling within the network. If the complexity and risk can be overcome, it seems highly likely that mesh systems will provide greater capacity than conventional systems for a given cost.

The aggregate bandwidth for each broadcast cell would be shared among the users within the cell. Therefore, the efficient allocation of spectrum is imperative. Fade margins are set low to keep the cell sizes small. Compared to P2P networks,

4.3. Techniques

Table 4.1: *Maximum link length as a function of network availability and rain margin for networks operating at 42 GHz within the European region [CRABS 1999].*

Rain Attenuation Margin	Network availability	
	99.9%	99.99%
10 dB	2.0–5.5 km	0.7–1.8 km
15 dB	3.5– km	1.0–3.0 km
20 dB	5.0– km	1.5–4.0 km
25 dB	>5.0 km	2.0–5.5 km

it will be impossible to design each link within a given cell to have the same availability level. The availability level for each link would be defined by the distance from the serving transmitter and the user service requirements for the link. Typically home users would have low availabilities within the range 99% - 99.9%, depending on the service provided. For the more demanding home users and businesses, the availabilities would be greater.

Therefore, such networks would be designed for a best case lower bound availability level (i. e. network availability). The network availability is then determined by the time percentage corresponding to the maximum rain attenuation given by the fade margin. Table 4.1 shows the maximum link lengths achievable at 42 GHz as a function of network availability and rain margin within the European region. This would define the limits of the cell size radius. The use of lower frequencies would increase the limit of the maximum link lengths possible.

4.3 Techniques

The Earth-space systems community has taken the lead in the development of fade mitigation techniques. For such systems, the challenges of overcoming propagation impairments are even greater than for terrestrial systems. It is only within the last decade that fade mitigation techniques have matured to make their transition from research subjects, into concrete applications within commercial systems.

Using such techniques, it may be possible for instance to design terrestrial systems with a fixed power margin, corresponding to the worst case of fading for a certain percentage of time. When larger fades occur due to rain, the FMT takes over to prevent the system from being unavailable.

Various methods exist to mitigate propagation impairments. The choice of technique must take into account operating frequency bands, performance ob-

4.3. Techniques

jectives of the system and characteristics of the network (e.g system architecture, multiple access schemes, etc). FMTs can be broadly characterised into three classes:

Power control involves the adjustment of the transmit power depending on the fading conditions occurring.

Signal processing control involves the use of more robust coding techniques, using extra time slots within the transmission burst frame or better modulation techniques.

Diversity selection involves the avoidance of the rain fade by using a different link. The other link can be different in terms of frequency, route or orientation.

Within each of these categories, there are a wide range of techniques for millimetre wave systems in general [Willis and Evans 1988; COST235 1996]. The following discussion would focus on the methods that are applicable to terrestrial systems suffering rain fading.

In terms of operation, the main objectives are to provide seamless performance when fades occur and to achieve efficient allocation of scarce bandwidth. It is crucial that the system reacts quickly to detect and mitigate the fade. Furthermore, any commercially implemented system has to be competitive, reliable and cost effective.

4.3.1 Power Control FMT

Most WLL (Wireless Local Loop) and FWA (Fixed Wireless Access) systems in the market already employ adaptive power control techniques. With power control FMT, the transmitter power is adjusted in order to increase the radiated power during fading conditions. The principle is closely analogous to increasing the power margin within a link budget. Given a reliable power control system, it could be possible to reduce the fixed margin during clear sky conditions, thereby improving the rate of frequency reuse. Two modes of control are possible. These are constant and adaptive power control.

Using constant power control during fading conditions, the power level is raised to a pre-assigned level with no consideration to the individual fading levels experienced by users or networks within the area. It has the advantage that

4.3. Techniques

it is easily implementable, but can cause interference to other neighbouring cell sites. In most cases, the power level will be adjusted with respect to the user that is farthest from the base station. This user is likely to be at or near cell boundaries. The use of sectoring strategies reduces the potential interference.

Adaptive power control has its origins from earth-space propagation studies, although it can also be applied to terrestrial links. It has the ability to compensate for fades whilst reducing the potential for interference outside the network. The level of transmit power is adjusted dynamically, based on information such as the distribution of fades experienced by users within the network. Information on the distribution of fades can be obtained by employing monitoring stations at the periphery of the network, or by user terminals sending information back on their received power levels.

In general, the fading experienced around the perimeter of the network is not uniform, so that if the most faded link is completely compensated, some parts of the perimeter will experience signal levels in excess of those for clear air operating conditions. Alternatively, mitigation at the level of the least faded link guarantees that interfering signals never exceed clear air levels, but provide reduced availability levels.

When applied to point to multi-point networks, power control schemes have to be controlled centrally, to ensure that transmit power levels within cell sites are at an acceptable level to reduce the potential for interference. This introduces complexity in the network design and associated stability problems with the technique. A feedback loop is possible where two or more transmitters interfere with each other, increasing their transmit power to compensate, and thereby interfering with each other even more.

Jones & Watson [1993] have investigated the use of adaptive power control to mitigate rain fading for point to multi-point networks operating within the frequency of 20–50 GHz. Using rain data from the UK, they analysed the effect of frequency, cell radius and sectoring, and the limits to power levels on the link availability. They show that for power schemes governed by the maximum fading level within the sector, the link availability possible is strongly dependent on the network radius. For availabilities of 99.99% with a power limit of 12 dB, a network radius of 5 km is achievable at 20 GHz. This decreases to 3 km and 2 km at operating frequencies of 30 and 40 GHz respectively.

The use of sectorisation schemes was found to have little effect on availability

4.3. Techniques

levels, when power control was governed by the maximum fade within the sector, but reduced the impact of interference beyond the network. A change in the number of sectors from 1–16 showed an order of magnitude reduction in interference levels, with the additional advantage of more frequency re-use.

4.3.2 Signal Processing FMT

These methods mitigate additional attenuation without increasing the transmit power. They either modify the allocated bandwidth or the link data rate.

Adaptive Coding

When a link is experiencing fading, the introduction of additional redundant bits to the information bits allows improved error correction at the receiver. The information bit error rate (BER) is maintained throughout the fade but the data rate is decreased. Adaptive coding uses a variable coding rate in order to mitigate the impairments due to propagation conditions. A gain in the range of 2 to 10 dB can be achieved depending on the coding rate [Willis 1991].

The limitations of this FMT are linked to additional bandwidth requirements. Adaptive coding at constant information data rate then translates into a reduction of the total system throughput when various links are experiencing fading simultaneously.

Adaptive Modulation

Advances in digital processing have enabled the ability to rapidly switch between modulation schemes within modems. Under clear sky conditions with high signal to noise ratios, high system capacity for a specified bandwidth can be achieved by using modulation schemes with high spectral efficiency (e.g. 16-PSK and 256-QAM). In case of fading, the modulation schemes can be changed to implement more robust schemes (e.g. BPSK and QPSK), where a higher proportion of the data is received. In cases where there are limitations to the bandwidth, this results in lower data rates.

The disadvantage is that with decreasing carrier to noise ratios during fading, the resulting spectral efficiency would be worse. Moreover, spectrally efficient modulation schemes have an added susceptibility to increase in noise levels.

Adaptive Data Rate Reduction

Adaptive data rate methods progressively reduce the transmission rates with increase in the levels of fading on a link. The reduction in system data rates leads

4.3. Techniques

to a reduction on receiver bandwidth, so that out of band noise is rejected. This can be complicated and costly to implement and also requires application services that can tolerate a reduction of the information rate. For services such as voice and video transmission, data rate reductions will show up as perceivable degradations in the quality of the transmission which would be unacceptable to users. In contrast, data services such as Internet access can tolerate extra delays introduced by a reduction in the data rate.

Space-Time Coding

Space-time coding is a subset of the multiple input and multiple output (MIMO) channel concept. Usually in MIMO, antenna arrays separated over short distances, transmit the same information to multiple antenna receiver arrays and is used to take advantage of multi-path propagation. With space time coding the data streams on each path are coded differently. The structure of the signal enables the exploitation of diversity in the spatial and temporal dimensions in order to obtain improved bit error performance and higher data rates without bandwidth expansion. At the receiver, the data streams are combined to retrieve the original transmission. Hence, quite significant coding gains can be obtained.

Adaptive Time Division Multiple Access

The use of adaptive time division multiple access schemes (A-TDMA) can reduce the fixed margin required during rain conditions to a low level. Most of the research into A-TDMA has been carried out within the context of satellite systems [Campora 1979, 1981; Barton and Dinwiddy 1988; Emerson et al. 1989].

The use of the scheme relies on the observation that only a few of the links within a TDMA network will be suffering severe fades at any time, as the storm passes over the network. A-TDMA similar to adaptive power control also lends itself to the concept of a network with a central intelligent node governing resource allocation. Each link is allocated a period (time slot) that it is allowed to transmit and receive information within the same frequency band as other links. A number of reserved time slots within the TDMA frame can then be allocated for use only in the event of a fade. Those links experiencing large fades are allowed extra time slots within the transmission bursts to correct for transmission errors. Since unfaded links would transmit at a higher bit rate than would be necessary, and consequently leaving spare capacity for faded links, it can be viewed as a trade-off between the increase in bandwidth and the reduction in fade margin.

4.3. Techniques

Within a P2MP network for example, there would be a large number of users, but only a small proportion would be experience severe fades at any time. Therefore, the number of additional time slots to be allocated would be small. This time slot factor can be identified as the bandwidth expansion required relative to a conventional link. A bandwidth expansion factor of less than 5% is needed to achieve an availability greater than 99.9% [Jones and Watson 1993]. The performance of such a scheme is high when the link fades over the whole network are highly uncorrelated. Hence, for longer link lengths there would be more significant improvements relative to short link lengths.

4.3.3 Diversity Selection FMT

Diversity selection techniques include time, frequency and spatial diversity. They mitigate fades by switching to a link not experiencing severe fading, or introducing a delay in transmitting the required information.

Time Diversity

This involves the use of store and forward techniques to delay transmission of information until the fading event has passed or the fading is down to a suitable level. It assumes that there is little time constraint for the transmission of data. Several approaches to transmission are possible.

Since the time series of a rain event contains peaks and troughs, the information can be sent when the fading decreases past a certain threshold and is within a trough. This adds complexity to the network design, as statistical information on the periods between troughs is needed.

Alternatively, a more conservative scheme is possible whereby transmission is delayed until the end of the fading event and the signal level is at an acceptable level. Due to its delay in transmission times (minutes to tens of minutes), it is not suitable for real-time communications. Data services such as file transfer/sharing and data warehousing can use such a scheme.

Frequency Diversity

Using frequency diversity, two or more frequency bands are used for transmission (e.g. 20 and 30 GHz). Data is normally sent on the higher frequency band as this allows higher data rates to be achieved during clear sky conditions. At the onset of fading, the higher frequency link would experience higher attenuation and has a higher probability of failure. Hence, the transfer of data is switched to the lower

4.4. FMT Implementation

frequency band. It requires a pair of terminals at each frequency at both ends of the link, and suffers from inefficient use of the radio resource as the aggregate bandwidth is doubled.

Spatial Diversity

The high degree of fading experienced within the millimetre wave band at low outage probabilities is caused principally by the passage of rain storms over the link. Radio propagation and rainfall data have demonstrated that such storms are localised events, with heavy rainfall occurring within a small rain cell of a few square kilometres, and lighter rainfall occurring over a much wider area. Hence, it is possible to take advantage of these micro-scale features to mitigate fades that occur. By utilising a rerouting strategy, the probability of simultaneous occurrence of fades on two geometrically separated links would be lower than the probability of the same fade occurring on an individual link.

In the case of site diversity, the links are spaced apart horizontally over a large enough distance to make the links roughly statistically independent. Studies have shown that the optimal separation distance for the operation of site diverse links is of the order of 10 km [Harden et al. 1978a].

Route diversity involves links having a common node separated by some angular separation. It relies on observations that micro-scale variations in rainfall occur down to a scale of a few hundred metres. For point to point networks, extra capacity in terms of additional bandwidth is not required for the use of site or route diversity. Point to multi-point networks on the other hand use multiple access schemes, and the use of route diversity would result in a reduction in the overall common resource pool. Initial investigations have shown that the overall effect of using route diversity on network capacity is small [Willis et al. 2002].

4.4 FMT Implementation

4.4.1 Operation

If fade mitigation schemes are to be implemented, it would be necessary to design a control system so that the link operates at maximum efficiency. The control scheme would need to obtain accurate data on link quality to initiate whatever mitigation scheme is considered. This information may be gained by the direct measurement of either attenuation, signal to noise ratio or bit error rate. Attenuation for P2P links may be measured directly at the receiver and when the signal

4.4. FMT Implementation

quality falls below a predefined threshold, the control scheme is initiated. For P2MP links, monitoring beacons could be used to indicate the distribution of fading levels over the network. Adaptive power control techniques and diversity techniques would be likely to use such measurements of either attenuation or signal to noise ratio.

BER is widely used for planning purposes of digital links because of its strong connection to system characteristics. It can also be used for initiation of the control system. At low data rates, the accuracy of BER measurements would be low. Fewer bits would be examined for the same sample time compared to higher data rates. Measurements using BER would be easy to incorporate into signal processing fade mitigation techniques.

Additionally, the control scheme would need statistical information on the duration of fades, coupled with their rates of change so as to respond quickly within a reasonable time delay. Precipitation events with strong and rapid variations will require very rapid initiation of the mitigation scheme. This can be a problem for adaptive circuits for timing and phase recovery to cope with the fast changes in signal level.

It may be possible to have fade mitigation schemes on P2P links switched on all the time as there are very little constraints on bandwidth. On the other hand, P2MP links cannot be implemented in such a way and the mitigation scheme would have to be switched on and off to conserve spare capacity within the network (see Willis et al. [2002]).

4.4.2 Combining FMTs

It is possible to have a combination of several fade mitigation techniques working in tandem to achieve greater performance targets for the networks without a significant increase in implementation complexity. In some cases where there is a requirement for extremely high availability levels (99.99%–99.999%), there is no alternative but to resort to such a combination. For example space-time coding and spatial diversity can be combined [Frigyes and Horvath 2003] to achieve gains 6–18 times higher than would be obtained with spatial diversity alone.

Also, with a combination of adaptive power control and A-TDMA, it is possible to increase the availability considerably, compared to the use of only one technique. Jones & Watson [1993] show that for P2MP networks of radii 2.5, 5 and 10 km, operating at 42 GHz, the minimum availabilities with the use of adaptive

4.5. Diversity Theory

power control together with A-TDMA were found to be 99.97%, 99.95%, and 99.9% respectively. This is in contrast to the use of only adaptive power control which results in availability levels of 99.95%, 99.9%, and 99.7% respectively for the same network radii.

4.5 Diversity Theory

Using two separate links to reduce the effect of rain attenuation, by taking into account the inhomogeneous nature of rain was first proposed by Hogg [1967]. Later, Hodge [1974] was also to propose the definitions of diversity. Furthermore, experimental data obtained in the UK in the 20–40 GHz range [Harden et al. 1978a] were to give an early indication of the improvement in link reliability, which can be obtained by the use of spatial diversity.

Figure 4.1 shows the general scenario of a route diversity station configuration. A receiving station (RX) is able to receive transmissions from two transmitting stations (TX₁ & TX₂), separated over some angular separation, θ . L₁ is the reference (primary) link that is used for most of the time. When fading levels are above the allocated margin for the reference link, the diversity system is initiated and switches to the diversity (secondary) link, L₂.

In comparison to space diversity, route diversity links have always have a common node. These two links may have the same lengths (symmetric case) or different lengths (asymmetric case), depending on the locations of the transmitting stations.

4.5.1 Diversity Performance Criteria

There are two measures of the advantage gained by diversity; these are diversity gain and diversity improvement.

Diversity gain provides a measure of the reduction in the fade margin or an increase in the signal power due to diversity. It is defined as the difference (in dB), between the reference attenuation for a single link and joint link exceeded at a certain percentage of time, $t\%$ or availability, $100 - t\%$. It is measured by the horizontal distance between the marginal and joint distribution curves, and is proportional to that distance if the attenuation scale is linear in dB. Thus,

$$G(t) = A_M(t) - A_D(t), \quad (4.1)$$

4.5. Diversity Theory

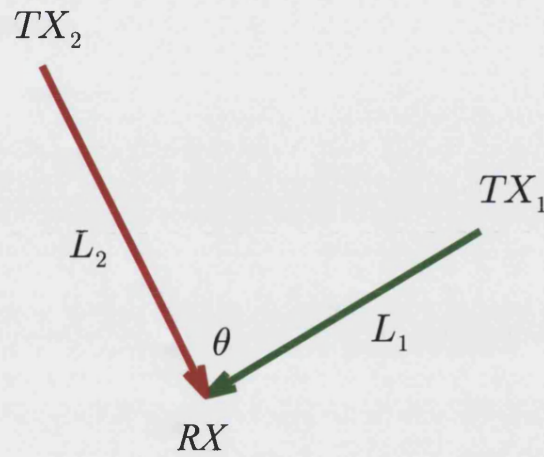


Figure 4.1: General representation of a route-diversity link configuration.

where, $A_D(t)$ is the attenuation exceeded in the combined diversity (joint) path, for time t and $A_M(t)$ is the attenuation exceeded for the unprotected (single) path. Hence, diversity gain is implicitly a function of the marginal attenuation.

The diversity improvement factor (sometimes expressed as a percentage within the literature) gives a measure of the increase in link availability. It is defined as the ratio of the single link to the joint link fade exceedance probabilities, for a given attenuation or fade depth exceeded. It is measured by the vertical distance between the marginal and joint distribution curves, and is proportional to that distance if the time percentage scale is logarithmic.

$$I(A) = \frac{P_M(A_M)}{P_D(A_M)}. \quad (4.2)$$

Similarly, $P_D(A_M)$ is the percentage of time in the combined diversity path with a fade depth larger than A_M dB and $P(A)$ is the time percentage for the unprotected path. Figure 4.2 illustrates how the diversity gain and improvement can be obtained from single and joint attenuation exceedance distributions.

Since for the current study, there are scenarios where the link pair can have different link lengths, the definition of improvement has to be amended to take this into account by specifying which link is the diversity with respect to. This is

4.5. Diversity Theory

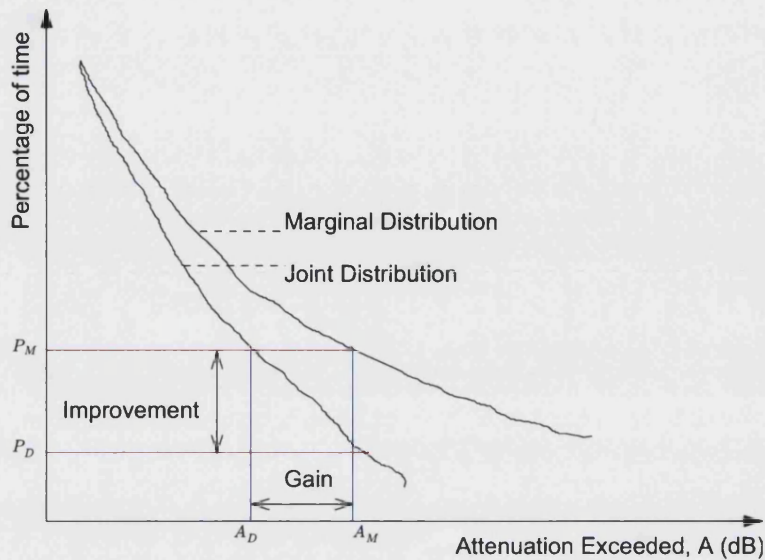


Figure 4.2: Diversity gain and improvement definitions.

termed the reference link. Equation 4.2 can also be re-written as;

$$I(A_{\text{ref}}[t\%]) = \frac{P_M(A_{\text{ref}}[t\%])}{P_D(A_{\text{ref}}[t\%])}, \quad (4.3)$$

where $A_{\text{ref}}(t\%)$ is the fade depth exceeded at time $t\%$ on the reference path. This can be further simplified to become;

$$I(A_{\text{ref}}[t\%]) = \frac{t\%}{P_D(A_{\text{ref}}[t\%])}, \quad (4.4)$$

where the probabilities are expressed in percentages with $P_M(A[t\%]) \equiv t\%$.

Although slightly more complicated in its definition, equation 4.3 has the advantage that the fade depth can be defined in relative instead of absolute terms. In most cases, this is preferable as system designers would like to know the new availability with the use of diversity, after designing a link for a given availability or exceedance percentage.

Diversity Selection Techniques

Three diversity combination techniques can be used to obtain the best signal during fading conditions. These are signal selection (switching), equal gain combin-

4.5. Diversity Theory

ing and maximal ratio combining. Switching is a method that chooses during each instant the signal with the largest signal to noise ratio from both links. This will correspond to the link suffering the least attenuation during a fading event. The expressions for the signal to noise ratio and attenuation in the case of two links is given by,

$$\text{SNR} = \max(\text{SNR}_1, \text{SNR}_2), \quad (4.5)$$

$$A = \min(A_1, A_2). \quad (4.6)$$

Maximal ratio combining is a subset of methods used to combine multiple received signals. The signal received in different channels is combined linearly to improve the signal to noise ratio optimally. It represents the best case when the two signals are combined. For identical receivers limited by internal noise, the maximal ratio combining process results in an output signal power that is the sum of the signal power received by both links [Schwartz et al. 1966]. For two links, this is given by,

$$\text{SNR} = \sum_{k=1}^2 \text{SNR}_k. \quad (4.7)$$

The expression for the maximal ratio combined signal attenuation is then given by,

$$A = -10 \log \left(\sum_{k=1}^2 10^{-\frac{A_k}{10}} \right). \quad (4.8)$$

Generally, most diversity schemes have employed a switching selection method as it is simpler to implement. For maximal ratio combining selection schemes, additional information on the phase of the incoming signals is needed so that they can be coherently combined. Usually phase estimation of the signals can only be done to within several degrees of the true phase. Hence, the resulting signal to noise ratio would lie between the limiting values of switching and maximal ratio combining which represent the lower and upper bounds respectively.

4.5.2 Balanced and Un-balanced Diversity

Capsoni et al. [1990; 1985], have highlighted the fundamental aspects of balanced and unbalanced diversity within the context of Earth-space orbital diversity. Some of the concepts are applicable to route diversity.

Consider two links of lengths L_1 and L_2 that have identical gains and losses with regards to antenna and transceiver equipment respectively. The power trans-

4.5. Diversity Theory

fer characteristics across both ends of the links would be expressed for rain by their attenuation distributions. L_1 is designated as the reference link and L_2 is the diversity link. The joint outage probability in a diversity system is given by,

$$F_D = \Pr(A_1 > M_1 \cap A_2 > M_2), \quad (4.9)$$

where A_1 and A_2 are the fades experienced on L_1 and L_2 respectively. M_1 and M_2 represent the respective fade margins exceeded. The joint outage probability can be expressed in terms of conditional probability from Bayes theorem, whereby,

$$F_D = \Pr(A_2 > M_2 | A_1 > M_1) \Pr(A_1 > M_1), \quad (4.10)$$

where $P(A | B)$ is the probability of A given B . If L_2 is the reference link and L_1 is the diversity link, the subscripts in equation 4.10 can be readily swapped.

Consider the case where $M_2 > M_1$ and define ΔM as,

$$M_2 = M_1 + \Delta M. \quad (4.11)$$

ΔM is the difference in margin between the two links and can be thought of as the extra margin in L_2 , if the margin in L_1 is fixed. Using equations 4.2 and 4.10, the improvements with respect to L_1 and L_2 are then,

$$I_1 = \frac{1}{\Pr(A_2 > M_2 | A_1 > M_1)}, \quad (4.12)$$

$$I_2 = \frac{1}{\Pr(A_1 > M_1 | A_2 > M_2)}. \quad (4.13)$$

Increasing ΔM increases I_1 and decreases I_2 , and vice versa. When $M_2 \gg M_1$, equation 4.10 will tend to 1. Hence the joint outage probability distribution becomes,

$$F_D = \Pr(A_2 > M_2), \quad (4.14)$$

The improvement obtained with respect to L_1 from such a scenario would be high, while there will be no improvement with respect to L_2 . But this is not diversity in its true sense, as only L_2 will be selected. This is an artifact of the large difference in the individual link attenuation distributions. The diversity system should be able to select between the two links, as and when the need arises during a fade event.

4.5. Diversity Theory

A compromise is obtained by making the two improvements equal. This is achieved by shifting the attenuation distribution of L_2 by an amount equal to $\Delta M = M_2 - M_1$. This ensures that the diversity system is balanced whereby $\Pr(A > M_1) = \Pr(A_2 > M_2)$. This also ensures that the request probability (probability of switching to another link), F_S of diversity is the same and the role of the two links can be interchanged i.e. $F_S = F_1 - F_D = F_2 - F_D$.

Therefore, a diversity system is defined to be balanced if the outage probabilities on both links is the same irrespective of their path lengths. For equal path lengths, the margins on both links would be the same. An unbalanced diversity system on the other hand would result when the outage probabilities on the individual links are not the same. For links of equal length, this ensues when the fade margins are different. Links having different lengths but the same fade margin would also be unbalanced.

Consider the P2P and P2MP network scenarios highlighted in § 4.2. For P2P networks, it will be possible to adjust the margins on both the reference and diversity links appropriately to achieve a balanced diversity scenario when the path lengths are not the same.

In the case of P2MP networks, a balanced diversity scenario is not achievable for all users within the network. Since the network would be designed for minimum level of availability over the whole area, individual user link availabilities would differ from this level depending on their relative distances from the transmitting base station. Users closer to the base station would have a higher level of availability compared to users on the periphery of the network. Additionally, although not generally likely, it is possible as a result of the process of network design and optimisation to have the reference link with a longer length than the diversity link.

4.5.3 Previous Studies

The earliest work to indicate the utility of route diversity for millimetre wave systems was presented by Jones & Watson [1993]. In it they show the potential of such a scheme to mitigate fades, and besides provide indirect information on the degree of fade correlation between links. They also noted the possible complexity in producing a model that would take into account link length, frequency and any possible climatic dependency.

There have also been some initial studies under the CRABS (Cellular Radio Ac-

4.6. Diversity Simulations

cess for Broadband Services) [CRABS 1998, 1999] project, focusing on route diversity [Tan and Pedersen 2000] and other propagation areas for point to multi-point systems, in the 40 GHz band. As a result of the project, the ITU-R has adopted a recommendation (Rec. ITU-R P.1410) for broadband millimetric radio access systems.

The EMBRACE (Efficient Millimetre Broadband Radio Access for Convergence and Evolution) project [Craig et al. 2002] has also explored the use of route diversity with field trials on system performance [Willis et al. 2002].

Recent simulation studies of route diversity at 30 GHz, using conventional rain radar data in Canada [Hendrantoro et al. 2002], show similar variation in route diversity to what would be described further on in the discussion. Additionally, criteria for determining the benefit of route diversity for a given subscriber location was proposed.

Paulson [2003a] has also presented the use of a spatio-temporal rain rate model (see § 2.6.3 on page 39) to predict route diversity statistics. The predictions were found to represent lower bounds on the realisable diversity improvement as the model assumes that both links are completely covered by a rain event.

Sinka & Bito [2003] have also analysed the use of route diversity to mitigate the effect of interference when raining in a P2MP network. They highlight that route diversity can lead to carrier to interference ($\frac{C}{I}$) improvements between 3–10 dB depending on user location within the network. Additionally, $\frac{C}{I}$ values with the use of diversity were close to clear air levels.

4.6 Diversity Simulations

The procedure involved in the calculation of diversity statistics for all possible combination of link geometries is now described.

As indicated in chap. 3, the CRIE database consists of 3199 PPI scans which have been interpolated to enable simulation of a point to multi-point star network configuration. In initial investigations [Usman et al. 2002, 2003], rain rate values estimated from only Z_H records were used for diversity simulations at a frequency of 42 GHz. This formed the basis of investigations under the EMBRACE project. Later, a combination of Z_H and Z_{DR} records were used for the simulations as these have been shown to provide better estimates of rain rate values. Simulated diversity scenarios were obtained for frequencies between 20–50 GHz. Hence, it is assumed that both links are under LOS conditions at all times, and at

4.6. Diversity Simulations

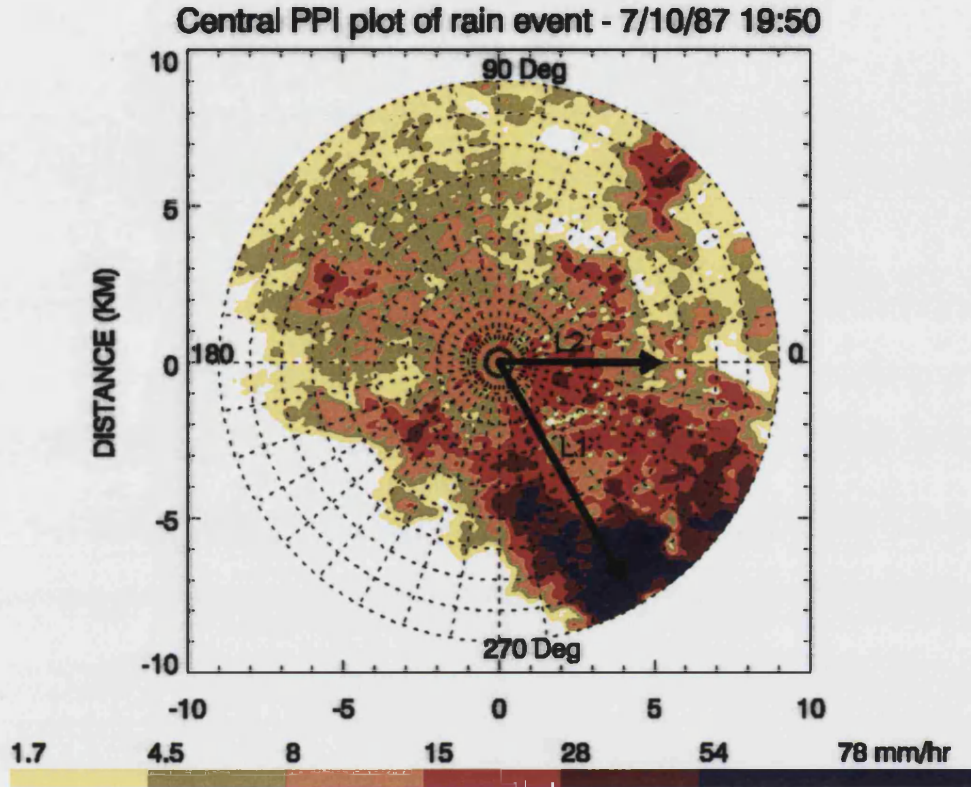


Figure 4.3: The simulation of attenuation over a rain field for a pair of convergent links.

0° elevation. The effect of multi-path propagation can be ignored.

Overlaid over each CPPI scan were two links, of lengths L_1 (0.5–9 km) and L_2 (0.5–9 km) converging at a common node (see figure 4.3). To a good approximation, the instantaneous rain fade experienced by a link of length L may be written as the integral of the specific attenuation, γ ,

$$A = \int_0^L \gamma(x) dx \approx \int_0^L kR^\alpha(x) dx. \quad (4.15)$$

Given radar derived rain rate estimates, R_i along the link path, this integration may be approximated by a summation,

$$A \approx k \sum w_i R_i^\alpha \Delta x_i, \quad (4.16)$$

4.6. Diversity Simulations

where w_i are the quadratic weights and Δx is the integration scale of the rain rate measurement, i.e $\sum_i \Delta x_i = L$.

The attenuation was calculated for each link and all angles (0–360) using specific attenuation relationships, obtained from FIM scattering calculations [Uzunoglu et al. 1976, 1977] in the 20–50 GHz range. This assumed a Marshal & Palmer drop size distribution [1948] with a RAL drop shape [Goddard and Cherry 1984b] (see § 2.15). For 42 GHz vertical polarisation, the specific attenuation relationship is to a very good approximation given by,

$$\gamma = 0.31R^{0.97} \text{ dB/km.} \quad (4.17)$$

Taking L_1 as the reference path at 0° , the rain attenuations on both links were calculated as L_2 (the diversity path) was rotated between 0° and 360° in 5° increments. This was repeated for L_1 at 5,10,15 up to 360° . This makes full use of the rain radar database in all azimuthal directions. As a consequence, the dependence of the diversity statistics on the preferred orientation of any anisotropy associated with rain cells and local topography on link orientation has been averaged out. This dependence is has been shown to be very weak [Hodge 1978].

The attenuation values were binned from 0 dB to the maximum attenuation value for each link. These were then used to construct a two dimensional probability matrix $p(m, n)$ for each angular separation, where m and n represent m^{th} and n^{th} attenuation levels of the reference and diversity links, respectively. From this probability density matrix, statistics for individual links and for diversity were derived. Hence, the two dimensional joint cumulative distribution at each angular separation and frequency $P(M, N, \theta, f)$, with regards to switching diversity is given by,

$$P(M, N, \theta, f) = \sum_{m=M}^{\infty} \sum_{n=N}^{\infty} p(m, n, \theta, f). \quad (4.18)$$

The marginal cumulative probability distribution of the reference link is obtained from equation 4.18 with $N = 0$ for all M . Similarly, $M = 0$ for all N gives the marginal cumulative distribution of the diversity link. Hence, using the expressions in equations 4.1, 4.4 and 4.18, the statistics of diversity gain and diversity improvement can be calculated. The diversity gain was obtained for seven availability levels 99%, 99.5%, 99.7%, 99.9%, 99.95%, 99.97% and 99.99%. Also, diversity improvement statistics were obtained for seven fade depths, $A(1\%)$, $A(0.5\%)$, $A(0.3\%)$, $A(0.1\%)$, $A(0.05\%)$, $A(0.03\%)$ and $A(0.01\%)$, with respect to the reference

4.7. Analysis of Results

path.

When considering asymmetric links, the diversity statistics were obtained for two cases. Firstly, for the unbalanced diversity case, where links having different lengths are assumed to have the same fade margin. The resulting joint cumulative distribution lies in the plane with the reference link attenuation equal to the diversity link attenuation. This lies along the diagonal of equation 4.18. For the balanced diversity case the link margins have been adjusted so that the exceedance probabilities are the same.

Evaluations for availability greater than 99.99% and fade depths exceeded for time percentages less than 0.01% of the time were not carried out due to limits on the statistical validity of the database. For the 2 year database with a 9 out of 28 day duty cycle, this corresponds to a total measurement time of 8 months. Typical duration of rain events is 20–30 min. With a scan every 10 min, this represents an average of 2.5 scans per event. Hence this gives approximately 1280 events over a 2 year period. Therefore statistical information for time percentages less than 0.1% often rely on 1 event.

4.7 Analysis of Results

As noted, the outputs from the simulations represent a multi-dimensional database parameterised by link availability, link separations and lengths, fade depths exceeded and frequencies of operation. An attempt has been made to extract the most important trends and to select illustrative graphs in order to provide a feel for the underlying behaviour of route diversity.

In the analysis of the simulation results, several factors were observed to influence the diversity performance. These were;

- The correlation between the links as a result of the spatial variation of the rain rate field over an angle θ .
- The difference in link lengths (i.e. link asymmetry) between the reference and diversity links, L_{ref} and L_{div} respectively.
- Whether the links were balanced in terms of their attenuation distributions, when considering asymmetric link cases.
- The given fade margin, $A(\%)$ and availability, $av(\%)$.
- The frequency of operation, f GHz.

4.7. Analysis of Results

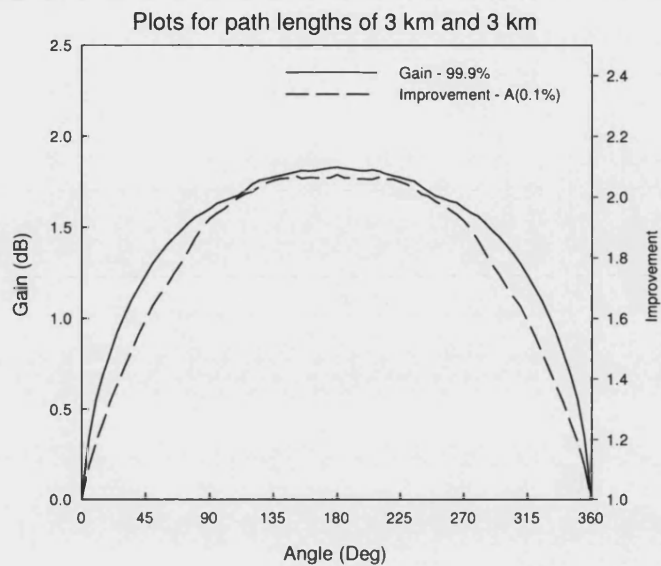


Figure 4.4: Diversity gain and improvement factor at 42 GHz (V-POL) for a reference and diversity links of 3 km showing the effect of link separation.

4.7.1 Spatial Variation

It is expected that as the angular separation between the links increases, the probability of a rain event affecting both links decreases, until it reaches a minimum at 180° . This gives an indirect indication on the correlation of attenuation between the two links, which is influenced by the correlation of the rain-rate field. Figure 4.4 shows the angular variation of diversity gain and improvement for two symmetric links of 3 km respectively. It can be seen that the plots are symmetric around 180° .

The diversity gain is for a link availability of 99.9%. It can be seen that at link separations of 45° , 90° and 120° the gain is approximately 1.3 dB, 1.5 dB and 1.7 dB respectively. Hence if the margin on both links before using diversity at 99.9% availability was say 12 dB each, the margin can be reduced by these values using diversity and still maintain the required availability.

The improvement factor for the same separations is 1.5, 1.8 and 1.9 respectively. This implies that increases in availability levels by 50%, 80% and 90% respectively are possible if the margin of 12 dB is maintained on both links. Between $0-90^\circ$, the diversity improvement increases rapidly but between $90-180^\circ$, the rate of increase is much less marked. The gain and improvements increase

4.7. Analysis of Results

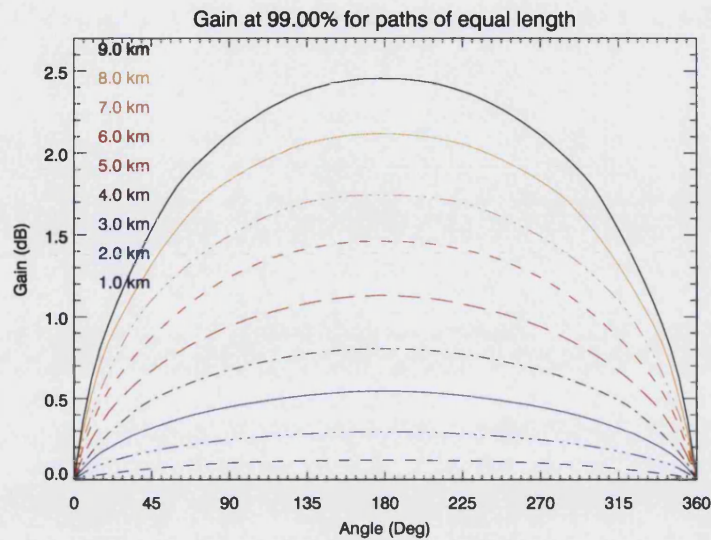


Figure 4.5: Diversity gain at 42 GHz (V-POL) showing the monotonic variation of diversity with link length increasing from 1 km (lowest plot) to 9 km (topmost plot).

at the rate of approximately 0.02 dB/degree and 0.008/degree respectively between 0–90°. Within the range 90–180° the rate of increase is 5×10^{-3} dB/degree and 5×10^{-4} /degree respectively. Also, at around 120° the difference in diversity from the maximum value at 180° is negligible with the curve showing a slightly flattened peak.

In total, it shows that for significant diversity advantage, link separations should be between 45–90°, with greater separations not having any significant increase from these values.

4.7.2 Variation with Link Length

Figures 4.5 and 4.6 show the variation of diversity gain and improvement for symmetric links having lengths between 1 km and 9 km. From this we can see a monotonic increase in the diversity advantage with increasing link length.

As expected, pairs of shorter links lengths (less than 2.5 km) are more likely to be effected by individual rain events than longer links. Hence, any diversity obtained would be small, as within that distance, the rain field correlation would be high. At 99% availability, the diversity gain varies between 0.05–1.5 dB at a separation of 45° for link lengths of 1–9 km. The improvement factor shows an

4.7. Analysis of Results

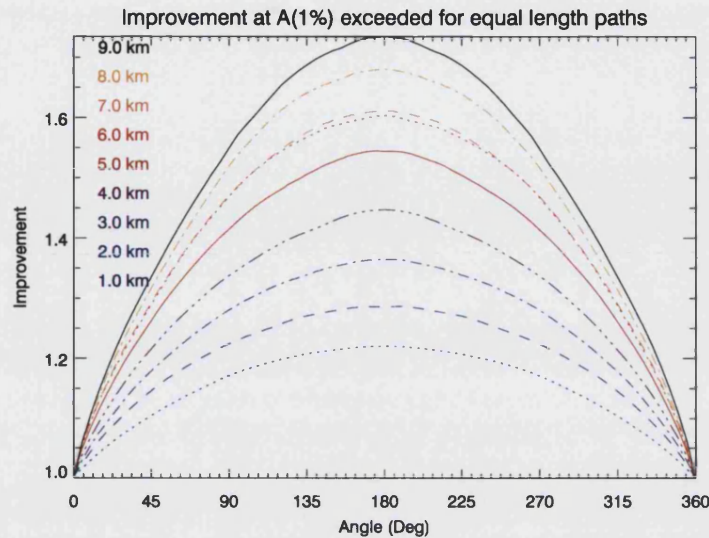


Figure 4.6: Diversity improvement at 42 GHz (V-POL) showing the monotonic variation of diversity with link length increasing from 1 km (lowest plot) to 9 km (topmost plot).

increase between 1.1 and 1.5.

When the asymmetric link scenario (reference and diversity links of different annual cumulative distributions) is considered, the micro-scale features of the rain field contribute less to the diversity statistics. In this case, the marginal attenuation statistics of both links start to play a significant part. This is shown in figures 4.7 and 4.8.

In the case of two symmetric links of 3 km (see figure 4.8), there is a spread in the joint attenuation diversity statistics for different link separations indicating, the effect of the spatial distribution of rainfall.

When the diversity link now becomes a 5 km link (see figure 4.7), the joint attenuation diversity statistics closely resemble the marginal attenuation statistics for the reference link (3 km). Since on average, the 3 km link will suffer less attenuation compared to a 5 km link irrespective of the spatial distribution of the rain field, the joint attenuation statistics would closely mirror the marginal statistics of the reference link.

As stated earlier, using a balanced diversity scenario by adjusting appropriately the associated margins on the links, the joint attenuation distributions become less closely correlated with the marginal distribution of the 3 km link.

4.7. Analysis of Results

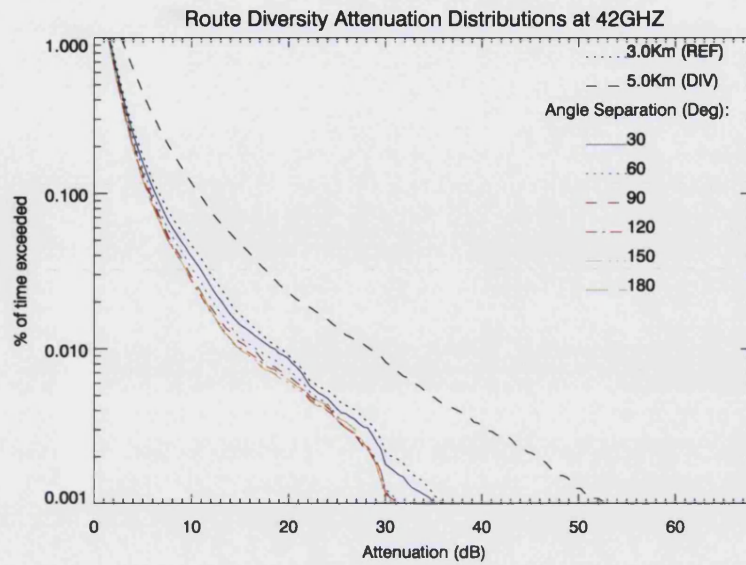


Figure 4.7: Marginal and joint attenuation distributions (at 42 GHz) for a reference 3 km link and a diversity 5 km link. Notice the little difference in the joint attenuation distributions with link separation.

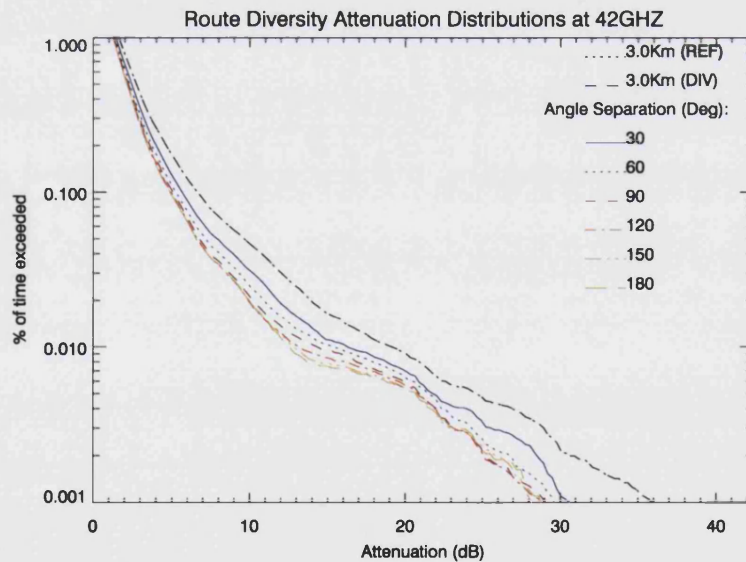


Figure 4.8: Marginal and joint attenuation distributions (at 42 GHz) for a reference 3 km link and a diversity 3 km link. Notice the influence of link separation on the joint attenuation distributions.

4.7. Analysis of Results

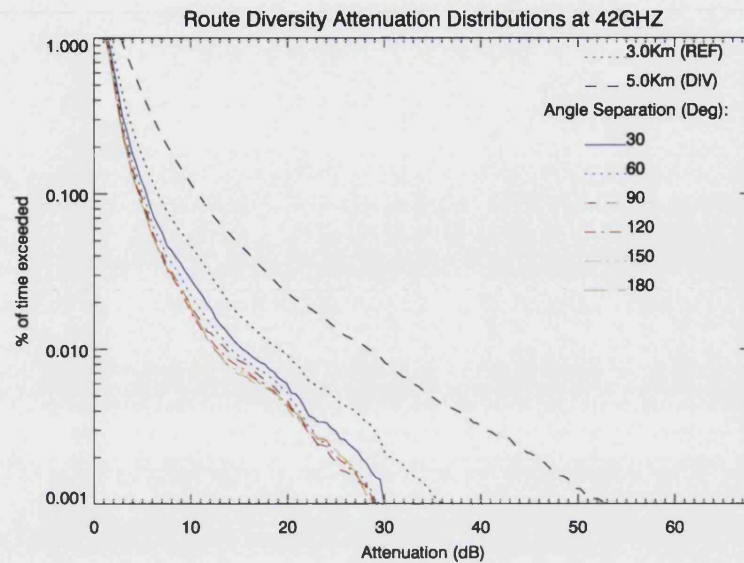


Figure 4.9: Marginal and balanced joint attenuation distributions (at 42 GHz) for a reference 3 km link and a diversity 5 km link.

Figure 4.9 shows the balanced joint attenuation distributions for a 3 km reference link and 5 km diversity link. Comparing this with figure 4.8 for the two symmetric links of 3 km it can be seen that there is very little difference in the joint attenuation statistics.

4.7.3 Variation with Availability Level and Fade Depth

Diversity gain and improvement were observed to increase with availability and fade depth respectively (see figures 4.10 and 4.11). At low availabilities and fade depths the low diversity advantage is as a result of widespread stratiform rain. Such rain events would completely cover both links and the rain rate variation would be fairly uniform over the area, whereas at the very high availabilities and fade depths, convective rain cells which are highly localised with higher rain rates would dominate the statistics.

Hence, any small separation between the links will make them far less correlated compared to the low availability scenario. The trends observed for links of equal length were the same for links of unequal length.

4.7. Analysis of Results

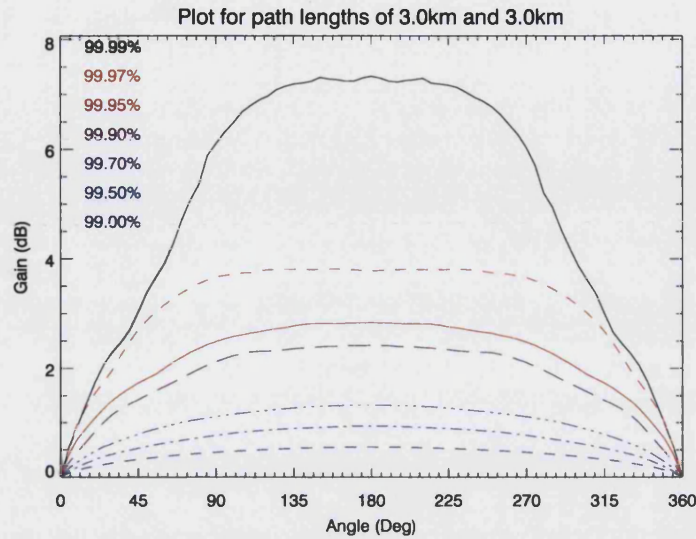


Figure 4.10: Diversity gain (at 42 GHz) for link pairs of 3 km showing the variation with reference link availability between 99% (lowest plot) to 99.99% (topmost plot).

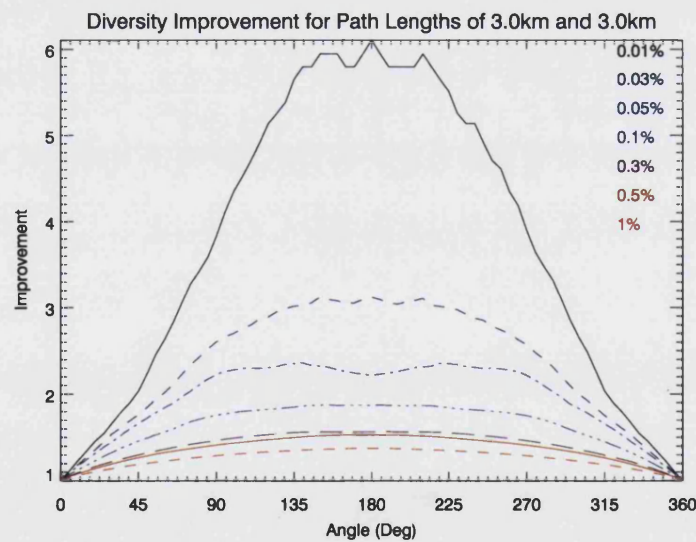


Figure 4.11: Diversity improvement (at 42 GHz) for link pairs of 3 km showing the variation with reference link fade depths exceeded between 1% (lowest plot) to 0.01% (topmost plot).

4.7. Analysis of Results

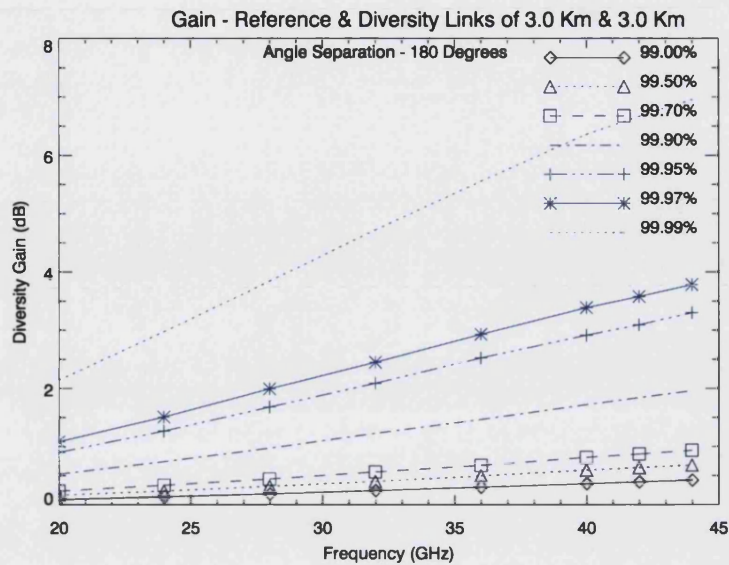


Figure 4.12: Diversity gain for link pairs of 3 km as a function of frequency (v-POL) at availability levels between 99–99.99%.

4.7.4 Effect of Frequency

Figure 4.12 shows the variation of diversity gain with frequency for several availability levels. A diversity link pair of 3 km separated by 180° is shown. As expected, diversity increases with frequency. Lower frequencies would experience lower attenuations within the same rain rate field compared to higher frequencies. Additionally, the range of variation in the attenuation statistics would be larger at higher frequencies for the same rain rate statistics. Hence, there is a higher probability of greater differences in the attenuations between the reference and diversity links.

The slowly increasing slope of diversity gain vs frequency with increasing availability is related to the slope parameter of specific attenuation (see equation 4.15), which similarly increases slowly with frequency. From Rec. ITU-R P. 838, the range of variation is between 1.1–0.9 for frequencies between 20–50 GHz at vertical polarisation.

Figure 4.13 shows the corresponding variation in diversity improvement with frequency. It shows that the diversity improvement is constant with frequency. This arises from the reformulated definition of diversity improvement employed (see § 4.5.1, and equations 4.3 and 4.4). Changing the frequency shifts the link

4.7. Analysis of Results

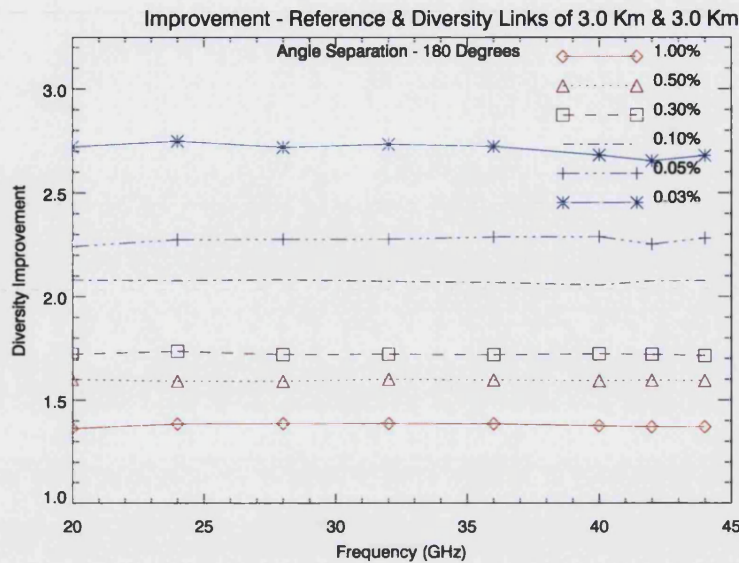


Figure 4.13: Diversity improvement for link pairs of 3 km as a function of frequency (V-POL) at fade depths exceeded at time percentages between 0.03–1%.

attenuation distributions to the right, but the ratio of marginal to joint exceedance probabilities remains the same. If equation 4.2 were to be employed, this would show the diversity improvement increasing with frequency.

The reformulated definition of diversity improvement therefore provides a convenient way of translating diversity statistics obtained at a particular frequency, to other frequencies of interest for the same link configuration without further scaling or processing. The advantage of this reformulated definition should also be applicable to site diversity for both terrestrial and earth-space systems.

4.7.5 Comparisons with other Investigations and Empirical Link Attenuation Statistics

Carleton University

The only study within this area similar in scope that the author is aware, is the work of Hendratoro et al. [2002]. They investigated the use of route diversity for links operating at 30 GHz using only radar Z_H data for the locality of Montreal, Canada.

Their results show that a modified sinusoidal model with an exponent, similar to the one presented here, best describes the azimuthal variation of diversity.

4.7. Analysis of Results

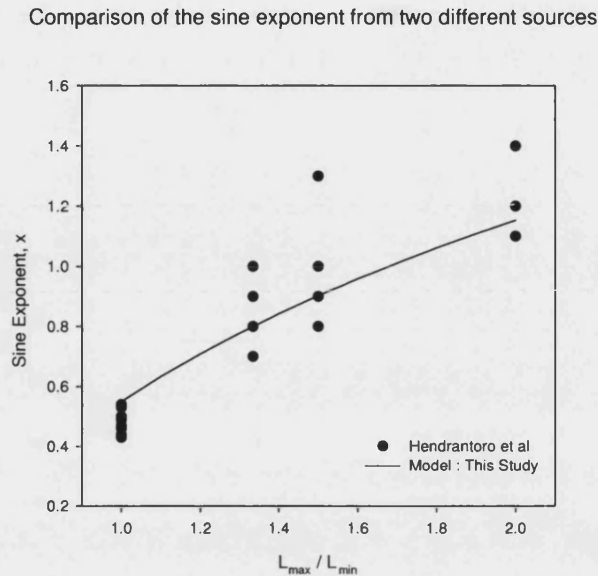


Figure 4.14: Comparison of the spatial variation sine exponent, x values obtained within this study and from Hendratoro et al. [2002].

Comparisons of the sine exponent values extracted from their paper together with our model (to be presented in equation 4.28) is shown in figure 4.14. It can be seen that in both cases there is a very similar trend of the exponent increasing with link asymmetry. Furthermore the model of equation 4.28 is close to the average values of the sine exponent at several link ratios.

Although it is not possible to compare directly the diversity gain values reported due to the different climates for Canada and the UK (Zone K and Zone E & F respectively of the old ITU-R zones). Using normalised gain however, the discrepancy in the marginal attenuations at the different sites can be factored out, leaving the effect of spatial variation of rain. This approach has been used for site diversity within the Earth-Space community for comparing results from various locations and frequencies [Hodge 1978; Capsoni et al. 1990; Lin and Levis 1993]. The normalised gain is defined as the ratio of the diversity gain to the marginal attenuations exceeded for the same percentage of time.

$$G_{\text{norm}}(t) = \frac{G(t)}{A(t)} \quad (4.19)$$

where $G(t)$ and $A(t)$ are the same as has been defined earlier.

4.7. Analysis of Results

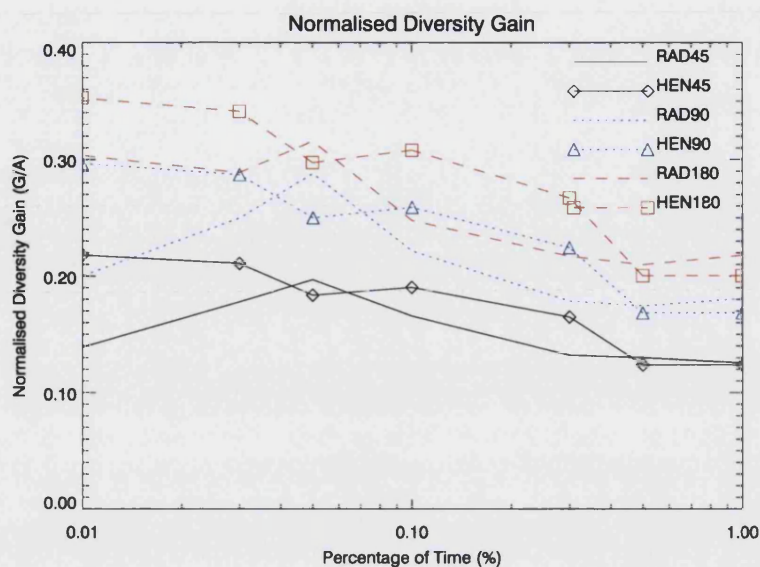


Figure 4.15: Comparison of the normalised diversity gains from Hendratoro et al. [2002] (HEN) and this study (RAD) for a link pair of 2 km at separations of 45, 90 and 180°.

Figure 4.15 compares the normalised gains for two link pairs of 2 km at frequencies of 30 GHz and 32 GHz. It can be seen that the normalised gains are very similar in both cases. Although by no means conclusive, it suggests that the spatial correlation of rain rates at both sites is very similar. Lack of more data on the marginal link distributions for other link lengths within the paper [Hendratoro et al. 2002] has precluded further comparative analysis.

Telenor Star Network

Distributions of marginal and joint link attenuations from a star link network situated in Kjeller, Norway [Lindholm 2001], have also been analysed to compare the measured diversity statistics with the radar derived diversity statistics. The star network consists of one transmitter and four receiver points operating at a frequency of 42 GHz. A map with link locations, angles and distances is shown in figure 4.16 and table 4.2 with the range for which the attenuation distribution for each link is valid.

Figure 4.17 shows the marginal and joint distributions of the star network for the one year period between September 2000 to August 2001. It can be seen that the Sia and Raelingen links have similar exceedance distributions due to the small difference in their path lengths. On the other hand the Skjetten and Lillestrom

4.7. Analysis of Results

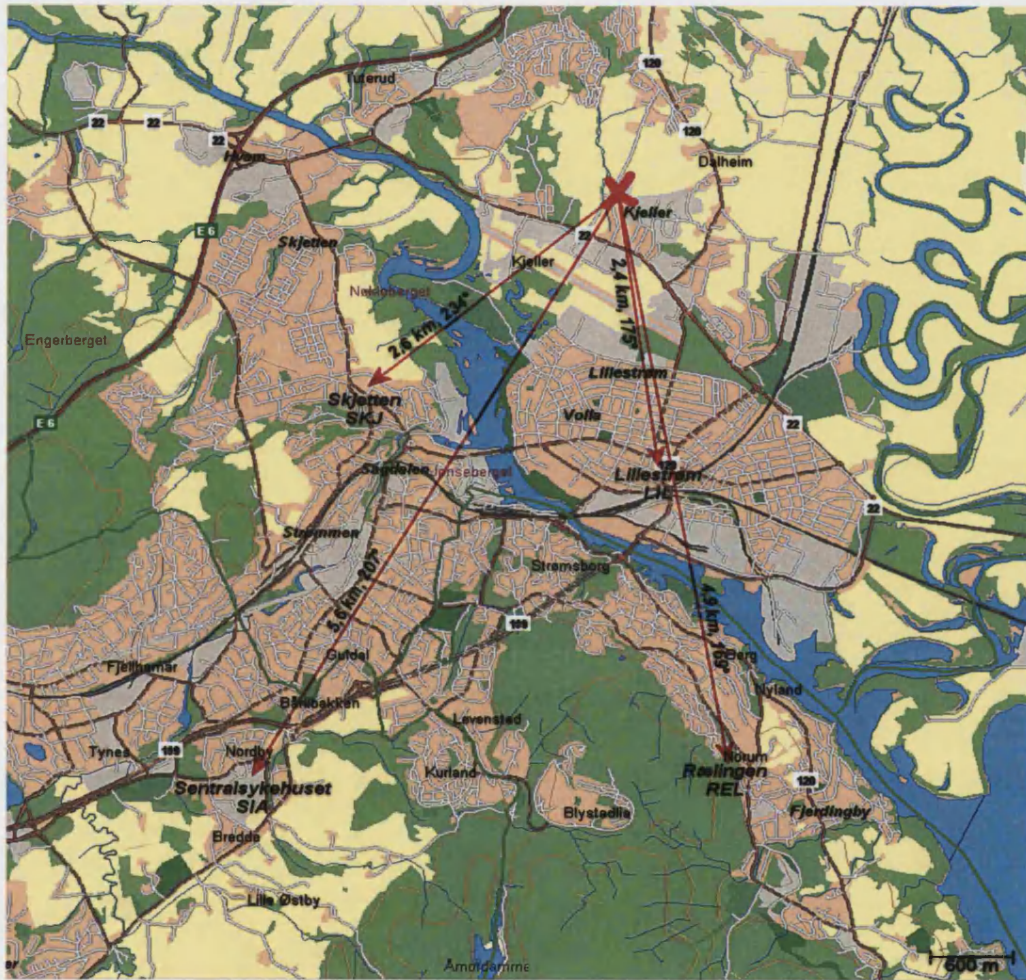


Figure 4.16: Map of Telenor star network links

4.8. Model Parameterisations

Table 4.2: Nodes in the Telenor Star network.

Receiver	Path Length (km)	Angle (N toward E)	Dynamic Range (dB)	Link Uptime
Skjetten	2.6	234	24	91%
SiA	5.6	207	30	64%
Lillestrøm	2.4	175	36	100%
Rælingen	4.9	169	25	90 %

distributions do not show any similarity in their attenuation distributions even though the path lengths are about the same. Between 0.1% and 1% of time the difference in the two distributions is up to 3 dB. No definite reason can be attributed for the difference as the link up time for both links is greater than 90%. A likely cause could be due to antenna wetting, leading to greater attenuations being experienced on the Skjetten link.

Similar to the analysis done in § 4.7.5, the normalised diversity was obtained for the Telenor link pair configurations. This is shown in figure 4.18. Good agreement is obtained when comparing the Sia and Rælingen links. Additionally there is good agreement comparing the normalised diversity gains when it is with respect to the Lillestrom link. On the other hand, there is very poor agreement for the Lillestrom-Rælingen and Skjetten-Rælingen diversity configurations. In general, the initial analysis with the attenuation distributions is encouraging but further analysis is required with the measured time series data to come to an adequate conclusion on the comparisons, especially in identifying any misleading artifacts within the data.

4.8 Model Parameterisations

4.8.1 Considerations

Based on the analysis of the diversity results, the following can be considered. The model to be developed has to take into account the decreased rate of variation in the diversity for angular separations between 120° – 240° and should be symmet-

4.8. Model Parameterisations

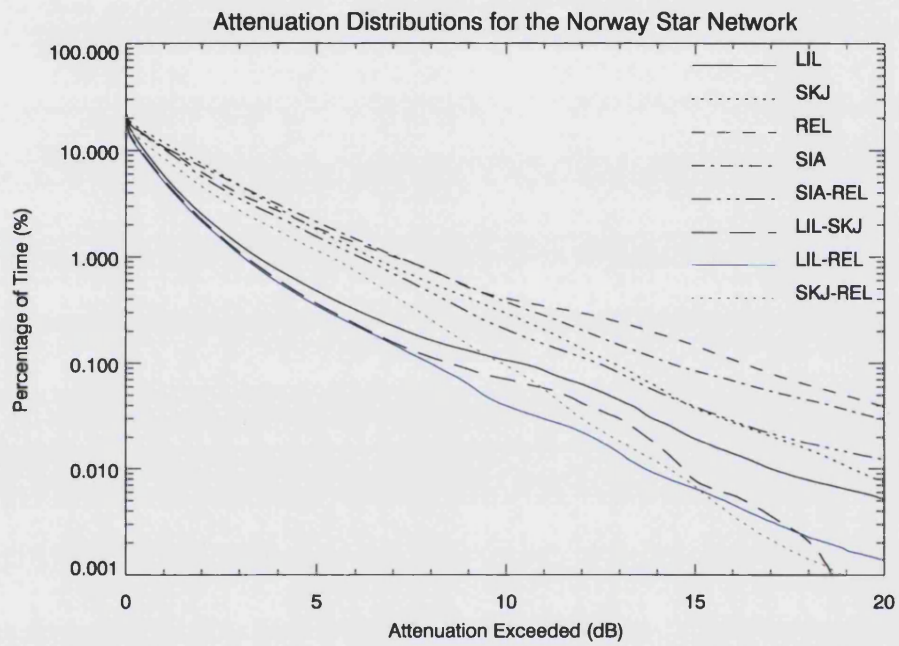


Figure 4.17: Marginal and joint attenuation distributions due to rain for the Norway network including the Raelingen (REL), Lillestrom (LIL), Skjetten (SKJ) and Sia (SIA) links. The period of measurement is between September 2000 to August 2001.

4.8. Model Parameterisations

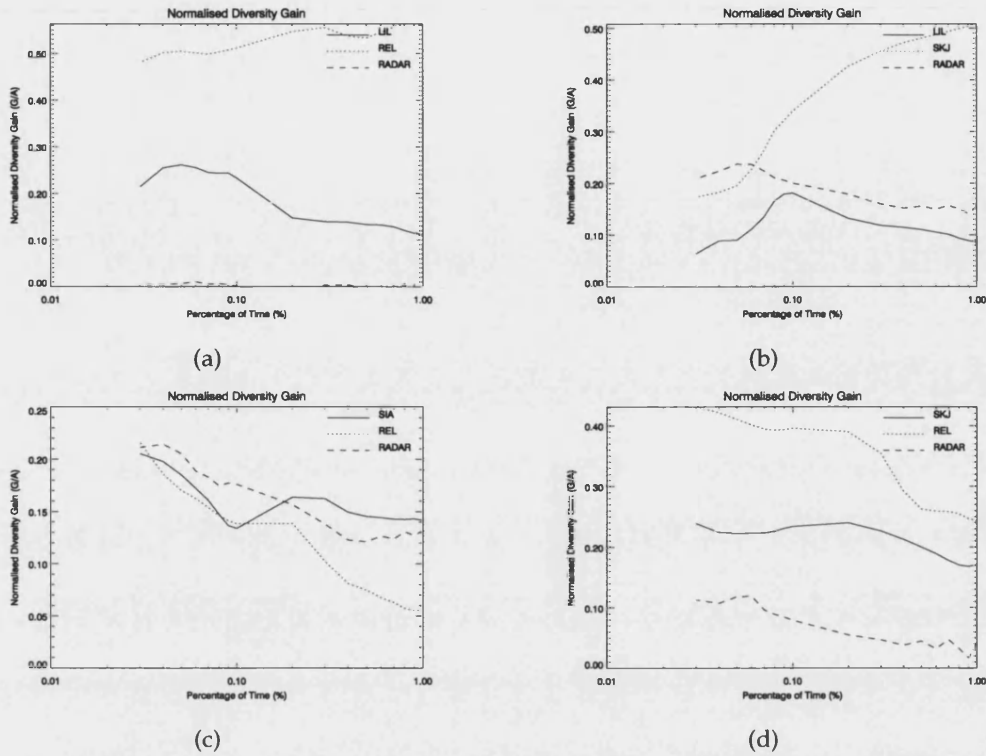


Figure 4.18: Comparisons of the normalised diversity gains of the links in the Norway star network with this study for the (a) LIL-REL, (b) LIL-SKJ, (c) SIA-REL, and (d) SKJ-REL links.

rical about 180° . The sinusoidal model of Tan & Pedersen [2000] which this study extends, takes symmetry into account.

However, the Tan & Pedersen model shape around its peak is inconsistent with observations from simulations in the current study. Furthermore, the sinusoidal model only took into account links of equal length with no consideration for link asymmetry and the different link margins realisable in practice. Lastly, although an analytical expression was given relating the maximum gain at 180° to other angular separations, no values or expressions were provided for maximum gain itself. Before presenting the model, it is pertinent to state certain assumptions that have formed the basis of its development.

4.8.2 Assumptions

It is assumed that the variation of diversity over the angular separations is symmetrical about 180° . For the majority of cases this assumption holds true but due to link asymmetry, the diversity curve does exhibit slight skewness in some cases

4.8. Model Parameterisations

(especially when there is a factor of 2 difference in path lengths).

The model proposed assumes both links are in a line of sight path and have the same fade margins irrespective of the link asymmetry. Therefore for symmetric links, the model produces balanced diversity statistics while for the asymmetric case, the statistics are for unbalanced diversity. Also, as stated earlier in § 4.6, the effects of the link pair orientation on the diversity statistics have been ignored. Studies have shown that such an effect on the statistics is negligible [Hodge 1978; Cherry and Goddard 1984]. Finally, due to data restriction, the range of the model limits application to link lengths of 1–9 km, availabilities between 99–99.99% and fade depths exceeded for A(1%)–A(0.01%).

4.8.3 Prediction Model

Expressions were sought for diversity gain and improvement for pairs of radial links. Examination of the simulation results suggested that these measures could be written as products of functions dependent upon different factors. With all the above points regarding diversity variation and the assumptions underlying its formulation, a route diversity prediction model is proposed in the form,

$$G(L_{ref}, L_{div}, \%, \theta) = G_{symmetric}(L_{max}, \%) h \left(\frac{L_{max}}{L_{min}} \right) S \left(\theta, \frac{L_{max}}{L_{min}} \right) C_{freq}(f), \quad (4.20)$$

$$I(L_{ref}, L_{div}, A(\%), \theta) = 1 + \left[I_{symmetric}(L_{max}, A(\%)) h \left(\frac{L_{max}}{L_{min}} \right) S \left(\theta, \frac{L_{max}}{L_{min}} \right) \right]. \quad (4.21)$$

Where $G_{symmetric}$ and $I_{symmetric}$ are the symmetric (i.e. equal length) path diversity gain and improvement as a function of link length, time percentage or fade depth. The path-asymmetry diversity reduction factor is denoted by h , while S is a trigonometric function describing the angular variation of diversity. L_{ref} and L_{div} (km) are the reference and diversity link paths respectively. L_{max} and L_{min} are the maximum and minimum respectively of L_{ref} and L_{div} .

Each function G , h , S , C , and I was examined by simulating results while keeping the other factors constant. Curve fitting was used to determine simple forms for each function. Several candidate model forms (polynomial, power, exponential, logarithmic functions etc) were tested using the coefficient of determination,

4.8. Model Parameterisations

Table 4.3: Diversity gain power law parameter estimates at different availabilities for symmetric links.

Availability (%)	a_G	b_G	Goodness of fit, R^2
99	0.123	1.366	0.99
99.5	0.218	1.308	0.99
99.7	0.342	1.259	0.99
99.9	0.648	1.173	0.99
99.95	0.810	1.165	0.99
99.97	1.132	1.169	0.99
99.99	2.041	1.077	0.99

R^2 as a goodness of fit measure;

$$R^2 = 1 - \frac{SS_{\text{error}}}{SS_{\text{total}}} \quad (4.22)$$

where SS_{error} is the sum of squares of the error between data and model predictions, and SS_{total} is the sum of squares of the data. Goodness of fit values approaching 1 indicate a good fit with values near zero indicating a very poor model fit.

4.8.4 Symmetric Link Maximum Gain and Improvement

At a certain availability level, the regression relationship between the maximum gain and link length (see Figure 4.19) is well approximated by a power law in the form of equation 4.23.

$$G_{\text{symmetric}}(L_{\text{max}}, \%) = a_G L_{\text{max}}^{b_G} \quad 1 \leq L_{\text{max}} \leq 9, \quad (4.23)$$

where, L_{max} (km) is the maximum link length of the two links, and % is the availability level of interest. The coefficients a_G and b_G are listed in table 4.3 for a selection of availabilities, together with values on the goodness of fit statistic. Figure 4.19 presents comparisons of the regression parameters with what has been calculated.

For a given fade depth exceeded at a certain percentage of time, the relationship between the improvement and link length exhibited a power law in the form

4.8. Model Parameterisations

Table 4.4: Diversity improvement power law parameter estimates at different time percentages for symmetric links.

Time (%)	a_I	b_I	Goodness of fit, R^2
1	0.082	0.491	0.98
0.5	0.114	0.431	0.99
0.3	0.106	0.535	0.99
0.1	0.155	0.559	0.98
0.05	0.196	0.566	0.99
0.03	0.324	0.406	0.95

of equation 4.24.

$$I_{\text{symmetric}}(L_{\text{max}}, A(\%)) = 10^{a_I L_{\text{max}}^{b_I}} - 1 \quad 1 \leq L_{\text{max}} \leq 9. \quad (4.24)$$

The coefficients a_I and b_I are listed in table 4.4 with comparisons of the regressions to calculations presented in figure 4.4.

4.8.5 Link Asymmetry Reduction Factor

By analysing the variation of the diversity gain when using symmetric links compared to when the links have different link lengths, a link asymmetry reduction factor has been obtained. This is defined to be the ratio of the maximum diversity gains for symmetric and asymmetric links. This is given by equation 4.25,

$$h\left(\frac{L_{\text{max}}}{L_{\text{min}}}, \%\right) = \frac{G_{\text{max}}(L_{\text{ref}}, L_{\text{div}}, \%)}{G_{\text{max}}(L_{\text{ref}}, L_{\text{ref}}, \%)} \quad (4.25)$$

Regressions from such analysis (see figure 4.21) have shown that the asymmetry reduction factor can be approximated by a power law of the form,

$$h\left(\frac{L_{\text{max}}}{L_{\text{min}}}, \%\right) = c \left(\frac{L_{\text{max}}}{L_{\text{min}}}\right)^{-d} \quad 1 \leq \frac{L_{\text{max}}}{L_{\text{min}}} \leq 2. \quad (4.26)$$

The parameters c and d are a function of the availability level or exceedance probability. Tables 4.5 and 4.6 lists the parameters for diversity gain and improvement respectively. From Figure 4.21 there is a noticeable clustering of the data points at link ratios of 1.5 and 2 respectively. This is purely due to link lengths within the data having intervals of 500m. Hence multiple data points will be produced

4.8. Model Parameterisations

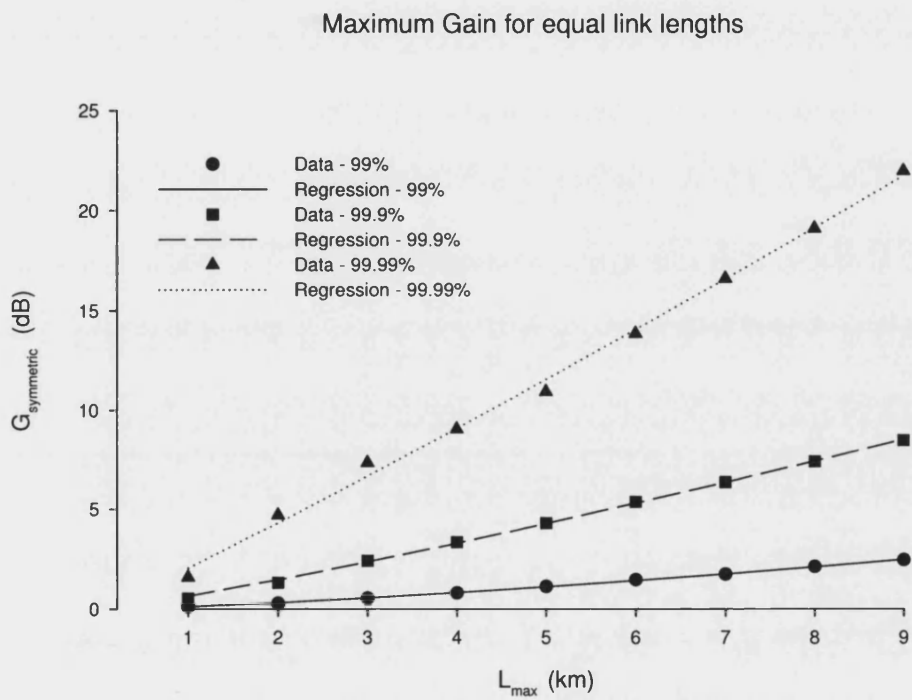


Figure 4.19: Regressions of the symmetric maximum diversity gain, $G_{\text{symmetric}}(L_{\text{max}}, \%)$ for link availabilities of 99%, 99.9% and 99.99%.

4.8. Model Parameterisations

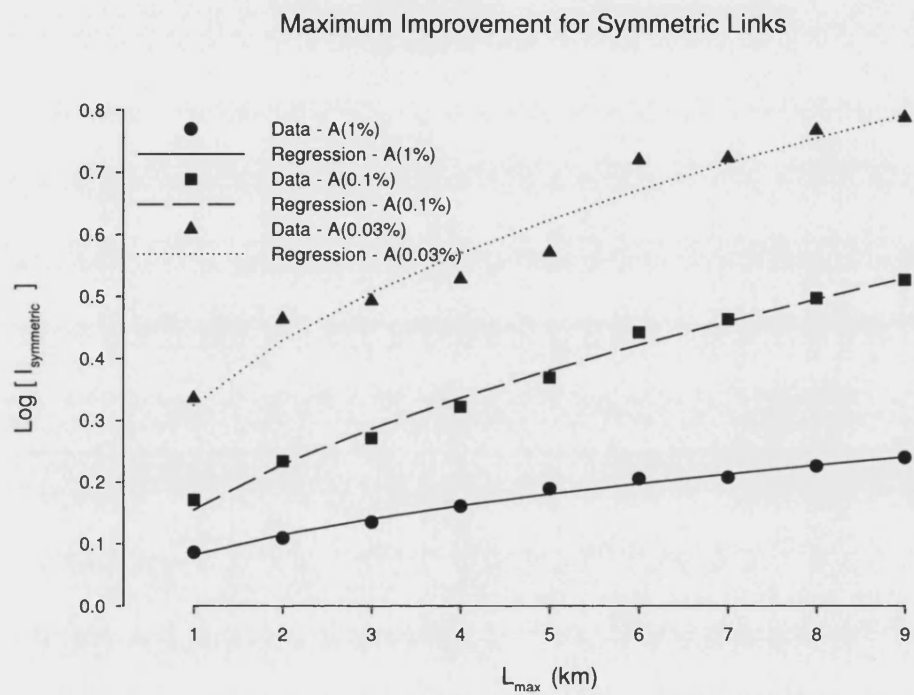


Figure 4.20: Regressions of the symmetric maximum diversity improvement, $I_{\text{symmetric}}(L_{\text{max}}, A(\%))$ for fade depths exceeded at 1%, 0.1% and 0.03% of time.

4.8. Model Parameterisations

Table 4.5: Diversity gain power law parameter values at different availabilities for asymmetric links.

Availability (%)	c_G	d_G	Goodness of fit, R^2
99	0.907	2.852	0.94
99.5	0.946	2.976	0.92
99.7	0.969	2.761	0.95
99.9	0.971	2.821	0.97
99.95	0.930	2.347	0.97
99.97	0.905	2.316	0.94
99.99	1.00	2.270	0.87

Table 4.6: Diversity improvement power law parameter estimates at different exceedance percentages for asymmetric links.

Time (%)	c_I	d_I	Goodness of fit, R^2
1	0.851	2.355	0.87
0.5	0.961	2.493	0.88
0.3	0.882	2.288	0.94
0.1	0.967	2.631	0.95
0.05	0.762	2.198	0.94
0.03	0.858	2.427	0.93

at link ratios of 1.5 and 2. All data points within the regression were each given equal weighting.

4.8.6 Angular Variation

The function,

$$S = \sin^x \left(\frac{\theta}{2} \right) \quad 0^\circ \leq \theta \leq 360^\circ, \quad (4.27)$$

was used to approximate the angular variation of both diversity gain and diversity improvement. The parameter x was chosen to optimise the goodness of fit to simulated data for symmetric and asymmetric links. The optimum value for symmetric links was found to be 0.55 and 0.84 for the diversity gain and improvement respectively. At other link combinations, regressions have provided an exponent function for the diversity gain and improvement as a function of link length ratio

4.8. Model Parameterisations

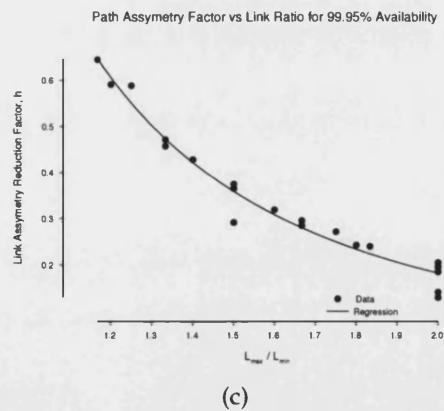
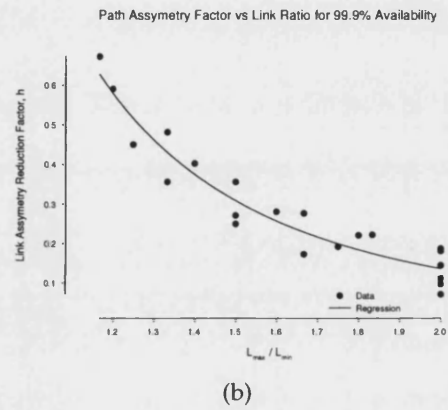
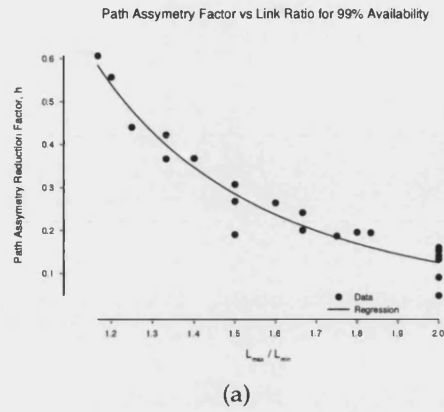


Figure 4.21: Regressions of the diversity gain path asymmetry reduction factor for availabilities; (a) 99%, (b) 99.9%, (c) 99.95%.

4.8. Model Parameterisations

given by,

$$\alpha_g = 0.87 \ln \left(\frac{L_{\max}}{L_{\min}} \right) + 0.55 \quad \text{for } 1 < \frac{L_{\max}}{L_{\min}} \leq 2, \quad (4.28)$$

$$\alpha_i = 0.61 \ln \left(\frac{L_{\max}}{L_{\min}} \right) + 0.84 \quad \text{for } 1 < \frac{L_{\max}}{L_{\min}} \leq 2, \quad (4.29)$$

where α_i and α_g are the coefficients for the improvement and gain respectively. L_{\max} and L_{\min} are the maximum and minimum link lengths for the diversity configuration $[L_1, L_2]$. Figure 4.22 shows the regression of the exponent for various link ratios. The trend is for higher link ratios to exhibit higher values of the exponent. Similarly to the asymmetry reduction factor clustering of data points are exhibited at integral values of the link spacing within the database.

4.8.7 Frequency Factor

To take into account the variation of the diversity with frequency, the gain as a function of frequency was normalised with respect to a diversity gain at a frequency of 42 GHz. A straight line best fit was obtained to the normalised values given by,

$$C_{\text{freq}} = 0.033f - 0.37 \quad 20\text{GHz} \leq f \leq 50\text{GHz}, \quad (4.30)$$

where f is the frequency in GHz. Figure 4.23 highlights the regressions. It can be seen that the variation in the correction factor between availabilities is less than the variation between frequencies for most cases.

4.8.8 Procedure for Calculation

The following describes the steps involved in the calculation of diversity gain and improvement from the model proposed.

1. Define L_{ref} , L_{div} and obtain L_{\max} and L_{\min} with,

$$L_{\max} = \max(L_{\text{ref}}, L_{\text{div}}), \quad (4.31)$$

$$L_{\min} = \min(L_{\text{ref}}, L_{\text{div}}). \quad (4.32)$$

Also, determine either the availability level, % if the gain is being calculated or the fade depth level at the given time percentage, $A(\%)$ for L_{ref} if the improvement is of interest. Furthermore, determine the angle subtended by the links, θ (see figure 4.1).

4.8. Model Parameterisations

2. Using equation 4.23 and parameters in table 4.3, calculate the symmetric gain, $G_{\text{symmetric}}$ for the availability level of interest using L_{max} . Refer to equation 4.24 and the parameters in table 4.4 for the corresponding symmetric improvement, $I_{\text{symmetric}}$.
3. Using equation 4.26 and tables 4.5 and 4.6, calculate the path-asymmetry reduction factor, h . If $L_{\text{ref}} = L_{\text{div}}$ then set $h = 1$.
4. Using equations 4.28 or 4.29, calculate the exponent, x for the trigonometric sine term and also calculate S . Where $S = \sin^x\left(\frac{\theta}{2}\right)$.
5. If the frequency of interest is not 42 GHz, then use the frequency correction factor, C_{freq} (equation 4.30) to adjust the values of diversity gain for frequencies between 20–50 GHz. The values of improvement do not need correction as indicated in § 4.7.4.
6. Using equation 4.20 for the diversity gain and equation 4.21, substitute the values obtained in steps 2–4 to obtain the predicted diversity gain, G (dB) and the diversity improvement, I .

4.8.9 Route Diversity and Model Performance

Table 4.7 shows the performance that can be obtained from the use of route diversity from a selection of example link configurations. The link separations are based on possible link realisations in practice. It shows the gains and improvements obtainable with the new link availabilities after the use of diversity.

The first two cases represent the case where there is some mild asymmetry between the links with their angular separations being less than 90° . At availability levels of 99.9 and 99.97% diversity gains of 0.36 dB and 0.87 dB are possible. Although such an improvement in the fade margin is small, the improvement in the availability levels is 12% and 37% respectively. The third case represents the scenario of severe link asymmetry whereby the diversity link is double the length of the reference link. Here, improvements in availability of 27% are possible.

Figures 4.24 and 4.25 show the distribution of the model prediction errors when compared to the simulated radar data. The errors are root mean square errors expressed as a percentage. In general, a majority of the prediction errors are less than 30% for all the cases compared from the simulated database with no particular preference to the model variables considered.

4.8. Model Parameterisations

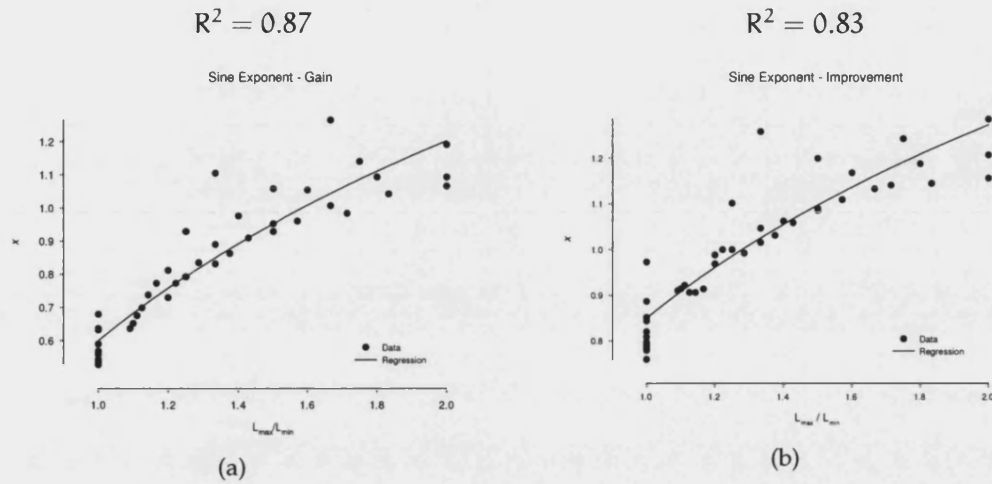


Figure 4.22: Regressions of the sine exponent for various link ratios with respect to the (a) diversity gain, and (b) diversity improvement. The corresponding goodness-of-fit values are for the regressions are shown centred above the respective plots.

Table 4.7: Example diversity scenarios with their resultant gains and improvements showing increases in availability levels.

L_{ref} (km)	L_{div} (km)	Angle, θ	Time, %	Availability, %	Gain (dB)	Improvement	New Availability, %
1.5	2.0	60	0.1	99.9	0.36	1.12	99.91
2.0	2.5	45	0.03	99.97	0.87	1.37	99.978
1.0	2.0	180	0.03	99.97	0.46	1.27	99.976
3.0	3.0	90	0.05	99.95	2.41	1.98	99.975
1.5	1.5	60	0.01	99.99	2.16	>1.78	99.994

4.8. Model Parameterisations

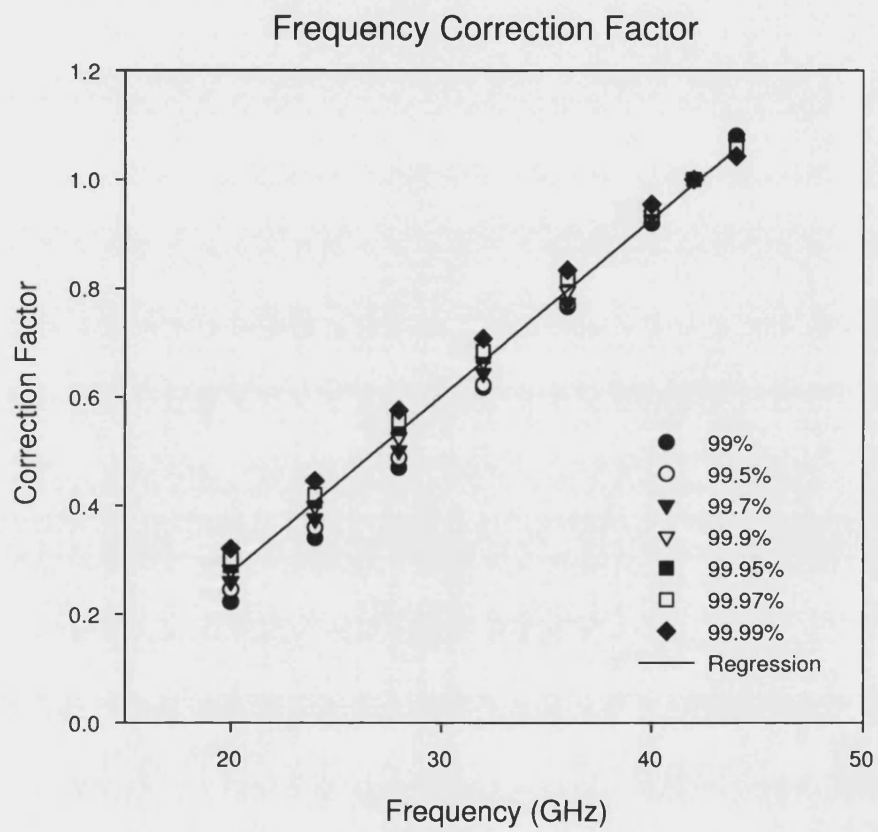


Figure 4.23: Regressions of the diversity gain frequency correction factor for availability between 99-99.99%.

4.8. Model Parameterisations

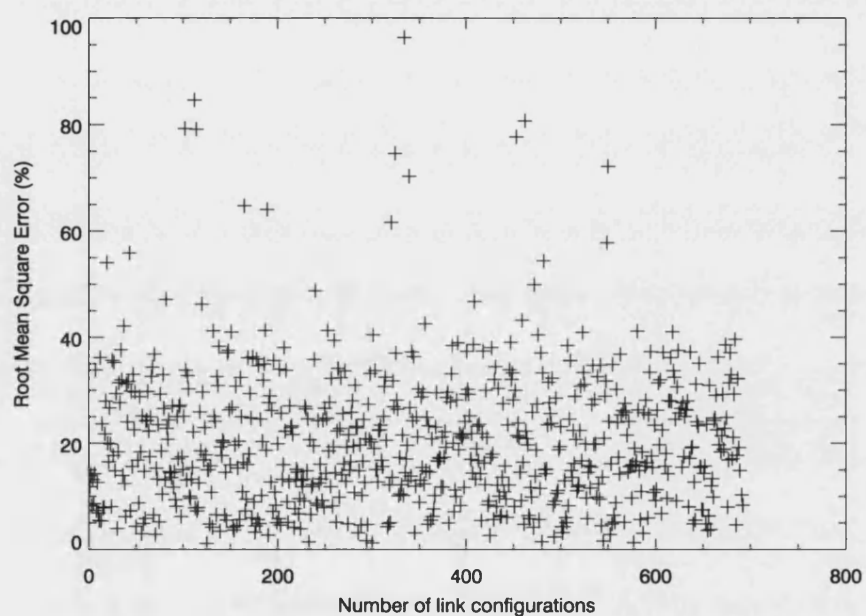


Figure 4.24: Distribution of model errors over all possible link configurations simulated. It can be seen that there is no discernible clustering of the errors indicating that the model performs equally well for all the model variables considered.

4.9. Concluding Remarks

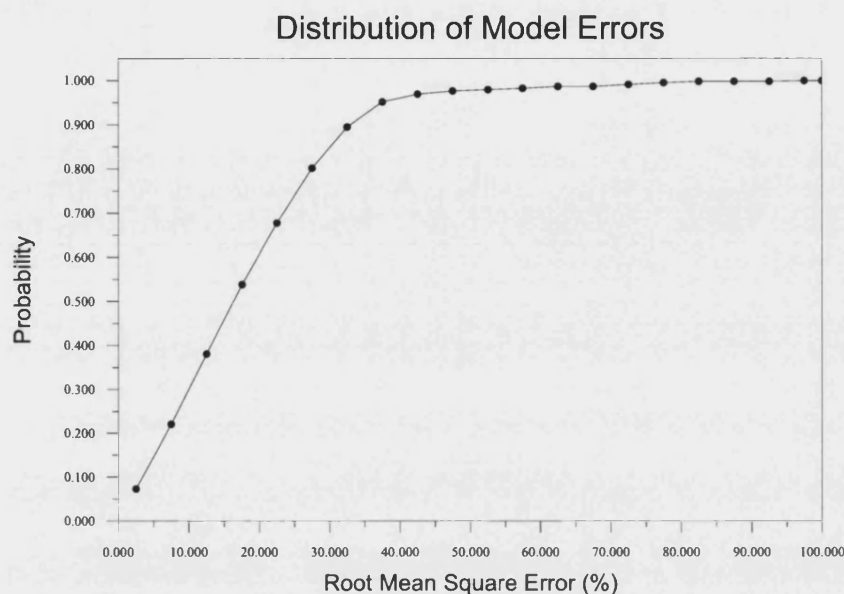


Figure 4.25: Cumulative distribution of model prediction errors

4.9 Concluding Remarks

Fade mitigation systems have become *derigueur* in the operation of current and future planned millimetre wave systems, especially with the availability requirements operators now expect from their networks. We have highlighted the diverse ways rain fades can be mitigated stressing that any candidate FMT has to take into account operating frequency bands, performance objectives of the systems and configuration of the network. In particular, the ability of route diversity to mitigate rain fades on point to point and point to multi-point networks based on the spatial characteristics of the rain field has been extensively analysed with respect to the major factors that influence the diversity statistics. Based on extensive attenuation simulations for link pair configurations between 1–10 km operating at frequencies of 20–50 GHz, route diversity shows significant variability both spatially and temporally with the following major trends.

- Diversity increases with an increase in link separation angle up to a maximum of 180°. Most of the increase occurs when links are separated by 45–90°. Further increases especially over 120° show a negligible increase in

4.9. Concluding Remarks

diversity. The diversity variation also exhibits high symmetry around link separations of 180° .

- There is a monotonic increase in the diversity advantage with increasing link length for the same length in both links.
- Considering link asymmetry, the diversity advantage is reduced/increased depending on the degree of asymmetry and whether the diversity is with respect to the shorter/longer link respectively. Therefore the spatial distribution of rainfall is a marginal factor in determining the diversity statistics compared to the marginal attenuation statistics.
- The standard way of defining the measures of diversity (i.e. gain and improvement) have largely been influenced by the Earth-space systems community where site diversity link paths toward a geosynchronous satellite have the same path lengths. For route diversity link paths, a situation of asymmetry becomes possible. In this case, the estimation of diversity statistics has to be made with respect to a particular link. Consequent upon this, the relative difference in margins between the link pair (i.e. whether the links are balanced or unbalanced) will have a critical impact on the diversity advantage expected. A large difference in link margins will depress diversity with respect to one of the links, while increasing diversity with respect to the other link. The balanced and unbalanced aspects of diversity would only be critical for point to point links. As noted, the nature of point to multi-point links within a broadcast network precludes any opportunity for “diversity balancing”.
- Diversity advantage was observed to increase with increases in availability and fade depth. At the high availability levels and fade depths, convective rain of shorter horizontal extent tends to dominate rain attenuation statistics, thereby making links less correlated. At the other end of the spectrum, stratiform rain which is much broader dominates rain attenuation statistics making links less correlated at low availability levels and fade depths.
- In terms of the frequency variation of diversity advantage, it is two pronged. The diversity gain increases with increase in operating frequency. Moreover, the rate of increase is independent of the availability. On the other hand, the diversity improvement statistics are independent of whatever variation with

4.9. Concluding Remarks

frequency. It is related to the interesting finding that when the diversity improvement factor is expressed in terms of the relative fade depth (e.g. $A[t\%]$) instead of the absolute fade depth (say 5 dB), the statistic is independent of frequency. Hence, this should provide a convenient way of translating diversity improvement statistics obtained from link data at a particular frequency, to other frequencies of interest between 20–50 GHz for the same link configuration without scaling or processing of the attenuation data. This reformulated definition is also applicable to site diversity for both terrestrial and Earth-space systems.

Comparisons of the statistics with investigations in the reported literature and empirical marginal and joint distributions show encouraging agreement with some of the results obtained within this study. Further investigations will be required to confirm the veracity of the trends.

Based on appropriate regression fitting analysis, a conceptually simple but accurate diversity model has been presented. It accommodates all the factors that influence the route diversity based on a fundamental assumptions. i.e. the fade margins on both links are the same. It represents an improvement from the model presented within ITU1410 with terms that are distinct and factorisable. In particular a modified sinusoidal term with an exponent best describes the azimuthal variation of diversity. Optimum values of the exponent for symmetric links were found to be 0.55 and 0.84 with respect to the diversity gain and improvement respectively. For asymmetric links, exponent values modelled agree closely with results obtained from the literature.

The influence of a change in climatic conditions will introduce large variations in the expected diversity statistics for any particular link configuration. Therefore, it is not foreseeable that the model parameter values (see § 4.8.4, 4.8.5) would be applicable to other climatic areas but the model form written as product of functions dependent upon the factors (L_1 , L_2 , $\%$, $A[\%]$, θ) should be invariant to location even when the same margin assumption does not hold.

A Generalised Model for the Joint Statistics of Attenuation on Route Diverse Links

This chapter presents the development of a generalised model for the prediction of joint attenuation exceedance statistics due to rain. The characteristics of correlation for a pair of links with a common node is investigated using the rain radar database. The effects of variations due to link asymmetry, separation between links and operating frequency are studied. Furthermore analysis is carried out to compare the results expected from theory with the radar simulations. Based on the simulations, a simple and accurate relationship is obtained for the correlation of log-attenuation experienced by pairs of links. This can then be used as a parameter to evaluate for the joint rain attenuation exceedance distribution on the assumption of bi-lognormality of attenuation.

5.1 Introduction

NOW, the impetus within the radio propagation community [COST255 1999; COST280 2000] is for the formulation of techniques that are able to produce the stochastic spatio-temporal series of rain rates and attenuation. These techniques are proving useful as inputs for the improved design of communication protocols, for the packet transfer of data on radio networks and the prediction of rain and attenuation statistics where data for a particular location is limited or non-existent. Such stochastic models (see § 2.6 for examples and underlying prin-

5.1. Introduction

principles), would be able to produce the first and second order, short and long term statistics of rain attenuation at whatever scale of interest and location, given some parameter values that are general to the rain medium.

Data sources on the first order statistics of rain rate and attenuation, given by their cumulative distributions, are generally available for several locations and can be used for comparing the performance of stochastic models. But information on second order statistics, such as the correlation of attenuation between pairs of links, is lacking for stochastic model refinement.

We have already presented the use of a model to predict second order statistics such as the diversity gain and improvement, which define the joint attenuation distribution for a pair of links. It was based on a number of assumptions, which restricted the applicability of the model to a narrow range of link configurations and fade margins.

For example, the model is only valid for link pairs where the shorter link is the reference link, with the longer link being the diversity link. In most cases this would hold true, but there would be circumstances where an operator would decide to assign the shorter of the two links as the diversity link. Furthermore, the diversity model is based on the assumption that both links, irrespective of their link lengths have the same fade margin. Therefore, a generalised model of diversity advantage is needed that is not constrained by limiting assumptions. To attain such a generalised model, it is imperative to refer to the statistical nature of rain and rain attenuation.

It has been observed that rain attenuation is random and approximately log-normally distributed [Lin 1973; Easterbrook and Turner 1967; Turner et al. 1966; Turner and Turner 1970; Galante 1975]. It has been shown that the attenuation of microwave radio signal caused by rain has a lognormal stationary distribution [3]. Lin has shown that rain attenuation in decibels is lognormally distributed [3], a result which is supported by experimental results reported by Turner et al. [4] -[6] and Galante [7]. Correspondingly, to an equally good approximation, the joint distribution of rain attenuation on two links is bi-log-normally distributed. Hence, The joint PDF of rain attenuation on N links is parameterised by N means and $\frac{1}{2}N(N + 1)$ covariances. These parameters (means and covariances) would completely determine the cumulative joint distribution and correspondingly the diversity advantage when considering a particular link scenario for any choice of fade margins.

5.2. The Statistics of Rain and Rain Attenuation

The mean and variance of a particular link can easily be estimated from existing information sources such as Rec. ITU-R P. 530. But information on the correlation/covariance of link rain attenuation to complete the picture is particularly lacking. The advantage of such a statistical approach is that the resulting model would have a weaker dependence on a particular location, as the correlation of link attenuation would be dependent on the relative occurrence of stratiform rain versus convective rain within a given region. An explicit parameter that defines this relative occurrence is the rain thunderstorm ratio. Several investigations have shown that the variation of this ratio over a climatic region is weak [Ito and Hosoya 2002; Rice and Holmberg 1973; Dutton and Dougherty 1979, 1984].

5.2 The Statistics of Rain and Rain Attenuation

The second order statistics of log rain attenuation (i.e correlation or covariance) are defined similar to the notation of Paulson [2002].

5.2.1 The Statistics of Specific Attenuation

Let $X(\mathbf{t})$ be the logarithm of the rain rate random field, $R(\mathbf{t})$ (mm/h) where \mathbf{t} denotes its position both in time and in a horizontal plane (x, y, t).

$$X(\mathbf{t}) = \ln R(\mathbf{t}) \quad \ln(\text{mm/h}). \quad (5.1)$$

The specific attenuation due to rain at a particular frequency and polarisation is given by the power law (see Rec. ITU-R P. 838),

$$\gamma(\mathbf{t}) = kR(\mathbf{t})^\alpha \quad (\text{dB/km}). \quad (5.2)$$

Then, the log specific attenuation may be written as:

$$\Gamma = \ln(k) + \alpha X(\mathbf{t}) \quad \ln(\text{dB/km}). \quad (5.3)$$

Therefore, if rain rate is log-normally distributed, so is the specific attenuation. The Gaussian random variables X and Γ are then completely parameterised by their means and variances, whereby,

$$\text{mean}[X(\mathbf{t})] \equiv E[X(\mathbf{t})] = \mu_X \quad \ln(\text{mm/h}), \quad (5.4)$$

$$\text{mean}[\Gamma(\mathbf{t})] \equiv E[\Gamma(\mathbf{t})] = \ln(k) + \alpha\mu_X \quad \ln(\text{dB/km}), \quad (5.5)$$

5.2. The Statistics of Rain and Rain Attenuation

$$\text{Var}[\Gamma(t)] \equiv E[\Gamma(t) - \text{mean}(\Gamma(t))]^2 = \sigma_\Gamma^2 = \alpha^2 \sigma_X^2 \ln(\text{dB}/\text{km})^2. \quad (5.6)$$

Let us consider a random variable, $Z(t)$ at two positions t_1 and t_2 . The auto-covariance is given by,

$$B_Z(t_1, t_2) \equiv \text{Cov}[Z(t_1), Z(t_2)] = E[Z(t_1)Z(t_2)] - E[Z(t_1)]E[Z(t_2)]. \quad (5.7)$$

Assume, the rain rate field R is well approximated as homogeneous and isotropic. For homogeneous fields the auto-covariance depends only on the lag, $\tau = t_1 - t_2$. Also, for homogeneous fields that are isotropic, the auto-covariance would be a scalar function of the lag magnitude $B_Z(\tau) \equiv B_Z(|\tau|)$. If both time and space coordinates are considered, then the lag magnitude is a weighted Euclidean norm of space-time [Paulson 2002].

The transformations between the auto-covariance functions of rain rate, R and specific attenuation, γ and the log variables X and Γ may be written as:

$$B_R(\tau) = \exp(2\mu_X + \sigma_X^2)(\exp(B_X(\tau)) - 1) \quad (\text{mm}/\text{hr})^2, \quad (5.8)$$

$$B_\gamma(\tau) = k^2 \exp(2\alpha\mu_X + \alpha^2\sigma_X^2)(\exp(\alpha^2 B_X(\tau)) - 1) \quad (\text{dB}/\text{km})^2. \quad (5.9)$$

5.2.2 The Statistics of Rain Attenuation

The rain attenuation on a link may be closely approximated by the integration of the specific attenuation along points on the link. This is given by,

$$A = \int_0^L \gamma(l) dl \quad (\text{dB}). \quad (5.10)$$

The temporal covariance of rain attenuation, B_A on single link in terms of the auto-covariance of specific attenuation, B_γ is then given by,

$$B_A(t) = \int_0^L \int_0^L B_\gamma(|l - l'|, t) dl dl' \quad (\text{dB}/\text{km})^2, \quad (5.11)$$

where l and l' denote the distances to points along the link. For two links of length L_1 and L_2 , the temporal cross covariance of rain attenuation would be given by,

$$B_{A_1 A_2}(t) = \int_0^{L_1} \int_0^{L_2} B_{\gamma_1 \gamma_2}(|l_1 - l_2|, t) dl_1 dl_2 \quad (\text{dB}/\text{km})^2, \quad (5.12)$$

5.2. The Statistics of Rain and Rain Attenuation

where $B_{\gamma_1\gamma_2}$ is the cross covariance of specific attenuation for the two links. The auto-correlation is then the normalised auto-covariance with $\rho(0) = 1$ given by,

$$\rho(\tau) = \frac{B(\tau)}{\sigma^2}, \quad (5.13)$$

where $\sigma^2 = B(0)$. Therefore, we can express the the correlation of attenuation for a pair of links as,

$$\rho_{A_1A_2}(\tau) = \frac{B_{A_1A_2}(\tau)}{\sqrt{B_{A_1}(0)B_{A_2}(0)}} = \frac{B_{A_1A_2}(\tau)}{\sigma_{A_1}\sigma_{A_2}}. \quad (5.14)$$

Assuming the joint distribution of log rain attenuation is normally distributed [Lin 1973; Galante 1975], then the joint probability of attenuations A_1 and A_2 being greater than some fade margin M_1 and M_2 respectively is:

$$P(\ln(A_1) > T_1, \ln(A_2) > T_2) = \int_{T_1}^{\infty} \int_{T_2}^{\infty} f(y_1, y_2) dy_1 dy_2, \quad (5.15)$$

where $T_1 = \ln(M_1)$, $T_2 = \ln(M_2)$ and $f(y_1, y_2)$ is the joint bivariate normal probability density function given by,

$$f(y_1, y_2) = \frac{(1 - \rho_{Y_1Y_2})^{-\frac{1}{2}}}{2\pi\sigma_{Y_1}\sigma_{Y_2}} \exp \left[-\frac{1}{2(1 - \rho_{Y_1Y_2})} \left\{ \left(\frac{y_1 - \mu_{Y_1}}{\sigma_{Y_1}} \right)^2 - 2\rho_{Y_1Y_2} \left(\frac{y_1 - \mu_{Y_1}}{\sigma_{Y_1}} \right) \left(\frac{y_2 - \mu_{Y_2}}{\sigma_{Y_2}} \right) + \left(\frac{y_2 - \mu_{Y_2}}{\sigma_{Y_2}} \right)^2 \right\} \right]. \quad (5.16)$$

In equation 5.15, μ_{Y_i} , σ_{Y_i} , and $\rho_{Y_1Y_2}$ are the means, variances and correlation respectively of the normal variables, Y_i given by,

$$\sigma_{Y_i}^2 = \ln \left(1 + \left(\frac{\sigma_{A_i}}{\mu_{A_i}} \right)^2 \right) \ln(\text{dB})^2, \quad (5.17)$$

$$\mu_{Y_i} = \ln \mu_{A_i} - \frac{1}{2} \ln \left(1 + \left(\frac{\sigma_{A_i}}{\mu_{A_i}} \right)^2 \right) = \ln \mu_{A_i} - \frac{1}{2} \sigma_{Y_i}^2 \ln(\text{dB}), \quad (5.18)$$

$$\rho_{Y_1Y_2} = \frac{1}{\sigma_{Y_1}\sigma_{Y_2}} \ln \left[\left\{ \rho_{A_1A_2} \sqrt{(e^{\sigma_{Y_1}^2} - 1)(e^{\sigma_{Y_2}^2} - 1)} \right\} + 1 \right], \quad (5.19)$$

where $\rho_{A_1A_2}$ is the correlation coefficient between A_1 and A_2 .

5.3. Parameter Estimation

The parameters μ_{A_i} and σ_{A_i} can be estimated from average annual attenuation distributions. If $\rho_{A_1 A_2}$ is available, then equations 5.17, 5.18, and 5.19 may be used to calculate μ_{Y_i} , $\sigma_{Y_i}^2$ and $\rho_{Y_1 Y_2}$. These parameters then completely define the average annual joint link attenuation PDF.

5.3 Parameter Estimation

The following describes the methods employed in the estimation of the first and second order moments of log attenuation. The CRIE rain radar database (see chap. 3, § 3.6) was used for the estimation of the the first and second order moments of log attenuation. Attenuation distributions for pairs of links, with lengths between 1 km and 9 km including all possible link separations between 0 & 360° were calculated, similar to the procedure described in § 4.6.

5.3.1 Parameter Estimation by Histogram Matching

It is possible to evaluate directly for the estimates of bivariate moments of log attenuation given in equations 5.17–5.19, by taking the natural logarithm of attenuation and directly evaluating for the sample moments. Such estimates are simple and fast to evaluate. For the current case this approach is not possible. Analysis of the distribution of log rain rate from the CRIE database has revealed that the distribution significantly departs from normality for log rain rates less than or equal to zero (see figure 5.1a). This is equivalent to rain rates less than 1 mm/h.

The main cause for departure of the distribution at the low rain rates is due to radar measurement and rain rate estimation errors, which start to become quite significant as the measured radar reflectivity values approach the noise threshold. Additionally, errors from the interpolation of the original PPI scan have been introduced, but such errors are not as significant compared to the former. Therefore, based on the sample distributions in figure 5.1a, direct sample estimates of the mean and variance would be biased.

For the estimates of means and variances of the log-attenuations on the link pairs, the use of a weighted best fit allows the influence of the samples that are less than a predefined cut off (or censoring point) to be minimised in the estimation.

Firstly, the natural logarithm of the attenuations was calculated and a histogram of the samples was obtained with bin widths of 0.1 ln(dB). The lower limit for the attenuation was taken to be 0.05 dB representing a minimum for the bins of -3 ln(dB). The cut-off, C_Y was chosen to be equivalent to the log-attenuation

5.3. Parameter Estimation

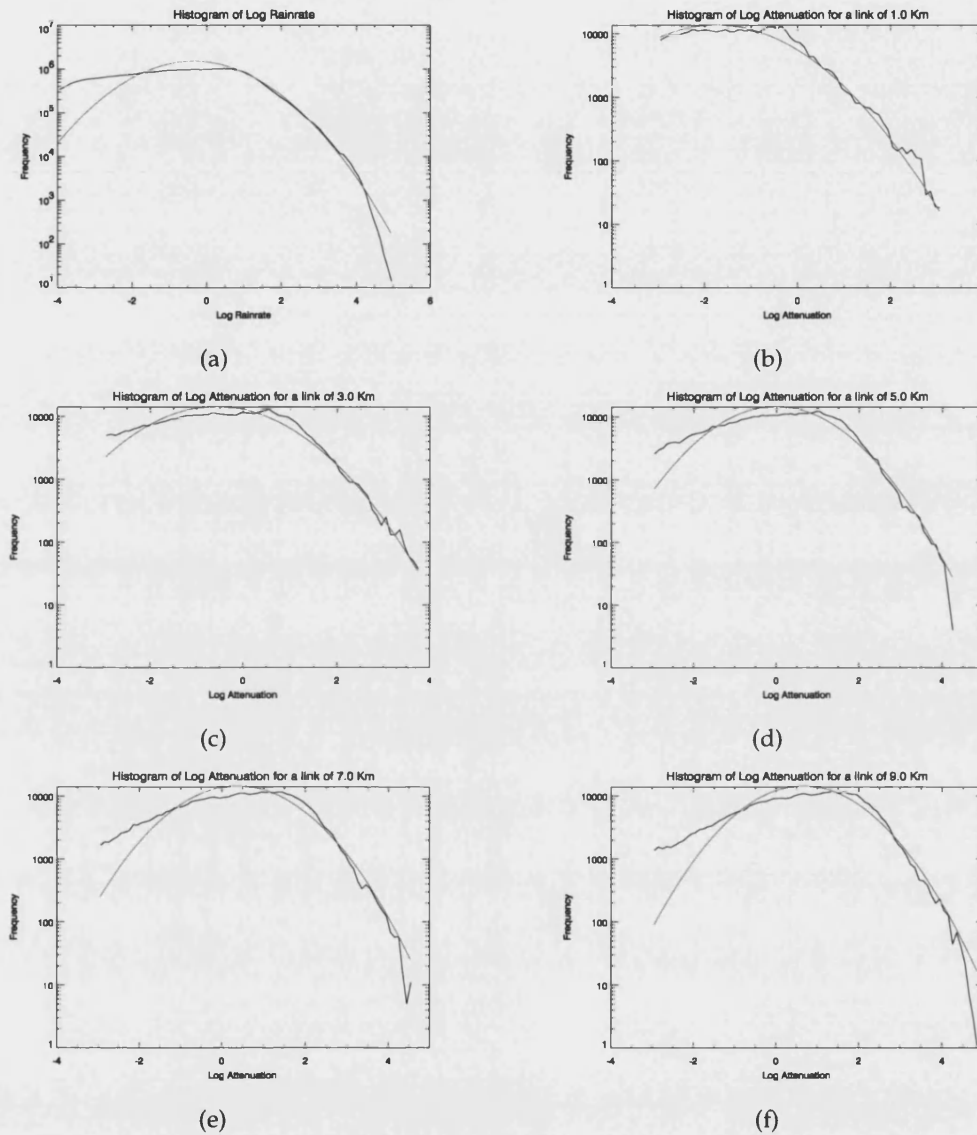


Figure 5.1: (black line) Histogram distribution of log rain rate (a) and log attenuation samples (at 42 GHz, vertical polarisation). The log attenuation samples are for paths of (b) 1 km, (c) 3 km, (d) 5 km (e) 7 km, and (f) 9 km. A weighted best-fit Gaussian distribution is shown for each distribution (red line).

5.3. Parameter Estimation

produced by a uniform rain rate of 1 mm/h across a link of length L i.e.

$$C_{\gamma} = \ln(kL) - \ln(\text{dB}), \quad (5.20)$$

where k is the constant parameter for the specific attenuation defined in equation 5.2 and varies with frequency. For the link lengths that can be simulated using the rain database, this is a good approximation to the true integrated attenuation across the link [Goddard and Thurai 1997].

The histogram is then re-binned into equi-likelihood bins i.e. the number of samples within each bin is approximately the same. This gives more weight to the tail of the distribution, ensuring that the model distribution closely approximates the log-attenuation distribution at the very low probability values. The difference between the sample and model distribution is then minimised using the chi-squared criterion,

$$\chi^2 = \sum \frac{(H_i - \hat{H}_i)^2}{\hat{H}_i}, \quad (5.21)$$

where H_i is the number of samples in the log-attenuation bin i i.e. $[i, i + 1] \Delta x$; \hat{H}_i is the number of samples expected if the sample is drawn from a normal distribution of mean μ_{γ_i} and variance $\sigma_{\gamma_i}^2$. Figures 5.1b to 5.1f show the best fit Gaussian distributions that have been estimated using such an approach. It can be seen that the resulting best-fit well approximates the sample distribution, even up to extreme occurrence values at the tails. Table 5.1 also lists the estimated means and variances of the links between 1–9 km for frequencies ranging 20–50 GHz.

Also, the moments of the log rain rate distribution (see figure 5.1a) were obtained from the rain radar database. The mean and variance of the log rain rate distribution, X was estimated to be $\mu_X = -0.52 \ln(\text{mm/h})$ and $\sigma_X^2 = 1.37 \ln(\text{mm/h})^2$ respectively using the same technique as highlighted above for the log-attenuation distributions. The estimated mean value is lower than what has been reported by Paulson & Gibbins [2000], using rain gauge data for the same locality. They report $\mu_X = -0.4 \ln(\text{mm/h})$.

The difference in the two estimates is largely due to the difference in spatial sampling and averaging introduced in the measurement by the two instruments. The rain sample volume of the radar is orders of magnitude greater than the rain sample volume of a rain gauge. Additionally, the effective censoring from the two data sets is different.

5.3. Parameter Estimation

Table 5.1: Link estimates of the mean μ_{Y_i} $\ln(\text{dB})$, and variance $\sigma_{Y_i}^2 \ln(\text{dB})^2$, of log-attenuation with increase in frequency. For each link length, the top row correspond to estimated values of the mean, while the values along the bottom are the estimated variances

L (km)	20	24	28	32	36	40	42	44 (GHz)
1	-3.461	-3.030	-2.678	-2.359	-2.071	-1.843	-1.738	-1.618
	1.452	1.434	1.413	1.377	1.333	1.303	1.302	1.275
1.5	-3.028	-2.613	-2.263	-1.928	-1.656	-1.426	-1.287	-1.199
	1.432	1.417	1.400	1.361	1.322	1.298	1.262	1.266
2	-2.707	-2.304	-1.930	-1.615	-1.349	-1.098	-0.9992	-0.8942
	1.402	1.398	1.359	1.340	1.318	1.279	1.268	1.239
2.5	-2.464	-2.055	-1.697	-1.355	-1.110	-0.8655	-0.7639	-0.6661
	1.411	1.391	1.352	1.310	1.293	1.277	1.252	1.241
3	-2.260	-1.871	-1.494	-1.210	-0.9095	-0.6621	-0.5651	-0.4688
	1.395	1.378	1.340	1.324	1.289	1.241	1.243	1.222
3.5	-2.110	-1.676	-1.330	-1.023	-0.7459	-0.5165	-0.3853	-0.2876
	1.393	1.357	1.335	1.304	1.278	1.245	1.227	1.209
4	-1.959	-1.540	-1.173	-0.8594	-0.6044	-0.3483	-0.2686	-0.1451
	1.378	1.360	1.317	1.305	1.267	1.234	1.228	1.203
4.5	-1.813	-1.416	-1.061	-0.7657	-0.4792	-0.243	-0.1260	-0.0248
	1.368	1.349	1.319	1.319	1.263	1.239	1.228	1.200
5	-1.708	-1.282	-0.9314	-0.6342	-0.3534	-0.1237	0.000	0.0839
	1.368	1.335	1.297	1.280	1.248	1.220	1.200	1.199
5.5	-1.606	-1.173	-0.8220	-0.5092	-0.2320	-0.0047	0.0894	0.1947
	1.358	1.317	1.291	1.260	1.226	1.217	1.209	1.190
6	-1.494	-1.083	-0.7168	-0.4170	-0.1335	0.0905	0.195	0.2998
	1.340	1.312	1.295	1.257	1.224	1.198	1.189	1.178
6.5	-1.384	-0.9928	-0.6292	-0.3099	-0.0400	0.1999	0.2796	0.4060
	1.324	1.314	1.275	1.249	1.224	1.193	1.195	1.139
7	-1.304	-0.8830	-0.5471	-0.2267	0.0428	0.2773	0.3791	0.4853
	1.314	1.290	1.262	1.238	1.211	1.192	1.170	1.160
7.5	-1.211	-0.8008	-0.4538	-0.1398	0.1175	0.3539	0.4716	0.5687
	1.315	1.284	1.270	1.232	1.201	1.167	1.148	1.149
8	-1.147	-0.7324	-0.3674	-0.0449	0.1787	0.4395	0.5505	0.6342
	1.307	1.286	1.246	1.209	1.200	1.171	1.142	1.134
8.5	-1.083	-0.6682	-0.3156	0.0010	0.2617	0.4935	0.6236	0.7049
	1.293	1.272	1.239	1.211	1.183	1.151	1.142	1.128
9	-1.012	-0.6063	-0.2412	0.0683	0.3461	0.5720	0.6738	0.7711
	1.296	1.259	1.227	1.215	1.170	1.158	1.298	1.116

5.3. Parameter Estimation

The estimation of the correlation of the log attenuation for pairs of links introduces further complications. The use of a two dimensional version of the best-fit employed for the estimation of the means and variances is not guaranteed to always converge to a consistent estimate for the correlation. This is due to less than 25% of the bivariate probability density being effectively used during the parameter estimation process as a result of censoring.

5.3.2 Maximum likelihood Parameter Estimation

An alternative approach which is consistent and unbiased in the estimates of the parameters of the bivariate distribution of log attenuation is using the framework of maximum likelihood estimation. In such a technique, the parameter estimates are based on direct analysis of the sample values, to maximise an objective function (likelihood) compared to fitting to an empirical distribution.

The framework of the method allows application to data sets which contain proportions of unreliable and/or corrupt samples. In this case, the absolute values of the samples below a certain threshold are not used in the calculation of the likelihood. Instead, their contribution to the final likelihood is estimated based on the number of samples that fall below the threshold or cut-off point.

General theory for the estimation of parameters from a bivariate Normal distribution in the presence of censoring or cutoff points

The Gaussian random variable, Z , which is equivalent to $\ln(A)$, the natural logarithm of attenuation is only valid within certain limits. In the univariate case the left and right cutoff points are x_l and x_r respectively. In the bivariate case the additional cutoff points are y_l and y_r respectively. Let us define a new random variable X , such that $X = \max(x_l, \min(x_r, Z))$, which becomes the censored observation with $x^T = [x, y]$.

The feature space for the censored observations is given as χ (see figure 5.2). This can be regarded as the union of nine disjoint regions; the open set χ_0 in which the observations are uncensored on both variates, the four line segments $\chi_1, \chi_2, \chi_3, \chi_4$ on which the observations are censored on one variate, and the segments $\chi_5, \chi_6, \chi_7, \chi_8$ at which the observations are censored on both variates.

The maximum likelihood estimate (MLE) of the parameters, $\theta = [\mu_1, \mu_2, \sigma_1, \sigma_2, \rho]$ is given by the maximisation of the log likelihood,

$$c(\theta) = \max \ln (L(\theta)), \quad (5.22)$$

5.3. Parameter Estimation

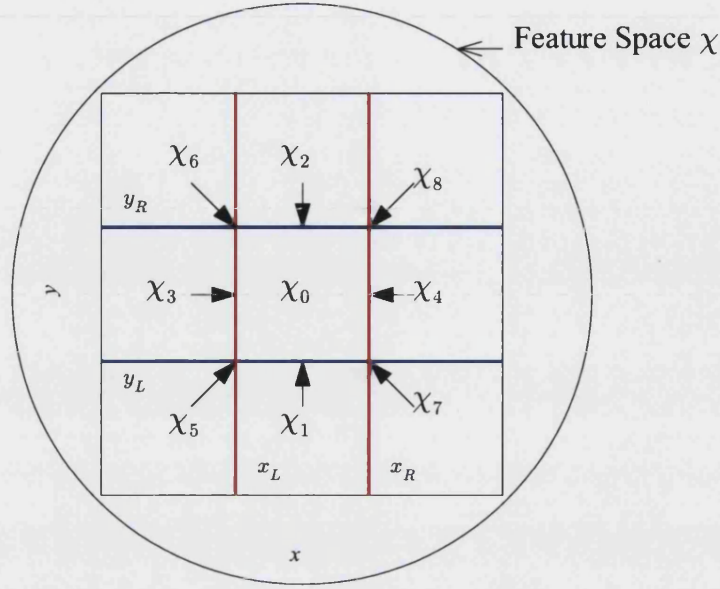


Figure 5.2: The different regions of the two-dimensional feature space induced by censoring where $L(\theta)$ is the likelihood function and is given by

$$L(\theta; \mathbf{x}) = \prod_{i=0}^n f(\mathbf{x}; \theta), \quad (5.23)$$

and $f(\mathbf{x}; \theta)$ is the density of \mathbf{x} .

Then for the problem under consideration, the likelihood function can be written as follows,

$$L(\theta; \mathbf{x}) = \prod_{i=1}^n \sum_{j=0}^8 I[\mathbf{x} \in \chi_j] P(\mathbf{x} \in \chi_j) f(\mathbf{x} | \mathbf{x} \in \chi_j), \quad (5.24)$$

where $I[\cdot]$ is an indicator function to denote which segment \mathbf{x} falls into. $P(\mathbf{x} \in \chi_j)$ represents the prior probability of an observation in the region χ_j and $f(\mathbf{x} | \mathbf{x} \in \chi_j)$ is the conditional distribution of \mathbf{x} , given that it is in the region χ_i . Noting that,

$$P(\mathbf{x} \in \chi_j) f(\mathbf{x} | \mathbf{x} \in \chi_j) = P(\mathbf{X} = \mathbf{x} \cap \mathbf{X} \in \chi_j), \quad (5.25)$$

5.4. Auto-correlation of Log-attenuation Estimates

from Bayes theory. Then equation 5.24 simplifies to,

$$L(\theta; \mathbf{x}) = \prod_{i=1}^n \sum_{j=0}^8 I[\mathbf{x} \in \chi_j] P(\mathbf{X} = \mathbf{x} \cap \mathbf{X} \in \chi_j). \quad (5.26)$$

The probability, $P(\mathbf{X} = \mathbf{x} \cap \mathbf{X} \in \chi_0)$ is simply the bivariate PDF. The probability, $P(\mathbf{X} = \mathbf{x} \cap \mathbf{X} \in \chi_j)$ for each line segment can be calculated using the relevant integral, for example on χ_1 , writing $\mathbf{x}^T = [x, y]$,

$$f(x; y = y_1) = f(z_1; z_2 \leq y_1) = \int_{z_2=-\infty}^{y_1} f(z_1, z_2) dz_2, \quad (5.27)$$

this becomes, after some re-arrangement and integration,

$$f(z_1; z_2 \leq y_1) = \phi\left(\frac{z_1 - \mu_1}{\sigma_1}\right) \Phi\left(\frac{1}{\sqrt{1 - \rho^2}} \left\{ \frac{y_1 - \mu_2}{\sigma_2} - \rho \frac{z_1 - \mu_1}{\sigma_1} \right\}\right), \quad (5.28)$$

where $\phi(\cdot)$ denotes the PDF of a univariate standard normal distribution and $\Phi(\cdot)$ denotes the CDF of a univariate standard normal. So,

$$P(\mathbf{X} = \mathbf{x} \cap \mathbf{X} \in \chi_1) = \phi\left(\frac{x_1 - \mu_1}{\sigma_1}\right) \Phi\left(\frac{1}{\sqrt{1 - \rho^2}} \left\{ \frac{y_1 - \mu_2}{\sigma_2} - \rho \frac{x_1 - \mu_1}{\sigma_1} \right\}\right). \quad (5.29)$$

Similar results can be obtained for χ_2, χ_3 and χ_4 . For the segments $\chi_j, j = 5, \dots, 8$, $P(\mathbf{X} = \mathbf{x} \cap \mathbf{X} \in \chi_j)$ is the probability that an observation has been censored on both variates and is found from the associated bivariate Normal CDF. Since in this case, the observations have only been left censored, for the right cutoff points, $x_r = y_r = \infty$. Therefore using equation 5.29 and 5.26 the maximum likelihood estimate, θ can be obtained numerically from the censored data.

An extended discussion on the framework can be found in various sources, in particular [Ord et al. 2004; Little and Rubin 1987].

5.4 Auto-correlation of Log-attenuation Estimates

Estimated values for the correlation of log attenuation as a function of link length, link separation and frequency of operation from rain radar data are presented.

Figure 5.3 shows the variation of the correlation estimates derived using the maximum likelihood method described in § 5.3.2, with angular separation be-

5.4. Auto-correlation of Log-attenuation Estimates

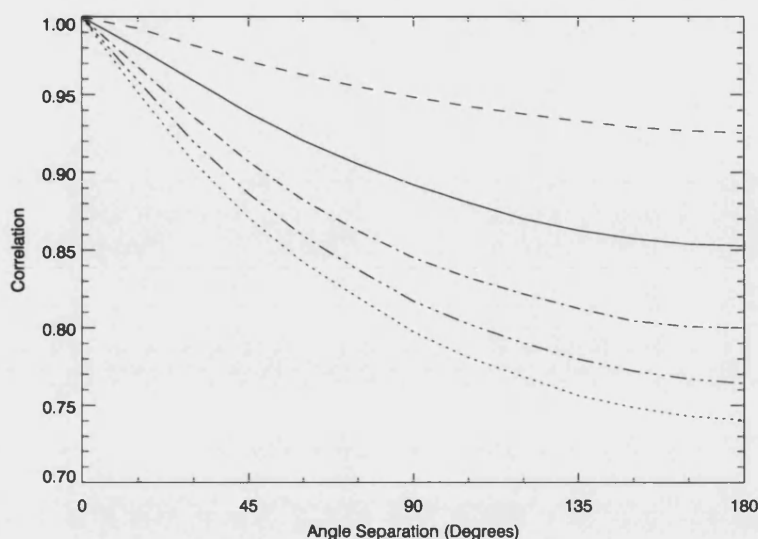


Figure 5.3: Plots indicating the correlation of log-attenuation for symmetric link lengths. Plots from top to bottom are for 1 (---), 3 (-), 5 (- ·), 7 (- · ·) and 9 (· · ·) kilometres.

tweens 0° and 180° and link lengths from 1 km and 9 km. The variation of the correlation between 180° and 360° link separations has not been shown as the correlation exhibits symmetry about 180° .

The correlation of the link pair is generally high (i.e. greater than 0.75), irrespective of link length and separation angle. At maximum link separation (i.e. 180°), the correlation of log-attenuation varies between 0.93 and 0.74 for link pair lengths between 1 km and 9 km respectively. When the correlation of log-attenuation is transformed to the correlation of attenuation, the lower bound is 0.6. The high correlation experienced especially for short links is due to the links converging at one end and still being within the typical de-correlation distance of rain.

The relatively high correlation between the links also indicates that, irrespective of link separation, most rain events effect both links. Correlation for individual rain events is expected to exhibit large variation from this mean value depending on the type of rain and event orientation.

For asymmetric links (see figure 5.4), the plots of correlation as a function of angle have an offset with a reduction of the correlation when there is no separation between the links. Analysis shows that this offset is directly proportional to the ratio of variances for the individual links (see § 5.5.1). Hence, the larger the

5.4. Auto-correlation of Log-attenuation Estimates

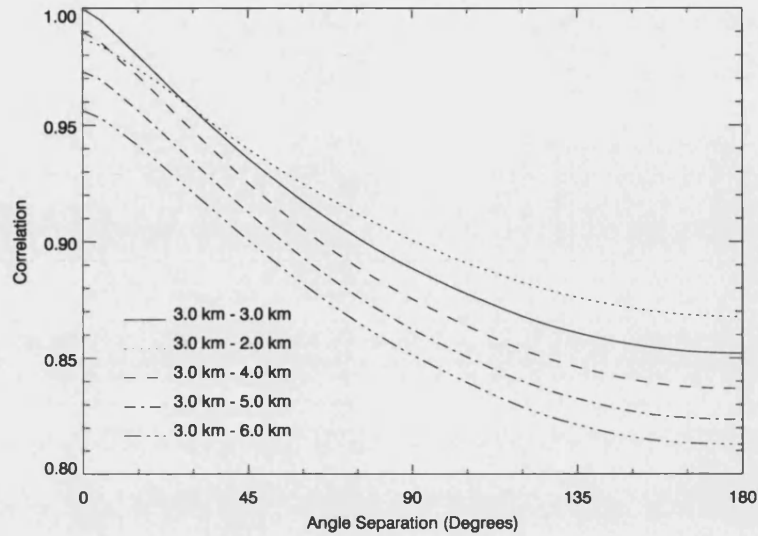


Figure 5.4: Plots indicating the correlation of log-attenuation for asymmetric links lengths.

link asymmetry, the larger the offset obtained compared to the symmetrical case. Furthermore, as expected from theory, the change in the frequencies of both links across the range 20–50 GHz has no measurable effect on correlation as seen in figure 5.5.

5.4.1 Theoretical Comparisons

Although no reported results on the correlation of attenuation or log-attenuation, with respect to route diverse links have been found in the literature, it is possible to evaluate the correlation numerically, based on certain assumptions with regards to the correlation of specific attenuation.

Consider the link pair of length L_{D1} and L_{D2} separated over some angle θ , given in figure 5.6. l_1 and l_2 are the elemental link distances for a point on each of the links. While, l'_1 and l'_2 represent the translation of that point by distances d_{11} and d_{22} respectively. This is given by,

$$d_{11} = |l'_1 - l_1|, \quad (5.30)$$

$$d_{22} = |l'_2 - l_2|. \quad (5.31)$$

We can also express the distance between the pair of points on the two links using

5.4. Auto-correlation of Log-attenuation Estimates

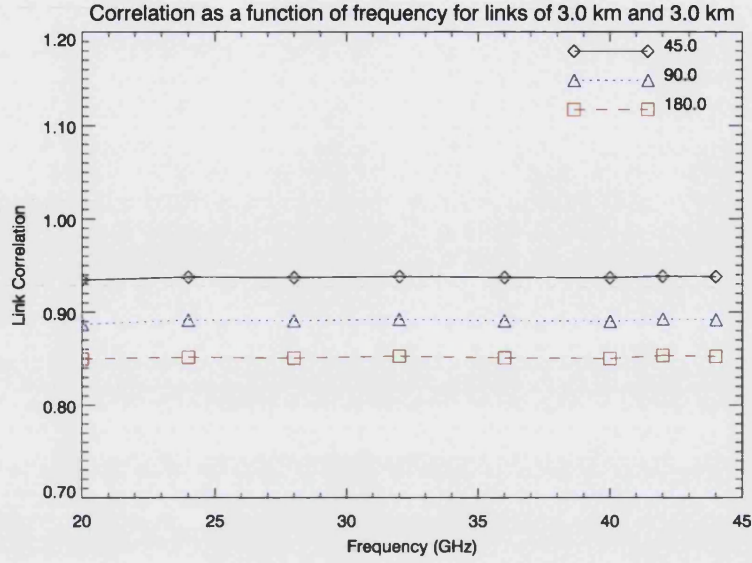


Figure 5.5: Correlation of log-attenuation for symmetric link lengths of 3 km as a function of frequency at link separations of 45, 90 and 180 degrees.

the cosine rule:

$$d_{12} = \sqrt{l_1^2 + l_2^2 - 2l_1l_2 \cos \theta}, \quad (5.32)$$

where θ is the angle between the two links.

The correlation of attenuations A_1 and A_2 on the two converging links can be denoted as [Crane and Horng Chung 1989; Kanellopoulos and Ventouras 1993],

$$\rho_{A_1 A_2} = \frac{H_{12}}{\sqrt{H_{11}H_{22}}}, \quad (5.33)$$

where

$$H_{12} = \int_0^{L_1} \int_0^{L_2} \rho_{\gamma_1 \gamma_2}(l_1, l_2) dl_1 dl_2, \quad (5.34)$$

$$H_{11} = \int_0^{L_1} \int_0^{L_1} \rho_{\gamma_1}(l_1, l'_1) dl_1 dl'_1, \quad (5.35)$$

$$H_{22} = \int_0^{L_2} \int_0^{L_2} \rho_{\gamma_2}(l_2, l'_2) dl_2 dl'_2. \quad (5.36)$$

The formulation in equations 5.33–5.36 can be shown to be equivalent to equation 5.14 in § 5.2 with some simple algebra. It is also applicable to the site diversity case where there are parallel links separated by some distance. In equations 5.34,

5.4. Auto-correlation of Log-attenuation Estimates

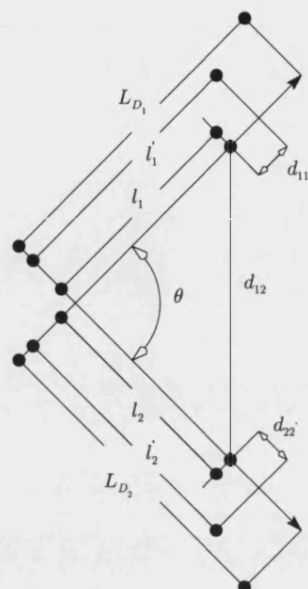


Figure 5.6: Configuration of a route diversity link pair (L_{D1} , L_{D2}) with a common node separated by an angle θ .

5.35 and 5.36, ρ_γ is either the correlation of specific attenuation for points along the link path or for points along a pair of links.

Lin [1975] has postulated a composite expression for the spatial correlation of specific attenuation given by,

$$\rho_\gamma = \frac{G}{\sqrt{G^2 + d^2}}, \quad (5.37)$$

where G is the characteristic distance in kilometres at which $\rho_\gamma = \frac{1}{\sqrt{2}}$ and is weakly dependent on frequency between 10 to 60 GHz. Typical values of G should range between 0.75 and 3 km. Figure 5.7 shows the variation of the correlation function of equation 5.37 assuming a characteristic distance of 1.5 km and over distances that are relevant to this investigation.

Ihara et al. [1986] and Morita & Higuti [1978] have shown that within the frequencies of 20–50 GHz, the approximation that the correlation of specific attenuation being equal to the correlation of rain rates, $\rho_\gamma \simeq \rho_R$ can be used for the estimation of the attenuation distribution. This is due to the values of the parameter α within the specific attenuation function (see ITU-R P. 838) being close to 1. This implies that γ is approximately linearly proportional to R between 20–50

5.4. Auto-correlation of Log-attenuation Estimates

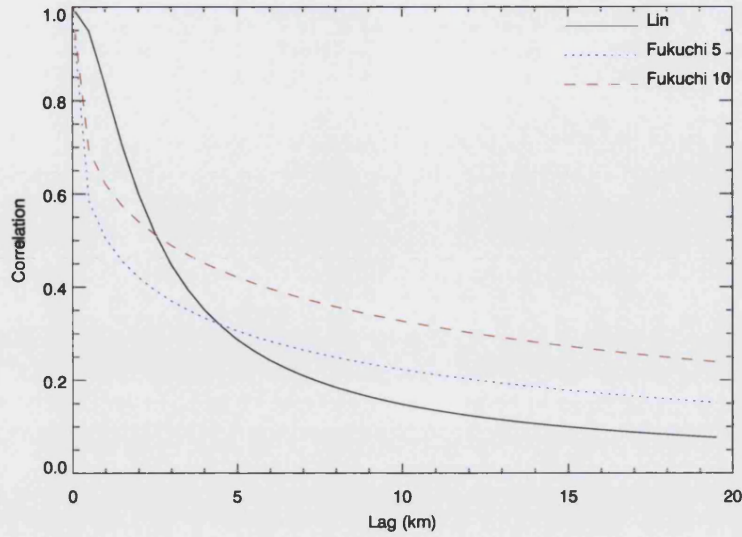


Figure 5.7: Variation of correlation of rain rate (Fukuchi) and correlation of specific attenuation (Lin) functions with distance. Functions presented by Fukuchi [1988] for rain rate integration times of 5 min (Fukuchi 5) and 10 min (Fukuchi 10) are also shown.

GHz.

Hence we can use expressions for the spatial correlation of rain rate reported in the literature [Fukuchi 1988; Morita and Higuti 1978; Capsoni and Matricciani 1982; Goldhirsh 1982] as a good approximation for the spatial correlation of specific attenuation. For the UK, Fukuchi [1988] has presented results on the spatial correlation of rain rate for a network of rain gauges with an integration time of 5 min, over a 5 year period given by:

$$\rho_{\gamma} \simeq \rho_R = \exp(-0.685d^{0.343}). \quad (5.38)$$

This is shown in figure 5.7 (denoted as Fukuchi 5) together with results reported from analysis of 10 min rain rate integration times. Expectantly, correlations derived from longer integration times exhibit higher values with distance. It also can be seen that the correlation function predicted by Lin is quite high compared to the observations by Fukuchi over distances less than 3 km but decreases rapidly with the correlation being less than 0.1 for distances greater than 10 km.

Therefore, we can use equations 5.34, 5.35 and 5.36 in combination with equations 5.33 and 5.19 to estimate the correlation of log attenuation from a knowledge

5.4. Auto-correlation of Log-attenuation Estimates

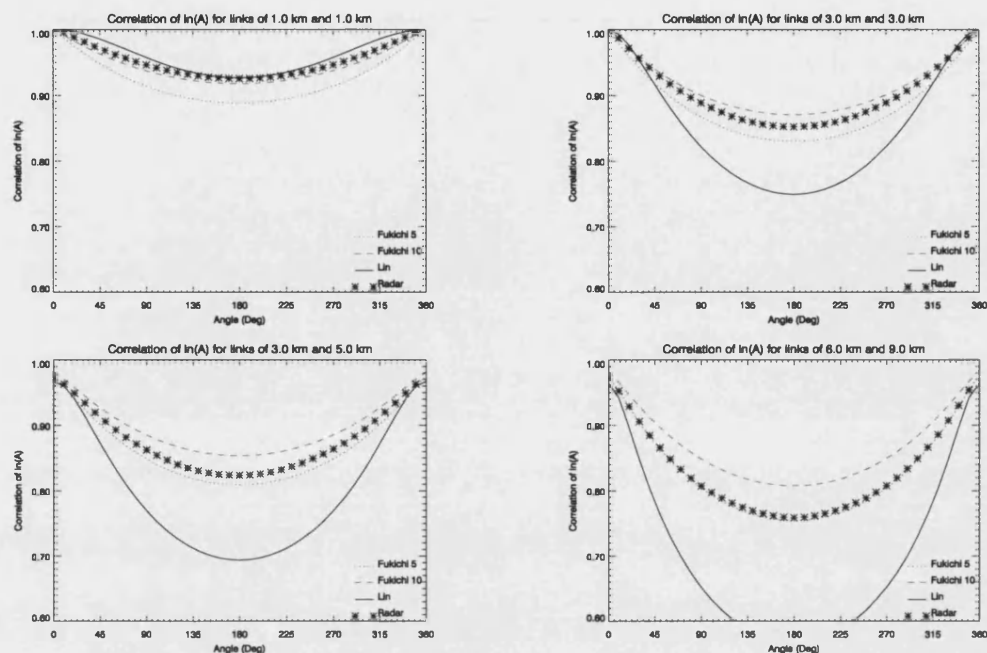


Figure 5.8: Comparison of correlation estimates of log attenuation from radar (\times , symbol) and theory using correlation functions from Lin (—, solid) and Fukuchi (5 and 10 minute integration times, - - -, dashed)

of the correlation of the specific attenuation.

Figure 5.8 shows comparisons between theoretical and radar derived correlations of log attenuation as a function link separation for several link configurations. In the calculation of Lin's correlation of specific attenuation function, a characteristic distance of 1.5 km has been assumed. It can be seen that the theoretically derived estimates for small link separations (i.e. less than 30°), using all three functions agree closely with radar derived estimates. But at the larger link separations, the use of the function postulated by Lin deviates by quite a large amount, especially for the longer link lengths.

Here the particular type of spatial structure of rain plays a significant role. The correlation on shorter links is largely affected by convective rain cells while for the longer link lengths, stratiform rain has a significant contribution to the correlation at the larger link separations. The expression given by Fukuchi (derived from 5 min rain rates) agrees well for both short and long link lengths irrespective of the link separation since it is obtained from data that contains both stratiform and convective events. In contrast, Lin's function more appropriately describes the correlation for a convective rain cell and therefore the attenuations on the longer

5.5. Generalised Route Diversity Model

links exhibit less correlation.

The observations seem to confirm the hypothesis that the major determinant of the correlation of attenuation observed for a pair of links, is the relative occurrence of stratiform and convective rain events, which occur over a link pair. Hence, networks within regions that have similar proportions of rain types would exhibit similar correlation values, irrespective of the difference in the rain rate cumulative distribution within each region.

The use of a rain rate correlation function derived from longer integration times (10 min) seems to have little or no effect on the correlation of log-attenuation for link pair lengths less than 3 km. Longer link pairs experience higher correlations with 10 min integration time.

5.5 A Generalised Bivariate Gaussian Route Diversity Model (GBGDM)

As stated earlier, the diversity model formulation presented within chap. 4 imposed certain restrictive limitations to its use. Both link margins had to be identical irrespective of the difference in link length. Its advantage was it provided a simple “back of the envelope” procedure for the evaluation of diversity, suitable for initial assessment of performance gains to be obtained before further in-depth analysis.

A new formulation is presented that removes the same-margin limitation and is based on the fundamental assumption that the marginal and joint attenuation distributions are log-normal with a simple function describing the correlation between the link pair. Furthermore, besides the calculation of joint statistics on route diverse networks, it allows for the evaluation of conditional probabilities.

5.5.1 Correlation Function

Based on the previous analysis and observations, regressions of the correlation of log-attenuation on pairs of links as a function of link length and link separation were carried out. Several candidate models were sought, but a reciprocal sinusoidal model was found to provide the best approximation:

$$\rho(L_1, L_2, \theta)_{\gamma_1, \gamma_2} = \frac{1}{r_0 + r_1 \sin\left(\frac{\theta}{2}\right)} \quad 0 \leq \theta \leq 360, \quad (5.39)$$

5.5. Generalised Route Diversity Model

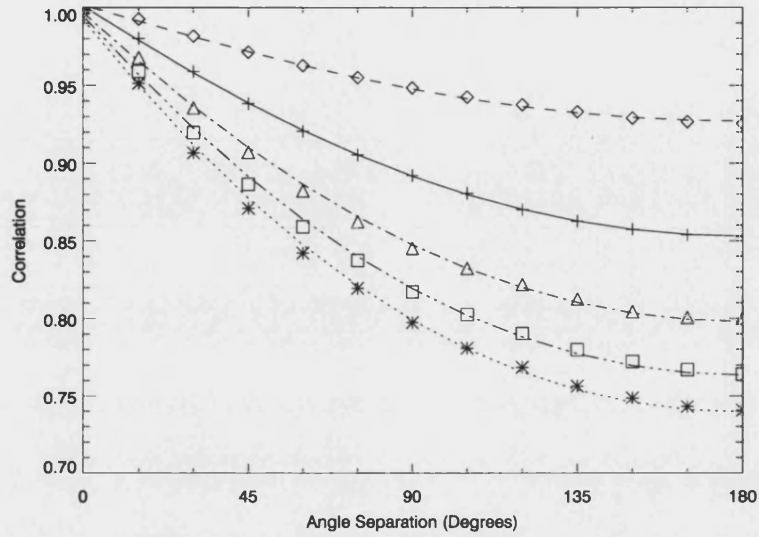


Figure 5.9: Regressions of the correlation of log attenuation for links lengths of 1 (---), 3 (-), 5 (-·-), 7 (-· ·) and 9 (...) kilometres.

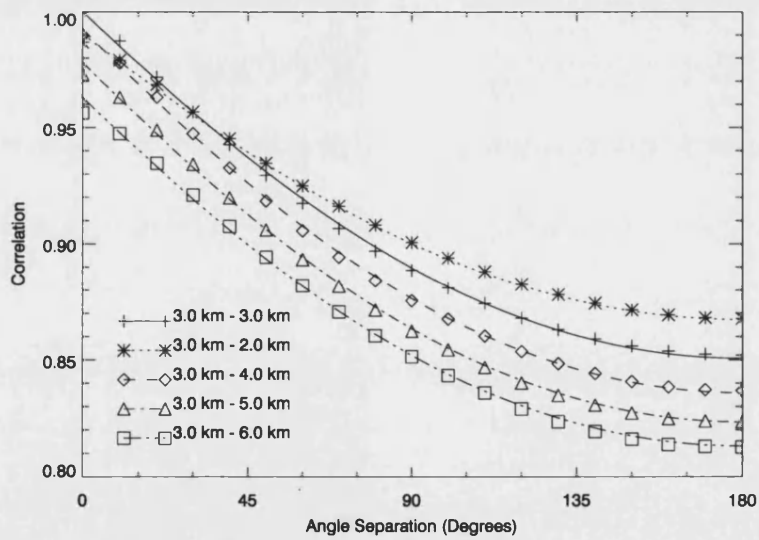


Figure 5.10: Regressions of the correlation of log attenuation for asymmetric links.

5.5. Generalised Route Diversity Model

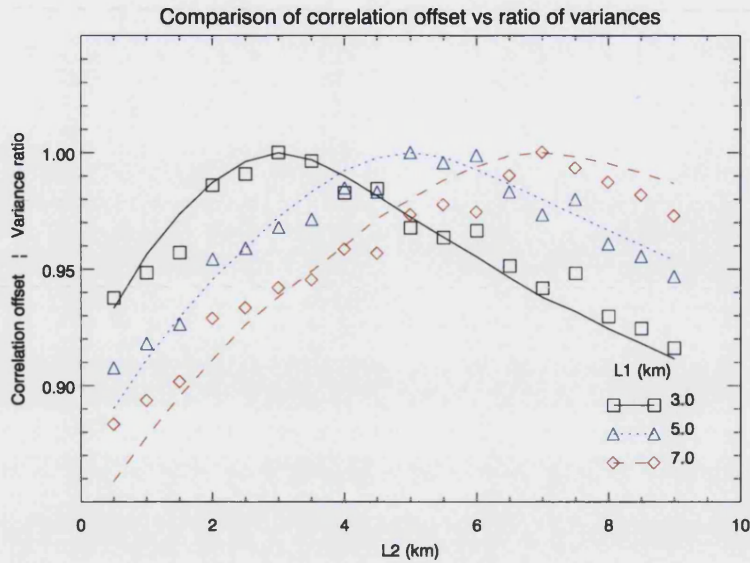


Figure 5.11: Comparisons of the suitability of the ratio of variances (symbols) to approximate the correlation offset (lines) for links pairs L_1 & L_2 .

where L_1 and L_2 are the respective link lengths in km, θ is the link separation and the parameters r_i are dependent on the link lengths. If we consider the denominator of equation 5.39 with $\sin(\frac{\theta}{2})$ being a variable, then the denominator represents a polynomial function with r_0 as a constant term (which is the reciprocal to the correlation offset) and r_1 as the slope. Analysis has shown that r_0 can to a very good approximation be expressed as the ratio of variances of the link pair given by

$$r_0 = \frac{\max(\sigma_{Y1}^2, \sigma_{Y2}^2)}{\min(\sigma_{Y1}^2, \sigma_{Y2}^2)}. \quad (5.40)$$

This is shown in figure 5.11.

The model is valid for link lengths between 1 km and 9 km operating at the same frequency in the range of 20–50 GHz. Figures 5.9 and 5.10 show the regressions for symmetric and asymmetric link lengths respectively, with the parameter r_1 for both symmetric and asymmetric links listed in table 5.2. In all cases, the regressions to the data were very good, with the difference between the model and observations being less than 1%.

5.5. Generalised Route Diversity Model

Table 5.2: Parameters of the proposed log attenuation correlation model for several link configurations.

$L_1(\text{km})$	$L_2(\text{km})$	r_1	$L_1(\text{km})$	$L_2(\text{km})$	r_1
1	1	0.0828	5	5	0.2517
	2	0.0902		6	0.2610
2	2	0.1332		7	0.2652
	3	0.1433		8	0.2665
	4	0.1449		9	0.2676
3	3	0.1758	6	6	0.2791
	4	0.1888		7	0.2890
	5	0.1922		8	0.2937
	6	0.1930		9	0.2945
4	4	0.2169	7	7	0.3063
	5	0.2287		8	0.3159
	6	0.2315		9	0.3186
	7	0.2320	8	8	0.3316
	8	0.2326		9	0.3386
			9	9	0.3506

5.5.2 Procedure for Calculation

A generalised procedure is presented which can be used to obtain the joint probability distribution for any set of link margins for link configurations between 1 and 9 km.

1. Define the link lengths L_1 and L_2 , and the separation θ between the links for the link configuration of interest.
2. Obtain the means μ_{A1}, μ_{A2} and variances $\sigma_{A1}^2, \sigma_{A2}^2$ of the individual links from measured attenuation distributions or using existing ITU-R recommendations (Rec. ITU-R P. 530).
3. Equations 5.17 and 5.18 can then be used to obtain the means μ_{Y1}, μ_{Y2} and variances $\sigma_{Y1}^2, \sigma_{Y2}^2$ of the log attenuation distribution in terms of the moments of the attenuation distribution obtained in step 2.
4. Using equations 5.39, 5.40 and table 5.2, obtain the correlation of log attenuation ρ_{Y1Y2} for the link lengths and angular separation. The values of the parameter r_1 listed do not depend on the designation of which link is the reference link. Hence, the notations L_1 and L_2 in table 5.2 can readily be swapped.

5.5. Generalised Route Diversity Model

5. Equations 5.16 and 5.15 can now be used to obtain the joint probability. For the numerical evaluation of the double integrals of the bivariate normal PDF, several techniques are available to obtain fast and very accurate results with very little implementation complexity [Drezner and Wesolowsky 1990; Owen 1956].
6. Finally, statistics of diversity advantage (i.e. gain and improvement) can be calculated based on the knowledge of the marginal and joint probability statistics.

5.5.3 Model Performance

Based on the regressions and the procedure for estimation of the joint probability distribution outlined earlier, the diversity gain for several link configurations have been compared.

Figures 5.12 and 5.13 show the comparisons between the diversity values at link separations of 30, 45, 90 and 180° for a selection of link length combinations. Here the diversity statistics show the balanced diversity case where the fade margins on the links result in both links having equal exceedance probability e.g 0.01% (i.e balanced diversity case) and hence would not be the same for asymmetric links. The model predictions yield smooth variations compared to the radar derived statistics which do not due to sampling statistics.

It can be seen that the agreement between the model and radar data is good for the exceedance time percentages of interest even for the very low probabilities that constitute the tail of the joint distribution. Figure 5.14 also shows the distribution of root mean square errors (RMSE) between the model and data. Where

$$RMSE = \sqrt{\frac{1}{n} \sum_{\theta=0}^{360} \left(\frac{Div_{GBGDM}(L_1, L_2, \%, A, f) - Div_{radar}(L_1, L_2, \%, A, f)}{Div_{radar}(L_1, L_2, \%, A, f)} \right)^2},$$

and Div are the diversity values for both diversity gain and improvement. The graph includes statistics from both diversity gain and improvement and represent 1286 link configurations that were compared. It can be seen that the model prediction error in the vast majority of cases is less than 30%.

5.5. Generalised Route Diversity Model

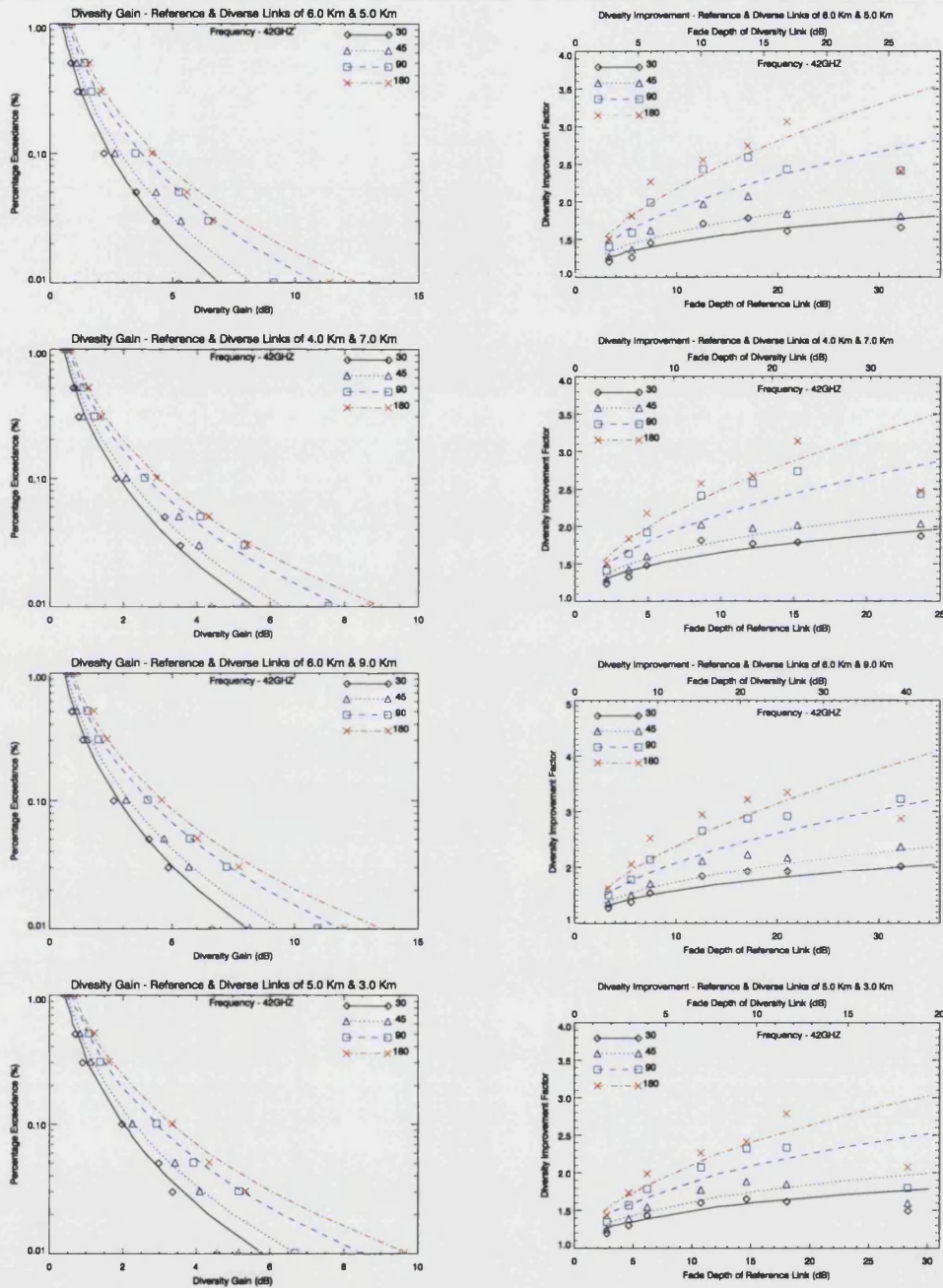


Figure 5.12: Comparisons of GBGDM (lines) vs radar (symbols) derived diversity advantage statistics for various link configurations and separations. The plots on the left column are for diversity gain while the right column is for diversity improvement. The diversity improvement graphs also include an axis the corresponding fade depth for the diversity link for some fade depth on a reference link.

5.5. Generalised Route Diversity Model

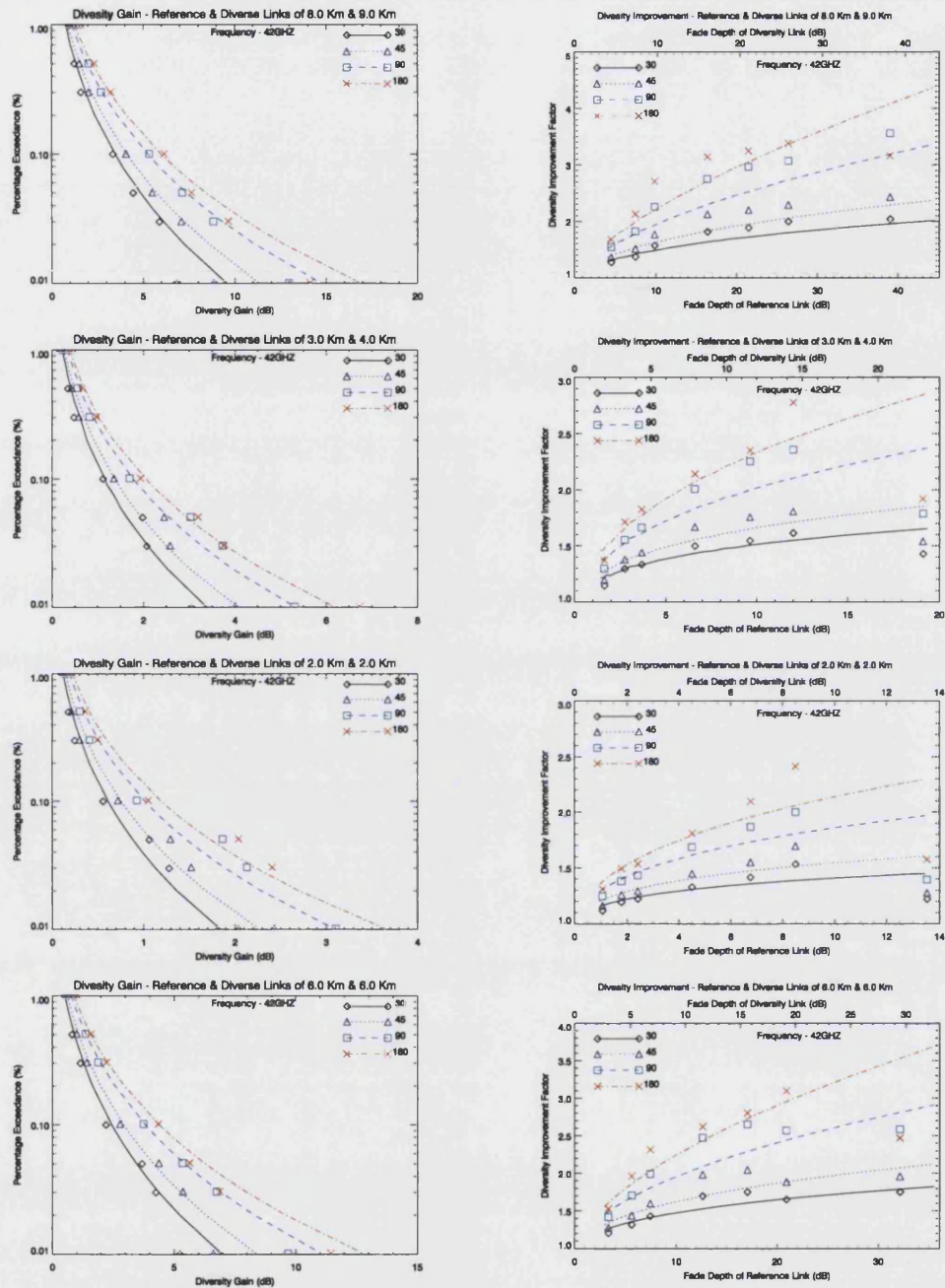


Figure 5.13: Comparisons of GBGDM (lines) vs radar (symbols) derived diversity advantage statistics for various link configurations and separations. The plots on the left column are for diversity gain (dB) while the right column is for diversity improvement. The diversity improvement graphs also include an axis the corresponding fade depth for the diversity link for some fade depth on a reference link.

5.5. Generalised Route Diversity Model

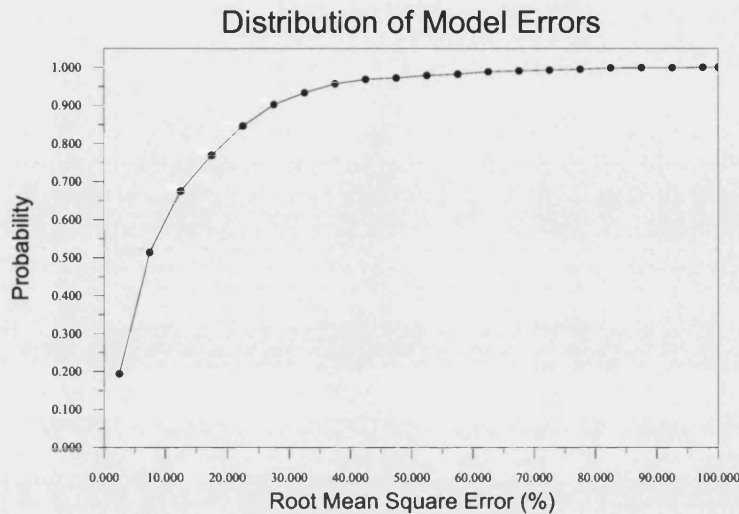


Figure 5.14: Cumulative distribution of model root mean square (RMSE) errors showing the probability of the error being less than abscissa.

5.5.4 Considerations

Effect of integration time

We have formulated a correlation model after comparisons with theory. As shown, the estimated values agree quite well with correlation values derived from 5 minute rain rate integration times. But as we have already indicated, rain rates for integration times of 1 minute or less are commonly sought and used for radio propagation. Hence it is left to answer the question: To what appreciable degree would diversity statistics using the correlation model approximate 1 minute derived diversity statistics?

Naturally for a decrease in integration time, the correlation of log attenuation would also decrease. The effect of shorter integration times would be most noticeable in the diversity statistics for long link pairs (greater than 3 km) and the larger link separations (greater than 45°). The greatest change would occur at maximum link separation (i.e. 180°) and the maximum applicable link length, which is 9 km.

Let us assume that for an integration time of 1 minute, the minimum bound observed for the correlation of log attenuation at 180° reduces by 0.1 from 0.74–0.64. This seems a reasonable assumption to make since it represents more than

5.6. Concluding Remarks

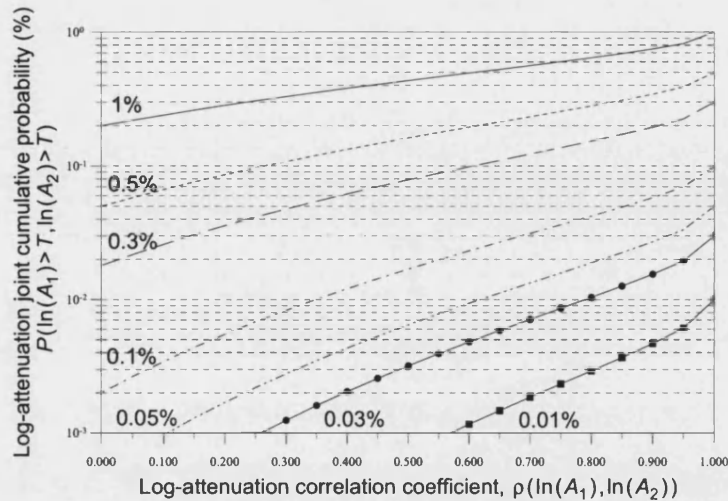


Figure 5.15: Relationship between log-attenuation correlation coefficient $\rho(\ln(A_1), \ln(A_2))$ and joint log-attenuation cumulative probability for different marginal cumulative probabilities. The statistics are for a link pair with $\mu_{Y_1, Y_2} = 0 \text{ ln(dB)}$ and $\sigma_{Y_1, Y_2} = 1 \text{ ln(dB)}^2$.

40% of the variation of the minimum for link lengths between 1–9 km.

With reference to figure 5.15, we can show the likely variation that the joint cumulative probability would undertake for such a reduction. Based on a link pair with mean 0 ln(dB) and variance of 1 ln(dB)^2 , the joint CDF would experience the steepest reductions when the marginal CDF is lowest. A reduction of the log-attenuation correlation from 0.74–0.64 for a link pair having marginal CDFs of 0.01% would correspond to a reduction in the joint CDF from approximately 0.0015 to 0.001. It represents a 33% reduction in the joint probability. At the higher marginal probabilities, the reduction in the joint CDF due to a reduction in correlation would be much less. Hence it is expected that the correlation model proposed is reasonably applicable for the prediction of joint attenuation statistics with regards to 1 minute integration times.

5.6 Concluding Remarks

The characteristics of correlation for route diverse links have been analysed showing the effects of the variation in link asymmetry and link separation. In general, the correlation between the links exhibit high values and this is primarily due

5.6. Concluding Remarks

to both links sharing a common node. Short links (less than 2 km) were found to experience very little de-correlation as a result of both links being largely or completely covered during a rain event.

Theoretical comparison of the correlation estimates shows good agreement with radar estimates and confirms the expectation that the magnitude of the correlation for links situated within a particular region is primarily determined by the relative occurrence of stratiform and convective rain structures.

Based on the simulations, a radar derived correlation model for the correlation has been presented. This can then be used as a parameter for the evaluation of the joint cumulative distribution of attenuation to obtain diversity statistics. Such a formulation is shown to be more general in scope allowing for various combinations of fade margins and provides quite satisfactory agreement compared with the observations.

Experimental attenuation time series for configurations of path lengths applicable to the formulation proposed were not available for verification. However, there is reason for optimism. Sensitivity analysis has shown that the likely effect of variations in integration time have a marginal effect on the predicted diversity statistics.

Conclusions and Suggestions for Further work

IN the following, we summarise the salient observations and results of the thesis with suggestions as to where future efforts might be directed to extend the investigations presented.

It is crucial to understand rainfall dynamics in approaching the study of rain attenuation on radio links. The general cycle of rainfall formation has been presented in chap. 2, showing how the action of drop impact and aggregation leads to a spectrum or distribution of drop sizes. The sizes of these drops vary widely from 0.5–8 mm, having shapes ranging from spherical to oblate.

In general, the DSD spectrum can be approximated with sufficient averaging to the exponential Marshal–Palmer drop size distribution. But for instantaneous measurements of DSDs and accurate estimation of rainfall rates, a Gamma drop size distribution normalised to the total liquid water content provides the best approximation. In this formulation, all the parameters of the distribution are independent and have a physical basis.

In terms of instrumentation, rain gauges and radars are the most frequently used for the estimation of rain rates. In particular rain gauges are considered as “ground truth” instruments when comparing other measurements. The factors affecting annual cumulative statistics of point rainfall rates have also been presented, indicating that integrated measurements of 1 minute rain fall rates are adequate to give suitable cumulative yearly statistics for radio propagation use. For such yearly statistics, the rain rates exceeded between 0.001–1% of time are

Chapter 6. Conclusions and Suggestions for Further work

often used for the design of radio systems. Using the synthetic storm technique and methods such as Taylor's Hypothesis, rain rate spatial statistics such as correlation of rain rates and rain cell size diameters can be obtained from time series data.

Recommendations on the use of yearly and monthly statistics in radio propagation applications, for locations around the world, have been provided by the ITU-R. Other prediction models in the literature for the estimation of cumulative yearly statistics have also been highlighted.

Convective and stratiform rain contain clusters of cells. Such cells have elliptical shapes that are twice as long than wide. Within such cells, rain rates tend to decrease exponentially from the centre of the cell. At high rain rates, these cells have small dimensional extent with the average cell diameter being approximately 2 km. In addition, several models on the structure of rain cells have been highlighted.

Recent investigations are now moving towards stochastic modelling. The stochastic dynamic variations of rain fields can be modelled using either pulse models, Markov chains or power spectral density models. These models are able to reproduce the first and second order statistics for a site and are useful as inputs to evaluate channel models and fade mitigation design for radio links.

Radars provide a distinct advantage in the observation of precipitation over wide areas. In addition their products have wide application within the areas of radio propagation and communications. We have highlighted in chap. 2 the historical genesis of radar meteorology and presented the principles of its operation in the measurement of the back scattered power from a spectrum of rain drops falling towards the ground. In particular, it has been shown that compared to conventional radar, dual polarisation radar measurements reduce the statistical uncertainties of the DSD parameters which are integral to the estimation of rain rates.

To achieve estimation errors to within 25%, dual polarisation radars have to be calibrated to within 1 dB for Z_H and 0.2 dB for Z_{DR} . The S-band CAMRa with its insensitivity to attenuation by rain, superior receiver performance, excellent calibration and high resolution satisfies these minimum constraints.

We have discussed the CRIE measurement campaign where PPI scans of precipitation were systematically collected over two years with no recourse to weather forecasts. In total, the database contained 3199 scans of roughly 1280 events. Re-

sultant rain rates were estimated based on comparing measured and FIM derived Z_H and Z_{DR} values within a lookup table using a functional relationship in which Z_H scales with R for a constant Z_{DR} . This was after occurrences of hail were optimally filtered from the dataset. Radar rain estimated statistics have to be compared with statistics from other sources to confirm their veracity. Consequently, statistics acquired from rain gauge, disdrometer and ITU recommendations show good agreement for the probability range that the rain database is statistically valid (i.e. for exceedance probabilities greater than 0.01% of time).

For the evaluation of attenuation statistics for point to multi-point links, the rain rates have been interpolated using a global RBF interpolation scheme onto a CPPI grid and down to intervals of 100 m. The performance of such an interpolation scheme proved superior compared to weighted distance methods in the retention of information contained within the PPI scans and adjusting to the varying data distribution of the radar. The use of segmented processing to reduce computation times can equally be applied to weighted interpolation schemes if required.

Fade mitigation systems have become *derigueur* in the operation of current and future planned millimetre wave systems, especially with the availability requirements operators now expect from their networks. We have highlighted in chap. 4 the diverse ways rain fades can be mitigated stressing that any candidate FMT has to take into account operating frequency bands, performance objectives of the systems and configuration of the network. In particular, the ability of route diversity to mitigate rain fades on point to point and point to multi-point networks based on the spatial characteristics of the rain field has been extensively analysed with respect to the major factors that influence the diversity statistics. It is clear that the route diversity can provide improvement for star-like networks. Based on extensive attenuation simulations for link pair configurations between 1–10 km operating at frequencies of 20–50 GHz, route diversity shows significant variability both spatially and temporally with the following major trends.

- Diversity increases with an increase in link separation angle up to a maximum of 180°. Most of the increase occurs when links are separated by 45–90°. Further increases especially over 120° show a negligible increase in diversity. The diversity variation also exhibits high symmetry around link separations of 180°.

Chapter 6. Conclusions and Suggestions for Further work

- There is a monotonic increase in the diversity advantage with increasing link length for the same length in both links.
- Considering link asymmetry, the diversity advantage is reduced/increased depending on the degree of asymmetry and whether the diversity is with respect to the shorter/longer link respectively. Therefore, the spatial distribution of rainfall is a marginal factor in determining the diversity statistics compared to the marginal attenuation statistics.
- The standard way of defining the measures of diversity (i.e. gain and improvement) have largely been influenced by the Earth-space systems community where site diversity link paths toward a geosynchronous satellite have the same path lengths. For route diversity link paths, a situation of asymmetry becomes possible. In this case, the estimation of diversity statistics has to be made with respect to a particular link. Consequent upon this, the relative difference in margins between the link pair (i.e. whether the links are balanced or unbalanced) will have a critical impact on the diversity advantage expected. A large difference in link margins will depress diversity with respect to one of the links, while increasing diversity with respect to the other link. The balanced and unbalanced aspects of diversity would only be critical for point to point links where especially high performance is expected. As noted, the nature of point to multi-point links within a network precludes any opportunity for “diversity balancing”.
- Diversity advantage was observed to increase with increases in availability and fade depth. At the high availability levels and fade depths, convective rain of shorter horizontal extent tends to dominate rain attenuation statistics, thereby making links less correlated. At the other end of the spectrum, stratiform rain which is much broader dominates rain attenuation statistics making links less correlated at low availability levels and fade depths.
- In terms of the frequency variation of diversity advantage, it is two pronged. The diversity gain increases with increase in operating frequency. Moreover, the rate of increase is independent of the availability. On the other hand, the diversity improvement statistics are independent of whatever variation with frequency. It is related to the interesting finding that when the diversity improvement factor is expressed in terms of the relative fade depth (e.g. $A[t\%]$)

instead of the absolute fade depth (say 5 dB), the statistic is independent of frequency. Hence, this should provide a convenient way of translating diversity improvement statistics obtained from link data at a particular frequency, to other frequencies of interest between 20–50 GHz for the same link configuration without scaling or processing of the attenuation data. This reformulated definition is also applicable to site diversity for both terrestrial and Earth-space systems.

Comparisons of the statistics with investigations in the reported literature and empirical marginal and joint distributions show encouraging agreement with some of the results obtained within this study. Further investigations are required to confirm the veracity of the trends.

As an example of the benefits of diversity in rain, a non-diversity service offering 99.9% availability (corresponding to typically a 15 dB fade depth) could obtain the same availability with 4 dB less margin, or alternatively increase availability to 99.97% for the same fade margin, with two-way diversity on a path length of 4 km.

Based on appropriate regression fitting analysis, a conceptually simple but accurate diversity model has been presented. It accommodates all the factors that influence the route diversity based on a fundamental assumption. i.e. the fade margins on both links are the same. It represents an improvement from the model presented within ITU-R P.1410 with terms that are distinct and factorisable. In particular, a modified sinusoidal term with an exponent best describes the azimuthal variation of diversity. Optimum values of the exponent for symmetric links were found to be 0.55 and 0.8 with respect to the diversity gain and improvement respectively. For asymmetric links, the exponent values modelled agree closely with results obtained from the literature.

The influence of a change in climatic conditions will introduce large variations in the expected diversity statistics for any particular link configuration. Therefore, it is not foreseeable that the model parameter values (see § 4.8.4, 4.8.5) would be applicable to other climatic areas but the model form written as product of functions dependent upon the factors (L_1 , L_2 , $\%$, $A[\%]$, θ) should be invariant to location even when the same margin assumption does not hold.

The characteristics of correlation for route diverse links have been analysed in chap. 5 showing the effects of the variation in link asymmetry and link separation. In general, the correlation between the links exhibit high values and this is

6.1. Further Work

primarily due to both links sharing a common node. Short links (less than 2 km) were found to experience very little de-correlation as a result of both links being largely or completely covered during a rain event.

Theoretical comparison of the correlation estimates shows good agreement with radar estimates and confirms the expectation that the magnitude of the correlation for links situated within a particular region is primarily determined by the relative occurrence of stratiform and convective rain structures.

Based on the simulations, a model for the correlation has been presented. This can then be used as a parameter for the evaluation of the joint cumulative distribution of attenuation to obtain diversity statistics. Such a formulation is shown to be more general in scope allowing for various combinations of fade margins and provides very good predictions compared with the observations.

Experimental attenuation time series for configurations of path lengths applicable to the formulation proposed were not available for verification. However, there is reason for optimism. Sensitivity analysis has shown that the likely effect of variations in integration time have a marginal effect on the predicted diversity statistics.

6.1 Further Work

There needs to be an analysis of measured times series attenuation data to confirm how closely the model predictions agree with empirical data. This needs to be obtained for the UK as a whole and other climatic regions. This would also help to ascertain to what extent do the diversity statistics vary with change in location. In this regard further analysis of the work of Hendrantoro et al, data available from experimental and commercial star network links would represent a good starting point. Barring acquisition of measured data it is interesting to note whether rain cell models and stochastic rain attenuation models are able to predict diversity statistics that agree with the results obtained. We have already noted the early work of Paulson in using stochastic modelling for the prediction of diversity statistics.

The performance of a network using fade mitigation depends not only on the long-term probability of link fades, but also on the extent to which fades occur over a shorter horizon. Although we have not considered the analysis of diversity over short time scales (over the months and seasons) such statistics are of importance especially in establishing extreme variations of the diversity which

6.1. Further Work

would help to formulate worst and best month statistics helpful in link budget design.

This would help the need for adequate understanding on the error performance and availability of diversity, for digital radio point to point systems. Error performance is specified for available time with a recommended measuring time of one month. For digital radio systems the worst month concept is usually used (see ITU-T G.821 and Rec G. 826). Rain is considered as flat within the occupied bandwidth which means there is an obvious relationship between BER and attenuation. Taking this into account, and using predicted annual and worst month joint attenuation distributions, the error performance and availability with the use of diversity can be established. Important measures are the errored seconds and the severely errored seconds per worst month.

In any diversity system there is a cost associated with sending identical traffic through two different nodes which results in a reduction in network capacity. Therefore the time that any diversity system is activated needs to be optimised so that the bandwidth cost is minimised. Thus statistics of rates of change and duration have an impact on the diversity switching. In general deeper fades are associated with higher rates of change which also imply short fade duration. These will require very rapid resource allocations in a network. The resulting switching criterion needs to consider these two requirements and activate the diversity system before attenuation reaches the fade margin of the link.

The implementation of a proper system for availability assurance combined with optimum frequency re-use is very important for the development of reliable services in this frequency range. Therefore, experiments are needed at the systems level to validate guidelines obtained from propagation simulations and experiments. For example the dynamic characteristics of rain attenuation would affect packet level performance which could severely restrict the application of certain classes of communication protocols.

There is even greater potential in the use of route diversity in conjunction with other fade mitigation techniques. Besides their technical merits the economic merits of such a combination either partially or wholly remains to be explored.

Above all, there is a crucial question that needs to be answered at the level of network design. What proportion of users would be able to obtain diversity to make it a realistic proposition in principle? In practice there needs to be an assessment of what percentage of users within a network need to satisfy a minimum

6.1. Further Work

threshold for the diversity to be economically viable. The nature of the network could have an impact. Typically network planners optimise for coverage, interference and capacity (in that order). Hence, the possible impact of diversity is not likely to be assessed until at the end of the process.

An extension to the applicability of the correlation model in chap. 5 to other climatic zones would be useful. Since the major determinant of the correlation would be the proportion of convective and stratiform events that occur, a statistic such as the thunderstorm ratio mentioned in the works of Ito and Hosoya [2002]; Rice and Holmberg [1973]; Dutton and Dougherty [1979, 1984] on rain rates would be a useful parameter to associate in the formulation of a log-attenuation correlation model that varies with climate. Barring the acquisition of measured link data, the theory of § 5.4.1 would be useful in this regard.

CRIE Data Format

The Chilbolton radar data comes in the form of three distinct measurements of reflectivity, Z_H differential reflectivity, Z_{DR} and linear depolarisation ratio, L_{DR} . The data stored contains either scans of Z_H & Z_{DR} or Z_H & L_{DR} measurements for PPI and RHI scans respectively.

The format can be summarised as follows:

- Blocks are fixed length, 4092 bytes long.
- Raster/Scan data records are of variable length. Each record corresponds to one ray containing up to 512 gates of Z_H and Z_{DR} data collected at the azimuth and elevation specified at the beginning of the record.
- A record of fixed length (64 bytes) precedes each scan. This is termed the Information Record (IR).
- Following the last record of a scan, the contents of the next two bytes have the following meaning:

255/255 Aborted raster

240/0 End of raster

255/1 Start of new scan, i.e. a new IR

The detailed format of the IR and data records is described below. Further information on the acquisition and use of the data can be obtained through the Radio Communications Research Unit, Rutherford Appleton Labs, Didcot, UK.

A.1. Information Record Format

A.1 Information Record Format

Byte	Information
0	Contains 255. This identifies the record as an information record
1	Tape recording is on
2	Hardware word 1 time set
3	Hardware word 2 time set
4	Hardware word 3 time set
5/6	Number of pulse pairs in average
7/8	Dead time in 4 microsecond units
9/10	Minimum range gate: valid numbers are 1 to 511
11/12	Maximum range gate: valid numbers are 2 to 512
13	Polarisation selection: 0 for Z_{DR} , 1 for L_{DR} , 3 for auto toggle.
14	Time series/cal range gate 1
15	Time series/cal range gate 2
16/17	Threshold (1/32) dB pre-scaled
18/19	Scale value to subtract from MTU(1/32) dB
20/21	Minimum angle in raster (arcmin)
22/23	Maximum angle in raster (arcmin)
24/25	Scale value to subtract from MTU(1/32) dB
26	Raster control indicator
27	Coordinate transformation indicator
28/29	Calibration return byte
30	Transmitter power
31	Day the scan was taken
32	Month the scan was taken
33	Year the scan was taken
34	Number of scans within this raster
35	Experiment identifier
36	Scan velocity. This byte is signed and equals (deg/sec)*50
37	Scan type: 1 for RHI, 2 for PPI, 3 for SP, 4 for fixed, 5 for Calibration and 6 for Time series
38	Nature of measurement polarisation: 0 for L_{DR} and 1 for Z_{DR}
39/40	Raster number of this scan

A.2. Raster/Scan format

Byte	Information
41/42	Not used
43/45	Operator identifier
46/47	Not used
48/49	Initial azimuth/elevation of raster, in arcmins
50/51	Increment in azimuth/elevation between scans, in arcmins
52/53	Tape number
54/55/56	Time the scan was taken, in 20ms units from 00 UT
57/58	Number of 4092 blocks recorded from tape open
59	Scans in raster completed (first scan = 1)
60/61	Number of ray records in raster completed
62/63	Central elevation of PPI/Azimuth of RHI in arcmins

A.2 Raster/Scan format

Start of 4092 byte block	Information record for the next raster	64 bytes
	Number of bytes to follow in first ray (1030)	2 bytes
	Azimuth (arc minutes)	2 bytes
	Elevation (arc minutes)	2 bytes
	Z _H - gate 1 (1/4 dB units)	1 byte
	Z _{DR} - (1/8 dB units) or L _{DR} (1/4 dB units) - gate 1	1 byte
	Z _H - gate 2 (1/4 dB units)	1 byte
	Z _{DR} - (1/8 dB units) or L _{DR} (1/4 dB units) - gate 2	1 byte
	Repeated to last gate	
	Number of bytes to follow in second ray	2 bytes
	Azimuth (arc minutes)	2 bytes
	Elevation (arc minutes)	2 bytes
	Z _H - gate 1 (1/4 dB units)	1 byte
	Z _{DR} - (1/8 dB units) or L _{DR} (1/4 dB units) - gate 1	1 byte
	Z _H - gate 2 (1/4 dB units)	1 byte

A.2. Raster/Scan format

	Z _{DR} - (1/8 dB units) or L _{DR} (1/4 dB units) - gate 2	1 byte
	Repeated to last gate	
	:	
	Number of bytes to follow in last ray	2 bytes
	Azimuth (arc minutes)	2 bytes
	Elevation (arc minutes)	2 bytes
	Z _H - gate 1 (1/4 dB units)	1 byte
	Z _{DR} - (1/8 dB units) or L _{DR} (1/4 dB units) - gate 1	1 byte
	Z _H - gate 2 (1/4 dB units)	1 byte
	Z _{DR} - (1/8 dB units) or L _{DR} (1/4 dB units) - gate 2	1 byte
	Repeated to last gate	
	End of Scan or Raster flag = 240; Aborted raster flag = 255	1 byte
	Either contains "1", (the first byte in the information record of the next scan) or "0" (first byte of series to pad out a com- plete 4092 byte block)	1 byte
	If another scan, the remainder of the In- formation Record, otherwise padding to 4092 bytes	63 bytes or variable
	Information Record for the next raster	64 bytes
	Number of bytes to follow in the first ray	2 bytes
	Azimuth (arc minutes)	2 bytes
	Elevation (arc minutes)	2 bytes
	:	

Appendix **B**

Comparisons

B.1 Comparisons of Same Margin Diversity Model Predictions and Radar data

The following figures compare the same margin diversity model (see chapter 5.22 on page 147) predictions with radar derived diversity values for different link configurations. Also included is the predictions using the model developed in this study with the sine coefficient, x set to 1.

B.1. Comparisons of Same Margin Diversity Model Predictions and Radar data

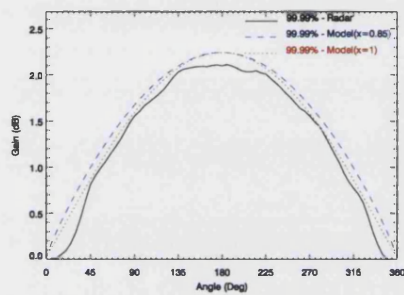


Figure B.1: Diversity plot for path lengths of 1.5 km and 2 km at 99.99% availability

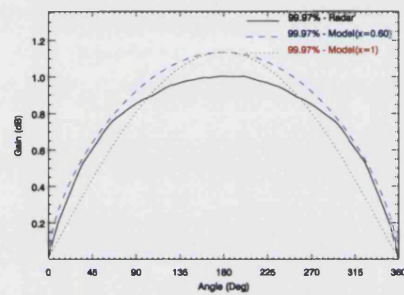


Figure B.2: Diversity plot for path lengths of 1 km and 1 km at 99.97% availability

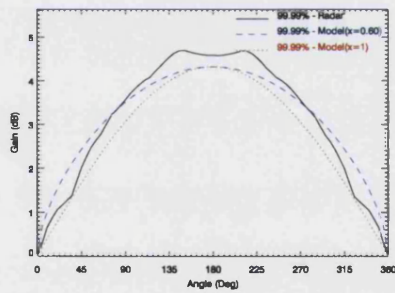


Figure B.3: Diversity plot for path lengths of 2 km and 2 km at 99.99% availability

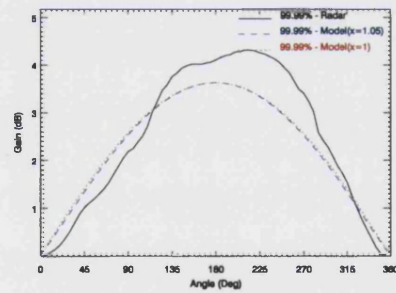


Figure B.4: Diversity plot for path lengths of 3.5 km and 5 km at 99.99% availability

B.1. Comparisons of Same Margin Diversity Model Predictions and Radar data

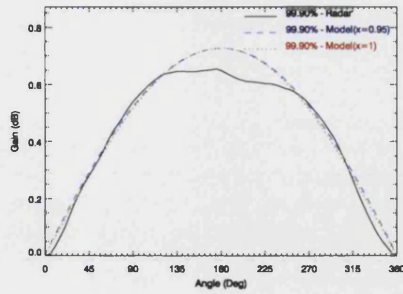


Figure B.5: Diversity plot for path lengths of 2 km and 3 km at 99.9% availability

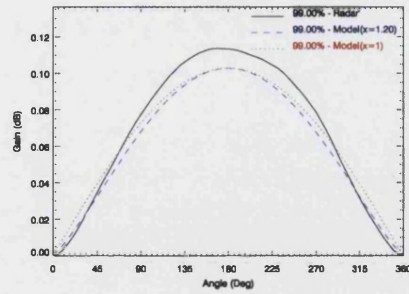


Figure B.6: Diversity plots for path lengths of 2 km and 4 km at 99% availability.

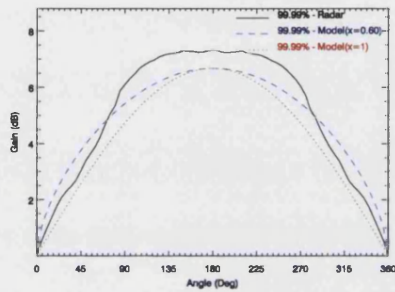


Figure B.7: Diversity plot for path lengths of 3 km and 3 km at 99.99% availability

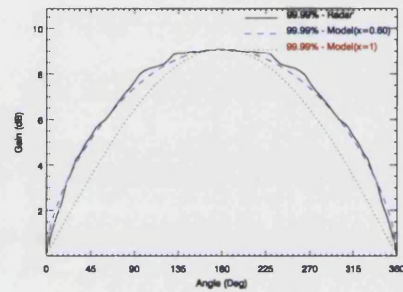


Figure B.8: Diversity plot for path lengths of 4 km and 4 km at 99.99% availability

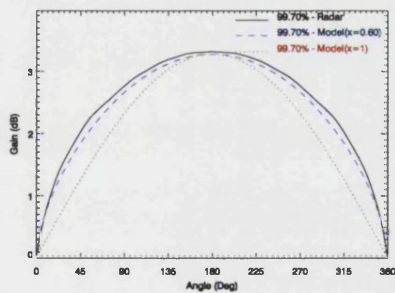


Figure B.9: Diversity plot for path lengths of 6 km at 99.7% availability

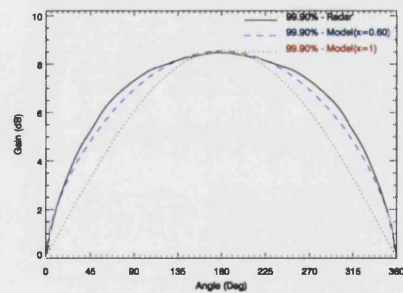


Figure B.10: Diversity plot for path lengths of 9 km at 99.9% availability

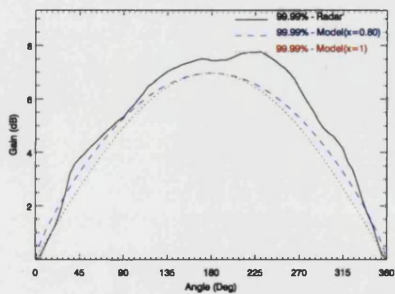


Figure B.11: Diversity plot for path lengths of 4 km and 5 km at 99.99% availability

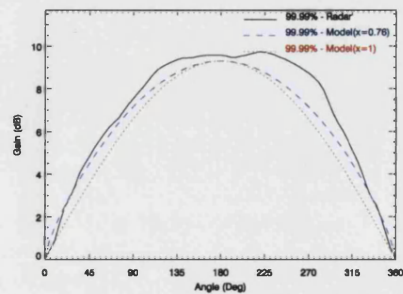


Figure B.12: Diversity plot for path lengths of 5 km and 6 km at 99.99% availability

B.1. Comparisons of Same Margin Diversity Model Predictions and Radar data

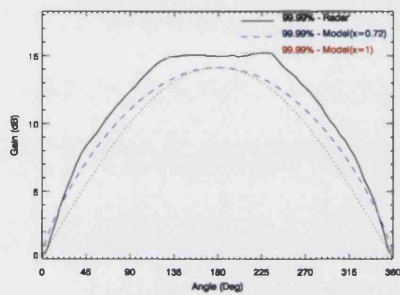


Figure B.13: Diversity plot for path lengths of 7 km and 8 km at 99.99% availability

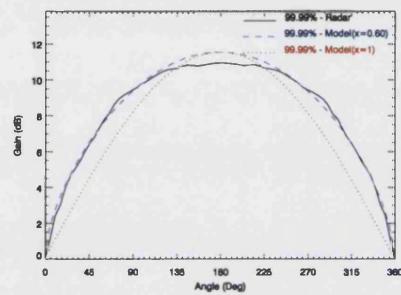


Figure B.14: Diversity plot for path lengths of 5 km at 99.99% availability

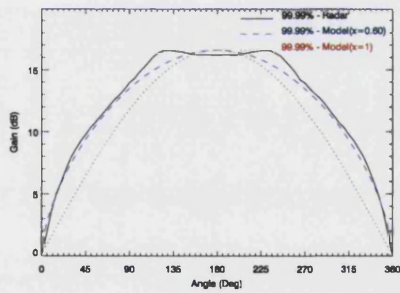


Figure B.15: Diversity plot for path lengths of 7 km and 7 km at 99.99% availability

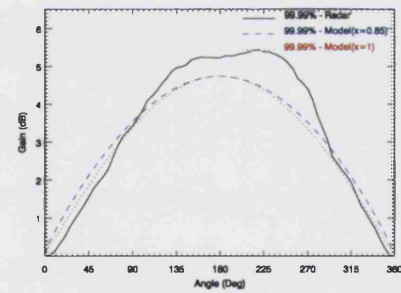


Figure B.16: Diversity plot for path lengths of 3 km and 4 km at 99.99% availability

References and Bibliography

- H. H. Al-Khatib, T. A. Seliga, and V. N. Bringi. Differential reflectivity and its use in the radar measurement of rainfall. Technical report, University of Ohio, Ohio, USA, 1979.
- O. Andrisano, V. Tralli, and R. Verdone. Millimeter waves for short-range multimedia communication systems. *Proceedings of the IEEE*, 86(7):1383–401, 1998.
- K. Andsager, K. V. Beard, and N. F. Laird. Laboratory measurements of axis ratios for large raindrops. *Journal of the Atmospheric Sciences*, 56:2673–2683, August 1999 1999.
- M. A. Askelson, J. P. Aubagnac, and J. M. Straka. An adaptation of the barnes filter applied to the objective analysis of radar data. *Monthly Weather Review*, 128(9):3050–82, Sept. 2000 2000.
- D. Atlas. Radar in meteorology. In *Battan Memorial and 40th Anniversary, Radar Meteorology Conference.*, Boston, USA, 1990. American Meteorological Society.
- D. Atlas, C. W. Ulbrich, and R. Meneghini. The multiparameter remote measurement of rainfall. *Radio Science*, 19(1):3–22, 1984.
- P. H. Austin and R. A. Houze. Analysis of the structure of precipitation patterns in new england. *Journal of Applied Meteorology*, 11:926 – 935, 1972.
- K. Aydin, T. A. Seliga, and V. Balaji. Remote sensing of hail with a dual linear polarisation radar. *Journal of Climate and Applied Meteorology*, 25:1475–1484, 1986.
- J. Bandera, A. D. Papatsoris, P. A. Watson, T. C. Tozer, J. Tan, and J. W. F. Goddard. Vertical path reduction factor for high elevation communication systems. *Electronics Letters*, 35 (18):1584–5, 1999.
- F. Barbaliscia, G. Ravaioli, and A. Paraboni. Characteristics of the spatial statistical dependence of rainfall rate over large areas. *IEEE Transactions on Antennas and Propagation*, 40 (1):8–12, 1992.
- S.L. Barnes. A technique for maximizing details in numerical weather map analysis. *Journal of Applied Meteorology.*, 3:396–409, Aug 1964 1964.
- S. K. Barton and S. E. Dinwiddy. A technique for estimating the throughput of adaptive tdma fade countermeasure systems. *International Journal of Satellite Communications*, 6 (3):10, 1988.
- L. J. Battan. *Radar observation of the atmosphere*. University of Chicago Press, 2nd edition,

REFERENCES AND BIBLIOGRAPHY

1973. ISBN 0-226-03919-6.
- K. V. Beard and C. Chuang. A new model for the equilibrium shape of raindrops. *Journal of the Atmospheric Sciences*, 44(11):1509 – 1524, June 1987 1987.
- K. V. Beard and A. R. Jameson. Raindrop canting. *Journal of Atmospheric Science*, 40:448–453, 1983.
- R. K. Beatson, J. B. Cherrie, and C. T. Mouat. Fast fitting of radial basis functions: Methods based on preconditioned gmres iteration. *Advances in Computational Mathematics*, 11(2-3):253–70, 1999.
- V. N. Bringi and V. Chandrasekar. *Polarimetric Doppler weather radar*. Cambridge University Press, 1st edition, 2001. ISBN 0 - 521 - 62384 - 7.
- V. N. Bringi, S. M. Cherry, M. P. M. Hall, and T. A. Seliga. A new accuracy in determining rainfall rates and attenuation due to rain by means of dual-polarization radar measurements. In *International Conference on Antennas and Propagation*, page 186. IEE London UK, 1978.
- G. Brussard. A meteorological model of rain induced cross-polarisation. *IEEE Transactions on Antennas and Propagation*, 24:5–11, 1976.
- G. Brussard and P. A. Watson. *Atmospheric modelling and millimetre wave propagation*. Chapman and Hall, 1994. ISBN 0412562308.
- G. H. Bryant, I. Adimula, C. Riva, and G. Brussaard. Rain attenuation statistics from rain cell diameters and heights. *International Journal of Satellite Communications*, 19(3):263–83, 2001.
- S. Callaghan and E. Vilar. Synthesis of two dimensional rain fields for systems using spatial diversity. In *2nd International Workshop, ESTEC, Noordwijk, Netherlands, 26-28 May 2003* 2003.
- A.S. Campora. A shared resource tdma approach to increase the rain margin of 12/14 ghz satellite systems. *The Bell System Technical Journal*, 58(9):9, 1979.
- A.S. Campora. Rain margin improvement using resource sharing on 12 ghz satellite downlinks. *The Bell System Technical Journal*, 60(2):10, 1981.
- C. Capsoni and E. Matricciani. Theoretical random process for prediction of rain attenuation statistics in site diversity satellite links above 10 ghz. *Electronics Letters*, 18(21):917 – 919, October 1982 1982.
- C. Capsoni and E. Matricciani. Orbital and site diversity systems in rain environment: Radar-derived results. *IEEE Transactions on Antennas and Propagation*, AP-33(5):517–22, 1985.
- C. Capsoni, F. Fedi, C. Magistroni, A. Paraboni, and A. Pawlina. Data and theory for a new model of the horizontal structure of rain cells for propagation applications. *Radio Science*, 22(3):395–404, 1987.
- C. Capsoni, E. Matricciani, and M. Mauri. Sirio-ots 12 ghz orbital diversity experiment at fucino. *IEEE Transactions on Antennas and Propagation*, 38(6):777–82, 1990.
- V. Chandrasekar and R. J. Keeler. Antenna pattern analysis and measurements for multi-parameter radar. *Journal of Technology*, 10:673–683, 1993.

REFERENCES AND BIBLIOGRAPHY

- S. M. Cherry and J. W. F. Goddard. The use of dual polarisation radar data to predict attenuation due to precipitation on earth-space paths. NRPP 34, Radio Communications Research Unit, Rutherford Appleton Laboratories, Didcot, United Kingdom, January 1984 1984.
- S. M. Cherry and J. W. F. Goddard. The use of dual-polarisation radar in rain scatter interference studies. In *Fourth International Conference on Antennas and Propagation*, volume 248, page 597. IEE London UK, 1985.
- COST210. *Influence of the atmosphere on interference between radio communications systems at frequencies above 1 GHz*. Number 1. European Commission, Luxembourg, 1991. ISBN 9282780236. URL <http://europa.eu.int>.
- COST235. *Radiowave propagation effects on next generation fixed services terrestrial telecommunications systems*. Number 1. European Commission, Luxembourg, 1996. ISBN 9282780236. URL <http://europa.eu.int>.
- COST255. *Radiowave propagation modelling for new satcom services at Ku-band and above*. European Commission, Luxembourg, 1999. URL <http://www.estec.esa.nl/xewww/cost255/>.
- COST280. *Propagation impairment mitigation for millimetre wave radio systems*. European Commission, 2000. URL <http://www.cost280.rl.ac.uk>.
- P. S. P. Cowpertwait. A generalized spatial-temporal model of rainfall based on a clustered point process. *The Royal Society. Proceedings: Mathematical, Physical and Engineering Sciences*, 450(1938):163 – 175, Jul. 8, 1995 1995.
- D.R. Cox and V.S. Isham. A simple spatial-temporal model of rainfall. *Proceedings of the Royal Society of London*, 415(1849):317–328, 1988. . Series A, Mathematical and Physical Sciences, Vol. 415, No. 1849. (Feb. 9, 1988), pp. 317-328. Abstract.
- CRABS. Studies of existing propagation data and methods. Technical report, European Union, 1998. URL <http://www.telenor.no/fou/prosjekter/crabs>.
- CRABS. Propagation planning for lmds. Report, European Union, 1999. URL <http://www.telenor.no/fou/prosjekter/crabs>.
- K. H. Craig, S. Hurley, and T. Tjelta. Propagation studies for enhanced broadband wireless access. In *27th URSI General Assembly*, page 4, Maastricht, Netherlands, August 2002 2002. International Union of Radio Science.
- R. K. Crane. Prediction of attenuation by rain. *IEEE Transactions on Communications*, COM-28(9, part 2):1717–33, 1980.
- R. K. Crane. Propagation modelling-past, present and future. In *Sixth International Conference on Antennas and Propagation*, volume 301, pages 546+474, Coventry, UK, 4-7 April 1989 1989. IEE.
- R. K. Crane. Space-time structure of rain rate fields. *Journal of Geophysical Research*, 95(D3): 2011–20, 1990.
- R. K. Crane. *Electromagnetic wave propagation through rain*. John Wiley & Sons, Inc, New York, USA, 1996.
- R. K. Crane and Shieh Horng Chung. A two-component rain model for the prediction of

REFERENCES AND BIBLIOGRAPHY

- site diversity performance. *Radio Science*, 24(5):641–65, 1989.
- G. P. Cressman. An operational objective analysis system. *Monthly Weather Review*, 87: 367–374, Oct 1959 1959.
- R. Doviak and D. Zrnic. *Doppler radar and weather observations*. Academic Press, London, 2nd edition, 1992.
- Z. Drezner and G. O. Wesolowsky. On the computation of the bivariate normal integral. *Journal of Statistical Computation and Simulation*, 35(1):101–107, 1990.
- G. Drufuca and I. Zawadzki. Statistics of raingauge data. *Journal of Applied Meteorology*, 14:1419 – 1430, December 1975 1975.
- E. J. Dutton and H. T. Dougherty. Year-to-year variability of rainfall for microwave applications in the u.s.a. *IEEE Transactions on Communications*, COM-27:829 – 832, May 1979 1979.
- E. J. Dutton and H. T. Dougherty. A second modelling approach to year-to-year rainfall variability in the u.s.a for microwave/millimetre wave applications. *IEEE Transactions on Communications*, COM-32(10):1145 – 1148, October 1984 1984.
- B. J. Easterbrook and D Turner. Prediction of attenuation by rainfall in the 10.7 to 11.7 ghz communication band. *Proceedings of the IEE*, 114:557–565, May 1967.
- D. J. Emerson, R. M. Nelhams, and B. L. Clark. Adaptive tdma for fade countermeasures. In *Proceedings of the Olympus Utilisation Conference*, 1989.
- L. Feral, F. Mesnard, H. Sauvageot, L. Castanet, and J. Lemorton. Rain cells shape and orientation distribution in south-west of france. *Physics and Chemistry of the Earth*, 25(10 - 12):1073 – 1078, 2000.
- L. Feral, H. Sauvageot, L. Castanet, and J. Lemorton. Hycell - a new hybrid model of the rain horizontal distribution for propagation studies: 1. modeling of the rain cell. *Radio Science*, 38(3):1056, 2003a.
- L. Feral, H. Sauvageot, L. Castanet, and J. Lemorton. Hycell - a new hybrid model of the rain horizontal distribution for propagation studies: 2. statistical modeling of the rain rate field. *Radio Science*, 38(3):1057, 2003b.
- U. C. Fiebig. A time series generator modelling rain fading. In *URSI Commission F*, Garmisch-Partenkirchen, 2002.
- G. B. Foote and P. S. Du Toit. Terminal velocity of raindrops aloft. *Journal of Applied Meteorology*, 8:249 – 253, 1969.
- R. Franke. Smooth interpolation of scattered data by local thin plate splines. *Computers & Mathematics with Applications*, 8(4):273–81, 1982.
- I. Frigyes and P. Horvath. Mitigation of rain induced fading: Route diversity vs route-time coding. In *IEE Conference on Antennas and Propagation*, page 2, Exeter, UK, 2003. IEE.
- H. Fukuchi. Correlation properties of rainfall rates in the united kingdom. *IEE Proceedings, Part H*, 135(2):83–88, 1988.
- F. M. Galante. Statistical evaluation of rain fades and fade durations at 11 ghz in the

REFERENCES AND BIBLIOGRAPHY

- European region [satellite links]. In *International Conference on Satellite Communication Systems Technology*, pages 302–7, London, UK, 7–10 April 1975. IEE.
- T. Givens and P. S. Ray. Response of a two-dimensional dual-doppler radar wind synthesis. *Journal of Atmospheric and Oceanic Technology*, 11(2 pt. 1):239–55, April 1994.
- J. W. F. Goddard and S. M. Cherry. The ability of dual-polarisation radar (copolar linear) to predict rainfall rate and microwave attenuation. *Radio Science*, 19(1):201–208, 1984a.
- J. W. F. Goddard and S. M. Cherry. Site diversity advantage as a function of spacing and satellite elevation angle, derived from dual-polarization radar data. *Radio Science*, 19(1):231–7, 1984b.
- J. W. F. Goddard and M. Thurai. Modelling of interference by hydrometeor scatter. NRPP 132, Radio Communications Research Unit, Rutherford Appleton Laboratories, Didcot, United Kingdom, 1992.
- J. W. F. Goddard and M. Thurai. Modelling of attenuation due to rain on terrestrial paths using Chilbolton radar data. NRPP 159, Radio Communications Research Unit, Rutherford Appleton Laboratories, Didcot United Kingdom, 1996.
- J. W. F. Goddard and M. Thurai. Radar-derived path reduction factors for terrestrial systems. In *Tenth International Conference on Antennas and Propagation*, volume 436, pages 553–396, Edinburgh, UK, Publ 1997. IEE.
- J. W. F. Goddard, S. M. Cherry, and V. N. Bringi. Comparison of dual polarisation radar measurements of rain with ground based disdrometer measurements. *Journal of Applied Meteorology*, 21:252–256, 1982.
- J. W. F. Goddard, J. D. Eastment, and M. Thurai. The Chilbolton advanced meteorological radar: A tool for multidisciplinary atmospheric research. *Electronics & Communication Engineering Journal*, 6(2):77–86, 1994a.
- J. W. F. Goddard, J. Tan, and M. Thurai. Technique for calibration of meteorological radars using differential phase. *Electronics Letters*, 30(2):166–7, 1994b.
- J. W. F. Goddard, K. Morgan, A. J. Illingworth, and H. Sauvageot. Dual polarisation measurements in precipitation using the Camra and Rabelais radar. In *27th Conference on Radar Meteorology*, page 4, Vail, USA, 1995. American Meteorological Society.
- J. Goldhirsh. Prediction methods for rain attenuation statistics at variable path angles and carrier frequencies between 13 and 100 GHz. *IEEE Transactions on Antennas and Propagation*, AP-23(6):786–91, 1975.
- J. Goldhirsh. A review on the application of nonattenuating frequency radars for estimating rain attenuation and space-diversity performance. *IEEE Transactions on Geoscience Electronics*, GE-17(4):218–39, 1979.
- J. Goldhirsh. Space diversity performance prediction for earth-satellite paths using radar modeling techniques. *Radio Science*, 17(6):1400–10, 1982.
- J. Goldhirsh. Rain cell size statistics as a function of rain rate for attenuation modeling. *IEEE Transactions on Antennas and Propagation*, AP-31(5):799–801, 1983.
- J. Goldhirsh. Rain-rate duration statistics over a five-year period: A tool for assessing slant path fade durations. *IEEE Transactions on Antennas and Propagation*, 43(5):435–9,

REFERENCES AND BIBLIOGRAPHY

- 1995.
- J. Goldhirsh. Two-dimension visualization of rain cell structures. *Radio Science*, 35(3): 713–29, 2000.
- J. Goldhirsh and B. Musiani. Rain cell size statistics derived from radar observations at wallops island, virginia. *IEEE Transactions on Geoscience and Remote Sensing*, GE-24(6): 947–54, 1986.
- J. Goldhirsh and B. H. Musiani. Dimension statistics of rain cell cores and associated rain rate isopleths derived from radar measurements in the mid-atlantic coast of the united states. *IEEE Transactions on Geoscience and Remote Sensing*, 30(1):28–37, 1992.
- E. Gorgucci, G. Scarchilli, and V. Chandrasekar. A robust estimator of rainfall rate using differential reflectivity. *Journal of Atmospheric and Oceanic Technology*, 11(2):586–92, April 1994.
- E. Gorgucci, V. Chandrasekar, and G. Scarchilli. Radar and surface measurement of rainfall during cape: 26 july 1991 case study. *Journal of Applied Meteorology*, 34:1570–1577, 1995.
- E. Gorgucci, G. Scarchilli, and V. Chandrasekar. Procedure to calibrate multiparameter weather radar using properties of the rain medium. *IEEE Transactions on Geoscience and Remote Sensing*, 37(1):269–276, Jan 1999 1999.
- B. Gremont. Simulation of rainfield attenuation for satellite communication networks. In *1st Workshop of the COST 280 Action "Propagation Impairments Mitigation for Millimetre-Wave Radio Systems"*, Malvern, UK., 1st-3rd July 2002 2002.
- B. Gremont and A. Tawfik. Markov modelling of rain attenuation for satellite and terrestrial communications. In Institute of Electrical Engineers, editor, *IEE International Conference on Antennas and Propagation*, Exeter, 31st March - April 3rd 2003 2003.
- B. Gremont, R. J. Watson, and P. A. Watson. Modelling and detection of rain attenuation for mf-tdma satellite networks utilizing fade mitigation techniques. In *Joint Cost272/Cost280 International Workshop*, Noordwijk, The Netherlands, 26th May 2003 2003. European Space Agency, ESTEC.
- K. L. S. Gunn and T. W. R. East. The microwave properties of precipitation particles. *Quarterly Journal of the Royal Meteorological Society*, 80:522 –, 1954.
- R. Gunn and G. Kinzer. The terminal velocity of fall for water droplets in stagnant air. *Journal of meteorology*, 6:243–248, 1949.
- M. P. M. Hall. A review of the application of multiple-parameter radar measurement of precipitation. *Radio Science*, 19(1):37–43, 1984.
- M. P. M. Hall, J. W. F. Goddard, and S. M. Cherry. Identification of hydrometeors and other targets by dual-polarization radar. *Radio Science*, 19(1):132–40, 1984.
- P. J. Hardaker, A. R. Holt, and J. W. F. Goddard. Comparing model and measured rainfall rates obtained from a combination of remotely sensed and in situ observations. *Radio Science*, 32(5):1785–96, 1997.
- B. N. Harden, J. R. Norbury, and W. J. K. White. Model of intense convective rain cells for estimating attenuation on terrestrial millimetric radio links. *Electronics Letters*, 10(23):

REFERENCES AND BIBLIOGRAPHY

- 483–4, 1974.
- B. N. Harden, J. R. Norbury, and W. J. K. White. Measurements of rainfall for studies of millimetric radio attenuation. *IEE Journal on Microwaves, Optics and Acoustics*, 1(6): 197–202, 1977.
- B. N. Harden, J. R. Norbury, and W. J. K. White. Attenuation/rain-rate relationships on terrestrial microwave links in the frequency range 10–40 ghz. *Electronics Letters*, 14, no.5: 154–5, 1978a.
- B. N. Harden, J. R. Norbury, and W. J. K. White. Estimation of attenuation by rain on terrestrial radio links in the uk at frequencies from 10 to 100 ghz. *IEE Journal on Microwaves, Optics and Acoustics*, 2, no.4:97–104, 1978b.
- G. Hendratoro, R. J. C. Bultitude, and D. D. Falconer. Use of cell-site diversity in millimeter-wave fixed cellular systems to combat the effects of rain attenuation. *IEEE Journal on Selected Areas in Communications*, 20(3):602–14, 2002.
- A. Hendry and G. McCormick. Radar observations of alignment of precipitation particles by electrostatic fields in thunderstorms. *Journal of Geophysical Research*, 81:5353–5357, 1976.
- D. B. Hodge. A 15.3 ghz satellite-to-ground path-diversity experiment utilizing the ats-5 satellite. *Radio Science*, 9(1):1–6, 1974.
- D. B. Hodge. Path diversity for earth-space communication links. *Radio Science*, 13(3): 481–7, 1978.
- D. C Hogg. Path diversity in propagation of millimeter waves through rain. *IEEE Transactions on Antennas and Propagation*, 15(3):410, 1967.
- D. C Hogg. Intensity and extent of rain on earth-space paths. *Nature*, 243:337 – 338, June 1973 1973.
- A. R. Holt, J. W. F. Goddard, G. J. G. Upton, M. J. Willis, A. R. Rahimi, P. D. Baxter, and C. G. Collier. Measurement of rainfall by dual-wavelength microwave attenuation. *Electronics Letters*, 36(25):2099 – 2101, 7 Dec 2000 2000.
- T. Ihara, H. Furuhashi, and T. Manabe. Modification of morita and higuti's prediction method of lognormal rain attenuation distribution by using spatial correlation of specific attenuation. *Transactions of the Institute of Electronics and Communication Engineers of Japan, Section E*, E69(2):139–47, Feb. 1986 1986.
- A. J Illingworth. Improved precipitation rates and data quality by using polarimetric measurements. In *Advanced Applications of Weather Radar*. Springer, 2003.
- A. J. Illingworth and T. M. Blackman. The need to represent raindrop size spectra as normalized gamma distributions for the interpretation of polarization radar observations. *Journal of Applied Meteorology*, 41(3):286–97, 2002.
- A. J. Illingworth and I. J. Caylor. Polarization radar estimates of raindrop size spectra and rainfall rates. *Journal of Atmospheric and Oceanic Technology*, 6(6):939–49, 1989.
- A. J. Illingworth and M. P. Johnson. The role of raindrop shape and size spectra in deriving rainfall rates using polarisation radar. In *29th International Conference on Radar Meteorology*, Montreal, Canada, 1999.

REFERENCES AND BIBLIOGRAPHY

- A. J. Illingworth, J. D. Hauser, and P. Amayenc. A comparison of optical shadowgraph instruments for measuring raindrop size spectra. *Journal of Atmospheric and Oceanic Technology*, 7:175 – 176, 1990.
- C. Ito and Y. Hosoya. The thunderstorm ratio as a regional climatic parameter: Its effects on different integration-time conversion, rain attenuation, site diversity and rain depolarization. In *27th URSI General Assembly*, page 4, Maastricht, Netherlands, August 2002 2002. International Union of Radio Science.
- ITU. Propagation data and prediction methods required for the design of terrestrial broadband millimetric radio access systems operating in a frequency range of about 20-50 GHz, April 2003a. URL <http://www.itu.int>.
- ITU. Characteristics of precipitation for propagation modelling, April 2003b. URL <http://www.itu.int>.
- S. M Jones and P. A Watson. Attenuation and countermeasures in millimetre-wave point to multi-point networks. *Radio Science*, 28(6):1057, 1993.
- J. Joss and A. Waldvogel. Comments: Some observations on the joss-waldvogel rainfall disdrometer. *Journal of Applied Meteorology*, 16:112 – 113, 1977.
- J. Joss, J. C. Thams, and A. Waldvogel. The variation of raindrop size distribution at locarno. In *International Conference on Cloud Physics*, Toronto, Canada, August 26 - 30 1968.
- J. D. Kanellopoulos and S. Ventouras. Prediction of the outage performance of an unbalanced orbital diversity earth-space system (log-normal case). *European Transactions on Telecommunications and Related Technologies*, 4(4):415–21, 1993.
- N. King. Broadband business and residential radio access. In *IEE Seminar New Access Network Technologies*, page 70, London, 31 Oct 2000. IEE.
- A. N. Kolmogorov. The local structure of turbulence in incompressible viscous fluid for very large reynolds numbers (in russian). *C. R. Acad. Sci. USSR*, 30(301):0, 1941 1941.
- T. Konrad. Statistical models of summer rain showers derived from fine scale radar observations. *Journal of Applied Meteorology*, 17:171 – 188, 1978.
- T. Kozu and K. Nakamura. Rainfall parameter estimation from dual radar measurements combining reflectivity profile and path integrated attenuation. *Journal of Atmospheric and Oceanic Technology*, 8:259–271, 1991.
- J.O Laws. Measurements of the fall velocity of water drops and raindrops. *Transactions of the American Geophysical Union*, 22:709 – 721, 1941.
- J.O Laws and D.A Parsons. The relation of rain drop size to intensity. *Transactions of the American Geophysical Union*, 24(2):452–460, 1943.
- M. J. Leitao and P. A. Watson. Application of dual linearly polarized radar data to prediction of microwave path attenuation at 10-30 ghz. *Radio Science*, 19(1):209–21, 1984.
- K. Lin and C. A. Levis. Site diversity for satellite earth terminals and measurements at 28 ghz. *Proceedings of the IEEE*, 81(6):897 – 904, June 1993 1993.
- S. H. Lin. Statistical behavior of rain attenuation. *Bell System Technical Journal*, 52(4):557–81, 1973.

REFERENCES AND BIBLIOGRAPHY

- S. H. Lin. A method for calculating rain attenuation distributions on microwave paths. *Bell System Technical Journal*, 54(6):1051–86, 1975.
- P. Lindholm. Marginal and joint attenuation cumulative distributions for the telenor 42 ghz star link network located at kjeller, norway. Telenor, Kjeller, Norway, 2001.
- R. J. A. Little and D. B. Rubin. *Statistical analysis with missing data*. Wiley Series In Probability And Mathematical Statistics. John Wiley & Sons, Inc, New York, 1987. ISBN 0-471-80254-9.
- H. Liu and V. Chandrasekar. Classification of hydrometeors based on polarimetric radar measurements: Development of fuzzy logic and neuro-fuzzy systems, and in situ verification. *Journal of Atmospheric and Oceanic Technology*, 17:140–164, 2000.
- F. K. Lutgens and E. J. Tarbuck. *The atmosphere*. Prentice Hall, 8th edition, 2001. ISBN 0-13-087957-6.
- P. Mahonen, T. Saarinen, Z. Shelby, and L. Munoz. Wireless internet over lmds: Architecture and experimental implementation. *IEEE Communications Magazine*, 39(5):126–32, 2001.
- J. Marshall and W. Hitschfield. Interpretation of the fluctuating echo from randomly distributed scatterers. *Canadian Journal of Physics*, 31:962–943, 1953.
- J. Marshall and W. Palmer. The distribution of rain drops with size. *Journal of meteorology*, 5:165, 1948.
- T. Maseng and P. M. Bakken. A stochastic dynamic model of rain attenuation. *IEEE Transactions on Communications*, COM-29(5):660–9, 1981.
- J. Mass. A simulation study of rain attenuation and diversity effects on satellite links. *COMSAT Technical Review*, 17(1):159 – 187, 1987.
- E. Matricciani and A. Pawlina. Statistical characterization of rainfall structure and occurrence for convective and stratiform rain inferred from long term point rain rate data. In *AP 2000 Millennium Conference on Antennas & Propagation*, Davos, Switzerland, 9-14 April 2000 2000. URSI.
- R. Medhurst. Rainfall attenuation of centimeter waves: Comparison of theory and measurement. *IEEE Transactions on Antennas and Propagation*, 13(4):550 – 564, 1965.
- K. Morita and I. Higuti. Statistical studies on rain attenuation and site diversity effect on earth to satellite links in microwave and millimeter wavebands. *The Transactions of the IECE of Japan*, E61(6):425 – 432, June 1978 1978.
- Morrison and Cross. Scattering of a plane electromagnetic wave by axisymmetric rain drops. *Bell System Technical Journal*, 53:955–1019, 1971.
- F. Moupfouma. Model of rainfall-rate distribution for radio system design. *IEE Proceedings H (Microwaves, Optics and Antennas)*, 132(1):39–43, 1985.
- F. Moupfouma and L. Martin. Point rainfall rate cumulative distribution function valid at various locations. *Electronics Letters*, 29(17):1503–5, 1993.
- J. R. Norbury. A rapid-response rain gauge. *Journal of Physics E: Scientific Instruments*, 4(8):601–602, 1971.

REFERENCES AND BIBLIOGRAPHY

- P. J. Northrop. A clustered spatial-temporal model of rainfall. *The Royal Society. Proceedings: Mathematical, Physical and Engineering Sciences*, 454(1975):1875 – 1888, 1998.
- J. A. Nystuen and J. R. Proni. A comparison of automatic rain gauges. *Journal of Atmospheric and Oceanic Technology*, 13:62 – 73, February 1996 1996.
- C. Onof, R. E. Chandler, A. Kakou, P. J. Northrop, H.S. Wheeler, and V.S. Isham. Rainfall modelling using poisson-cluster processes: A review of developments. *Stochastic Environmental Research and Risk Assessment (SERRA)*, 14(6):384 – 411, 2000.
- K. J. Ord, S. Arnold, A. O'Hagan, and J. Forster. *Kendall's Advanced Theory of Statistics*. Hodder Arnold, 6th edition, 2004.
- L. Ordano. Assessment of correlation properties of rainfall intensity measured in Italy. In *Fifth International Conference on Antennas and Propagation*, pages xxviii+596+379, York, UK, 30 March-2 April 1987 1987. IEE.
- D. B. Owen. Tables for computing bivariate normal probability. *Annals of Mathematical Statistics*, 27:1075–1090, 1956.
- A. Paraboni, G. Masini, and C. Riva. The spatial structure of rain and its impact on the design of advanced tlc systems. In *Fourth Ka-band utilisation conference*, pages 169 – 172, Venice, Italy, Nov. 2-4, 1998 1998.
- K. Paulson. A spatial-temporal model of rain rate random fields. *Radio Science*, 37(5): 21–28, Sept. 2002 2002.
- K. Paulson. Prediction of diversity statistics on terrestrial microwave links. *Radio Science*, 38(3):1047, 2003a.
- K. S. Paulson. The simulation of rain effects on millimetre wave networks by the fractal disaggregation of radar data. Didcot, United Kingdom, April 2003 2003b.
- K. S. Paulson and C. J. Gibbins. Rain models for the prediction of fade durations at millimetre wavelengths. *IEE Proceedings Microwaves, Antennas and Propagation*, 147(6):431–6, 2000.
- A. Pawlina. Some features of ground rain patterns measured by radar in north Italy. *Radio Science*, 19(3):855 – 861, May-June 1984 1984.
- A. Pawlina and M. Binaghi. Radar rain intensity fields at ground level: New parameters for propagation impairments prediction in temperate regions. In *7th URSI Commission F Open Symposium on Wave Propagation and Remote Sensing*, pages 217 – 220, Ahmedabad, India, 1995. URSI.
- J. R. Probert-Jones. The radar equation in meteorology. *Quarterly Journal of the Royal Meteorological Society*, 88(378):485, 1962.
- H. R. Pruppacher and K. V. Beard. A wind tunnel investigation of the internal circulation and shape of water drops falling at terminal velocity in air. *Quarterly Journal of the Royal Meteorological Society*, 96:247 – 256, 1970.
- H. R. Pruppacher and R. L. Pitter. A semi-empirical determination of the shape of cloud and rain drops. *Journal of the Atmospheric Sciences*, 28:86 – 94, 1971.
- J. D. Reid. Decorrelation time of weather signals. In *Preprints of the 14th Radar Meteorology Conference*, Boston, USA, 1970. American Meteorological Society.

REFERENCES AND BIBLIOGRAPHY

- P. L. Rice and N. R. Holmberg. Cumulative time statistics of surface point rainfall rates. *IEEE Transactions on Communications*, COM - 21:1131 – 1136, 1973.
- I. Rodriguez-Iturbe, D.R. Cox, and V.S. Isham. A point process model for rainfall: Further developments. *Proceedings of the Royal Society of London*, A(417):283 – 298, 1988.
- R. R. Rogers. A review of multiparameter radar observations of precipitation. *Radio Science*, 19(1):23–36, 1984.
- P. Rouvrais. Battling the bottleneck with wireless. *Alcatel Telecommunications Review.*, 4: 269–76, 2000 2000.
- C. L. Ruthroff. Rain attenuation and radio path design. *Bell System Technical Journal*, 49(1): 121–35, 1970.
- J. W. Ryde. Echo intensity and attenuation due to clouds, rain, hail, sand and dust storms at centimetre wavelengths. Technical report, General Electric Company, Wembley, England, 1941.
- J. W. Ryde and D. Ryde. Attenuation of centimetre waves by rain, hail and clouds. Technical report, General Electric Company, Wembley, England, 1944.
- E. T Salonen and Baptista. J. Poires. A new global rainfall rate model. In *Tenth International Conference on Antennas and Propagation*, volume 436, pages 2.182 – 2.185, Edinburgh, UK, 1997. Institution of Electrical Engineers.
- H. Sauvageot, F. Mesnard, and R. S. Tenorio. The relation between the area-average rain rate and the rain cell size distribution parameters. *Journal of the Atmospheric Sciences*, 56 (1):57–70, 1999.
- M. Schwartz, W. R. Bennett, and S. Stein. *Communications systems and techniques*, volume 4 of *Inter-University Electronics Series*. McGraw-Hill, New York, 1966.
- T. A. Seliga and V. N. Bringi. Potential use of radar differential reflectivity measurements at orthogonal polarizations for measuring precipitation. *Journal of Applied Meteorology*, 15(1):69–76, 1976.
- T. A. Seliga, V. N. Bringi, and H. H. Khatib. A preliminary study of comparative measurements of rainfall rate using the differential reflectivity radar technique and a raingauge network. *Journal of Applied Meteorology*, 20:1362 – 1368, November 1981 1981.
- D. Shepard. A two-dimensional interpolation function for computer mapping of irregularly spaced data. Technical report, Havard Univ., Center for Environmental Design Studies, Cambridge, MA, USA, 20 March 1968 1968.
- C. Sinka and J. Bito. Site diversity against rain fading in lmds systems. *IEEE Microwave and Wireless Components Letters*, 13(8):317 – 319, August 2003 2003.
- M. I. Skolnik. *Introduction to radar systems*. McGraw-Hill, New York, 3rd edition, 2002.
- D. P. Stapor and T. Pratt. Generalised analysis of dual polarisation radar measurements of rain. *Radio Science*, 19:90–98, 1984.
- J. J. Stephens and A. L. Polan. Spectral modification by objective analysis. *Monthly Weather Review*, 99:374–378, 1971.
- J. J. Stephens and J. M. Stitt. Optimum influence radii for interpolation with the method

REFERENCES AND BIBLIOGRAPHY

- of successive corrections. *Monthly Weather Review*, 98:680–687, 1970.
- J. M. Straka, D. Zrnic, and A. Ryzhkov. Bulk hydrometeor classification and quantification using polarimetric radar data: Synthesis of relations. *Journal of Applied Meteorology*, 39: 1341–1371, 2000.
- J. Tan and L. Pedersen. Study of simultaneous coverage and route diversity improvement under rainy periods for lmds systems at 42 ghz. In *Proceedings of the ESA Millenium Conference on Antennas and Propagation (AP-2000)*, volume 444, page 4, Davos, Switzerland, April 2000 2000.
- P. Tattelman and D. D. Grantham. A review of models for estimating 1 min rainfall rates for microwave attenuation calculations. *IEEE Transactions on Communications*, COM-33 (4):361–72, 1985.
- G. I. Taylor. The spectrum of turbulence. *Proceedings of the Royal Society of London*, 164 (919):476 – 490, February 1938 1938.
- J. Testud, S. Oury, R. A. Black, P. Amayenc, and D. Xiankang. The concept of "normalized" distribution to describe raindrop spectra: A tool for cloud physics and cloud remote sensing. *Journal of Applied Meteorology*, 40(6):1118–40, 2001.
- Le Bouar E. et al Testud, J. The normalized intercept parameter no^* to describe the variability of the particle size distribution of hydrometeors and to parameterize the rain and cloud relations. In *30th International Conference on Radar Meteorology*, Munich, Germany, 2001.
- K. I. Timothy, M. C. Mondal, and S. K. Sarkar. Dynamical properties of rainfall for performance assessment of earth-space communication links at ku and ka bands. *International Journal of Satellite Communications*, 16:53 – 57, 1998.
- A. Tokay and D. A. Short. Evidence from tropical raindrop spectra of the origin of rain from stratiform versus convective clouds. *Journal of Applied Meteorology*, 35(3):355–71, March 1996.
- A. Tokay, A. Kuger, and W. F. Krajewski. Comparison of drop size distribution measurements by impact and optical disdrometers. *Journal of Applied Meteorology*, 40(11):2083 – 2097, 2001.
- A. Tokay, K. R. Wolff, P. Bashor, and O. K. Dursun. On the measurement errors of the joss-waldvogel disdrometer. In *31st International Conference on Radar Meteorology*, volume P3A.2, page 4, Seattle, WA, USA, 2003. American Meteorological Society.
- J. Tournadre. Determination of rain cell characteristics from the analysis of topex altimeter echo waveforms. *Journal of Atmospheric and Oceanic Technology*, 15:387 – 406, 1998.
- R. J. Trapp and III Doswell, C. A. Radar data objective analysis. *Journal of Atmospheric and Oceanic Technology*, 17(2):105–20, Feb. 2000.
- TRMM. Tropical rainfall measuring mission. Technical report, National Aeronautics and Space Administration (NASA), 1997. URL <http://trmm.gsfc.nasa.gov>.
- D. Turner, B. J. Easterbrook, and J. E. Golding. Experimental investigation into radio propagation of 11 to 11.5 gc/s. *Proceedings of the IEE*, 113:1477–1489, September 1966.
- D. J. W. Turner and D. Turner. Attenuation due to rainfall on a 24 km microwave link

REFERENCES AND BIBLIOGRAPHY

- working at 11, 18 and 36 ghz. *Electronics Letters*, 6(19):298 – 298, 14 May 1970 1970.
- C. W. Ulbrich. Natural variations in the analytical form of the raindrop size distribution. *Journal of Climate and Applied Meteorology*, 22(10):1764–75, 1983.
- C. W. Ulbrich. A review of the differential reflectivity technique of measuring rainfall. *IEEE Transactions on Geoscience and Remote Sensing*, GE-24(6):955–65, 1986.
- C. W. Ulbrich and D. Atlas. The rain parameter diagram: Methods and applications. *Journal of Geophysical Research*, 83(C3):1319–25, 1978.
- I. Usman, M. J. Willis, and R. J. Watson. Route diversity analysis and modelling for millimetre wave point to multi-point systems. In *1st International Workshop Cost 280 - Propagation Impairment Mitigation for Millimetre Wave Radio Systems*, page 10, Malvern, UK, July 2002 2002.
- I. Usman, P. Lindholm, M. J. Willis, and R. J. Watson. Rain fade countermeasure prediction and performance for millimetre broadband fixed wireless communication systems. In *International Conference on Antennas and Propagation (ICAP)*, volume 2, page 4, Exeter, United Kingdom, 31st March - 3rd April 2003 2003. Institute of Electrical. ISBN 0 85296 752 7.
- N. Uzunoglu, B. G. Evans, and A. R. Holt. Evaluation of the scattering of an electromagnetic wave from precipitation particles by the use of fredholm integral equations. *Electronics Letters*, 12(12):312–13, 10 June 1976.
- N. K. Uzunoglu, B. G. Evans, and A. R. Holt. Scattering of electromagnetic radiation by precipitation particles and propagation characteristics of terrestrial and space communication systems. *Proceedings of the Institution of Electrical Engineers*, 124(5):417–24, 1977.
- W. Vogel, G. W. Torrence, and J. Allnutt. Rain fades on low elevation angle earth-satellite paths: Comparative assessment of the austin, texas, 11.2 ghz experiment. *Proceedings of the IEEE*, 81(6):885 – 896, June 1993 1993.
- A. Waldvogel and J. Joss. The influence of a cold front on the drop size distribution. In *Conference on Cloud Physics*, pages 6 – 7, Fort Collins, Colorado, 1970.
- H.S. Wheeler, V.S. Isham, D.R. Cox, R. E. Chandler, A. Kakou, P. J. Northrop, L. Oh, C. Onof, and I. Rodriguez-Iturbe. Spatial-temporal rainfall fields: modelling and statistical aspects. *Hydrology and Earth System Sciences*, 4(4):581 – 601, 2000.
- M. J. Willis. Fade counter-measures applied to transmissions at 20/30 ghz. *Electronics & Communication Engineering Journal*, 3(2):88–96, 1991.
- M. J. Willis and B. G. Evans. Fade countermeasures at ka band for olympus. *International Journal of Satellite Communications*, 6:301 – 311, July - September 1988 1988.
- M. J. Willis, A. Paulsen, I. Usman, P. Lindholm, K. S. Paulson, T. Tjelta, and C. Adams. The application of diversity to the embrace mm-wave lmds network. In *Ist International Workshop-COST Action 280. Propagation Impairment Mitigation for Millimetre Wave Radio Systems*, page 4, Malvern, UK, 2002. URL <http://www.cost280.rl.ac.uk/>.
- M. K. Yau and R. R. Rogers. An inversion problem on inferring the size distribution of precipitation areas from rain gauge measurements. *Journal of Atmospheric Science*, 41: 439–447, 1984.

REFERENCES AND BIBLIOGRAPHY

- I. Zawadzki. Statistical properties of precipitation patterns. *Journal of Applied Meteorology*, 12:459 – 472, April 1973 1973.
- D. Zrnica, R. Doviak, and D. W. Burgess. Probing tornadoes with a pulse doppler radar. *Quarterly Journal of the Royal Meteorological Society*, 103:707–720, 1977.